Quantifying the Effects of Permafrost Degradation in Arctic Coastal Environments via Satellite Earth Observation

Dissertation zur Erlangung der Doktorwürde
„doctor rerum naturalium" (Dr. rer. nat.)
der Philosophischen Fakultät der
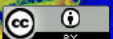Julius-Maximilians-Universität Würzburg

vorgelegt von

Marius Balthasar Philipp

aus Dillingen a.d. Donau

März 2023

Titelbild:

Das Titelbild zeigt eine Falschfarbendarstellung einer Küstenlinie nahe Drew Point in Alaska, basierend auf Sentinel-1 Satellitendaten. Für den roten Kanal wurde hierbei die Median-Rückstreuung in einer vertikal-horizontal Polarisation, für den grünen Kanal die Median-Rückstreuung in einer vertikal-vertikal Polarisation, und für den blauen Kanal die Standardabweichung der Rückstreuung in einer vertikal-vertikal Polarisation gewählt. Die Illustration deckt den Zeitraum Juni September 2020 ab.

II

Eingereicht am: 30.03.2023

Tag des Kolloquiums: 07.11.2023

Von: Marius Balthasar Philipp

Ort: Lehrstuhl für Fernerkundung der Julius-Maximilians-Universität Würzburg, in Kooperation mit dem Deutschen Fernerkundungsdatenzentrum (DFD) des Deutschen Zentrums für Luft- und Raumfahrt (DLR)

Erstbetreuerin: Prof. Dr. Claudia Künzer, Universität Würzburg

Zweitbetreuer: Prof. Dr. Christof Kneisel, Universität Würzburg

This dissertation was prepared at the department "Land Surface Dynamics" of the German Remote Sensing Data Center (DFD), Earth Observation Center (EOC), German Aerospace Center (DLR), Oberpfaffenhofen, Germany.

"What we know is a drop, what we don't know is an ocean."

Isaac Newton

Table of Contents

Acknowledgement

This thesis would not have been possible without the guidance and support of many people to whom I would like to express sincere gratitude:

To my mentor and supervisor at the German Remote Sensing Data Center (DFD) of the German Aerospace Center (DLR), Prof. Dr. Claudia Kuenzer, for her continuous support and valuable guidance, while at the same time giving me the freedom and trust to freely explore and develop my ideas. Thanks to her profound experience in remote sensing, clear guidance, and moral support, I was able to successfully finish my thesis within three years. Her uninterrupted commitment and quick response to any of my matters is highly appreciated.

To my mentors at the University of Wuerzburg, Prof. Dr. Christof Kneisel and Prof. Dr. Tobias Ullmann, for agreeing to supervise this thesis and their helpful advice and feedback on my dissertation. In particular, I want to express my deep gratitude towards Tobias for his moral support throughout the entire course of this thesis.

To Dr. Andreas Dietz, team leader at DLR-DFD, for his frequent support, advice, and feedback on my work. I very much appreciated the open-minded and supportive working atmosphere within a great team.

To my colleagues at DLR-DFD, for the valuable discussions, feedback, joint lunch breaks, and general support. Special thanks go hereby to Dr. Celia Baumhoer and Dr. Mariel Dirscherl for their highly appreciated comments on my studies and thesis. It has been a great pleasure for me to work on my PhD thesis at the DFD-DLR. The fantastic working atmosphere and highly competent colleagues enriched my time at DLR.

To Dr. Martin Wegmann at the University of Wuerzburg, who always supported me and helped on laying the foundation of my career in remote sensing.

To my wonderful parents Karin and Bernhard Philipp, for their endless support and trust in both me and my decisions, even in the most difficult times. I'm grateful for having been raised by such wonderful people who helped shaping me into the person I am today and which I can be proud of.

To my sister Marisa Philipp and her limitless support and selflessness towards me. Her moral advice and encouragement in times of hardship are deeply appreciated.

To my aunt Ulrike Philipp for always caring about me and raising my motivation with delicious meals.

Finally, to Christina Haering for her love, care, and unlimited moral support, especially during the most intense stages of this past journey towards my PhD. Her ability to help me find the necessary strength and faith in both me and my path is invaluable.

Summary

Permafrost degradation is observed all over the world as a consequence of climate change and the associated Arctic amplification, which has severe implications for the environment. Landslides, increased rates of surface deformation, rising likelihood of infrastructure damage, amplified coastal erosion rates, and the potential turnover of permafrost from a carbon sink to a carbon source are thereby exemplary implications linked to the thawing of frozen ground material. In this context, satellite earth observation is a potent tool for the identification and continuous monitoring of relevant processes and features on a cheap, long-term, spatially explicit, and operational basis as well as up to a circumpolar scale.

A total of 325 articles published in 30 different international journals during the past two decades were investigated on the basis of studied environmental foci, remote sensing platforms, sensor combinations, applied spatio-temporal resolutions, and study locations in an extensive review on past achievements, current trends, as well as future potentials and challenges of satellite earth observation for permafrost related analyses. The development of analysed environmental subjects, utilized sensors and platforms, and the number of annually published articles over time are addressed in detail. Studies linked to atmospheric features and processes, such as the release of greenhouse gas emissions, appear to be strongly under-represented. Investigations on the spatial distribution of study locations revealed distinct study clusters across the Arctic. At the same time, large sections of the continuous permafrost domain are only poorly covered and remain to be investigated in detail. A general trend towards increasing attention in satellite earth observation of permafrost and related processes and features was observed. The overall amount of published articles hereby more than doubled since the year 2015. New sources of satellite data, such as the Sentinel satellites and the Methane Remote Sensing LiDAR Mission (Merlin), as well as novel methodological approaches, such as data fusion and deep learning, will thereby likely improve our understanding of the thermal state and distribution of permafrost, and the effects of its degradation. Furthermore, cloud-based big data processing platforms (e.g. Google Earth Engine (GEE)) will further enable sophisticated and long-term

analyses on increasingly larger scales and at high spatial resolutions.

In this thesis, a specific focus was put on Arctic permafrost coasts, which feature increasing vulnerability to environmental parameters, such as the thawing of frozen ground, and are therefore associated with amplified erosion rates. In particular, a novel monitoring framework for quantifying Arctic coastal erosion rates within the permafrost domain at high spatial resolution and on a circum-Arctic scale is presented within this thesis. Challenging illumination conditions and frequent cloud cover restrict the applicability of optical satellite imagery in Arctic regions. In order to overcome these limitations, Synthetic Aperture RADAR (SAR) data derived from Sentinel-1 (S1), which is largely independent from sun illumination and weather conditions, was utilized. Annual SAR composites covering the months June September were combined with a Deep Learning (DL) framework and a Change Vector Analysis (CVA) approach to generate both a high-quality and circum-Arctic coastline product as well as a coastal change product that highlights areas of erosion and build-up. Annual composites in the form of standard deviation (sd) and median backscatter were computed and used as inputs for both the DL framework and the CVA coastal change quantification. The final DL-based coastline product covered a total of 161,600 km of Arctic coastline and featured a median accuracy of ±6.3 m to the manually digitized reference data. Annual coastal change quantification between 2017 2021 indicated erosion rates of up to 67 m per year for some areas based on 400 m coastal segments. In total, 12.24% of the investigated coastline featured an average erosion rate of 3.8 m per year, which corresponds to 17.83 km^2 of annually eroded land area. Multiple quality layers associated to both products, the generated DL-coastline and the coastal change rates, are provided on a pixel basis to further assess the accuracy and applicability of the proposed data, methods, and products.

Lastly, the extracted circum-Arctic erosion rates were utilized as a basis in an experimental framework for estimating the amount of permafrost and carbon loss as a result of eroding permafrost coastlines. Information on permafrost fraction, Active Layer Thickness (ALT), soil carbon content, and surface elevation were thereby combined with the aforementioned erosion rates. While the proposed experimental framework provides a valuable outline for quantifying the volume loss of frozen ground and carbon release, extensive validation of the utilized environmental products and resulting volume loss numbers based on 200 m segments are necessary. Furthermore, data of higher spatial resolution and information of carbon content for deeper soil depths are required for more accurate estimates.

Zusammenfassung

Als Folge des Klimawandels und der damit verbundenen „Arctic Amplification"
wird weltweit eine Degradation des Dauerfrostbodens (Permafrost) beobachtet, welche
schwerwiegende Auswirkungen auf die Umwelt hat. Erdrutsche, erhöhte Oberflächen-
verformungsraten, eine zunehmende Wahrscheinlichkeit von Infrastrukturschäden,
verstärkte Küstenerosionsraten und die potenzielle Umwandlung von Permafrost von
einer Kohlenstoffsenke in eine Kohlenstoffquelle sind dabei beispielhafte Auswirkun-
gen im Zusammenhang mit dem Auftauen von gefrorenem Bodenmaterial. In diesem
Kontext ist die Satelliten-gestützte Erdbeobachtung ein wirkmächtiges Werkzeug zur
Identifizierung und kontinuierlichen Überwachung relevanter Prozesse und Merkmale
auf einer kostengünstigen, langfristigen, räumlich expliziten und operativen Basis und
auf einem zirkumpolaren Maßstab.

Insgesamt 325 Artikel, die in den letzten zwei Jahrzehnten in 30 verschiedenen
internationalen Zeitschriften veröffentlicht wurden, wurden auf Basis der adressierten
Umweltschwerpunkte, Fernerkundungsplattformen, Sensorkombinationen, angewand-
ten raum-zeitlichen Auflösungen und den Studienorten in einem umfassenden Überblick
über vergangene Errungenschaften und aktuelle Trends untersucht. Zusätzlich wur-
den zukünftige Potenziale und Herausforderungen der Satelliten-Erdbeobachtung
für Permafrost-bezogene Analysen diskutiert. Auf die zeitliche Entwicklung der un-
tersuchten Umweltthemen, eingesetzten Sensoren und Satelliten-Plattformen sowie
die Zahl der jährlich erscheinenden Artikel wurde detailliert eingegangen. Studien zu
atmosphärischen Eigenschaften und Prozessen, wie etwa der Freisetzung von Treibhaus-
gasemissionen, waren stark unterrepräsentiert. Deutliche geografische Schlüssel-Gebiete,
auf welche sich der Großteil der Studien konzentrierte, konnten in Untersuchungen
zur räumlichen Verteilung der Studienorte identifiziert werden. Gleichzeitig sind große
Teile des kontinuierlichen Permafrost-Gebiets nur spärlich abgedeckt und müssen noch
im Detail untersucht werden. Es wurde ein allgemeiner Trend zu einer zunehmenden
Aufmerksamkeit bezüglich der Satelliten-gestützten Erdbeobachtung von Permafrost
und verwandten Prozessen und Merkmalen beobachtet. Die Gesamtzahl der veröf-
fentlichten Artikel hat sich dabei seit dem Jahr 2015 mehr als verdoppelt. Neue

Quellen für Satellitendaten, wie beispielweise die Sentinel-Satelliten und die Methane Remote Sensing LiDAR Mission (Merlin), sowie neuartige methodische Ansätze, wie Datenfusion und Deep Learning, werden dabei voraussichtlich unser Verständnis bzgl. des thermischen Zustands und der Verteilung von Permafrost-Vorkommen sowie die Auswirkungen seines Auftauens verbessern. Darüber hinaus werden Cloud-basierte Big-Data-Verarbeitungsplattformen (z.B. Google Earth Engine (GEE)) anspruchsvolle und langfristige Analysen in immer größeren Maßstäben und mit hoher räumlicher Auflösung erleichtern.

In dieser Arbeit wurde ein besonderer Fokus auf arktische Permafrost-Küsten gelegt, die eine zunehmende Vulnerabilität gegenüber Umweltparametern wie dem Auftauen von gefrorenem Boden aufweisen und daher von verstärkten Erosionsraten betroffen sind. Ein neuartiger Ansatz zur Quantifizierung der arktischen Küstenerosion innerhalb des Permafrost-Gebiets mit hoher räumlicher Auflösung und auf zirkum-arktischem Maßstab wird in dieser Dissertation präsentiert. Schwierige Beleuchtungsbedingungen und häufige Bewölkung schränken die Anwendbarkeit optischer Satellitenbilder in arktischen Regionen ein. Um diese Einschränkungen zu überwinden, wurden Synthetic Aperture RADAR (SAR) Daten von Sentinel-1 (S1) verwendet, die weitgehend unabhängig von Sonneneinstrahlung und Wetterbedingungen sind. Jährliche SAR-Komposite, welche die Monate Juni bis September abdecken, wurden mit einem Deep Learning (DL)-Ansatz und einer Change Vector Analysis (CVA)-Methode kombiniert, um sowohl ein qualitativ hochwertiges und zirkum-arktisches Küstenlinienprodukt als auch ein Produkt für die Änderungsraten (Erosion und küstennahe Aggregation von Sedimenten) der Küste zu generieren. Jährliche Satelliten-Komposite in Form von der Standardabweichung (sd) und des Medians der SAR Rückstreuung wurden hierbei berechnet und als Eingabedaten sowohl für den DL-Ansatz als auch für die Quantifizierung der CVA-basierten Küstenänderung verwendet. Das endgültige DL-basierte Küstenlinienprodukt deckt insgesamt 161.600 km der arktischen Küstenlinie ab und wies eine Median-Abweichung von ±6,3 m gegenüber den manuell digitalisierten Referenzdaten auf. Im Zuge der Quantifizierung von jährlichen Küstenveränderungen zwischen 2017 und 2021 konnten Erosionsraten von bis zu 67 m pro Jahr und basierend auf 400 m Küstenabschnitten identifiziert werden. Insgesamt wiesen 12,24% der untersuchten Küstenlinie eine durchschnittliche Erosionsrate von 3,8 m pro Jahr auf, was einer jährlichen erodierten Landfläche von 17,83 km^2 entspricht. Mehrere Qualitäts-Datensätze, die beiden Produkten zugeordnet sind, wurden auf Pixelbasis bereitgestellt, um die Genauigkeit und Anwendbarkeit der präsentierten Daten, Methoden und Produkte weiter einordnen zu können.

Darüber hinaus wurden die extrahierten zirkum-arktischen Erosionsraten als Grundlage in einem experimentellen Ansatz verwendet, um die Menge an Permafrost-Verlust

und Kohlenstofffreistzung als Konsequenz der erodierten Permafrost-Küsten abzuschätzen. Dabei wurden Informationen zu Permafrost-Anteil, Active Layer Thickness (ALT), Höhenmodellen und der Menge an im Boden gespeichertem Kohlenstoff mit den oben genannten Erosionsraten kombiniert. Während der präsentierte experimentelle Ansatz einen wertvollen Ausgangspunkt für die Quantifizierung des Volumenverlusts von gefrorenem Boden und der Kohlenstofffreisetzung darstellt, ist eine umfassende Validierung der verwendeten Umweltprodukte und der resultierenden Volumenzahlen erforderlich. Zusätzlich werden für genauere Abschätzungen Daten mit höherer räumlicher Auflösung und Informationen zum Kohlenstoffgehalt für tiefere Bodentiefen benötigt.

Russian Summary

Деградация вечной мерзлоты наблюдается во всем мире как следствие изменения климата, которое имеет серьезные последствия для окружающей среды. Таким образом, оползни, повышенная скорость деформации поверхности, растущая вероятность повреждения инфраструктуры, ускоренная береговая эрозия и потенциальное превращение вечной мерзлоты из поглотителя углерода в источник углерода являются показательными последствиями, связанными с оттаиванием мерзлого материала грунта. В этом контексте спутниковое наблюдение за Землей является мощным инструментом для идентификации и непрерывного мониторинга соответствующих процессов и характеристик на дешевой, долгосрочной, пространственной и оперативной основе, а также вплоть до циркумполярного масштаба.

В общей сложности 325 статей, опубликованных в 30 различных международных журналах за последние два десятилетия, были исследованы по изучаемым экологическим очагам, платформам дистанционного зондирования, комбинациям датчиков, прикладным пространственно-временным разрешениям и месту исследования в обширном обзоре прошлых достижений, текущих , а также будущие возможности и проблемы спутникового наблюдения Земли для анализа вечной мерзлоты. Подробно рассматривается развитие анализируемых объектов окружающей среды, используемых датчиков и платформ, а также количество ежегодно публикуемых статей с течением времени. Исследования, связанные с атмосферными особенностями и процессами, такими как выбросы парниковых газов, представлены крайне недостаточно. Исследования пространственного распределения мест проведения исследований выявили отчетливые исследовательские кластеры по всей Арктике. В то же время большие участки сплошной области вечной мерзлоты охвачены слабо и требуют детального изучения. Наблюдалась общая тенденция к увеличению внимания к наземным спутниковым наблюдениям вечной мерзлоты и связанных с ней процессов и особенностей. Общее количество опубликованных статей более чем удвоилось с 2015 года. Новые источники спутниковых данных, такие как спутники Sentinel и миссия LiDAR для

дистанционного зондирования метана (Merlin), а также новые методологические подходы, такие как объединение данных обучения, тем самым, вероятно, улучшит наше понимание теплового состояния и распределения вечной мерзлоты, а также последствий ее деградации. Кроме того, облачные платформы обработки больших данных (например, Google Earth Engine (GEE)) в дальнейшем позволят проводить сложный и долгосрочный анализ во все более крупных масштабах и с высоким пространственным разрешением.

В этой диссертации особое внимание было уделено арктическим побережьям вечной мерзлоты, которые характеризуются повышенной уязвимостью к параметрам окружающей среды, таким как таяние мерзлых грунтов, и, следовательно, связаны с усиленной скоростью эрозии. В частности, в рамках этой диссертации представлена новая система мониторинга для количественной оценки скорости эрозии арктических берегов в области вечной мерзлоты с высоким пространственным разрешением и в циркумарктическом масштабе. Сложные условия освещенности и частая облачность ограничивают возможности применения оптических спутниковых снимков в арктических регионах. Чтобы преодолеть эти ограничения, были использованы данные радара с синтезированной апертурой (SAR), полученные от Sentinel-1 (S1), которые в значительной степени не зависят от солнечного освещения и погодных условий. Ежегодные составные данные SAR, охватывающие период с июня по сентябрь, были объединены со структурой глубокого обучения (DL) и подходом анализа вектора изменений (CVA) для создания как высококачественного продукта для циркумарктической береговой линии, так и продукта для прибрежных изменений, который выделяет участки эрозии и наростов. Годовые композиты в форме стандартного отклонения (sd) и медианного обратного рассеяния были рассчитаны и использованы в качестве входных данных как для структуры DL, так и для количественной оценки прибрежных изменений CVA. Окончательный продукт береговой линии на основе DL охватывал в общей сложности 161.600 км береговой линии Арктики и имел медианную точность ±6,3 м по сравнению с оцифрованными вручную справочными данными. Ежегодная количественная оценка изменения береговой линии в период с 2017 по 2021 год показала скорость эрозии до 67 м в год на основе 400-метровых участков побережья для некоторых районов. Всего на 12,24% исследованной береговой линии средняя скорость эрозии составила 3,8 м в год, что соответствует 17,83 км^2 ежегодно эродируемой площади суши. Несколько слоев качества, связанных с обоими продуктами, сгенерированной DL-береговой линией и скоростью изменения берегов, предоставляются на основе пикселей для дальнейшей оценки точности и применимости предлагаемых данных, методов и продуктов.

Наконец, извлеченные скорости циркумарктической эрозии использовались в

качестве основы для экспериментальной оценки количества вечной мерзлоты и потерь углерода в результате эрозии береговых линий вечной мерзлоты. Таким образом, информация о доле вечной мерзлоты, толщине активного слоя (ALT), содержании углерода в почве и высоте поверхности была объединена с вышеупомянутыми скоростями эрозии. В то время как предлагаемая экспериментальная схема обеспечивает ценную схему для количественной оценки потери объема мерзлого грунта и выброса углерода, необходима обширная проверка используемых экологических продуктов и результирующих значений потери объема на основе 200-метровых сегментов. Кроме того, для более точных оценок требуются данные с более высоким пространственным разрешением и информация о содержании углерода в более глубоких слоях почвы.

List of Figures

List of Tables

Abbreviations and Acronyms

AATSR	Advanced Along Track Scanning Radiometer
ABoVE	Arctic-Boreal Vulnerability Experiment
AC	Atlas of the Cryosphere
ACD	Arctic Coastal Dynamics Database
AI	Artificial Intelligence
ALANIS	Atmosphere-Land Interactions Study
ALOS	Advanced Land Observing Satellite
ALT	Active Layer Thickness
AMIS	Agricultural Market Information System
AMPAC	Arctic Methane and Permafrost Challenge
AMSR2	Advanced Microwave Scanning Radiometer 2
AMSR-E	Advanced Microwave Scanning Radiometer - Earth Observing System
AOI	Area of Interest
ASAR	Advanced Synthetic Aperture Radar
Asc	Ascending
ASI	ARTIST Sea Ice
ASTER	Advanced Spaceborne Thermal Emission and Reflection Radiometer
AVHRR	Advanced Very High Resolution Radiometer
AVNIR-2	Advanced Visible and Near Infrared Radiometer Type 2
BN	Batch Normalization
CACOON	Changing Arctic Carbon cycle in the cOastal Ocean Near-shore
CALM	Circumpolar Active Layer Monitoring
CAVM	Circumpolar Arctic Vegetation Map
CCI	Climate Change Initiative
CliC	Climate and Cryosphere
CNES	National Centre for Space Studies
CNN	Convolutional Neural Networks
Conv	Convolution
COSMO-Skymed	Constellation of small Satellites for Mediterranean basin Observation
CVA	Change Vector Analysis
dB	decibel
DCW	Digital Chart of the World

DEM	Digital Elevation Model
Desc	Descending
DGPS	Differential Global Positioning System
D-InSAR	Differential Interferometric Synthetic Aperture Radar
DL	Deep Learning
DLR	German Aerospace Center
DMSP	Defense Meteorological Satellite Program
DSM	Digital Surface Model
DUE	Data User Element
ECV	Essential Climate Variables
Envisat	Environmental Satellite
EOC	Earth Observation Center
ESA	European Space Agency
ETM+	Enhanced Thematic Mapper Plus
EVI	Enhanced Vegetation Index
FAO	Food and Agriculture Organization of the United Nations
GAUL	Global Administrative Unit Layers
GBM	Gradient Boosting Machines
GCOS	Global Climate Observing System
GEE	Google Earth Engine
GLCNMO	Global Land Cover by the National Mapping Organization
GLIMS	Global Land Ice Measurements from Space
GMT	Greenwich Mean Time
GOME	Global Ozone Monitoring Experiment
GPS	Global Positioning System
GRACE	Gravity Recovery And Climate Experiment
GRD	Ground Range Detected
GSHHG	Global Self-consistent, Hierarchical, High-resolution Geography Database
GSHHS	Global Self-consistent, Hierarchical, High-resolution Shorelines
GTN-P	Global Terrestrial Network for Permafrost
HWSD	Harmonized World Soil Database
IHO	International Hydrographic Organization
InSAR	Interferometric Synthetic Aperture Radar
IPCC	Intergovernmental Panel on Climate Change
IPDA	Integrated Path Differential Absorption
IW	Interferometric Wide
JERS-1	Japanese Earth Resources Satellite 1
LiDAR	Light Detection and Ranging
LST	Land Surface Temperature
MAGT	Mean Annual Ground Temperature
MEaSUREs	Making Earth System Data Records for Use in Research Environments
MERIS	Medium Resolution Imaging Spectrometer
Merlin	Methane Remote Sensing LiDAR Mission
ML	Machine Learning
MODIS	Moderate Resolution Imaging Spectroradiometer
MOSES	Modular Observation Solutions for Earth Systems

MSS	Multi Spectral Scanner
MTL	Mean Tidal Level
MV	Moving Window
NASA	National Aeronautics and Space Administration
NCSCDv2	Northern Circumpolar Soil CarbonDatabase version 2
NDVI	Normalized Difference Vegetation Index
NGEE	Next-Generation Ecosystem Experiments
NHL	Northern High Latitudes
NOAA	National Oceanic and Atmospheric Administration
OCS	Organic Carbon Stocks
OMI	Ozone Monitoring Instrument
OSM	OpenStreetMap
RA-2	Radar Altimeter 2
PALSAR	Phased Array L-Band Synthetic Aperture Radar
PeRL	Permafrost Region Pond and Lake
PERMOS	Swiss Permafrost Monitoring Network
PRISM	Panchromatic Remote-sensing Instrument for Stereo Mapping
PSI	Persistent Scatterer Interferometry
QTH	Qinghai Tibet Highway
QTP	Qinghai Tibet Plateau
QTR	Qinghai Tibet Railway
RADAR	Radio Detection and Ranging
RCP	Representative Concentration Pathways
ReLU	Rectified Linear Unit
ReSALT	Remotely Sensed Active Layer Thickness
RGB	Red-Green-Blue
RMSprop	Root Mean Square Propagation
S1	Sentinel-1
S2	Sentinel-2
SAR	Synthetic Aperture RADAR
SCI	Science Citation Index
SCIAMACHY	Scanning Imaging Absorption Spectrometer for Atmospheric Chartography
sd	standard deviation
SE	Snow Extent
SEARCH	Study of Environmental Arctic Change
SLC	Scan Line Corrector
SMAP	Soil Moisture Active Passive
SPOT	Satellite Pour l'Observation de la Terre
SR	Surface Reflectance
SRES	Special Report on Emission Scenarios
SRTM	Shuttle Radar Topography Mission
SSM/I	Special Sensor Microwave/Imager
SWE	Snow Water Equivalent
TM	Thematic Mapper
TROPOMI	TROPOspheric Monitoring Instrument
TSP	Thermal State of Permafrost
TTOP	Temperature at the Top of Permafrost

USA	United States of America
UTM	Universal Transverse Mercator
VGI	Volunteered Geographic Information
VH	vertical-horizontal
VV	vertical-vertical
WDBII	CIA World Data Bank II
WMO	World Meteorological Organization
WoS	Web of Science
WVS	World Vector Shorelines

Chapter 1

Introduction[*]

1.1 Scientific Relevance

Roughly one quarter of the terrestrial land area on the Northern Hemisphere is covered by permafrost, making it an integral part of the cryosphere (J. Brown et al., 2002). The amount of carbon which is stored in its frozen masses is almost double in quantity compared to the carbon content that is present in the atmosphere (Schuur et al., 2015; Pörtner et al., 2019). The thawing of permafrost triggers the release of this carbon content to the atmosphere in the form of greenhouse gases, which in turn could cause climate change to accelerate more rapidly than estimated by current Earth system models (Schuur et al., 2015). A global economic damage within the realm of trillions of dollars due to abrupt releases of methane and caused by the thawing of permafrost is hereby predicted if no mitigation actions are taken (Whiteman et al., 2013). Thus, substantial consequences for human society and the environment can be expected by a widespread degradation of permafrost. An increasing thickness of the active layer (L. M. Farquharson et al., 2019), the development of geological hazards, (Arenson & Jakob, 2015), amplified coastal erosion rates (Isaev et al., 2019; Cunliffe et al., 2019; B. M. Jones et al., 2018), magnified rates of surface deformation (X. Zhang et al., 2019; Rudy et al., 2018; C. Wang et al., 2017), and the release of greenhouse gases (C. Song et al., 2012; Watts et al., 2014; Curasi et al., 2016) are hereby just some examples of the implications associated with the climate change driven degradation of permafrost soils.

Permafrost is defined as ground material that remains constantly frozen for two or more consecutive years (Van Everdingen et al., 2005). Over 65% of terrestrial area

---

[*]Parts of this chapter are based on Philipp et al. (2021), Philipp et al. (2022), and Philipp et al. (2023).

above 60°N and roughly 24% of exposed land on the Northern Hemisphere is underlain by this continuously frozen ground material which highlights its importance (Bartsch, Höfler, et al., 2016; A. M. Trofaier et al., 2017). Figure 1.1 illustrates the permafrost fraction in percent across the Northern Hemisphere for the year 2017 based on data by Obu et al. (2021b).

Definition of Permafrost:

Permafrost, which is also characterized as permanently frozen ground, is defined as ground material (soil, sediment, or rock) that remains constantly frozen for two or more consecutive years (Subcommittee, 1988). Furthermore, permafrost is commonly divided into separate zones depending on the relative amount of frozen ground in a given area (J. Brown et al., 2002):

Isolated: <10%; Sporadic: 10 50%; Discontinuous: 50 90%; Continuous: 90 100%
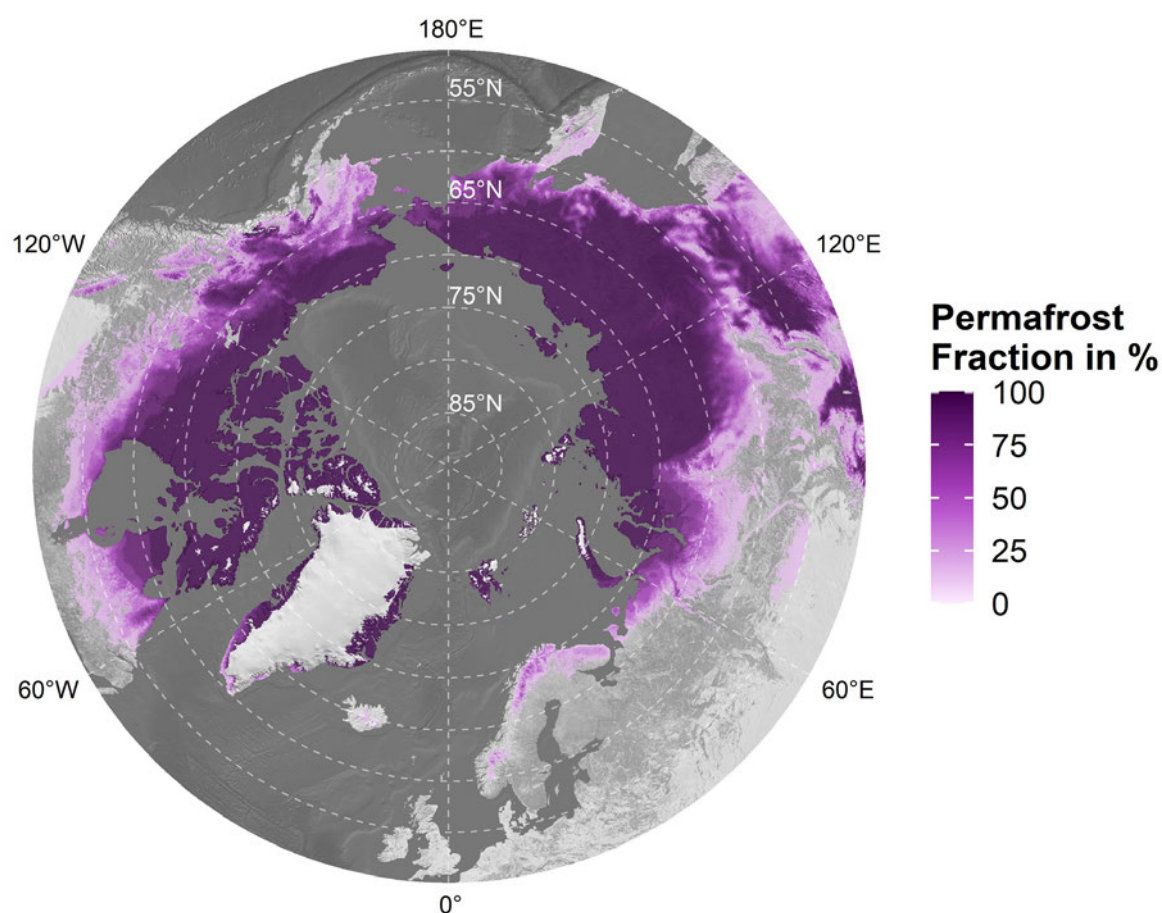
Figure 1.1: The fraction of permafrost across the Northern Hemisphere for the year 2017 based on data by Obu et al. (2021b). A shaded relief by Natural Earth (n.d.) was used as a background map. Modified after Philipp et al. (2023).

On top of the permafrost lies the so-called active layer, which is defined as the uppermost ground layer that varies in thickness and, unlike the continuously frozen permafrost, seasonally freezes and thaws (Duguay et al., 2005). Figure 1.2 provides a schematic overview of the ground profile in permafrost environments, including permafrost, the active layer, deep unfrozen ground, and the temperature profile. In order to fully assess the degradation of permafrost, an understanding of both the dynamics of the active layer thickness and the thermal state of permafrost is crucial (W. Chen et al., 2003; Westermann et al., 2014). Bodies and layers of non-frozen ground material in the form of crypegs and taliks can be present in permafrost (Van Everdingen et al., 2005). Cryopegs are hereby defined as permanently croytic soils with temperatures below 0°C but at the same time remain unfrozen due to dissolved-solids that are present in the pore water (Van Everdingen et al., 2005). Taliks are further separated into closed taliks which represent depressions in the frozen ground below lakes and rivers, whereas open taliks connect the sub- and supra-permafrost water and therefore completely penetrate the layer of frozen ground material (Van Everdingen et al., 2005; Stephani et al., 2020).
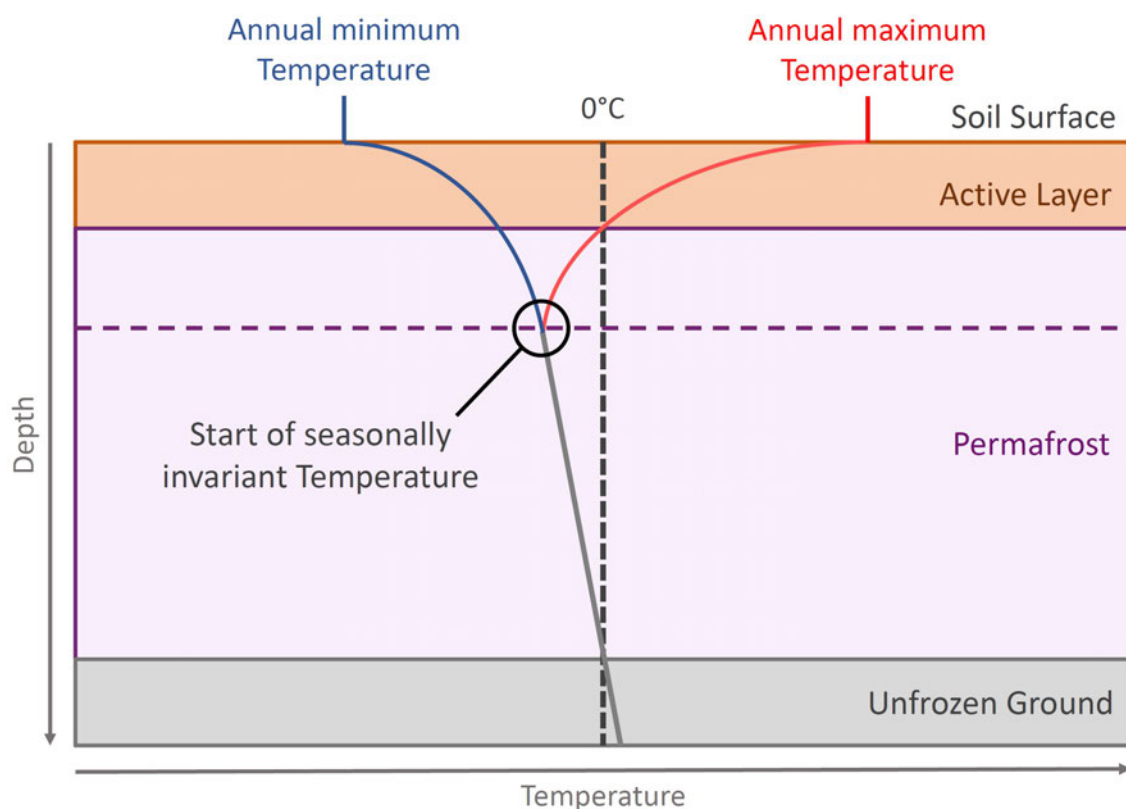
Figure 1.2: Schematic cross-section of the ground profile in permafrost environments including the active layer, permafrost, deep unfrozen ground, and seasonal temperature variations of the ground. The blue line represent the annual minimum temperature and the red line the annual maximum temperature for a given depth. The purple dashed line visualises the minimum depth of seasonally invariant ground temperature. Modified after Arctic Development and Adaptation to Permafrost in Transition (ADAPT) (n.d.).

1.1.1 Permafrost in a warming World

The term "Arctic amplification" refers to the phenomenon of temperatures rising twice as fast in the Arctic compared to the global average temperature increase (J. Cohen et al., 2014). Annual mean surface air temperatures have increased by roughly 2°C since the year 1900 based on data from weather stations distributed over the Northern High Latitudes (NHL), while strongest temperature increase is taking place during the winter and autumn seasons (Serreze & Barry, 2011). During the period 1970 2010 the snow extent across the Northern Hemisphere was observed to have decreased by 7% 11% for the months March and April compared to the snow cover prior to the year 1970 (R. D. Brown & Robinson, 2011). Furthermore, no less than half of the vegetated areas within the Arctic is projected to shift to a different class by the mid of this century based on the CAVM and several climate change scenarios (Pearson et al., 2013). Another major driver for Arctic greening has been identified to be the longer duration and earlier start of the non-frozen season (Y. Kim et al., 2012).

Increasing ground temperatures are reported for the majority of regions within the permafrost domain (Romanovsky et al., 2010). As a consequence, a substantial decrease of the permafrost extent is predicted in projections on the future distribution of frozen ground (Slater & Lawrence, 2013; Pastick et al., 2015; S. Zhao et al., 2019). Permafrost temperatures across high-mountain and polar regions are reported to have increased on average by 0.29°C ± 0.12°C within the time span 2007 2016, as mentioned in the Intergovernmental Panel on Climate Change (IPCC) Special Report on the Ocean and Cryosphere in Changing Climate by Pörtner et al. (2019).

The thawing of permafrost has drastic implications for the environment. The infographic in Figure 1.4 illustrates various landscape processes and features related to the degradation of permafrost, including coastal erosion (e.g. Günther et al., 2013; K. Barnhart et al., 2014; Novikova et al., 2018; Obu, Lantuit, Grosse, et al., 2017), thermokarst ponds and lakes (e.g. Rey et al., 2019; L. Wang, Jolivel, et al., 2018; Nitze et al., 2017; L. Farquharson et al., 2016), thaw slump activities (e.g. Luo, Niu, et al., 2019; Swanson & Nolan, 2018; Segal et al., 2016), wild fires (e.g. B. M. Jones et al., 2015; Gibson et al., 2018; Zhou, Liu, et al., 2019), patterned ground (e.g. Kartoziia, 2019; Lousada et al., 2018), the deepening of the active layer (e.g. M. Jorgenson & Osterkamp, 2005; H. Park et al., 2016; Grosse et al., 2016), magnified surface deformation rates due to thaw settlement and frost heave (e.g. Strozzi et al., 2018; Antonova et al., 2018; J. Hu et al., 2016; Short et al., 2014), landslides (e.g. Kääb, 2002; Hao et al., 2019; Kharuk et al., 2016), changing rock glacier movements (e.g. Kääb, 2002; Strozzi et al., 2020; Brenning, Long, & Fieguth, 2012), and the aforementioned emissions of previously

stored greenhouse gases (e.g. Nassar et al., 2014; Hartley et al., 2015; Jørgensen et al., 2015; Anthony et al., 2016, 2018; Schneider et al., 2009). In addition, a change in the organization of of soil carbon stocks, vegetation composition, and hydrological flowpaths are further consequences of degrading frozen ground (M. T. Jorgenson et al., 2013). The warming of permafrost also negatively impacts its physical stability, which in turn lowers the load capacity for human infrastructure such as railroads, pipelines, and buildings (F. Chen et al., 2012; Hinzman et al., 2005; Hjort et al., 2018). Additionally, more frequent mass movements and ground surface deformations in the form of e.g. detachments of the active layer have the potential to become geohazards and thus endanger exposed human infrastructure (Radosavljevic et al., 2016; Couture et al., 2018; B. M. Jones et al., 2018; M. T. Jorgenson & Grosse, 2016). Both the size and quantity of surface water areas within the permafrost domain are highly dynamic, as the expansion of lakes is cased by thermoerosion while subsurface drainage leads to the disappearance or shrinking of lakes (B. M. Jones et al., 2011; Yoshikawa & Hinzman, 2003). Increasing input rates from groundwater to surface streams are thereby the result of thinning permafrost, which consequently forces changes in chemical properties and temperature of lakes and rivers (Hinzman et al., 2005). Example photographs of a patterned ground, a pingo, thaw lakes and ponds, coastal erosion, and thaw slumping in a permafrost environment is provided in Figure 1.3.

The expanding risk of structural damage through the thawing of permanently frozen ground makes infrastructure engineering in permafrost environments exceptionally challenging (Schnabel et al., 2020). The reduced load capacity of the warming ground in combination with magnified surface deformation rates lead to an increased risk of foundation failure (Humlum et al., 2003; Qingbai et al., 2002). By the year 2050, it is anticipated that roughly 70% of Arctic infrastructure will be situated in regions that are classified as vulnerable to ground subsidence and permafrost degradation (Meredith et al., 2019). This is of particular importance for heated structures such as pipelines and heated buildings which have to be elevated above the ground using pilings with ventilated space in between so that a heat exchange and the consequent thawing of frozen ground can be prevented (Schnabel et al., 2020). Nonetheless, replacing the original surface cover in permafrost environments with unheated but warmer materials such as asphalt roads can already cause ground temperatures to rise (Schnabel et al., 2020). Proactive cooling methods of the frozen ground are therefore recommended to lower maintenance fees on buildings and other infrastructure that are caused by the thawing of permafrost (G. Cheng, 2005; Schnabel et al., 2020; Humlum et al., 2003; F. Chen et al., 2012).
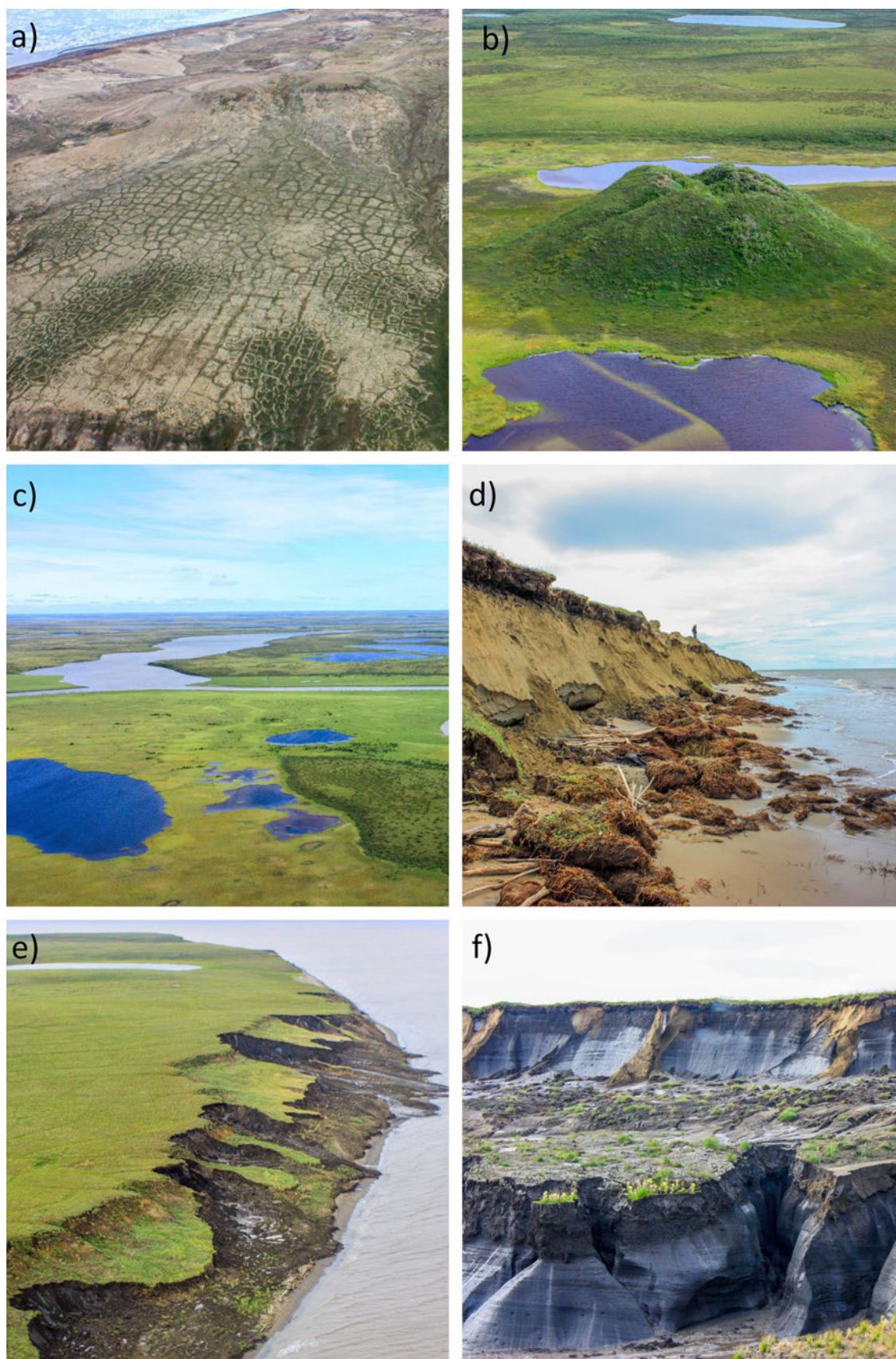
Figure 1.3: A variety of common processes and features in permafrost environments. (**a**) Patterned ground, (**b**) pingos, (**c**) thaw lakes and ponds, (**d**) coastal erosion, and (**e**, **f**) thaw slumps are displayed. Photos taken by Tobias Ullmann. Modified after Philipp et al. (2023) & Department of Remote Sensing - University of Würzburg (2023).
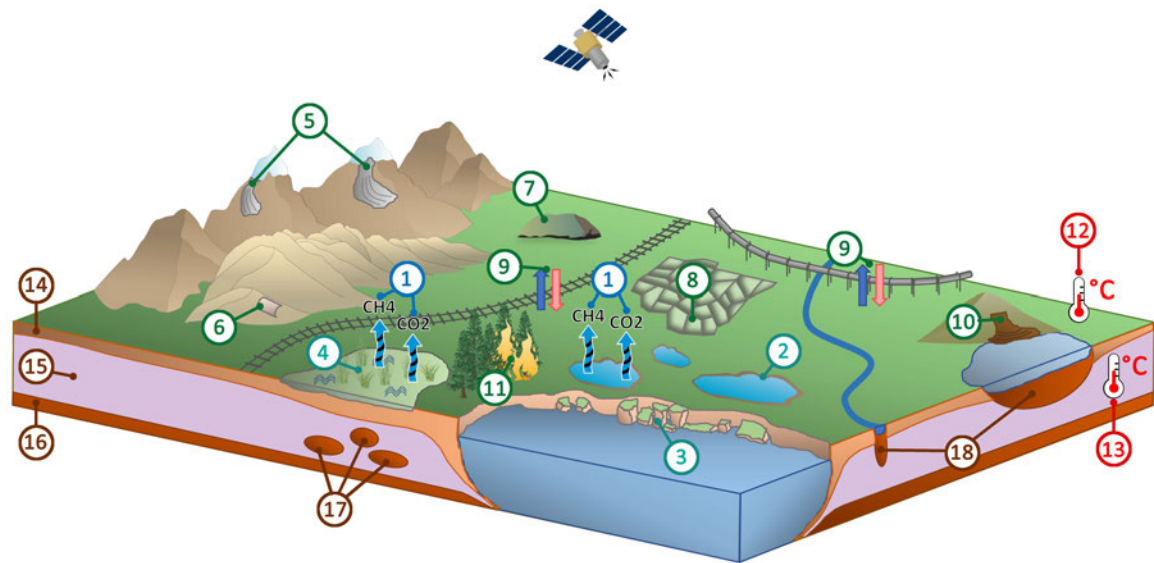
Atmospheric Features and Processes
1: *Greenhouse gas emissions*

Surface Water Features and Processes
2: Surface water extent dynamics
3: *Coastal erosion*
4: Bog/fen development

Surface Land Features and Processes
5: Rock glaciers
6: Landslides
7: Pingo development
8: Patterned ground
9: *Frost heave and thaw settlement*

10: Thaw slumps
11: *Wild fires*

Thermal Features and Processes
12: *Land surface temperature dynamics*
13: *Ground temperature dynamics*

Subsurface Features and Processes
14: Active layer thickness dynamics
15: Permafrost
16: Unfrozen ground
17: Cryopeg
18: Talik

Figure 1.4: The info-graphic illustrates various permafrost related processes and features. Processes are thereby written in italics. Several symbols illustrated in the infographic were modified or adopted according to courtesy of the Integration and Application Network, University of Maryland Center for Environmental Science (n.d.). Modified after Philipp et al. (2021).

A further critical aspect about permanently frozen ground is the aforementioned massive amount of present organic carbon content. Current estimates indicate that roughly 1460–1600 billion tonnes of organic carbon is stored in permafrost, which is roughly twice the amount of carbon that is currently present in the atmosphere (Schuur et al., 2015; Pörtner et al., 2019). An ongoing thawing of permafrost could therefore trigger the emerge of organic carbon stocks in the form of greenhouse gas emissions and further speed up climate change through a positive feedback loop (M. Yang et al., 2010; Schuur et al., 2015). Arctic greening could hereby act as a carbon sink to some extent, however, the predicted amount CO_2 uptake via vegetation in the NHL varies strongly

across different models (Voigt et al., 2017; Abbott et al., 2016; A. M. Trofaier et al., 2017). Amplified carbon emissions of up to 75% through Arctic rivers and coastal erosion, and a fourfold increase of carbon releases caused by fires are hereby expected by the end of the century based on an expert assessment by Abbott et al. (2016). It is further mentioned that permafrost environments are likely to become carbon sources by the year 2100 independent of the climate scenario. However, the authors also stress that around 65% 85% of carbon releases related to permafrost could still be mitigated by lowering human emission rates (Abbott et al., 2016). Models dedicated to predict future permafrost carbon releases are frequently based on Representative Concentration Pathways (RCP) scenarios (Kleinen & Brovkin, 2018). RCPs were developed as a starting point for long- and near-term climate modelling approaches and represent four different pathways for the future development of greenhouse gas concentrations (Van Vuuren et al., 2011). Each pathway is thereby labeled after a different potential radioactive forcing value (2.6, 4.5, 6.0, or 8.5 W/m^2) predicted for the year 2100 (Van Vuuren et al., 2011). While carbon releases under the moderate warming scenario RCP4.5 are predicted to be 6 33 Pg carbon by the end of the century, the total amount of released carbon under the strong warming scenario RCP8.5 is estimated to range between 23 174 Pg carbon (Schuur et al., 2015; Koven, Schuur, et al., 2015; Koven, Lawrence, & Riley, 2015; Anthony et al., 2018). According to Schaefer et al. (2014), the continuous degradation and the associated release of carbon could lead to a global temperature increase of 0.29 ± 0.21°C by the end of the century under the scenario RCP8.5, which threatens the goal to not overshoot the desired warming target of no more than 2°C over pre-industrial temperatures in 2100. The authors further express their concerns regarding the lack of such permafrost related carbon emission pathways in climatic projections that are communicated in the IPCCs Fifth Assessment Report (AR5) (Schaefer et al., 2014).

1.1.2 Efforts in monitoring Permafrost Landscapes from Space

In recognition of its significance, permafrost was added to the list of the 50 Essential Climate Variables (ECV) as specified by the Global Climate Observing System (GCOS) of the World Meteorological Organization (WMO) (Grosse et al., 2016; A. M. Trofaier et al., 2017). The relevant parameters for the ECV permafrost are hereby both "Permafrost temperature (K)" and "Depth of active layer (m)" (European Space Agency, n.d.-g). In addition to ongoing projects, such as European Space Agency (ESA) "LST_cci" or "Snow_cci", permafrost was also included in the list of ESA Climate Change Initiative (CCI) programs (European Space Agency, n.d.-g; Westermann et al., 2018). Table 1.1 provides details for a variety of frequently cited in literature, ongoing, and recent networks and programs in the context froze ground.

As a subsurface feature, permafrost itself cannot be directly monitored from space. Nonetheless, several land surface processes and features (Figures 1.3 & 1.4), which are associated by permafrost and its degradation, can be remotely measured and analyzed via satellites. The thermal state of permafrost can hereby indirectly be assessed through such land surface target features (Westermann et al., 2014). Table 1.2 lists several review articles dedicated the satellite remote sensing of permafrost and published during the last two decades.

Table 1.1: A variety of recent and ongoing programs and networks associated with permafrost. Modified after Philipp et al. (2021).

Name	Objective	Runtime	Reference
Global Terrestrial Network for Permafrost (GTN-P)	Management and organisation of permafrost data.	since 1998	Biskaborn et al. (2015); International Permafrost Association; Arctic Portal; Alfred-Wegener-Institut (n.d.)
Swiss Permafrost Monitoring Network (PERMOS)	Documentation of changes and of the current state of mountain permafrost in the Swiss Alps.	since 2000	Vonder Mühll et al. (2008); PERMOS (n.d.)
PermaNET – Permafrost Long-Term Monitoring Network	Monitoring of alpine-wide permafrost.	2007 - 2013	Mair et al. (2011); PermaNet Alpine Space (n.d.)
Permafrost Carbon Network	Quantification of the role of permafrost on future climate change.	since 2011	Permafrost Carbon Network (n.d.)
ArcticNet	Investigating the impacts of climate change in the Canadian North.	since 2003	ArcticNet (n.d.-b,-a)
Cooperative Global Air Sampling Network	International effort in gathering regular discrete air flask samples.	since 1967	NOAA Earth System Research Laboratories (n.d.-a)

Table 1.1: Continued.

Name	Objective	Runtime	Reference
PAGE21	Studying the feedback mechanisms and vulnerability of permafrost environments associated with increasing greenhouse gas emissions.	2011 - 2015	PAGE21 (n.d.)
Circumpolar Active Layer Monitoring (CALM)	Observing the response of the active layer and near-surface permafrost to climate change over long (multi-decadal) time scales.	since 1991	Shiklomanov et al. (2008); International Permafrost Association (n.d.-a)
Thermal State of Permafrost (TSP)	Database for assessing the changes in distribution and temperatures of permafrost.	since 2007	Romanovsky et al. (2010); International Permafrost Association (n.d.-b)
ESA Atmosphere-Land Interactions Study (ALANIS)	Contribution and interaction of boreal Eurasia to greenhouse gas concentration.	2010 - 2012	Hayman et al. (2010); Marconcini et al. (2010)
ESA Data User Element (DUE) Permafrost	Establishment of a systematic and satellite-based permafrost monitoring program.	2009 - 2012	Heim et al. (2011); European Space Agency (n.d.-f)
ESA GlobPermafrost	Development, implementation, and validation of permafrost related products by integrating data from Earth observation.	2016 - 2019	Bartsch, Grosse, et al. (2016); European Space Agency (n.d.-c)
ESA Climate Change Initiative (CCI) Permafrost	Development of permafrost maps as Essential Climate Variables (ECV) products via space-borne observations.	2018 - 2021	Westermann et al. (2018); European Space Agency (n.d.-g)
Arctic-Boreal Vulnerability Experiment (ABoVE)	Major field campaign in western Canada and Alaska to help predict and understand ecosystem responses of climate change in the Arctic and Boreal regions.	since 2015	Miller et al. (2019); National Aeronautics and Space Administration (NASA) (n.d.)

Table 1.1: Continued.

Name	Objective	Runtime	Reference
Climate and Cryosphere (CliC)	Enhance our understanding of the cryosphere and its interactions with the global climate system as well as to build-up the utilization of cryospheric observations for detecting climate change.	since 2001	Allison et al. (2001); Climate and Cryosphere (CliC) (n.d.)
Next-Generation Ecosystem Experiments (NGEE) Arctic	Enhance our predictive understanding of carbon-rich Arctic system feedbacks and processes to the climate.	2012 - 2022	S. Wullschleger et al. (2011); S. D. Wullschleger (2019)
Study of Environmental Arctic Change (SEARCH)	Understanding the impact of shrinking land/sea ice and degrading permafrost on the Arctic and global systems.	since 2001	Study of Environmental Change (SEARCH) (2005); SEARCH (n.d.)
PermaSAR	Development of methodologies to detect subsidence through remote sensing investigations in permafrost domains.	2015 - 2019	Antonova et al. (2019)
SatPerm - Satellite-based Permafrost Modeling across a Range of Scales	Studying the feasibility of satellite observations as input for permafrost modelling.	2015 - 2018	University of Oslo - Department of Geosciences (n.d.)
COmbining remote sensing and field studies for assessment of Landform Dynamics and permafrost state on Yamal (COLD Yamal)	Development of methodologies for the observation of permafrost and linked land surface features on the Yamal peninsula.	2013 - 2016	Central Institute for Meteorology and Geodynamics Section Climate Change Impacts (n.d.)
Horizon 2020 Nunataryuk	Analysing the impacts of thawing coastal and sub-sea permafrost and developing mitigation strategies for the population of Arctic coastal environments.	2017 - 2022	Lantuit (2019); NUNATARYUK (n.d.)

(Table continues on the next page ...)

Table 1.1: Continued.

Name	Objective	Runtime	Reference
Modular Observation Solutions for Earth Systems (MOSES)	A joint observation system that primarily targets four events: ocean eddies, hydrological extreme events, the thawing of permafrost, and heat waves.	2017 - 2021	Alfred-Wegener-Institute (n.d.-b)
PETA-CARB	Quantification of the amount, distribution, and vulnerability of deep carbon stocks in permafrost deposits.	2013 - 2018	Alfred-Wegener-Institute (n.d.-c)
CARBOPERM	Investigations on the turnover, formation, and the release of organic carbon stored in northern Siberian permafrost environments.	2013 - 2016	Schwamborn & Wetterich (2015)
KoPf	Joint research project dedicated to examine carbon dynamics in north-eastern Siberian landscapes, which are underlain by permafrost, via field observations and mathematical models.	2017 - 2020	KoPf (n.d.)
Changing Arctic Carbon cycle in the cOastal Ocean Nearshore (CACOON)	Quantifying the effects of degrading terrestrial permafrost and changes in freshwater exports of organic matter to Arctic coastal waters.	2018 - 2021	Alfred-Wegener-Institute (n.d.-a)

(... end of continued table.)

Disadvantageous environmental conditions in Arctic environments, such as steep sun angles, continuous cloud cover, polar night and low light intensities, but also technical constraints of satellite imagery including the decorrelation between SAR observations, complicates remote sensing investigations of permafrost and its associated features and processes (Duncan et al., 2020; Zwieback et al., 2016; Westermann et al., 2014). The implementation of thermal satellite data derived from e.g. Advanced Very High Resolution Radiometer (AVHRR) or Moderate Resolution Imaging Spectroradiometer (MODIS) allows for modelling the thickness of the active layer and for estimating indices related to thawing (T. Zhang et al., 2004). Optical imagery based

on Landsat data provides land surface information since 1972, which can be used for change detection analyses (T. Zhang et al., 2004). On the other hand, investigations based on Landsat data are limited by scarce data acquisitions for the temporal window 1989 1998 for a large portion of the Arctic (Bartsch, Höfler, et al., 2016). In addition, cloud cover strongly impacts both optical and thermal satellite scenes, leading to data gaps and thus confine their applicability (T. Zhang et al., 2004; A. M. Trofaier et al., 2017). In contrast, Radio Detection and Ranging (RADAR) data acquired in the form of SAR is largely independent of sun illumination and cloudiness or other weather condition and may therefore overcome the restrictions of thermal and optical images (Kääb et al., 2005; Kääb, 2008). Surface movements can be assessed with high accuracy via Differential Interferometric Synthetic Aperture Radar (D-InSAR) analyses (Short et al., 2014). However, decorrelation between individual SAR acquisitions caused by altering surface attributes including soil moisture, snow cover or vegetation heavily impair the usability of D-InSAR (Zwieback et al., 2016; Westermann et al., 2014). There is a strong potential in the complementary use of optical and SAR data for analyses in the context permafrost, since working with SAR data might be successful where optical data fails, and vice versa (Westermann et al., 2014). Another promising field of application for RADAR data is the detection of surface soil thawing and freezing via passive RADAR sensors such as the Special Sensor Microwave/Imager (SSM/I), which provides ongoing data with a global coverage and multiple observations per day since the year 1987 (T. Zhang et al., 2004). That being said, the high temporal data frequency is contrasted by a poor spatial resolution of multiple kilometres per pixel (André et al., 2015). Several articles mention the lack of space-borne data with a high spatial resolution which is essential for many permafrost-related analyses (Kääb et al., 2005; Bartsch, Höfler, et al., 2016; M. T. Jorgenson & Grosse, 2016). Although high resolution satellite imagery is available and was also successfully implemented in various studies on investigating smaller scale features and processes (e.g. Ulrich et al., 2014; B. M. Jones et al., 2018; Godin et al., 2019), the restricted access and oftentimes expensive acquisition plans strongly limit the applicability (Kääb et al., 2005; Boyle et al., 2014). In order to detect and analyse highly dynamic features and processes, there is also a need for frequent and long-term satellite acquisitions in addition to a better spatial resolution (Bartsch, Höfler, et al., 2016; A. M. Trofaier et al., 2017). Combining remote sensing data from different sources is hereby of particular interest in order to overcome platform- and sensor-specific constraints for investigating processes and features in the context of permafrost, including coastal erosion, dynamics in vegetation cover, permafrost distribution, or emerging greenhouse gases with high spatial resolution and temporal frequency (M. T. Jorgenson & Grosse, 2016; Runge & Grosse, 2019).

Table 1.2: A variety of remote sensing of permafrost related review articles published during the past two decades. Modified after Philipp et al. (2021).

Author	Title
T. Zhang et al. (2004)	Application of Satellite Remote Sensing Techniques to Frozen Ground Studies
Kääb et al. (2005)	Remote sensing of glacier- and permafrost-related hazards in high mountains: an overview
Kääb (2008)	Remote sensing of permafrost-related problems and hazards
National Research Council (2014)	Opportunities to use remote sensing in understanding permafrost and related ecological characteristics: Report of a workshop
Arenson et al. (2016)	Detection and analysis of ground deformation in permafrost environments
M. T. Jorgenson & Grosse (2016)	Remote Sensing of Landscape Change in Permafrost Regions
Bartsch, Höfler, et al. (2016)	Land Cover Mapping in Northern High Latitude Permafrost Regions with Satellite Data: Achievements and Remaining Challenges
A. M. Trofaier et al. (2017)	Progress in space-borne studies of permafrost for climate science: Towards a multi-ECV approach
Duncan et al. (2020)	Space-Based Observations for Understanding Changes in the Arctic-Boreal Zone

1.1.3 Erosion of Arctic Permafrost Coasts

Approximately one-third of Earth's coastlines is located within the permafrost domain (Lantuit et al., 2012). A widespread phenomenon which is linked to the degradation of frozen ground is the previously mentioned erosion of Arctic coastlines (Günther et al., 2013; Novikova et al., 2018; Obu, Lantuit, Grosse, et al., 2017). Accelerated rates of erosion in recent years are hereby frequently reported for Arctic environments (B. M. Jones et al., 2020; Lantuit et al., 2012). Average erosion rates more than doubled for unlithified coasts of Siberia, Canada, and Alaska since the year 2000 (Irrgang et al., 2022). Not only the thawing of permafrost alone, but the interplay of several drivers are amplifying the erosion of Arctic coasts (B. M. Jones et al., 2020, 2018). Environmental factors, such as the decreasing extent of sea ice (L. M. Farquharson et al., 2018; M. Wang & Overland, 2009, 2012; Mahoney et al., 2014), the increasing length of the open-water period (Crawford et al., 2021; K. R. Barnhart et al., 2016), rising air and sea temperatures (J. Cohen et al., 2014; Serreze & Barry, 2011; Alexander et al., 2018), and increasing storm frequencies

(Hakkinen et al., 2008) all contribute to the accelerated retreat of Arctic coasts. In addition, degrading permafrost leads to a destabilization of the coastline and therefore further increases its vulnerability to erosion processes (B. M. Jones et al., 2020; Lantuit et al., 2012). A continuous sea level rise is also expected to put additional stress on coastal cliffs by the end of the century (Shadrick et al., 2022; Oppenheimer et al., 2019). Figure 1.5 visualizes various features and processes linked to amplified erosion rates of Arctic permafrost coasts. The amplified risk of infrastructure damage (Shadrick et al., 2022; Fritz et al., 2017; Radosavljevic et al., 2016; Nielsen et al., 2022) and alterations in fish and wildlife habitats (B. M. Jones et al., 2018; M. T. Jorgenson & Grosse, 2016; Overduin et al., 2014) can be observed as consequences of eroding permafrost coastlines. Moreover, the erosion of permafrost coastlines trigger the release of previously stored organic carbon content into the oceans (Couture et al., 2018; B. M. Jones et al., 2018; Nielsen et al., 2022; Tanski et al., 2019; Vonk et al., 2012; Terhaar et al., 2021).
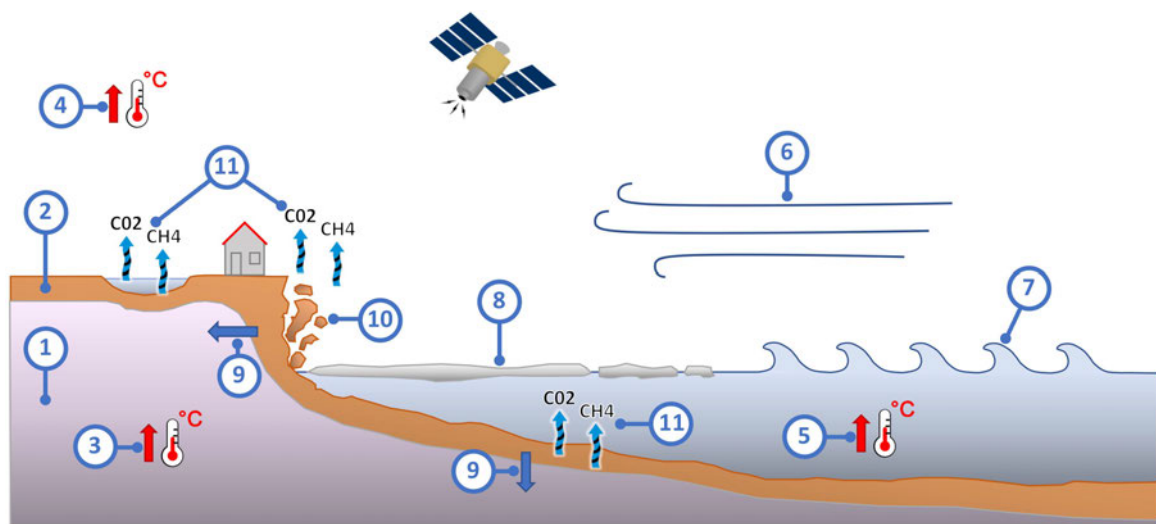
Figure 1.5: The info-graphic illustrates diverse features and processes linked to amplified erosion rates of Arctic permafrost coasts: (**1**) Permafrost, (**2**) unfrozen ground material, (**3**) rising permafrost temperatures, (**4**) rising air temperatures, (**5**), rising sea temperatures, (**6**) rising storminess, (**7**) wave action, (**8**) decreasing sea ice extent, (**9**) decreasing permafrost extent, (**10**) coastal erosion, (**11**) organic carbon release. Some symbols within the info-graphic were adopted or modified according to courtesy of the Integration and Application Network, University of Maryland Center for Environmental Science (n.d.). Modified after Philipp et al. (2022).

In order to effectively evaluate the implications of eroding permafrost coastlines on the environment, but also on human infrastructure and society, high resolution and large scale quantification of changing coastlines in the Arctic is required. Satellite remote sensing is hereby a powerful tool for spatially explicit, quick, and low coast analyses over diverse spatial scales. The applicability of diverse SAR data in the context

of monitoring coastal change was recently investigated in a study by Bartsch, Ley, et al. (2020). Even though the application was considered to be feasible, the authors also mentioned remaining challenges, including issues with ambiguous scattering behaviour, complications with viewing geometries, and inconsistent data acquisitions (Bartsch, Ley, et al., 2020).

First attempts to quantify coastal erosion on a circum-Arctic scale were undertaken by Lantuit et al. (2012), who published a geomorphological categorization for 100,000 km of Arctic coastline divided into 1,315 segments. Information on volumetric ground ice content, shore material, soil organic carbon content, and several other parameters are provided, in addition to coastal change rates (Lantuit et al., 2012). Another recent study by Rolph et al. (2022) introduced a physics-based model, called "ArcticBeach v1.0", designed for coastal erosion simulations on a circum-Arctic scale. Coastal retreat rates, as simulated by the model, were hereby in the same magnitude range as the reference data from two test sites (Rolph et al., 2022).

1.2 Research Motivation

According to the scientific background presented in the previous sections, the main focus of this thesis lies on the exploitation of space-borne remote sensing data for a better understanding on erosion processes of coastlines in permafrost environments and the associated environmental implications by (1) assessing the applicability of SAR data for analyzing Arctic coastal environments, (2) quantifying annual coastal erosion rates in permafrost environments with high resolution and on a pan-Arctic scale, and (3) linking the extracted erosion rates with the amount of permafrost and carbon that is lost during that process.

1.3 Research Objectives

In order to close existing gaps in high resolution and continuous quantification of coastal erosion rates in permafrost environments as well as to comply with the research motivation introduced in section 1.2, this thesis aims to build a comprehensive monitoring framework based on SAR satellite data to measure annual erosion rates with high spatial resolution and on a pan-Arctic scale. In this regards, this thesis investigates the usability of SAR data in combination with a DL work-flow and the feasibility of CVA for detecting coastal change in permafrost regions. The three primary research objectives of this thesis can be expressed more precisely as follows:

- **Objective 1:** The initial research objective of this thesis is to conduct a comprehensive bibliographic analysis on recent developments in the investigation of processes and features associated to permafrost via satellite data. In particular, the spatial distribution of study areas, the applied spatio-temporal resolution, spatial scales, length of the observation period, the type of incorporated satellite data and platform, and the frequency of studied environmental foci are analyzed.

- **Objective 2:** The second and primary research objective of this thesis covers the development of a circum-Arctic monitoring framework for quantifying current and future coastal change rates with high spatial resolution and on an annual basis. The feasibility of C-Band SAR backscatter data from S1 together with a DL based segmentation approach for generating a high quality Arctic coastline product is investigated. In addition, the applicability of CVA based on SAR backscatter data for monitoring coastal change is assessed and evaluated.

- **Objective 3:** The last research objective constitutes an experimental framework for estimating permafrost and carbon loss associated to Arctic coastal erosion. The previously derived coastal erosion rates based on S1 SAR backscatter and CVA are intersected with publicly available data on soil carbon, permafrost extent, active layer thickness, and surface elevation.

Several key research questions have been formulated in order to fulfill the research objectives defined in this thesis. With respect to the formulated objectives, the first group of research questions focuses on the bibliographic analysis, Specifically, the following questions shall be addressed:

Research Questions 1

- *How does the publication frequency for studies that investigate permafrost-related features and processes via space-borne data change over time?*

- *How are the study areas distributed across the permafrost domain? What are the study hotspots?*

- *What environmental foci are studied the most and what foci are studied the least?*

- *What spatio-temporal resolutions were applied to address different environmental topics?*

- *What satellite platforms and data types are frequently applied?*

- *What are existing research gaps in the context of satellite-based analyses of permafrost related processes and features and how can they be addressed?*

The second group or research questions focuses on the circum-Arctic monitoring framework for quantifying Arctic coastal erosion rates within the permafrost domain. In this regard, specific focus lies on the potential and limitations of DL for generating a circum-Arctic coastline product, the applicability of S1 SAR backscatter data in Arctic coastal environments, and CVA for quantifying coastal change rates.

Research Questions 2

- *Is the application of S1 SAR backscatter data feasible for monitoring coastal change in Arctic environments?*

- *How can space-borne remote sensing in combination with Artificial Intelligence (AI) be integrated to generate a high quality Arctic coastline product for permafrost environments? What are the challenges and how can they be overcome?*

- *How can CVA be combined with S1 SAR backscatter data to contribute in monitoring Arctic coastal change rates?*

- *Can the proposed data and methods be transferred to quantify coastal change in different latitudinal regions? What needs to be considered?*

Lastly, the third group of research questions addresses the intersection of previously derived Arctic coastal erosion rates with the amount of carbon and permafrost, that is lost during that process. In particular, the applicability of openly available products and potential uncertainties are addressed.

Research Questions 3

- *What are the relevant environmental parameters to estimate permafrost loss and carbon release associated to coastal erosion? What products for these parameters are openly available?*

- *What challenges are present when quantifying permafrost and carbon loss based on the utilized data and methods? How can they be overcome?*

1.4 Thesis Outline

This thesis consists of five chapters which are shortly outlined below.

Chapter 1 provides a brief introduction on the scientific relevance of permafrost in a warming world. In addition, previous efforts in monitoring permafrost landscapes from space, the effects of thawing frozen ground on the erosion of Arctic permafrost coasts, as well as current research gaps and future monitoring requirements are presented. Lastly, the research motivation and objectives of this thesis are summarized.

Chapter 2 presents a review on trends in satellite earth observation for permafrost related analysis. A total of 325 articles published in 30 different international journals during the past two decades were investigated based on the environmental focus, study location, platform, resolution of applied remote sensing data, and sensor combinations. Moreover, previous accomplishments and future challenges and prospects are provided.

Chapter 3 introduces a novel framework for circum-Arctic quantification of Annual erosion rates of permafrost coasts. In particular, the applicability of S1 SAR backscatter in combination with DL and CVA is investigated based on ten test sites that are distributed across the entire Arctic and covering 1038 km of coastline. The feasibility of the proposed data and methods as well as future potentials are discussed.

Chapter 4 presents an experimental framework for estimating permafrost and carbon loss associated to Arctic coastal erosion. The previously generated coastal erosion product is hereby combined with publicly available data on Arctic permafrost extent, Active Layer Thickness (ALT), soil organic carbon content, and surface elevation. A discussion o the applicability and uncertainties of the proposed data and methods is provided.

Chapter 5 briefly summarizes the entire thesis with respect to the fulfilment of research objectives and questions outlined in Chapter 1.3. Moreover, opportunities for future development and improvements are highlighted.

Chapter 2

A Review on Trends in Satellite Earth Observation for Permafrost related Analyses[*]

The following chapter provides a comprehensive overview of recent trends in satellite earth observation for studying permafrost related processes and features. A total of 325 articles were investigated based on annual publication frequency, geographical study hot spots, the relationship between the first author's institution nationality and the study country, the distribution of addressed environmental foci, the applied spatio-temporal resolutions and scales, as well as the distribution of satellite platforms and sensor types. In addition, a collection of publicly available and permafrost related datasets is presented.

2.1 Review Objectives and Methodology

SCI papers related to remote sensing of permafrost were searched via the Web of Science (WoS) (formerly known as ISI Web of Knowledge) platform. The literature was filtered using a search string with the following conditions: At minimum one of the following terms "Satellite", "Earth Observation", or "Remote Sensing" and the term "Permafrost" have to be present in either keywords, abstract, or title of an article. In case one of the keywords "Satellite", "Earth Observation", or "Remote Sensing" is already present in the name of a journal, only the term "Permafrost" has to be present in either keywords, abstract, or title. Furthermore, only articles in English language were considered in this review. Remaining publications were further filtered

---

[*]This chapter is based on Philipp et al. (2021).

based on the publication date, which was limited from January 2000 until February 2020. Therefore, a time span of two decades was covered. The number of publications which met the initial filtering criteria was over 700. The remaining literature was further filtered to eleven international journals which have a thematic focus on earth observation. In addition to articles from remote sensing specific journals, further publications from 19 acclaimed non-earth observation specific international journals were included. The total number of remaining articles after filtering by journals was 536. The last phase of literature filtering consisted of manually screening the articles based on the following criteria: (1) Exclusion of extra-terrestrial investigations (permafrost occurrences on Mars). (2) Remote sensing data has to be utilized in the analysis of a study. (3) Articles that exclusively used airborne data as the only remote sensing data source were excluded, since the main interest of this review lies on satellite-based observations of permafrost and its associated processes and features. (4) The main investigation has to be about permafrost, or it has to be at least directly connected to frozen ground. Thus, if the term "Permafrost" occurred in the abstract but no actual analysis was dedicated to permafrost or any associated feature/process, the article was taken into consideration for this review. An overview of the filtering approach is provided in Figure 2.1. The final 325 remaining articles that met all of the above-mentioned requirements were subsequently investigated based on the following parameters:

- The annual number of published articles

- The number of investigations per country

- The nationality of the first authors institution

- Spatial study hot spots across the globe

- The number and distribution of investigated environmental categories

- The number and distribution of investigated research foci

- Distribution of the spatio-temporal resolutions of remote sensing data

- The temporal window covered in time series analyses

- Distribution of spatial scales

- Number and distribution of remote sensing platforms

- Sensor types and sensor combinations utilized
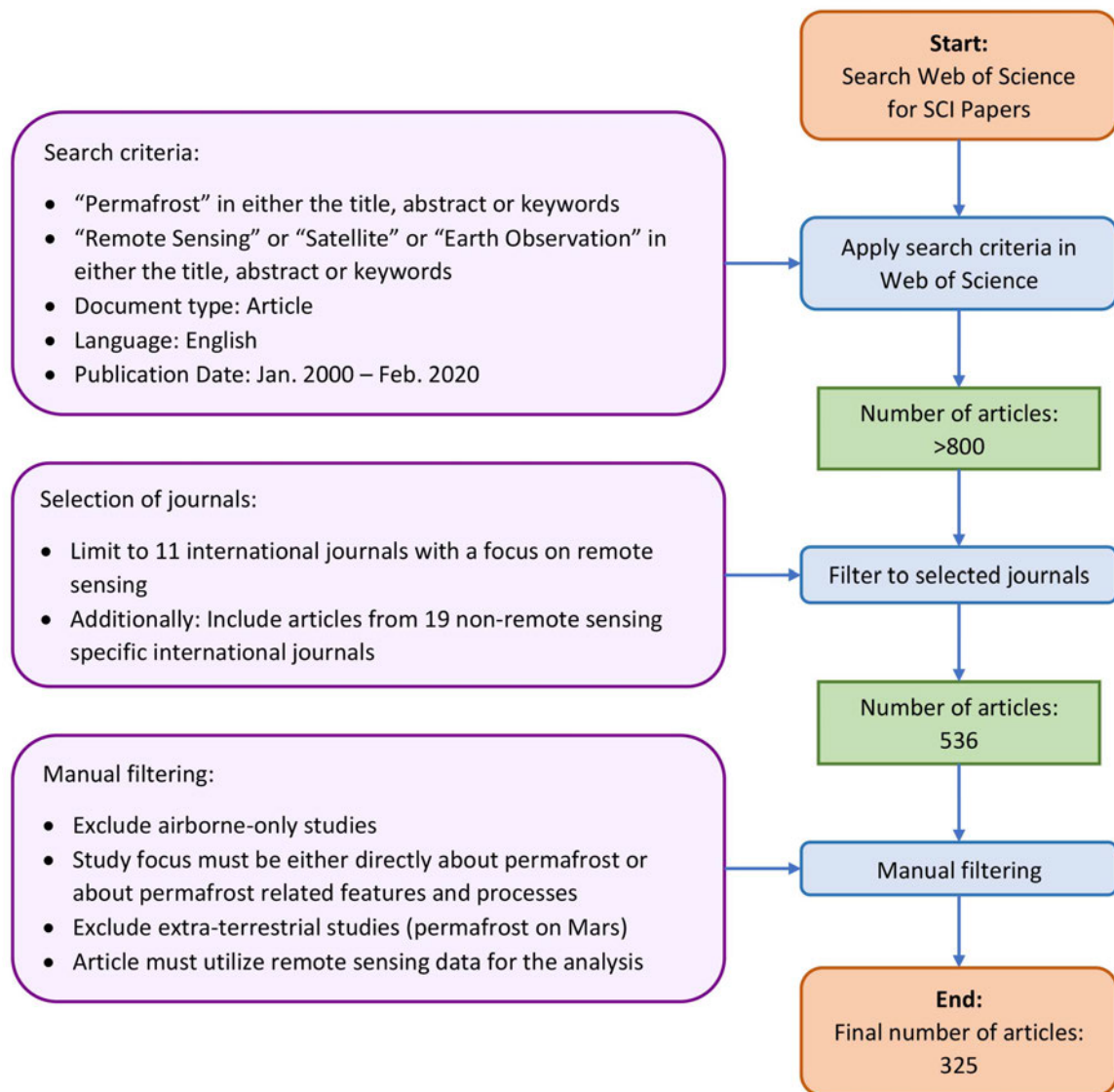
Figure 2.1: Flow chart of the selection process for relevant articles within this review. Modified after Philipp et al. (2021).

Table 2.1 lists all journals and the associated number of articles included in this review. The above-mentioned filtering approach may led to the exclusion of some relevant articles published in journals which were not considered in this review process. Adding more journals would, however, go beyond the scope of this review. On the same basis, non-English articles were not taken into consideration. Therefore, this strategy should constitute an acceptable compromise for a representative overview of recent trends and current efforts in satellite remote sensing for analyses related to frozen ground.

Table 2.1: List of reviewed Science Citation Index (SCI) journals. Infos about the number of covered articles per journal and their respective 5-year impact factor as well as the impact factor for the year 2019 are provided according the Web of Science Clarivate Analytics (n.d.) (rounded to the first decimal place). Source: Philipp et al. (2021).

Journal Name	No. of reviewed Articles	Impact Factor 2019	Impact Factor 5 year
Remote Sensing	60	4.5	5
Remote Sensing of Environment	34	9.1	9.6
Permafrost and Periglacial Processes	29	2.7	2.7
Environmental Research Letters	28	6.1	6.7
The Cryosphere	21	4.7	4.9
Geomorphology	17	3.8	3.9
Journal of Geophysical Research: Biogeosciences	15	3.4	4.2
Biogeosciences	14	3.5	4.2
Global Change Biology	14	8.6	9.8
Journal of Geophysical Research: Earth Surface	10	3.6	4
Hydrological Processes	10	3.3	3.6
International Journal of Remote Sensing	8	3	2.7
Journal of Geophysical Research: Atmospheres	8	3.8	4.3
IEEE Journal of Selected Topics in Applied Earth Observations and Remote Sensing	7	3.8	3.9
Science of the Total Environment	7	6.6	6.4
Scientific Reports	6	4	4.6
IEEE Transactions on Geoscience and Remote Sensing	5	5.9	6
Water Resources Research	5	4.3	5
Nature Communications	4	12.1	13.6
Nature Geoscience	3	13.6	16.1
Journal of Applied Remote Sensing	3	1.4	1.3
GIScience & Remote Sensing	3	6	4.2
Global and Planetary Change	3	4.4	5.1
Remote Sensing Letters	2	2.3	2.4
International Journal of Applied Earth Observation and Geoinformation	2	4.7	5.4
Frontiers in Earth Science	2	2.7	NA

Table 2.1: Continued.

Journal Name	No. of reviewed Articles	Impact Factor 2019	Impact Factor 5 year
ISPRS Journal of Photogrammetry and Remote Sensing	2	7.3	8.6
IEEE Geoscience and Remote Sensing Letters	1	3.8	3.7
Earth System Science Data	1	9.2	9.6
Palaeogeography, Palaeoclimatology, Palaeoecology	1	2.8	3
Total	**325**		

(... end of continued table.)

All research articles considered in this review were linked to the following five environmental categories "Subsurface Features and Processes", "Thermal Features and Processes", "Surface Land Features and Processes", "Surface Water Features and Processes", and "Atmospheric Features and Processes". Subsurface processes and features, such as dynamics in the ALT, dynamics in the freezing and thawing of the soil, or the distribution of permafrost are all covered by the category "Subsurface Features and Processes". The category "Thermal Features and Processes" encompasses topics related to heat fluxes and dynamics in ground temperature or land surface temperature. Surface movements (e.g. frost heave/thaw settlement), dynamics in the vegetation cover, snow cover, and other land surface related topics are covered by "Surface Land Features and Processes". "Surface Water Features and Processes" includes all topics related to the surface water, such as coastal erosion, lake extent dynamics, or lake ice. Finally, the category "Atmospheric Features and Processes" encompasses all environmental topics associated to the atmosphere, including evapotranspiration or greenhouse gas emissions. Each environmental focus was subsequently classified as a sub-category of one of the presented spheres. Several articles featured multiple environmental foci across different categories. Findings from a selection of highly cited and representative articles are provided per category.

The applied spatio-temporal resolution of utilized earth observation data is another important parameter investigated in this review. Four categories were established for the temporal resolution. Namely the categories, "Time Series", "Multitemporal", "Bitemporal", and "Unitemporal". Within the context of this review, a study was categorized as a "Time Series" if ten or more time steps were used. In case 3 9 times steps were applied, the study was classified as "Multitemporal". In terms of spatial resolution, it was differentiated between the four classes low (>1000 m), medium

low (100 1000 m), medium high (10 100 m) or high (<10 m). Moreover, different categories for scales were defined as follows: circum-Arctic, national, regional large (>250.000 km^2), regional small (10.000 250.000 km^2), and local (<10.000 km^2).

Even though studies based on aerial-only remote sensing data were excluded from the review process, many articles applied aerial footage either in conjunction with satellite data, for validation, as a historical reference, or other complementary use. Therefore, the category "aerial" was also included in the analysis on platform frequency. Lastly, a variety of openly available and permafrost related data sets are presented.

2.2 Results of the Literature Review

Key findings on the spatial distribution of study sites, the amount of annually published articles in the context of remote sensing of permafrost, as well as distribution and relationships between study and author countries are presented in the following sections. Additionally, details on the number and frequency of environmental research foci and the spatio-temporal resolutions across all investigated articles are provided. Moreover, applied sensor combinations and the frequency of utilized platforms are visualized and described in detail.

2.2.1 Temporal Development of Permafrost related Studies

The degradation of frozen ground and its associated features and processes received increasing attention in recent years (Grosse et al., 2016; A. M. Trofaier et al., 2017). This rise in awareness is also reflected in the number of annually published articles, which increased during the observed time frame from January 2000 until February 2020 (Figure 2.2). The rise in publication number was particularly high during the last decade, with the year 2018 having the most publications (62) across all years observed within this review. One potential reason could be that permafrost was added as an ECV to the ESA CCI program line-up in the same year (European Space Agency, n.d.-g; Westermann et al., 2018). Only twelve articles are listed for the year 2020, which can be attributed to the observed time span that was limited to February 2020. Based on the trend in publication numbers over the past two decades, a continuously increasing amount of remote sensing studies related to permafrost and its associated features/processes can be expected in future years.
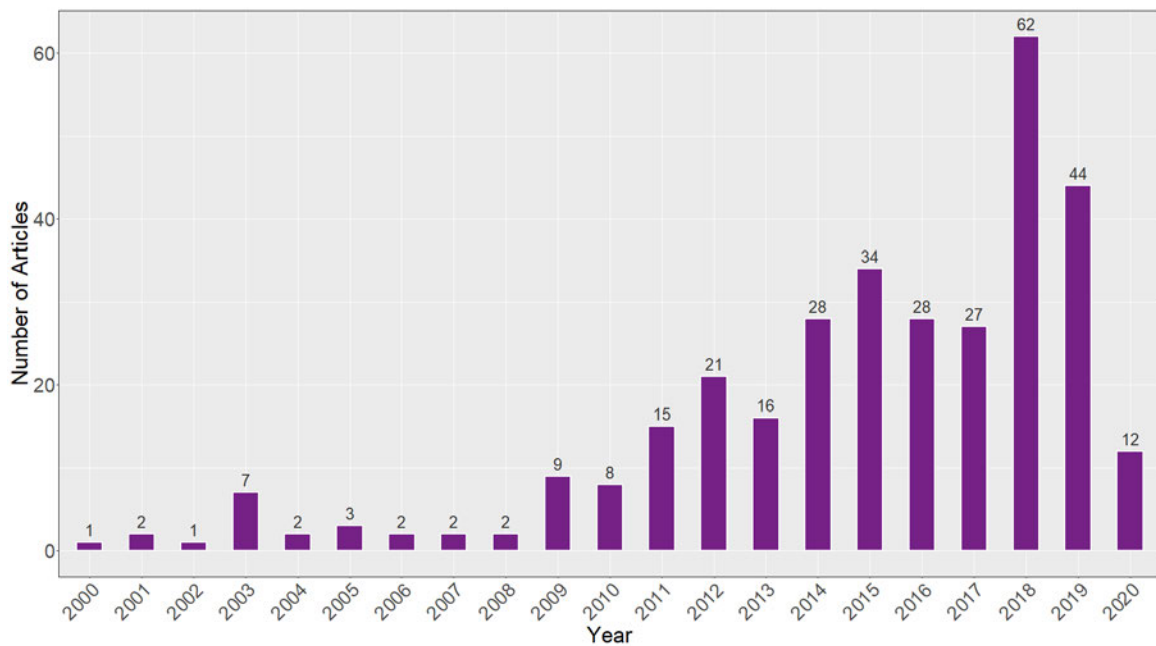
Figure 2.2: Number of published satellite Earth observation studies related to permafrost per year based on the reviewed articles. Modified after Philipp et al. (2021).

2.2.2 Distribution of Study Countries and first Author Institution Nationalities

The frequency of the first author's institution nationalities and the number of studies per country are illustrated in Figure 2.3. With 75 articles, Russia was revealed to be the most studied country, closely followed by Canada (71), the USA (68), and China (54) (Figure 2.3 a,b). In case of the nationality of the first authors institution, USA is most common with 91 articles. Other frequent institution nationalities are China (57), Germany (48) and Canada (47) (Figure 2.3 c,d). The high positions of China, Canada and the USA in both study and author frequency can be explained by the widespread permafrost occurrences in all three countries as visualized in Figure 1.1. In contrast, Russia, as the most studied country, appears strongly under-represented in terms of author frequency. Especially, since Russia features the largest distribution of permafrost across all countries based on the permafrost fraction by Obu et al. (2021b). As previously mentioned in section 2.1, only articles in English language were considered in this review. This might explain the low amount of Russian institution nationalities. Germany, on the other hand, is among the most common author nationalities, even though almost no permafrost occurrences, with the exception of mountain permafrost located at the Zugspitze (Gallerman et al., 2017), are present in this country.
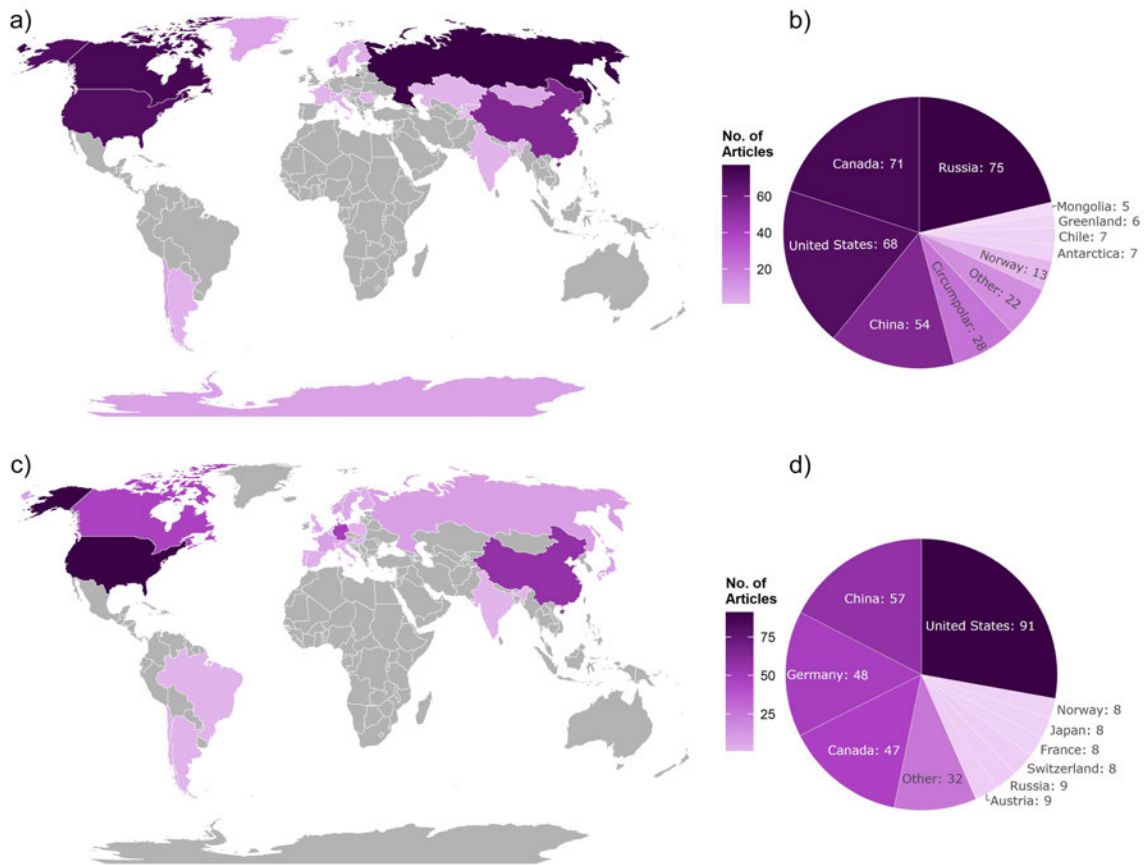
Figure 2.3: Map showing the frequency of study countries (**a**) and the relative distribution (**b**). Circumpolar studies are thereby not included in the map (**a**). Next to the study countries, the frequency of first author institution nationalities are displayed via a map (**c**) and the relative distribution as a pie chart (**d**). Some articles featured study areas in more than one country. Modified after Philipp et al. (2021).

The relationships between the institution nationalities and study countries is visualized in Figure 2.4. The Sankey diagram reveals a tendency for authors to conduct their investigations in the same country as the first author's institution nationality, provided that the respective country features permafrost occurrences. Thus, 93% of investigations in China were undertaken by Chinese institutions. A total of 80% of studies applied in the USA are associated with American institutions, followed by 7% of Canadian institutions. The two most common institution nationalities that conducted their analysis in Canada are Canadian (58%) and German (21%). In contrast, institution nationalities of studies carried out in Russia are distributed more heterogeneously. Most investigations were hereby carried out by German institutions (36%), followed by the USA (21%), Russia (10%), and Austria (6%). As one of the top three author countries, German institutions applied almost half (48%) of their investigations in Russia, followed by Canada (26%) and the USA (9%). The majority of circum-Arctic studies were conducted by American institutions (46%), followed by German institutions (11%).
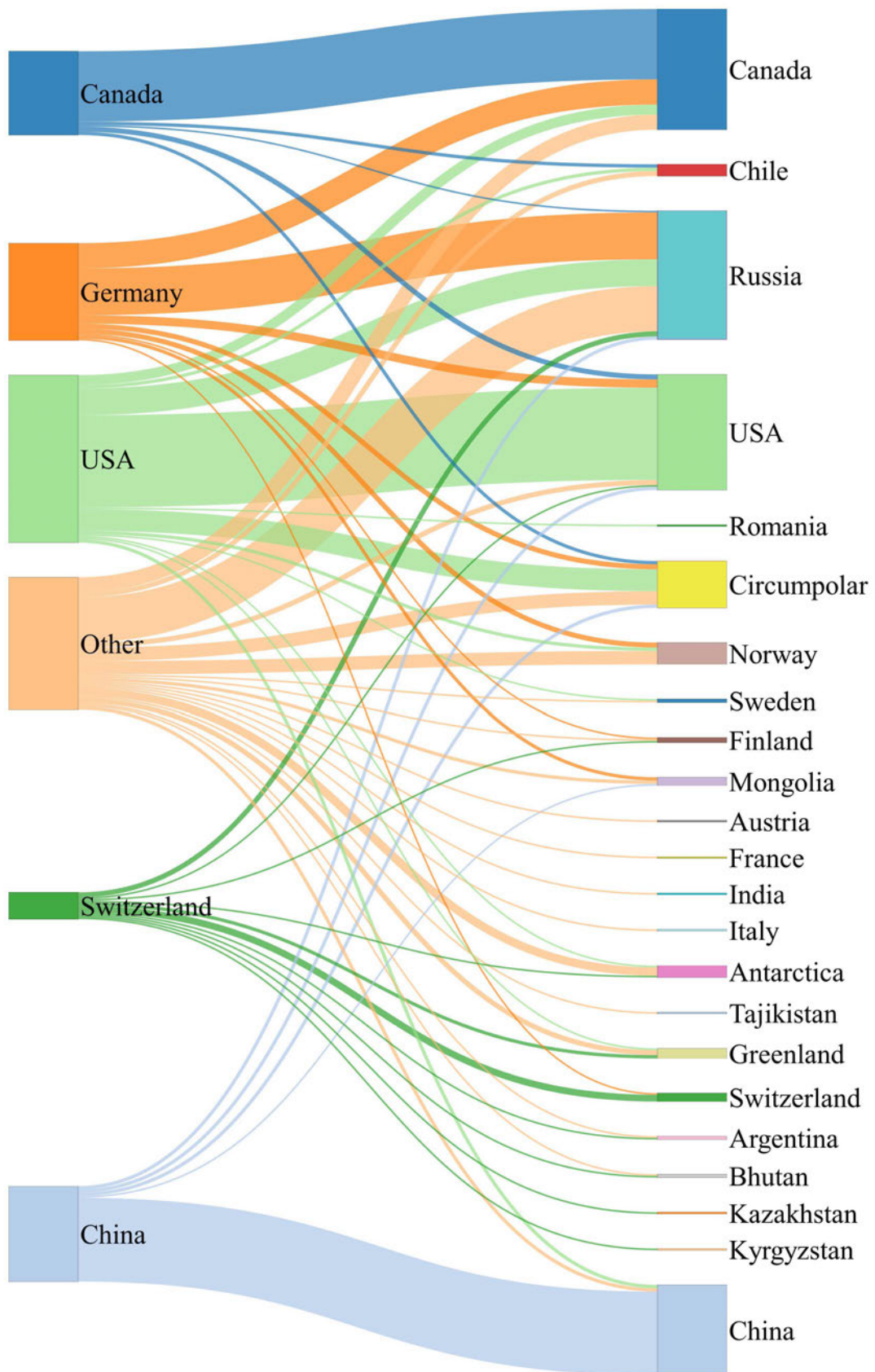
Figure 2.4: Sankey diagram of the relationship between the top five most frequent first author institution nationalities (left side) and the investigated countries (right side). Modified after Philipp et al. (2021).

2.2.3 Spatial Distribution of reviewed Articles

Only 9% of the reviewed articles conducted their analyses on a circum-Arctic scale (e.g. Oelke et al., 2003; Oelke & Zhang, 2004; Euskirchen et al., 2006; Epstein et al., 2012; Soliman et al., 2012; Watts et al., 2012; Fichot et al., 2013; K. Barnhart et al., 2014; Watts et al., 2014; André et al., 2015; Y. Kim et al., 2015; Paltan et al., 2015; Y. Yi et al., 2015; H. Park et al., 2016; Bartsch et al., 2017; Muster et al., 2017; Xia et al., 2017; Kroisleitner et al., 2018; Lyu & Zhuang, 2018; Suzuki et al., 2018; Liang et al., 2019; Raynolds et al., 2019; Obu et al., 2020; Naeimi et al., 2012; Nassar et al., 2014; Forkel et al., 2015; T. Hu et al., 2019). The spatial distribution of all other non-circum-Arctic investigations is illustrated in Figure 2.5. Specific key study regions can be identified across the four most studied countries Russia, Canada, the USA, and China.

The vast majority of studies applied in the USA are located in Alaska. Regions of particular interest are thereby the North Slope Borough together with its Arctic Coastal Plain (e.g. Frost et al., 2018; Engram et al., 2018; Schaefer et al., 2015; Lyons et al., 2013; K. Hinkel et al., 2017; Frohn et al., 2005; Nitze et al., 2017; Kupilik et al., 2018; B. M. Jones et al., 2018; Strozzi et al., 2018; Iwahana, Uchida, et al., 2016; Stephani et al., 2020; Hachem et al., 2012; Raynolds & Walker, 2016; Marchand et al., 2018; L. Liu et al., 2014; Nitze et al., 2018; Anthony et al., 2018, 2016; Tape et al., 2018; Gangodagamage et al., 2014; Lara et al., 2018; Muster et al., 2019; Piliouras & Rowland, 2020; Högström et al., 2018; L. Liu et al., 2015; Andresen & Lougheed, 2015; Balser et al., 2014; Tape et al., 2011; Ping et al., 2011; L. Liu et al., 2010; E. Kim & England, 2003; Liljedahl et al., 2016) (Figure 2.5 key study region 1), Seward Peninsula (e.g. Ulrich et al., 2014; Regmi et al., 2012; Engram et al., 2018; Liljedahl et al., 2016; Anthony et al., 2016; Iwahana, Harada, et al., 2016; M. C. Jones et al., 2012) (Figure 2.5 key study region 2), as well as the Yukon Kuskokwim Delta (e.g. Whitley et al., 2018; M. T. Jorgenson et al., 2018; Michaelides et al., 2019; Muster et al., 2019; Piliouras & Rowland, 2020) (Figure 2.5 key study region 3). Only three studies did not exclusively apply their research in Alaska. Two of which conducted their analyses in the Rocky Mountains located in southwestern Colorado (Brenning, 2009; Evans et al., 2018) (Figure 2.5 key study region 4), whereas the third exception is a paper published by T. Zhang et al. (2003), who investigated dynamics in freezing and thawing of the near-surface soil throughout the contiguous states of the USA.

The Tuktoyaktuk Coastlands and Mackenzie Delta within the Northwest Territories are the major study hot spots in Canada (e.g. Nill et al., 2019; Nguyen et al., 2009; Segal et al., 2016; Zwieback et al., 2018; Samsonov et al., 2016; Olthof et al., 2015; Marchand et al., 2018; Muskett & Romanovsky, 2009; Brooker et al., 2014; Fraser et

al., 2014; S. Kokelj et al., 2015; Kohnert et al., 2018; Vesakoski et al., 2017; Beighley et al., 2015; Zwieback et al., 2019; Muster et al., 2019; Fouest et al., 2018; Doxaran et al., 2015, 2012; Piliouras & Rowland, 2020) (Figure 2.5 key study region 5). The Northwest Territories featured a number of further investigations (e.g. Y. Zhang et al., 2014; Fraser et al., 2014; Chasmer et al., 2014; Marchand et al., 2018; Chasmer et al., 2011; Carpino et al., 2018; Quinton et al., 2011; Gibson et al., 2018; Chasmer & Hopkinson, 2017; Helbig et al., 2016; Connon et al., 2014; Quinton et al., 2003; Abis & Brovkin, 2017; Morse & Wolfe, 2015). Additional frequently studied regions were identified to be the eastern shore of Hudson Bay in proximity to the Inuit village of Umiujaq in Northern Quebec (e.g. L. Wang et al., 2017; Freitas et al., 2019; Beck et al., 2015; L. Wang, Marzahn, et al., 2018; Watanabe et al., 2011) (Figure 2.5 key study region 6) and Herschel Island in the Yukon territory (e.g. Cunliffe et al., 2019; Short et al., 2011; Obu, Lantuit, Myers-Smith, et al., 2017; Lantuit & Pollard, 2008; Ramage et al., 2018; Coch et al., 2020; Irrgang et al., 2018; Ramage et al., 2017). Both Arctic islands and the mainland of the Nunavut territory appear poorly investigated, despite the presence of continuous permafrost in these regions.

Several key study areas were identified in Russia, one of which is the Lena River Delta (e.g. Muskett & Romanovsky, 2009; Zwieback et al., 2018; Morgenstern et al., 2011; Antonova et al., 2016; Langer et al., 2010, 2013; Nitze & Grosse, 2016; Antonova et al., 2018; Strozzi et al., 2018; J. Chen et al., 2018; Runge & Grosse, 2019; Stettner et al., 2018; Reschke et al., 2012; Ulrich et al., 2014; Zwieback et al., 2016; Morgenstern et al., 2013; Grosse et al., 2007; Westermann et al., 2017; Grosse et al., 2005; Muster et al., 2019; Juhls et al., 2019; Mikola et al., 2018; Fuchs et al., 2018; Heim et al., 2014; Günther et al., 2013; Piliouras & Rowland, 2020) (Figure 2.5 key study region 7). Other key study areas were observed to be the Gydan and Yamal Peninsulas and the areas in proximity (e.g. D. Walker et al., 2009; Widhalm et al., 2017; Dvornikov et al., 2018; Bartsch et al., 2019; Kizyakov et al., 2018; Novikova et al., 2018; A. Trofaier et al., 2013; Frost et al., 2014; Nitze et al., 2018; Frost & Epstein, 2014; Forbes et al., 2010; Liljedahl et al., 2016; Flessa et al., 2008; Abis & Brovkin, 2017; Bohn et al., 2015; Rawlins et al., 2015; Piliouras & Rowland, 2020; Sannel & Kuhry, 2011) (Figure 2.5 key study region 8), and the Kolyma Lowland (e.g. Nitze et al., 2017; Sakai et al., 2016; Broderick et al., 2015; Curasi et al., 2016; Frost & Epstein, 2014; Anthony et al., 2016; Muster et al., 2019; Günther et al., 2013; Piliouras & Rowland, 2020; Siewert et al., 2015; Loranty et al., 2014; C. G. Griffin et al., 2011) (Figure 2.5 key study region 9). The Central Yakutia Lowland features a few other clusters as well (e.g. S.-E. Park et al., 2011; Runge & Grosse, 2019; Nitze et al., 2017; Dupeyrat et al., 2018; Séjourné et al., 2015) (Figure 2.5 key study region 10). Although most studies out of any country were conducted in Russia, there are still many regions within the

continuous permafrost zone that remain to be investigated.
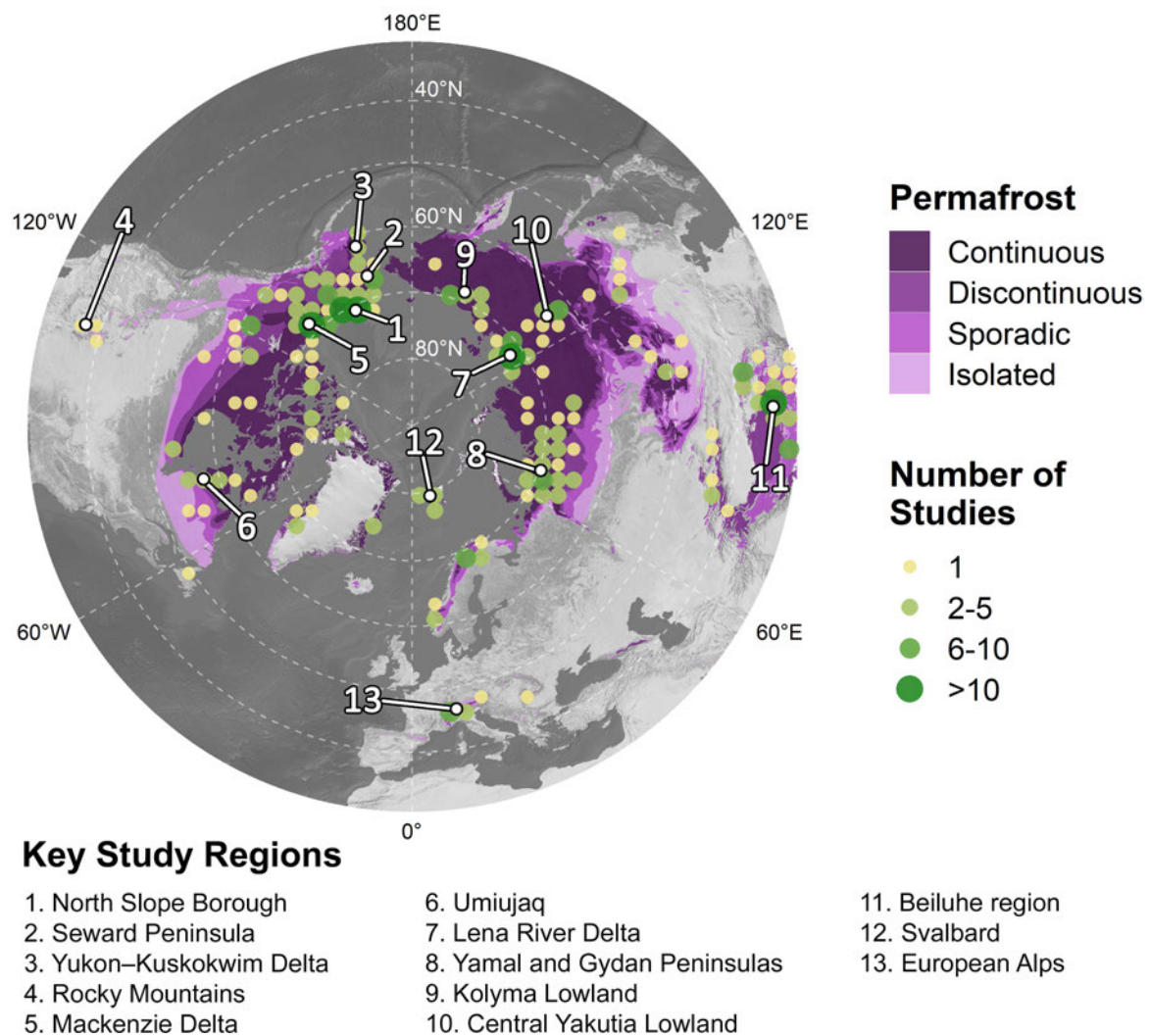
Figure 2.5: Spatial distribution of study areas across the reviewed articles for the Northern Hemisphere combined with the circum-Arctic permafrost map by J. Brown et al. (2002) (purple coloured areas). One study may have more than one study area. A shaded relief by Natural Earth (n.d.) was used as a background map. All data is illustrated in a polar Lambert azimuthal equal area projection. Circum-Arctic studies were excluded from this visualization. 13 key regions with study clusters are highlighted and labelled. Modified after Philipp et al. (2021).

In case of China, the majority of studies focused their investigations inside the Qinghai Tibet Plateau (QTP), with a specific interest on the Beiluhe region (e.g. F. Chen et al., 2013, 2012; C. Wang et al., 2017; Y. Song et al., 2018; C. Wang, Zhang, Paloscia, et al., 2018; Niu et al., 2018; Yin et al., 2018; Luo, Yin, et al., 2019; Jia et al., 2017; Z. Zhang et al., 2018; P. Tang et al., 2017; C. Xie et al., 2010; Tian et al., 2016; Z. Zhang et al., 2019; Tian et al., 2017; C. Wang, Zhang, Zhang, et al., 2018; Luo, Niu, et al., 2019; L. Huang et al., 2020) (Figure 2.5 key study region 11). Both the Qinghai Tibet Highway (QTH) and the Qinghai Tibet Railway (QTR) with a length

of 1.956 km are thereby main study interests (e.g. X. Zhang et al., 2019; F. Chen et al., 2013, 2012; C. Wang et al., 2017; Niu et al., 2018; Yin et al., 2018; Jia et al., 2017; Z. Zhang et al., 2018; P. Tang et al., 2017; Zou et al., 2014; Chang & Hanssen, 2015; C. Xie et al., 2010; Z. Zhang et al., 2019; C. Wang, Zhang, Zhang, et al., 2018).

Aside from the previously mentioned regions, Svalbard in Norway (e.g. Westermann et al., 2012, 2011; Rouyet et al., 2019; Eckerstorfer et al., 2017; Bernhardt et al., 2017; Kasprzak et al., 2020; Lousada et al., 2018; Woelders et al., 2018) 2.5 key study region 12) and the European Alps (e.g. Bertone et al., 2019; Strozzi et al., 2020; Gruber & Hoelzle, 2001; Kääb, 2002; Strozzi et al., 2004; Kenyi & Kaufmann, 2003; Ravanel et al., 2017; Strozzi et al., 2010) 2.5 key study region 13) are further frequently investigated areas. In addition, a significant amount of articles put their research focus on Greenland (e.g. Westermann, Elberling, et al., 2015; Strozzi et al., 2018, 2020; Jørgensen et al., 2015; Westergaard-Nielsen et al., 2018; Finger Higgens et al., 2019) and Scandinavia (e.g. Eriksen et al., 2017; Jagdhuber et al., 2014; Torbick et al., 2012; Gisnås et al., 2013; Zwieback et al., 2016; Etzelmüller et al., 2001; Hartley et al., 2015; Sannel & Kuhry, 2011).

The vast majority (94%) of articles applied their analysis across the Northern Hemisphere. However, a number of authors also dedicated their research to features and processes in the context of permafrost on the Southern Hemisphere 2.6. A common study region is hereby the Andes, with a particular focus on the kinematics of rock glaciers and the distribution of mountain permafrost (e.g. Brenning, Long, & Fieguth, 2012; Villarroel et al., 2018; Nagy et al., 2019; Monnier et al., 2014; Janke et al., 2017; Brenning, Peña, et al., 2012; Batbaatar et al., 2020; Strozzi et al., 2020) (2.6 key study region 1). Another common study area is hereby the South Shetland Islands and specifically Byers Peninsula on Livingston Island within the Antarctic region (e.g. Strozzi et al., 2018; Mink et al., 2014; López-Martínez et al., 2012; Moura et al., 2012; Vieira et al., 2014; Miranda et al., 2020) (2.6 key study region 2). Furthermore, rock glaciers in the McMurdo Dry Valleys were the subject of one single article (Bockheim, 2014) (2.6 key study region 3). Finally, modelling of near-surface temperatures of permafrost across the entire Antarctic was conducted in a recent study by Obu et al. (2020). A minimum permafrost temperature of $-36°C$ was hereby modelled which represents the global minimum based on worldwide efforts in modelling permafrost temperatures (Obu et al., 2020).
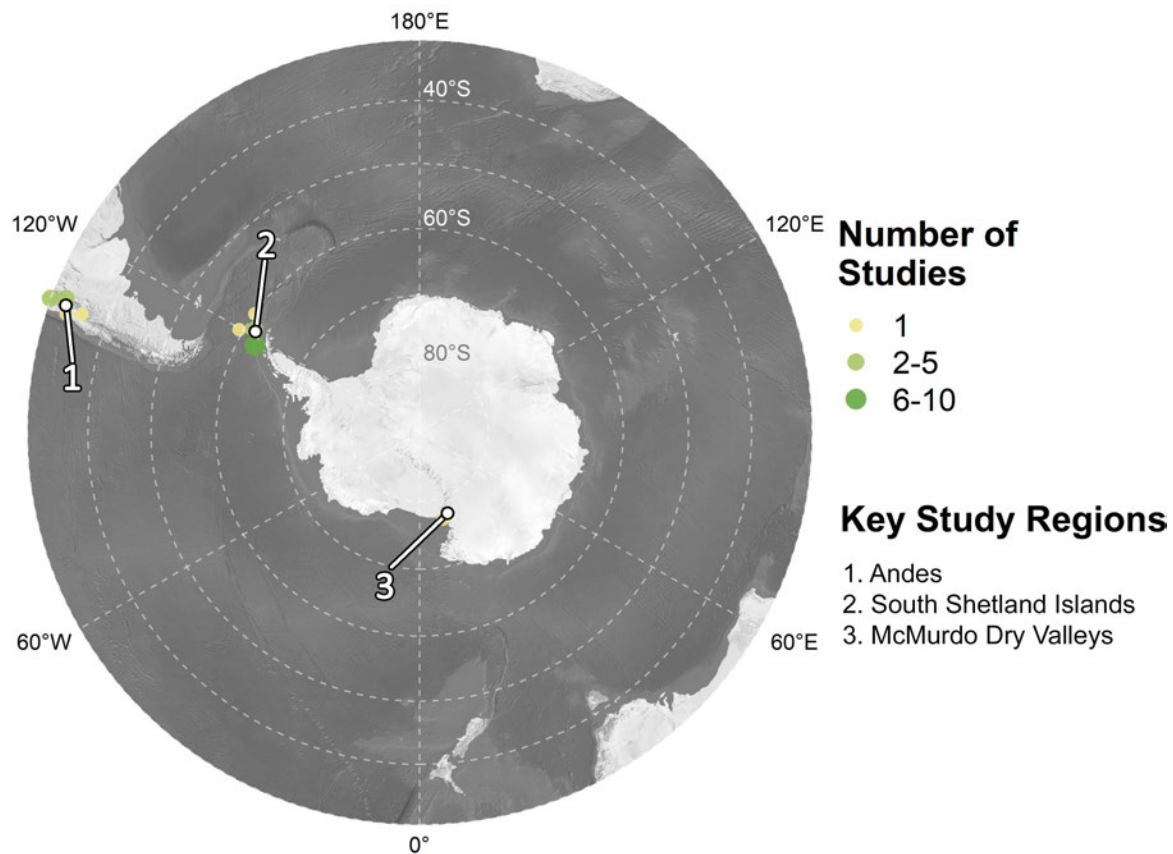
Figure 2.6: Spatial distribution of study areas across the reviewed articles for the Southern Hemisphere. One study may have more than one study area. A shaded relief by Natural Earth (n.d.) was used as a background map. All data is illustrated in a polar Lambert azimuthal equal area projection. Circum-Antarctic studies were excluded from this visualization. Three key regions with study clusters are highlighted and labelled. Modified after Philipp et al. (2021).

2.2.4 Categorization of environmental Research Foci

The distribution of research foci and the associated categories are visualized in Figure 2.7. Roughly 25% of studies are associated with "Surface Water Features and Processes", which makes it the second most common category. Within this category, almost half of all articles dedicated their work on "Lake Extent/Dynamics" (∼47% in category; ∼12% in total). Relatively small numbers of articles are associated with other environmental foci, such as "Coastal Erosion" (∼14% in category; ∼4% in total), "Ocean Colour" (∼7% in category; ∼1% in total), or "Wetland Dynamics" (∼6% in category; ∼1% in total).

"Surface Land Features and Processes" represents the most common category with ∼43% of articles associated to it. The most frequently investigated research foci are thereby "Vegetation Cover (Dynamics)" (∼27% in category; ∼12% in total), "Frost Heave/Thaw Settlement" (∼16% in category; ∼7% in total), "Rock Glacier Map-

ping/Dynamics" (∼10% in category; ∼4% in total), "Thaw Slump Mapping/Dynamics" (∼10% in category; ∼4% in total), and "Wildfires" (∼10% in category; ∼4% in total).

Roughly 21% of articles are linked to the category "Subsurface Features and Processes". Common environmental topics are hereby "Permafrost Distribution" (∼32% in category; ∼7% in total), "Active Layer Thickness (Dynamics)" (∼21% in category, ∼4% in total), and "Freeze/Thaw Dynamics" (∼18% in category; ∼4% in total).

Both "Atmospheric Features and Processes" and "Thermal Features and Processes" represent the least frequent categories with ∼4% and ∼7%, respectively. In case of "Atmospheric Features and Processes", most studies dedicated their efforts on "Methane/Carbon Dioxide Emissions" (∼75% in class; ∼3% in total). The most frequent topic within "Thermal Features and Processes" was revealed to be "Land Surface Temperature (Dynamics)" (∼50% in category; ∼3% in total), closely followed by "Ground Temperature (Dynamics)" (∼43% in category; ∼3% in total).
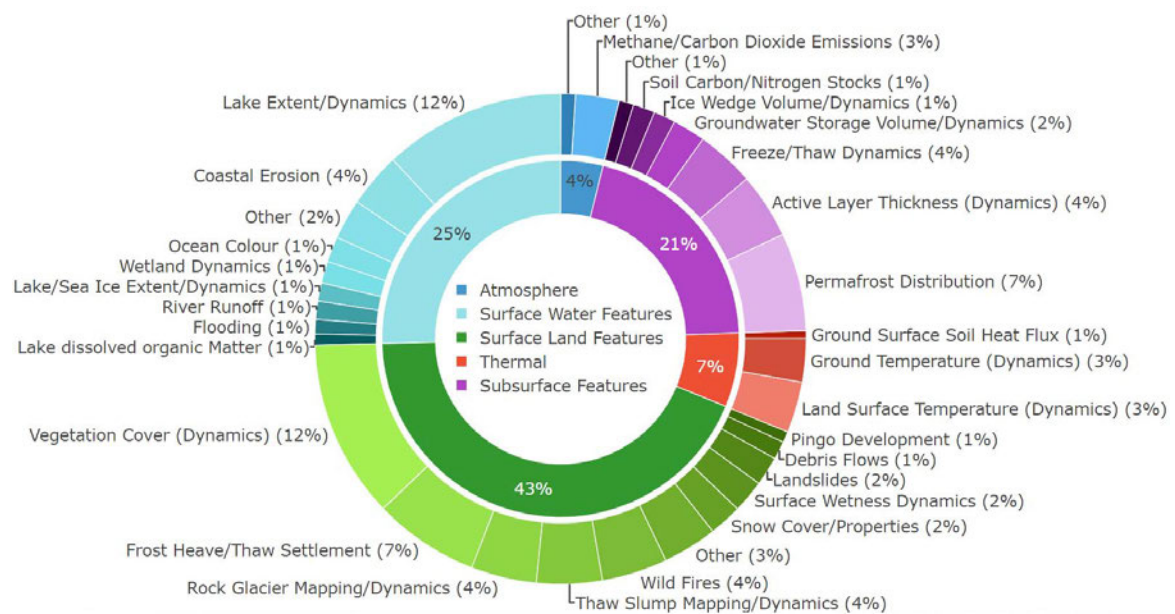
Figure 2.7: Distribution and frequency of the study foci across the reviewed articles. Research foci are categorized into the five spheres "Subsurface Features and Processes", "Thermal Features and Processes", "Surface Land Features and Processes", "Surface Water Features and Processes", and "Atmospheric Features and Processes". Modified after Philipp et al. (2021).

The top 25 most frequently investigated environmental foci across all categories are displayed in Figure 2.8. The two most frequently occurring foci are hereby "Lake Extent/Dynamics" (50 articles) and "Vegetation Cover (Dynamics)" (49 articles). All other environmental topics are covered significantly less compared to the two aforementioned topics. Further commonly investigated environmental foci are "Frost

Heave/Thaw Settlement" (29 articles), "Permafrost Distribution" (27 articles), "Active Layer Thickness (Dynamics)" (18 articles), "Rock Glacier Mapping/Dynamics" (18 articles), "Thaw Slump Mapping/Dynamics" (18 articles), and "Wildfires" (18 articles), amongst others.
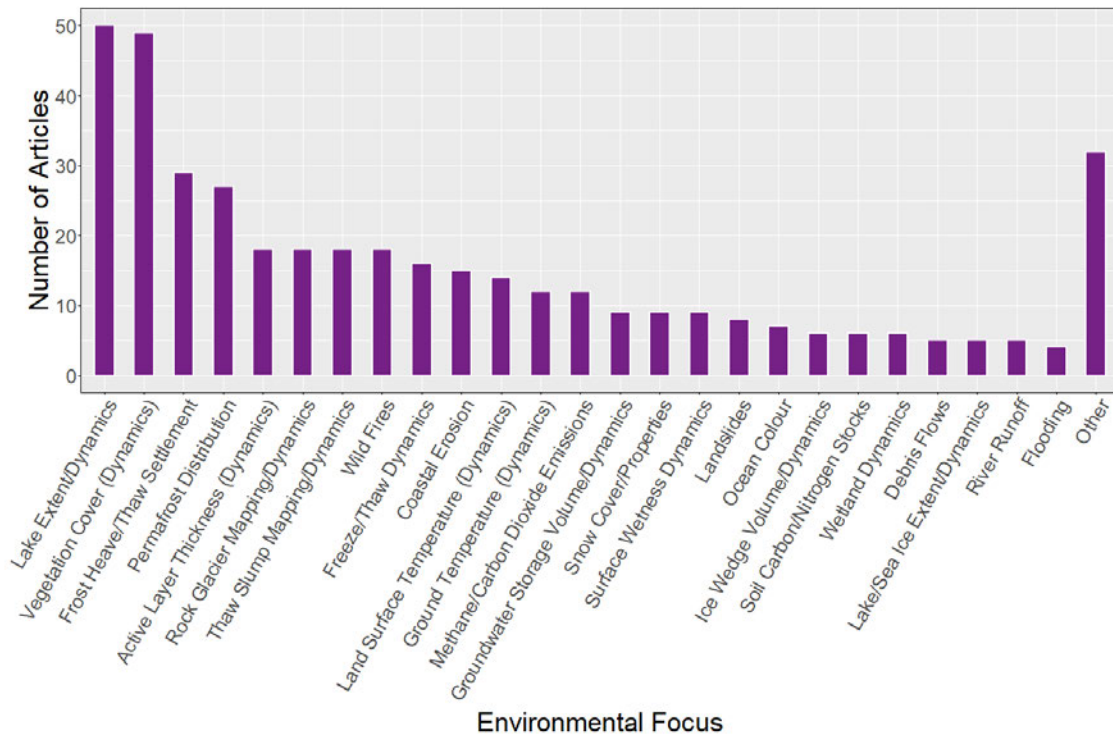
Figure 2.8: The top 25 most frequently studied environmental foci across the reviewed articles. Several articles covered more than one environmental focus.

Figure 2.9 a) visualizes the temporal development of the distribution of the 15 most frequent environmental foci on an annual basis. Similar to Figure 2.2, a general trend to a higher publication number per topic can be observed, specifically during the second half of the observation period. Looking at foci related to "Subsurface Features and Processes", the mapping of the permafrost occurrences is among the earliest publications in the context of satellite earth observation of permafrost and related features/processes. First investigations date back to the year 2001. However, major attention to this topic was brought back not before the last 10 years, with 2018 and 2019 having the most publications about it. Studies on the storage volume and dynamics of groundwater peaked, similar to several other topics, in 2018. A general increase in attention to the active layer thickness and its dynamics can be observed since 2013. Dynamics in freezing and thawing behaviour was, for the most part, studied between 2010 and 2020, with most articles published in both years 2015 and 2019.

As for the environmental category "Thermal Features and Processes", first efforts in studying ground temperature dynamics were conducted in 2003. Greatest attention to this topic could be observed for 2018, followed by 2019 and 2015. In contrast, investigations related to land surface temperature first occurred in 2009, with 2012 featuring the most publications.

Addressing the topics linked to "Surface Land Features and Processes", earliest study efforts on the effects of wildfires within the permafrost domain can be reported for 2009. In increase in related publications can be observed since 2016. Attention on thaw slumps was particularly high within the years 2014 and 2018. Although first efforts in studying the effects of snow cover and associated parameters on frozen ground already started in 2006, publication associated to this topic are in general sparsely distributed. Research on the dynamics of rock glaciers is overall scarce, although it is spread out through time rather evenly, with peaks in 2012 and 2019. Research efforts on thaw settlement and frost heave started in 2010 with a trend towards a higher annual publication rate since 2014. Lastly, the majority of studies related to vegetation cover (dynamics) were published during 2010 2020, with a peak in 2018.

In case of the category "Surface Water Features and Processes", earliest investigations on eroding permafrost coastlines from a satellite earth observation perspective can be reported for 2008. However, the topic regained attention not before the year 2018. In contrast, lake extents and their dynamics were studied on a rather regular basis within the last two decades. Peaks were hereby observed for the years 2013 and 2018.

Finally, emissions of carbon dioxide and methane was the only topic associated to the category "Atmospheric Features and Processes" and listed under the top 15 most frequently investigated environmental foci. Within the context of this review, earliest research efforts can be dated back to the year 2008. The overall largest amount of annual publications was observed for the year 2015.

A general overview on the temporal development of annually published articles for each of the environmental categories "Subsurface Features and Processes", "Thermal Features and Processes", "Surface Land Features and Processes", "Surface Water Features and Processes", and "Atmospheric Features and Processes" is provided in Figure 2.9 b). An increasing discrepancy in the cumulative sum of articles per year can be observed across the individual categories over time. The growing difference in article quantity over time and across different categories is particularly visible during the last decade. Greatest rise in publication frequency can be observed for the category "Surface Land Features and Processes". Slightly weaker increases in the article quantity can be reported for both categories "Subsurface Features and Processes" and "Surface

Water Features and Processes". Comparably overall weak increases in published articles can be observed for "Atmospheric Features and Processes" and "Thermal Features and Processes".
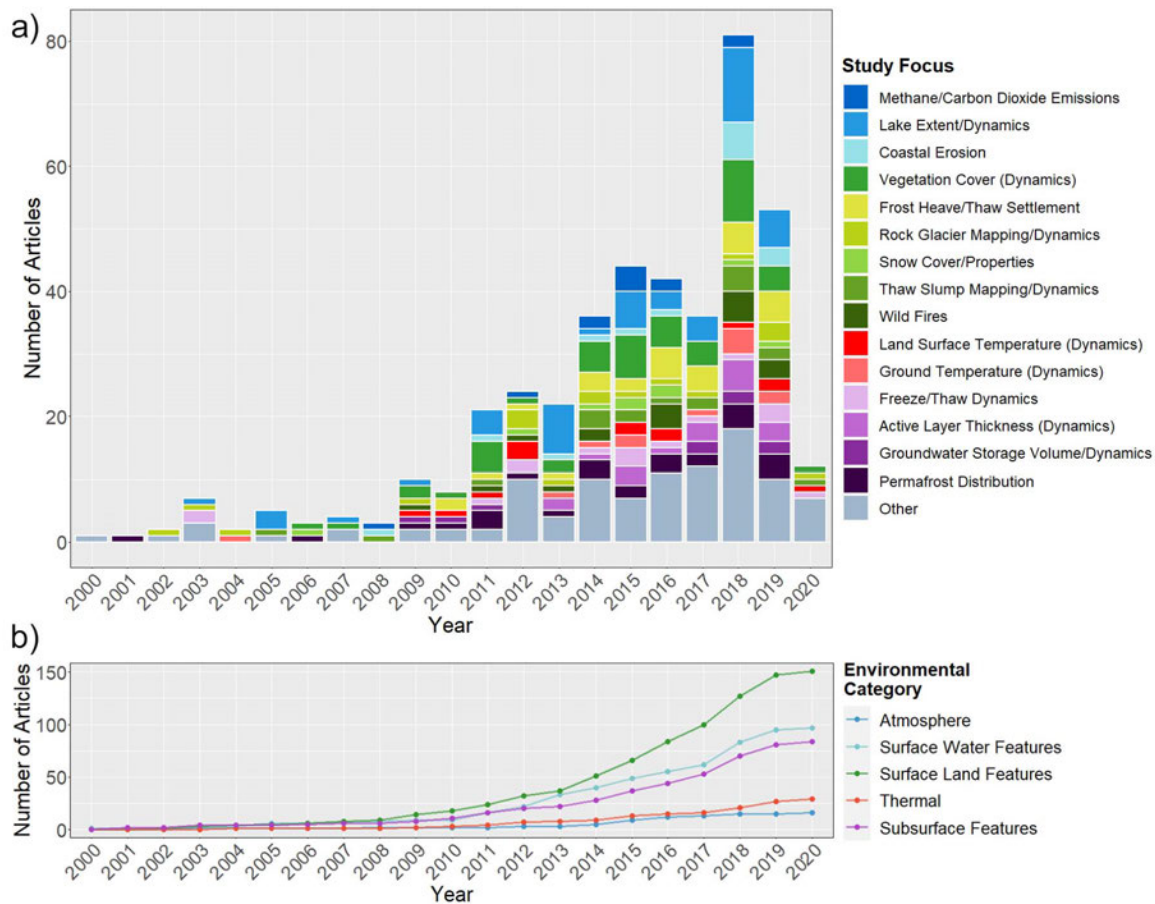
Figure 2.9: (**a**) Frequency of the top 15 most frequent environmental foci across the reviewed articles per year. Various articles covered more than one environmental focus. (**b**) The cumulative sum of articles per environmental category and per year. Modified after Philipp et al. (2021).

Since the frequency of studied environmental foci are not only distributed over time but also over space, the spatial distribution of environmental research foci across the reviewed articles was investigated. In particular, quantity and geographical spread of individual topics were studied on a country basis. Figure 2.10 illustrates the study focus distribution for the top four most frequently studied countries and studies that applied their analyses on a circum-Arctic scale.

The most common environmental category in Canada proved to be "Surface Land Features and Processes" with 40%. Articles dedicated to "Surface Water Features and Processes" represent 33% of studies within this country. Significantly smaller study efforts were undertaken within the category "Subsurface Features and Processes" (17%), while both categories "Thermal Features and Processes" and "Atmospheric Features

and Processes" were investigated the least with 6% and 4% of articles, respectively. Most research efforts were directed towards the extents of lakes and thaw slumping. Furthermore, dynamics in vegetation cover and permafrost distribution were also frequently covered subjects.

In case of the USA, the environmental category "Surface Land Features and Processes" was, again, studied the most with 39%. The second most frequent category is "Surface Water Features and Processes" with 32%, followed by "Subsurface Features and Processes" with 25%. Both spheres "Atmospheric Features and Processes" and "Thermal Features and Processes" each represent only 2% of studies. Most efforts were dedicated to study lake extent (dynamics). Further common topics are wildfires, vegetation cover (dynamics), and permafrost distribution.

The category "Surface Land Features and Processes" was also studied the most in Russia with 43% of articles. Articles associated to "Surface Water Features and Processes" make up 34%, followed by "Subsurface Features and Processes" with 15%. Again, the two least frequently studied categories were "Atmospheric Features and Processes" (5%) and "Thermal Features and Processes" (3%). The highest number of studies located in Russia were investigating lake extents and dynamics in the vegetation.

In China, the category "Surface Land Features and Processes" proved once more to be associated with the most (43%) articles. In contrast to the previously covered countries, the second most frequent category in China was observed to be "Subsurface Features and Processes" with 27%, followed by "Surface Water Features and Processes" with 14%. Articles linked to "Thermal Features and Processes" make up 10%, while studies related to "Atmospheric Features and Processes" were least frequent with 5%. Dynamics in thaw settlement and frost heave were hereby studied the most. Other common environmental foci were related to the vegetation cover, lake extents, and the active layer thickness.

Finally, a total of 28 articles applied their investigations on either a circum-Antarctic, or a circum-Arctic scale. In contrast to the distribution of categories within individual countries, the following two categories "Surface Land Features and Processes" and "Subsurface Features and Processes" are distributed equally and make up 29% of studies, each. Similarly frequent is the category "Surface Water Features and Processes" which is associated to 26% of investigations. At last, the categories "Thermal Features and Processes" and "Atmospheric Features and Processes" make up 11% and 6%, respectively. The most frequently analysed topic on a circumpolar scale was hereby dynamics in soil freezing and thawing. Further common research foci were observed to be vegetation cover and snow cover.
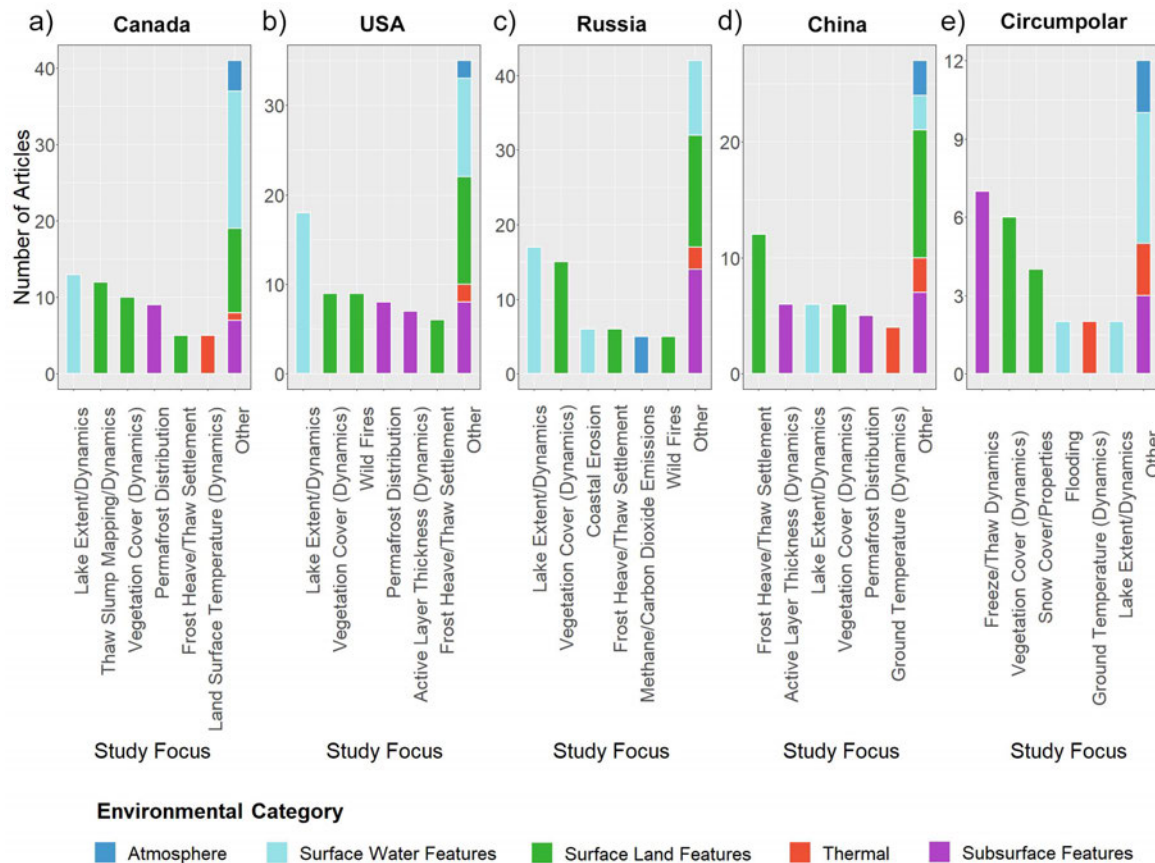
Figure 2.10: Study focus distribution for the top four most frequently studied countries and circum-Arctic studies. Featured countries are Canada (**a**), United States (**b**), Russia (**c**) China (**d**) and circumpolar studies (**e**). Modified after Philipp et al. (2021).

2.2.4.1 Subsurface Features and Processes

The frequency of studied environmental foci which are linked to subsurface processes and features was 21% (e.g. Haq & Baral, 2019; S. Panda et al., 2012; Dulamsuren et al., 2016; Xu et al., 2019; Ou, Leblon, et al., 2016; Ou, LaRocque, et al., 2016; Bibi et al., 2019; Landerer et al., 2010; Pastick et al., 2014; Kremer et al., 2011; Hugelius et al., 2010; S. K. Panda et al., 2010; Cao et al., 2019; Etzelmüller et al., 2006; Bai et al., 2018; Y. Shi et al., 2018; Fraser et al., 2018; Muskett & Romanovsky, 2011; Gagarin et al., 2020; Zheng et al., 2019; J. Wang et al., 2020; Yin et al., 2017; Y. Yi et al., 2018; Bernard-Grand'Maison & Pollard, 2018; B. M. Jones et al., 2016). Geographical hot spots were hereby observed in the QTP, the Mackenzie Delta in Canada, and in Alaska. In addition, a couple of circum-Arctic investigations are linked to this category. The most frequent environmental focus in this category was identified to be the distribution of permafrost. Additional information based on satellite data can hereby improve modelling accuracies in the context of permafrost distribution (Riseborough et al., 2008). Space-borne imagery was used within two studies by Obu et al. (2019) and

Westermann, Østby, et al. (2015) for Mean Annual Ground Temperature (MAGT) investigations across the entire Northern Hemisphere and specifically for the North Atlantic permafrost area, as well as for developing permafrost zonation maps. In this context, Obu et al. (2019) mentioned that the total land area underlain by frozen ground is 22% in case of the Northern Hemisphere. The modelled numbers suggest therefore around 2×10^6 km^2 less area underlain by permafrost compared to numbers of previous modelling efforts (Obu et al., 2019). The mentioned circumpolar maps on the distribution of permafrost as well as the MAGT are openly available products and also listed in Table 2.2. A higher resolution but smaller scale approach on mapping permafrost distribution was undertaken by Y. Zhang et al. (2014), who modelled permafrost occurrences for a region in the Canadian Northwest Territories covering ~8836 km^2. Space-borne derived land cover information made it possible to map occurrences of permafrost with finer resolution compared to previously released maps. Nonetheless, the comparatively low spatial resolutions of available data on ground and soil conditions were hereby significant limitations factors (Y. Zhang et al., 2014).

The environmental focus with the second greatest number of articles within this category is "Active Layer Thickness (Dynamics)". Pastick et al. (2013) modelled the ALT in the Yukon River Flats, Alaska with a spatial resolution of 30 m based on Landsat satellite imagery, airborne electromagnetic data, and further spatial information. A successful application of the proposed data and methods for estimating ALT was hereby communicated by the authors. The authors further mention that an increased quantity in field observations as well as geological and topographical data of higher resolution could improve the model output (Pastick et al., 2013). The application of the Remotely Sensed Active Layer Thickness (ReSALT) algorithm on Interferometric Synthetic Aperture Radar (InSAR) analyses based on L-band data acquired by the Advanced Land Observing Satellite (ALOS) Phased Array L-Band Synthetic Aperture Radar (PALSAR) sensor was performed in a study by Schaefer et al. (2015) in order to estimate ALT close to Barrow in Alaska. Good agreement between the ALT estimations based on ReSALT and in-situ measurements could be observed for ~76% of the investigation regions. On the other hand, ALT was overestimated for ~1% and underestimated for ~23% of the study area, which was attributed to the presence of gravel, unsaturated soils, and artifacts in the InSAR analyses. The authors suggest to implement data on gravel distribution and size as well as detailed information on soil moisture for future studies in order to improve the output quality on ALT estimations based on the ReSALT algorithm (Schaefer et al., 2015). Another study by Widhalm et al. (2017) implemented TerraSAR-X based X-band SAR data for modelling the ALT at 10 m spatial resolution for an area associated with deep ALT in central Yamal, Russia. A positive correlation between the backscatter

signal and the ALT was thereby observed. The authors attributed uncertainties to the surface roughness, soil moisture, vegetation cover, and heterogeneity within one pixel. Furthermore, the authors speculated on the usefulness of polarimetric SAR in the context of differentiating between the aforementioned uncertainties and other mechanisms responsible for variations in the scattering behaviour (Widhalm et al., 2017).

Several articles also dedicated their research efforts to "Freeze/Thaw Dynamics". X. Li et al. (2012) investigated changes in the thawing and freezing cycle over the QTP via daily passive RADAR data derived from SSM/I. Between 10 and 50 fewer days of frozen soils were observed from 1988 2007. The authors further identified postponed freezing of the soil by 10.1 ± 11.2 days and earlier starting dates of soil thawing by 14.3 ± 13.0 days. Hydrological and ecological conditions and their impacts on the thaw-freeze behaviour require hereby further investigation, while rising air temperatures are speculated to be a key factor on the freeze-thaw behaviour (X. Li et al., 2012). In another study by Roy et al. (2015), the feasibility of applying L-band passive RADAR data for monitoring freezing and thawing dynamics was tested over Canada. A good agreement between reference data and the weekly satellite-based freeze-thaw observations was reported. At the same time, ice cover throughout the transition period, the presence of liquid water in snow, as well as growing vegetation were identified to be remaining challenges for the precise monitoring of freeze-thaw dynamics (Roy et al., 2015). T. Hu et al. (2019) introduced in a recent publication a continuous and globally applied record on thawing and freezing dynamics of the near-surface soil via passive RADAR imagery derived from the Advanced Microwave Scanning Radiometer - Earth Observing System (AMSR-E) and the Advanced Microwave Scanning Radiometer 2 (AMSR2). The freeze/thaw dynamics output of the model was in good agreement with in-situ reference data. The authors further suggested a synergistic use with additional high resolution satellite products in future studies, which could potentially also increase the resolution of the freeze-thaw analysis (T. Hu et al., 2019).

2.2.4.2 Thermal Features and Processes

A generally sparse spatial distribution of study areas could be observed for the category "Thermal Features and Processes", which can be explained by the relatively low number of articles (e.g. C. Li et al., 2019; Hachem et al., 2009; K. P. Klein et al., 2019; Muster et al., 2015; Ran et al., 2018) associated to this category. The key geographical study region was hereby identified to be the QTP. Further isolated study locations were observed in Canada, Alaska, Norway, Greenland, the Lena Delta, and additionally some circumpolar investigations. Several articles addressed the use

of Land Surface Temperature (LST) as a potential proxy for assessing permafrost and its thermal state. Satellite-based LST measurements derived from MODIS were compared by with air and ground temperatures for Northern Quebec, Canada in a publication by Hachem et al. (2012). Results revealed hereby better agreement for air temperatures, taken 1 3 m above ground, vs. subsurface (3 5 cm) temperatures. Snow cover and a diversity of different ground materials were hypothesized to be major sources of uncertainty in correlation analyses between ground temperature measurements and satellite-derived LST data. The authors further stressed the limited usability of remote sensing LST data within the Arctic domain as a consequence of heavy cloud contaminations. Nonetheless, the applicability could be improved by combining LST data from both satellites, Aqua and Terra, as well as by applying temporal interpolation algorithms on the fragmented data (Hachem et al., 2012). Batbaatar et al. (2020) undertook further investigations in a recent study on the use of LST for mapping permafrost occurrences in proximity to the volcano Ojos del Salado in Chile. The authors thereby utilized LST time series data derived from MODIS and the Advanced Spaceborne Thermal Emission and Reflection Radiometer (ASTER) to investigate the "zero curtain", which stands for the transition phase from liquid to ice and is caused by the release of latent heat. The applicability of this method to delineate boundaries of permafrost occurrences was classified to be feasible for arid regions, however, and in agreement with Hachem et al. (2012), the authors communicated snow cover, cloudiness, and heterogeneity of surface materials to be major limitations factors (Batbaatar et al., 2020).

Another common environmental focus in this category was "Ground Temperature (Dynamics)" with 14 articles addressing this topic. Gisnås et al. (2013) applied an equilibrium model called CryoGRID 1.0 that is based on the Temperature at the Top of Permafrost (TTOP) model originally introduced by Smith & Riseborough (1996). MAGT and permafrost occurrences across Norway were thereby estimated with a spatial resolution of 1 km² (Gisnås et al., 2013). An overall good agreement between in-situ data and the modelled MAGT values were reported. Additionally, a minimum MAGT of −3.5°C was identified, which indicates generally warm MAGTs for most areas in Norway (Gisnås et al., 2013). At best 0.2% of the mainland permafrost in Norway is predicted to remain stable by 2071 2100, in case of the severe degradation of permafrost scenario A2 as mentioned in the IPCC Special Report on Emission Scenarios (SRES) (Gisnås et al., 2013). Continuous development efforts on the CryoGRID 1.0 model were undertaken by Westermann, Østby, et al. (2015), who extended the analysis for estimating MAGT over the North Atlantic permafrost region. The authors highlighted the need for further investigations on uncertainties in required model parameters, such as land cover maps, which may impact the output quality

(Westermann, Østby, et al., 2015). Developments on the CryoGRID model ultimately cumulated in the application on the entire Northern Hemisphere and with a spatial resolution of 1 km^2 (Obu et al., 2019). The authors hereby included information on the land cover from the ESA CCI project, ERA-Interim climate reanalysis data, and remote sensing based LST measurements. Average deviation between in-situ borehole measurements and modelled MAGT was revealed to be ± 2 °C (Obu et al., 2019). Next to the Northern Hemisphere, the CryoGRID 1.0 model was also utilized in a later study for modelling the MAGT across the Antarctic (Obu et al., 2020).

2.2.4.3 Surface Land Features and Processes

The majority (43%) of investigated environmental foci are associated with the category "Surface Land Features and Processes" (e.g. Klinge et al., 2018; M. K. W. Jones et al., 2019; S. Yi et al., 2011; Q. Yu et al., 2015; Forkel et al., 2012; Lu & Zhuang, 2011; Bartsch et al., 2009; Xue et al., 2009; Mohammadimanesh et al., 2019; Boike et al., 2016; Pastick et al., 2019; Lara et al., 2016; Yamazaki et al., 2007; Chimitdorzhiev et al., 2016; Herzschuh et al., 2013; X. Li et al., 2019; Holloway et al., 2016; Eshqi Molan et al., 2018; J. C. Jorgenson et al., 2018; J. Hu et al., 2016; Sun et al., 2015; Meng et al., 2015; Kizyakov et al., 2017; X. Shi et al., 2014; Necsoiu et al., 2016; Gong et al., 2019; R. Zhao et al., 2016; Dini et al., 2019; Juszak et al., 2014; Ulrich et al., 2009; Xu et al., 2018; Nagai et al., 2013; Y. Yi et al., 2019; X. Wang et al., 2017; Belshe et al., 2013; Veremeeva & Gubin, 2009; Davidson et al., 2016). Geographical hotspots in the Mackenzie Delta, the Lena Delta, Yamal and Gydan Peninsulas, and northern Alaska were identified. Further frequently studied regions were observed in alpine regions, including the Andes and European Alps, the South Shetland Islands in the Antarctic, and the QTP.

The most common environmental focus within this category proofed to be "Vegetation Cover (Dynamics)". Large amounts of in-situ measurements were coupled with Normalized Difference Vegetation Index (NDVI) time series analysis based on data from AVHRR on a circumpolar scale and covering the years 1982 2010 in a study by Epstein et al. (2012) in order to estimate changes in the phytobiomass of the Arctic tundra. An average growth of 19.8% in above-ground biomass was revealed, which implies substantial consequences for a wide range of aspects of the tundra ecosystem, including the active layer thickness, wildlife, hydrology, permafrost distribution, and anthropogenic land use. In addition, the authors highlighted the relevance of extensive and continuous field works in future investigations as a basis for quality control (Epstein et al., 2012). Another study by Kharuk et al. (2015) dedicated their work to the growth response of larch trees distributed across the permafrost domain of central

Siberia by linking satellite based optical data derived from Aqua and gravimetric data derived from the Gravity Recovery And Climate Experiment (GRACE) mission with climate data and locally extracted tree-ring samples. A productivity increase in larch stands was hereby reported for the beginning of the current century. Tree ring growth rates correlated, amongst others, with drought conditions and air temperatures from the early summer months, as well as with water from permafrost- and snow-melt (Kharuk et al., 2015). Y. Song et al. (2018) investigated vegetation cover changes in proximity to the QTP engineering corridor via an Enhanced Vegetation Index (EVI) time series based on MODIS data and covering the years 2000 2016. A trend towards decreasing vegetation cover was hereby observed for about one-fifth of the vegetation, which was linked to the degradation of permafrost and overgrazing. As a result of degrading permafrost, water infiltration increased which in turn caused the retreat of shallow rooted alpine meadows (Y. Song et al., 2018).

"Frost Heave/Thaw Settlement" was the second most frequently investigated topic within the category "Land Surface Features and Processes". F. Chen et al. (2012) studied the deformation of the surface along the QTR by applying Persistent Scatterer Interferometry (PSI) on L- and C-band SAR data. Substantial rates in deformation of ± 20 mm/yr were hereby observed alongside the embankment. Proactive cooling methods in the form of using e.g. crushed stone or block stone were recommended by the authors, instead of solely relying on techniques designed for the protection of permafrost in proximity to the embankment of the QTR (F. Chen et al., 2012). Other surface displacement investigations were undertaken by, e.g. Short et al. (2011), who tested the application of L-, C-, and X-band SAR imagery based on ALOS-PALSAR, RADARSAT-2, and TerraSAR-X for measuring the surface displacement on Herschel Island. The high temporal and spatial resolution of X-band TerraSAR-X data provided a feasible basis for detecting thaw slumps. At the same time, high noise levels limited the applicability of X-band SAR data for long-term observations of surface movements. Furthermore, C-band was considered overall more reliable, although L-band imagery revealed generally best results. Long-term observations of the stability of permafrost are highly important, which highlights the promising prospects of satellite-based L- and C-band SAR imagery (Short et al., 2011). Strozzi et al. (2018) also dedicated their work to surface movement analyses via SAR satellite data for a selection of low-land permafrost areas located in both the Antarctic and the Arctic. The authors revealed high coherence levels between individual scenes within the snow-free summer months, which allowed for computing one-year interferograms and therefore long-term analysis on the surface deformation. Nonetheless, small rates in deformation were reported to be limitation factors in accurately estimating annual movement rates. Site-specific in-situ data in combination with longer temporal observation windows are thereby

required for the validation of future InSAR measurements (Strozzi et al., 2018).

A significant number of articles dedicated their work to the topic "Rock Glacier Mapping/Dynamics". Kääb (2002) was among the earliest authors to investigate mountain permafrost from a remote sensing perspective. The author hereby applied photogrammetry techniques on both space-borne and airborne optical imagery, which allowed for the creation of a DEM per stereo-pair of images. Differences in DEMs from different observation times allowed for the quantification of movement rates from e.g. rock glaciers and landslides in the Swiss Alps. It was thereby estimated that the horizontal accuracy equals the pixel size (Kääb, 2002). Kinematics of rock glaciers in Greenland, the Swiss Alps, and the Andes were investigated via SAR interferometry based on data from TerraSAR-X, the Constellation of small Satellites for Mediterranean basin Observation (COSMO-Skymed), the Japanese Earth Resources Satellite 1 (JERS-1), and S1 in a recent study by Strozzi et al. (2020). The authors reported good performance of S1 imagery alongside SAR data of very high resolution derived from other platforms. S1-based long-term monitoring of moving rock glaciers are further expected to be important proxies for evaluating the condition of mountain permafrost in future investigations (Strozzi et al., 2020).

Both environmental foci "Wildfires" and "Thaw Slump Mapping/Dynamics" were further frequently addressed topics within this category. D. Brown et al. (2016) hereby dedicated their work to the effects of wildfires on the permafrost occurrence for a study site in the White Mountains National Recreation Area, Alaska, covering 100 km^2. The degradation and extent of permafrost was observed to be strongly influenced by high burn severities, which affected the drainage conditions and consequently resulted in the drying of soils (D. Brown et al., 2016). Another work by L. Huang et al. (2020) was among the few studies that applied DL for their investigations. The authors identified 220 thaw slumps via imagery from CubeSat across an area covering 5200 km^2 and located within the Beiluhe region of the QTP (L. Huang et al., 2020).

2.2.4.4 Surface Water Features and Processes

About 25% of studied foci across all reviewed articles are linked to the category "Surface Water Features and Processes" (e.g. Yao et al., 2018; Necsoiu et al., 2013; Carroll & Loboda, 2018; J. Liu et al., 2009; Turner et al., 2014; Duan et al., 2017; Jepsen et al., 2016; Wanchang et al., 2000; Gao et al., 2013; Lantz & Turner, 2015; Mętrak et al., 2019; Sjöberg et al., 2013; K. M. Hinkel et al., 2005; Karlsson et al., 2014; Mao et al., 2018; Muster et al., 2013; Lara et al., 2019; Zakharova et al., 2018; Günther et al., 2015; Ulrich et al., 2017). Geographical hot spots were hereby observed in the Mackenzie Delta, the North Slope and its Arctic Coastal Plain in Alaska, Yamal

and Gydan Peninsulas, and the Lena Delta. "Lake Extent/Dynamics" was by far the most frequently investigated environmental focus with almost half of all articles within this category being associated to this topic. Morgenstern et al. (2011), e.g., investigated the geographical distribution of thermokarst lakes and basins located in proximity to the Lena River Delta and within the Yedoma uplands. Much of the study area was influenced by thermokarst, with thermokarst basins making up four times the area compared to thermokarst lakes. The authors further classified 33.7% of the Kurungnakh Island's surface area to be at risk of future thermokarst processes. At the same time, Morgenstern et al. (2011) hypothesized that future lake extension and erosion caused by thawing deposits might be limited due to the widespread degradation of the original Yedoma landscapes from past thermokarst processes. Lyons et al. (2013) investigated the quantification of errors in mapping lake extents via Landsat data. A total of seven satellite images derived from two sensors, the Thematic Mapper (TM) and the Multi Spectral Scanner (MSS), where analysed. Rising error rates were hereby observed for smaller lake sizes. The authors further associated varying spectral properties depending on suspended materials in lakes, vegetation, and lake depth to be limiting factors for a threshold approach. Moreover, the authors suggest minimizing the effects of seasonality in order to investigate inter-annual changes and long-term trends (Lyons et al., 2013). Another recent study by Rey et al. (2019) also incorporated Landsat imagery in addition to electromagnetic airborne surveys to detect changes in the lake extent. The time series investigation revealed more asynchronous dynamics for lakes within the discontinuous permafrost domain, in contrast to the more synchronous dynamics of lake extents in landscapes of continuous permafrost. The authors hypothesize that more synchronous lake extents in the continuous permafrost areas are mainly controlled by hydro-climatic factors, whereas a more widespread subsurface-connectivity may explain the differences in lake extent dynamics across discontinuous permafrost areas. The authors further argue that a continuous thawing of the frozen ground could once again potentially lead to synchronous lake dynamics, caused by widespread sub-surface-connectivity. In agreement with Morgenstern et al. (2011), dynamics in lake extents are expected to decrease in the future, as thawing permafrost acts as a low-pass filter on hydro-climatic processes and their variability (Rey et al., 2019).

"Coastal Erosion" was the second most common environmental topic in this category, although this focus featured drastically fewer publications compared to "Lake Extent/Dynamics". Coastal erosion rates on Herschel Island located in the western part of the Canadian Arctic were quantified over a temporal window of 50 years via IKONOS satellite data and historical airborne imagery in a study by Lantuit & Pollard (2008). A generally decreasing trend in the rates of coastal erosion could be

observed, although ice-rich shorelines with surface features linked to ground-ice (e.g. thaw slumps) revealed increasing erosion rates (Lantuit & Pollard, 2008). Another study by K. Barnhart et al. (2014) utilized passive RADAR data with a pixel size of 25 km in order to investigated the influence of changing sea ice concentrations on Arctic coastlines. The pan-Arctic analysis revealed a doubling in the length of the open water season since 1979, which consequently makes Arctic coasts more vulnerable to fluvial erosion induced by wave actions. The authors further stress the complex relationship between the length of the open water period and eroding coastlines, which is further influenced by the present ice content, geomorphological conditions, orientation, lithology, and storminess (K. Barnhart et al., 2014). A recent study by Isaev et al. (2019) addressed the cliff retreat of a permafrost coast via high resolution Quickbird-2 satellite imagery and handheld Differential Global Positioning System (DGPS) for a permafrost coast located in the south-western Baydaratskaya Bay in Russia. Similar to the findings of K. Barnhart et al. (2014), wind-driven wave action throughout the open-water period was observed to have a greater influence on erosion rates compared to rising air temperatures alone (Isaev et al., 2019).

A number of additional articles investigated other topics linked to surface water processes and features, including wetland dynamics (e.g. Reschke et al., 2012; Torbick et al., 2012), dynamics in the sea/lake ice extent (e.g. K. Barnhart et al., 2014; Engram et al., 2018; Surdu et al., 2016), or ocean colour (e.g. Doxaran et al., 2012; Heim et al., 2014).

2.2.4.5 Atmospheric Features and Processes

Even though a noteworthy number of articles focused their work on a topic linked to "Atmospheric Features and Processes" (e.g. C. Song et al., 2012; Watts et al., 2014; Curasi et al., 2016; J. Liu et al., 2003; Flessa et al., 2008; Nassar et al., 2014; Bohn et al., 2015; Hartley et al., 2015; Jørgensen et al., 2015; Rawlins et al., 2015; Anthony et al., 2016; Helbig et al., 2016; Anthony et al., 2018; Kohnert et al., 2018; W. Yang et al., 2020; Nassar et al., 2014; Hammerling et al., 2015; Crowell et al., 2018), said category was still the least investigated environmental category within this review analysis. This relative scarcity in published articles in the context of permafrost and atmosphere emphasizes the requirement of satellite earth observation of degrading frozen ground and its effects on carbon emissions. A study by C. Song et al. (2012) covered the effects of thawing natural wetlands on the release of methane. Exceptionally high emission rates of CH_4 were hereby observed during the spring season caused by bubbling, next to emissions of methane from thaw lakes. The authors strongly suggest to include the effects of spring thawing into permafrost-carbon models,

especially since the mentioned thawing process is expected to increasing under climate change (C. Song et al., 2012). Watts et al. (2014) focused their work on linking surface moisture and surface temperature with methane releases in Arctic wetlands. Due to the especially strong dynamics in surface water in northern high latitudes, the authors advise future research to take potential effects of fractional water scaling for regional modelling into consideration. The authors further raise their concerns in regard to insufficient resolution of applied remote sensing data that does not allow for the detection of small scale variations in soil moisture and temperature, which in turn may lead to an overestimation of predicted emission rates. Nevertheless, new sources of satellite data with better spatial resolution and/or temporal frequency, e.g. via the Soil Moisture Active Passive (SMAP) satellite, may provide a means for large scale modelling with lower uncertainty rates (Watts et al., 2014). Emission of carbon dioxide were intersected with subsurface water tracks and their distribution across a tundra landscape in Siberia in a study by Curasi et al. (2016). Shrub expansion is positively influenced by the favourable conditions provided by water tracks, which can be a helpful proxy for investigations on geographical variations in current and future carbon cycles (Curasi et al., 2016).

According to a recent study by Jackson et al. (2020), methane emission rates in high latitudes (>60°N) were not indicating a noteworthy increase when comparing the year 2017 with the average emission rates during 2000 2006. Similar results were also reported by Dlugokencky et al. (2009), who suggest that the turnover point for a continuously increasing emission rate of CH_4 as a consequence of thawing frozen ground has yet to be reached in the Arctic. Nevertheless, the authors also state that thawing permafrost has a strong potential for increased emission rates of methane in the future (Dlugokencky et al., 2009).

Anthony et al. (2016) dedicated their work on CH_4 emissions from thaw lakes across the Arctic. The authors observed a direct proportional relationship between the amount of eroded soil carbon caused by thawing frozen ground, and the emissions from increasing thermokarst lake extents (Anthony et al., 2016). Details about rising carbon emissions via rapid thawing of frozen ground beneath Arctic lakes were provided in another study by Anthony et al. (2018). Moreover, CH_4 hotspots were analysed in an airborne survey covering a total area of ~30.000 km^2 over north-western Canada and Alaska, as communicated by Elder et al. (2020). Results of the campaign revealed 2 million methane hotspots in proximity (~40 m) to lakes (Elder et al., 2020).

The transatlantic and collaborative community initiative Arctic Methane and Permafrost Challenge (AMPAC) by ESA and the National Aeronautics and Space Administration (NASA) aims to tackle the problem of investigating thawing permafrost

and methane release throughout the Arctic via a interdisciplinary research approach (European Space Agency, n.d.-a, 2020). New satellite earth observation missions such as the Methane Remote Sensing LiDAR Mission (Merlin) and Sentinel-5P are hereby viable new sources of data for future investigations on Arctic emissions in the context of permafrost degradation. Sentinel-5P constitutes a recent satellite mission by ESA for monitoring key atmospheric elements, including CH_4, CO, NO_2, CH_2O, O_3, and SO_2 via the TROPOspheric Monitoring Instrument (TROPOMI) (Veefkind et al., 2012). The mission provides extended data in combination with records from previous instruments such as the Ozone Monitoring Instrument (OMI), the Scanning Imaging Absorption Spectrometer for Atmospheric Chartography (SCIAMACHY), or the Global Ozone Monitoring Experiment (GOME) (D. Griffin et al., 2019). Numerous studies employed data derived from Sentinel-5P for investigations on methane concentrations in the atmosphere since its launch in February 2017 (e.g. H. Hu et al., 2018; Lorente et al., 2021; Schneising et al., 2019; Varon et al., 2019). The TROPOMI instrument installed on Sentinel-5P outperforms other current satellite systems in terms of spatial resolution, signal-to-noise ratio, and spectral range, which allows for better trace gas detection, as mentioned in a recent review article by Duncan et al. (2020). At the same time, the authors also highlight remaining challenges for passive satellites such as Sentinel-5P in the form of continuous cloud cover, steep sun angles, bright surfaces (e.g. snow), and low light intensities (Duncan et al., 2020). By utilizing active satellite systems, such as the Light Detection and Ranging (LiDAR) instrument on board the upcoming Merlin mission, present limitations of passive sensors can partly be overcome. Merlin constitutes hereby a Franco-German space mission by the French National Centre for Space Studies (CNES) and the German Aerospace Center (DLR) for measuring methane concentrations in the atmosphere on large to global scales (Ehret et al., 2017). Merlin will thereby be the first satellite mission to monitor methane from space by using Integrated Path Differential Absorption (IPDA) LiDAR (Pierangelo et al., 2016). As an active system, the LiDAR sensor enables measurements of atmospheric methane independent of the lighting conditions or season across all latitudes (Stephan et al., 2011). Moreover, the capability of penetrating through thin cirrus clouds further enhances the observation potential of the active LiDAR system (German Aerospace Centre (DLR), n.d.). Combining the use of passive and active sensors is hereby a powerful means to overcome present challenges and enhance our knowledge on emission rates throughout the Arctic (Duncan et al., 2020).

2.2.5 Applied spatio-temporal Resolutions

Figure 2.11 a) visualizes the overall distribution of applied temporal resolutions across the reviewed publications. The majority of articles (47%) applied a time series

in their investigations. The second most frequent temporal resolution was unitemporal with 28%, followed by multitemporal with 21%. Lastly only 4% of articles featured bitemporal analyses. As seen in Figure 2.11 b), a tendency towards longer time series in more recent studies could be observed for articles published during 2000 2020. This can be explained by the longer satellite data records that were available for more recent studies, compared to earlier published works. Figure 2.12 illustrates the frequency of different time series lengths applied across the reviewed articles. More than half of articles, which employed time series investigations, cover a temporal window of less than 10 years. Moreover, 39% of articles with time series analysis observe periods even less than 5 years. 47% of articles with time series analysis observed temporal time frames of 10 years or more, while 21% even covered at least 20 years. Minimum time series lengths are less than a year, while maximum lengths are up to 44 years. A median time series length of 9 years could be observed.
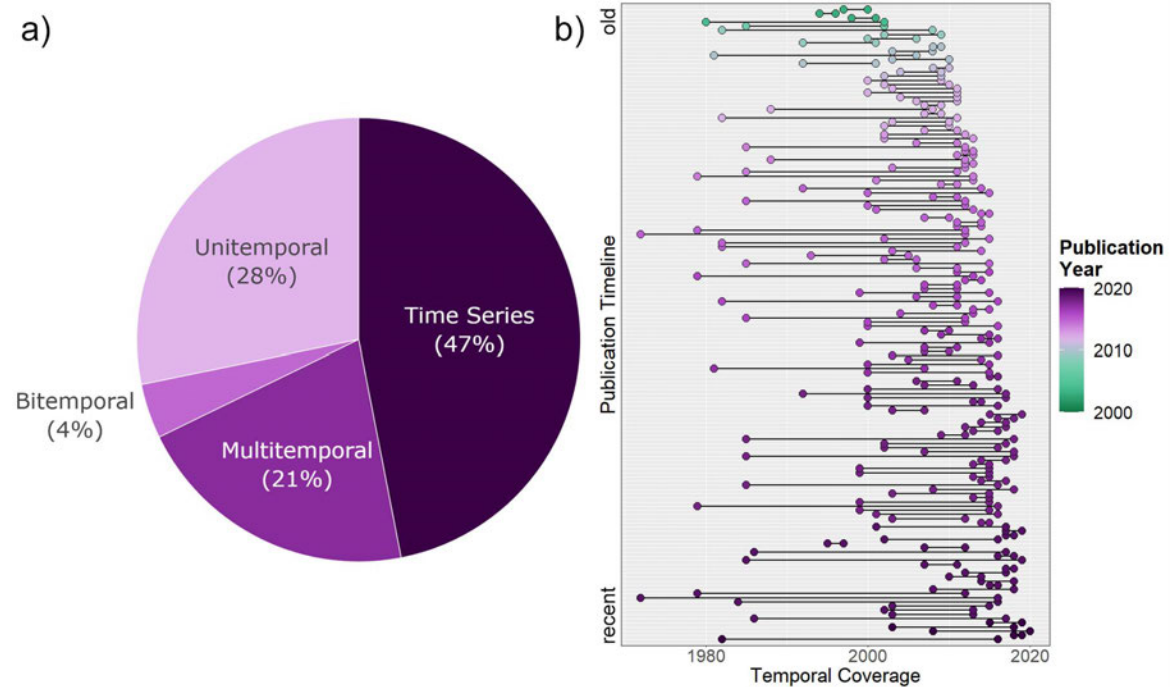
Figure 2.11: (**a**) Distribution of the applied temporal resolution across the reviewed articles. Within the context of this thesis, "Multitemporal" describes analyses which use 3–9 time steps. On the other hand, an analysis is classified as a "Time Series" in this thesis if ten or more time steps are covered. (**b**) Timeline visualizing the length of applied time series across the reviewed articles. The y-axis visualizes the temporal order in which articles that employed time series investigations were published, the x-axis shows the temporal coverage of applied time series per article. The colour gradient refers to the publication year. Modified after Philipp et al. (2021).
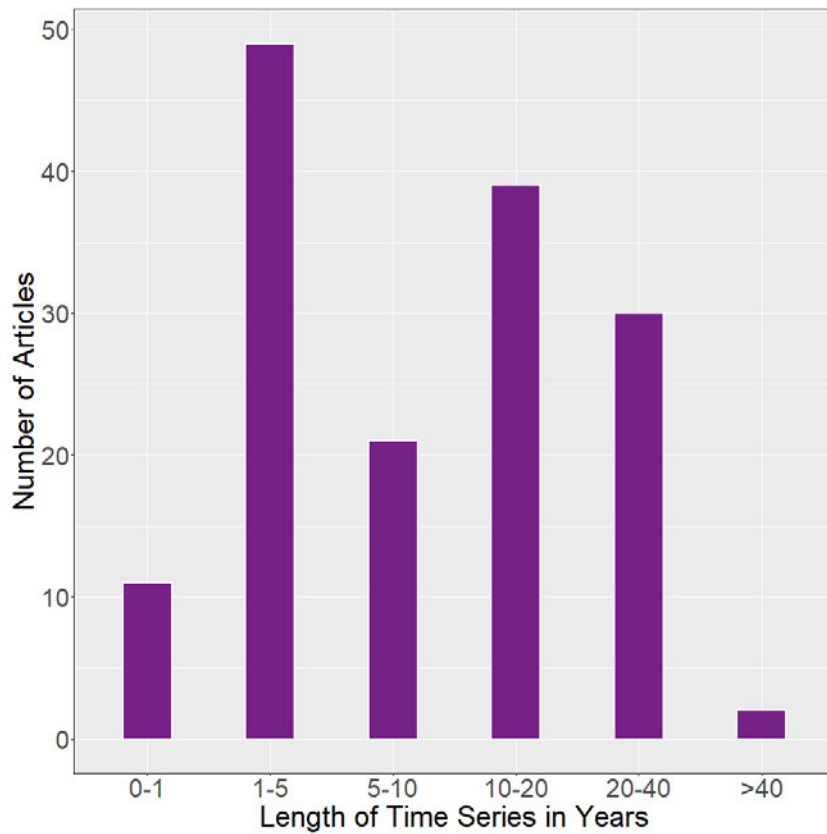
Figure 2.12: The number of publications that applied different time series lengths across the reviewed articles. Modified after Philipp et al. (2021).

In addition to visualizing the distribution of temporal resolutions and lengths of applied time series, the distribution of applied spatial resolution and scales across the reviewed articles is illustrated in Figure 2.13. The majority of articles (62%) performed their investigations on processes and features related to frozen ground on local scales. 16% of studies applied their analysis on small regional scales, while 12% conducted their research on large regional scales. Studies that performed circumpolar investigations only make up 8% of articles, whereas national studies are barely present with just 1%. In summary, most investigations were conducted on small to local scales (Figure 2.13 a).

Details on the applied spatial resolutions within each scale is visualized in Figure 2.13 b). 52% of studies, which were performed over areas smaller than 10.000 km^2, relied on remote sensing imagery of high resolution. Further 38% of investigations utilized imagery of medium high resolution within the same scale. 6% of analyses were performed on spatial resolutions between 100 1000 m, and only 4% are based on imagery with spatial resolutions coarser than 1 km^2. All resolution categories are also present across investigations on small regional scales. Contrary to local studies, the amount of utilized high resolution imagery is significantly lower with only 11%. On

the other hand, the majority (57%) of investigations relied on medium high resolution data. Analyses on large regional and national scales did not incorporate any high resolution imagery. Moreover, the relative amount of medium-low and low resolution data generally increases with the applied scale. Consequently, roughly three-quarters (74%) of circum-Arctic studies relied on satellite data of low resolution. Within the circum-Arctic scale, four studies utilized medium low resolution data and two further studies applied medium high resolution imagery. One single investigation combined high resolution satellite and airborne data for mapping lakes and ponds on a pan-Arctic scale (Muster et al., 2017). In general, a strong relationship between the applied spatial resolution and the size of the study area was identified. There is a tendency for small scale studies to utilize high resolution imagery, whereas large scale studies usually depend on satellite imagery of lower spatial resolution.
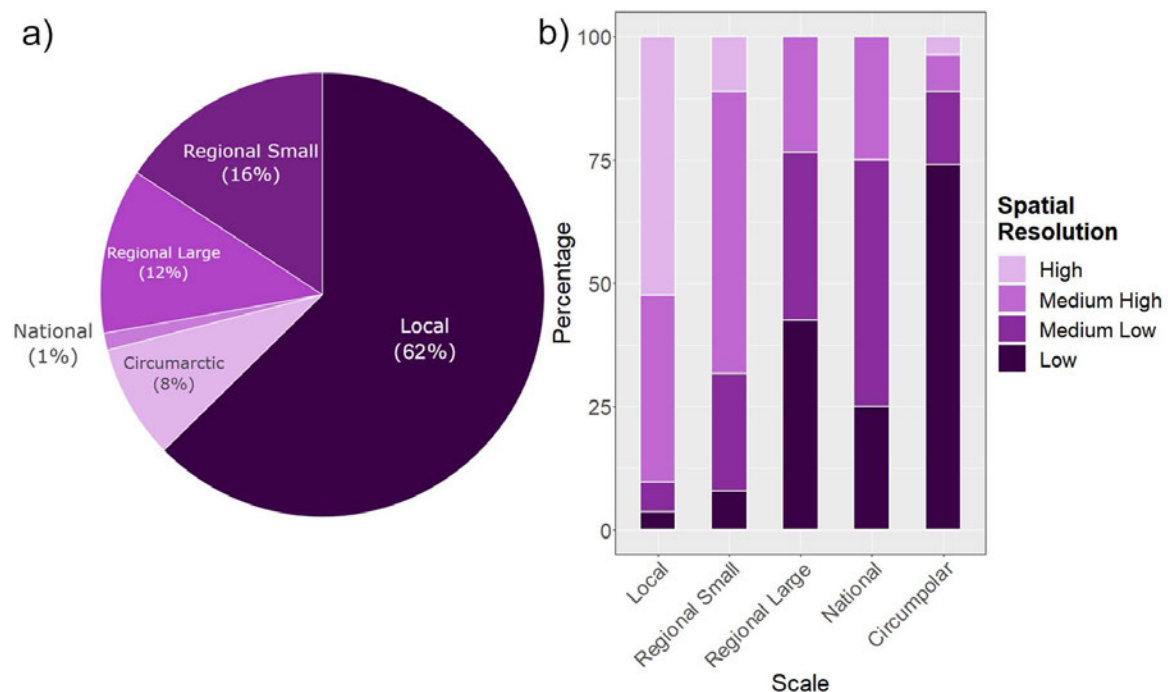
Figure 2.13: (**a**) Distribution of the applied spatial scales across the reviewed articles. The scales are categorized as circum-Arctic, national, regional large ($>250,000$ km^2), regional small ($10,000$–$250,000$ km^2), or local ($<10,000$ km^2). (**b**) Applied spatial resolutions per scale. Spatial resolutions are categorized as low (>1000 m), medium low (100–1000 m), medium high (10–100 m), or high (<10 m). Modified after Philipp et al. (2021).

The covered area, length of time series, and applied spatio-temporal resolutions for the top 20 most common environmental foci is illustrated in Figure 2.14. The majority of study region extents cover relatively small areas (100 10.000 km^2 or even <100 km^2). In particular, investigations on rock glaciers, frost heave/thaw settlement, ice wedge volumes, coastal erosion, and thaw slumps are for the most part conducted on small spatial scales. In contrast, the majority of studies on the dynamics of freezing

and thawing are conducted on large (>1 Mio. km^2) to pan-Arctic scales (Figure 2.14 a).

Most studies carried out their analyses on medium-high (10 100 m) to high (<10 m) resolutions. This can be observed in particular for investigations on rock glacier movements, ice wedges, eroding coastlines, soil carbon/nitrogen stocks, thaw slumps, and lake extents. The application of high resolution data is also reflected in the previously identified smaller study area extents for the aforementioned topics. Likewise, lower spatial resolutions could be observed for investigations that are typically applied on larger scales, such as studies on the dynamics of ground water storage volume, or dynamics in soil freezing and thawing (Figure 2.14 b).

As previously mentioned, 47% of all articles utilized as time series approach in their analyses. This is also reflected in the top 20 most common environmental topics, all of which featuring publications that applied time series analyses, with the topic soil carbon/nitrogen stocks being the only exception. Nearly all articles related to either frost heave/thaw settlement, the dynamics in ground water storage volume, or the dynamics in soil freezing and thawing included a time series in their research approach. On the other hand, investigations on soil nitrogen and carbon stocks, ice wedge volume/dynamics, and permafrost distribution are for the most part studied on a unitemporal basis (Figure 2.14 c).

The time series frequency, which, in the context of this review, describes the temporal size of individual time steps within a time series analysis, differs across various topics. Some environmental topics feature mostly higher frequencies in the form of weekly or even daily time steps (e.g. dynamics in ground and land surface temperature, or dynamics in soil freezing and thawing), while other topics indicate more evenly distributed time series frequencies (e.g. dynamics in the vegetation cover and lake extents). In case of the environmental topic "Ice Wedge Volume/Dynamics", only one publication included a time series in its study approach (Figure 2.14 d).

Analogous to the frequency of time series, the length of applied time series also differed significantly across various topics. Some environmental foci feature mainly long time series of 10 years or more (e.g. ice wedge volume, eroding coastlines, thickness of the active layer, dynamics in the vegetation cover and lake extents), while others cover mostly shorter temporal windows of 5 years or less (e.g. landslides, dynamics of rock glaciers, and frost heave/thaw settlement). The environmental topic "Ice Wedge Volume/Dynamics" suggests all of its related articles to include time series lengths of over 20 years. Nonetheless, and as previously stated, only a single publication by Fraser et al. (2018) featured a time series analysis in the context of studying dynamics in ice wedges and within the scope of this review (Figure 2.14 e).
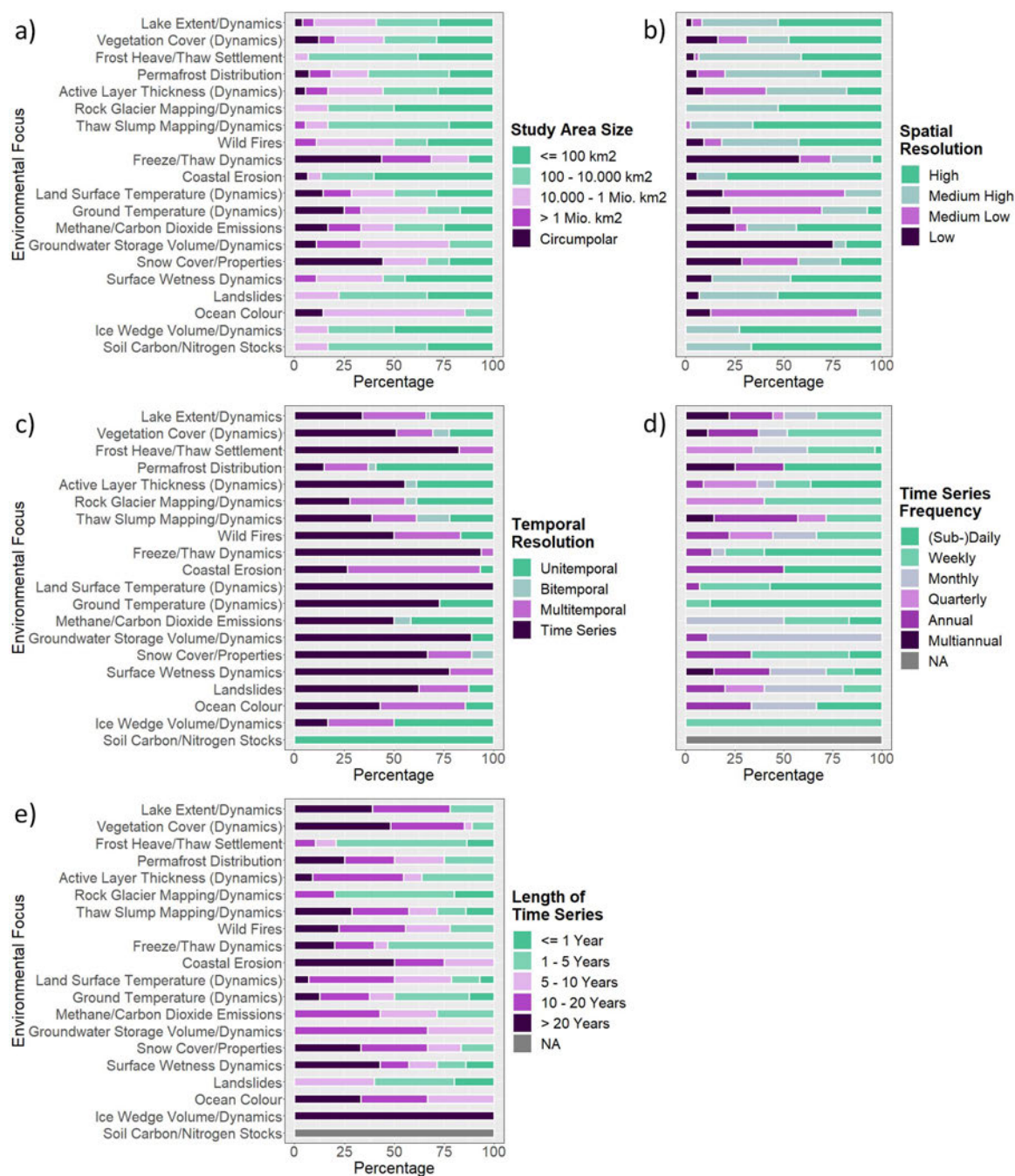
Figure 2.14: Distribution of spatio-temporal resolutions for the top 20 most frequent environmental topics across the reviewed articles. The y-axis is ordered by topic frequency. (**a**) Spatial extent of the study area. (**b**) Spatial resolution that is either low (>1000 m), medium low (100–1000 m), medium high (10–100 m), or high (<10 m). (**c**) Temporal resolution of reviewed studies. If at least ten time steps are used it is considered a time series within this review. (**d**) Temporal resolution applied within time series studies. (**e**) Length of applied time series analysis. Modified after Philipp et al. (2021).

2.2.6 Platform and Sensor Distribution

The distribution of sensor types and platforms is visualized in Figure 2.15. Optical imagery proofed hereby to be the predominantly used data type (55%). The second most common data type was SAR, which covers 20% of all data types. A further 9% is attributed to thermal imagery and another 7% is associated to passive RADAR data (Figure 2.15 b).

As illustrated in Figure 2.15 a), "Aerial" proved to be the most frequent platform (31% of all platforms), despite the exclusion of aerial-only remote sensing investigations in this review. Mainly optical imagery was hereby utilized, although some studies also included aerial-based electromagnetic, LiDAR, and RADAR measurements.

Making up 27% of all platforms, the Landsat mission (satellites Landsat 1 8) was identified to be the most common satellite platform. Similar to airborne data, mainly imagery of optical nature was utilized. Only a few investigations exploited the thermal capabilities of the sensors on board the Landsat satellites.

Both Terra and Aqua proved to be frequently utilized satellites across the reviewed articles. Thermal data derived from the ASTER and MODIS sensors were the main focus, followed by optical measurements. A handful of studies also took advantage of the passive RADAR data generated by the AMSR-E sensor on board of Aqua.

A large number of permafrost related investigations relied on high resolution optical satellite data. Specifically, imagery from QuickBird-2, Worldview-1 3, GeoEye-1, IKONOS, the RapidEye system, Gaofen-1/2, and the Satellite Pour l'Observation de la Terre (SPOT) satellites were commonly used. TerraSAR-X, RADARSAT-1/2, and S1 constitute hereby the most popular SAR-only satellite platforms.

Data generated by the ALOS satellite was also included in several studies. The majority of investigations thereby exploited the SAR capabilities of the PALSAR sensor. A handful of articles also worked with optical imagery from the Panchromatic Remote-sensing Instrument for Stereo Mapping (PRISM) and Advanced Visible and Near Infrared Radiometer Type 2 (AVNIR-2) on board the satellite.

The Environmental Satellite (Envisat) provides a variety of different data types generated by various sensors. Mainly SAR data generated by the Advanced Synthetic Aperture Radar (ASAR) sensor was utilized. Several studies also implemented thermal data from the Advanced Along Track Scanning Radiometer (AATSR), altimetric data by the Radar Altimeter 2 (RA-2), and optical imagery from the Medium Resolution Imaging Spectrometer (MERIS). Furthermore, a single study investigated trace gases in the atmosphere with data from the SCIAMACHY sensor.

Another noteworthy platform was the Defense Meteorological Satellite Program (DMSP). Only passive RADAR data from the SSM/I sensor on board the DMSP satellites was hereby used. Furthermore, a few studies included gravimetric measurements generated by the GRACE mission in their research frameworks. Additionally, optical images from the CORONA satellite program enabled long time series investigations or were alternatively implemented as a historical reference for analyses on change detection.

Lastly, there were only eight studies which employed optical data from S2. Both satellites S2A and S2B were just recently launched in 2015 and 2017 (European Space Agency, n.d.-h), respectively, which might explain the lack of articles working with data from these satellites.
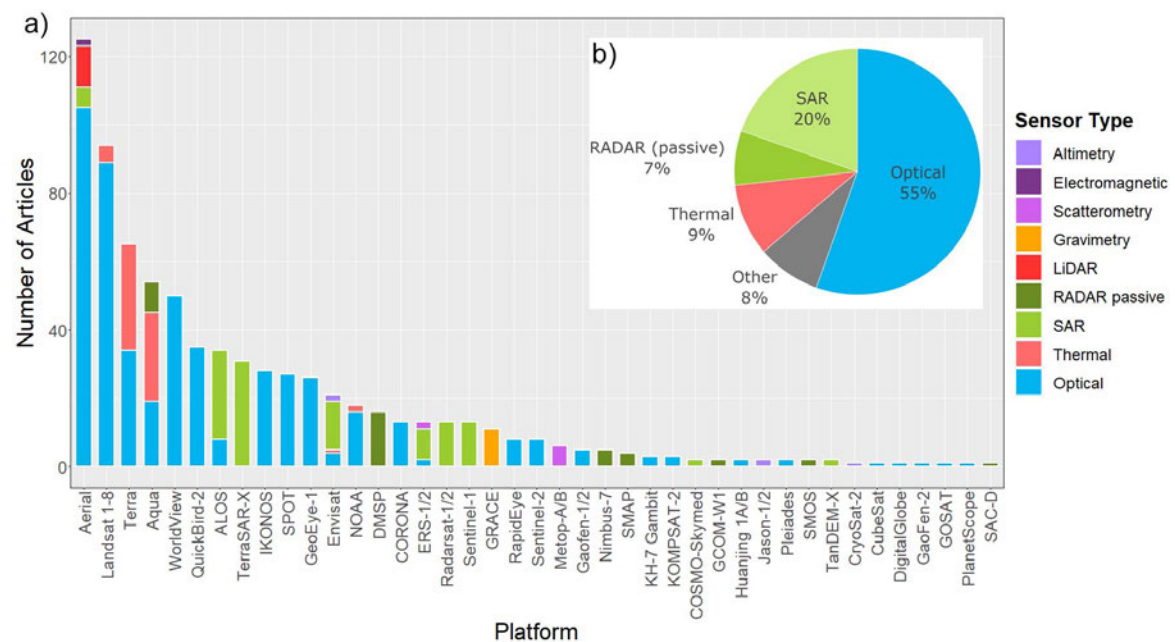
Figure 2.15: The frequency of utilized remote sensing platforms within the reviewed articles (**a**). Several platforms carry multiple sensors. Therefore, the frequency of applied sensor types is shown per platform (**a**). The overall distribution of sensor types across all platforms is visualized in (**b**). "Aerial" was also considered for the platform frequency investigation since many articles employed aerial photography either for validation, as a historical reference, or other complementary use with satellite imagery and is therefore included for completeness. Modified after Philipp et al. (2021).

Figure 2.16 a) visualizes the frequency and distribution of utilized platforms on an annual basis. Aerial imagery was applied in almost every year over the observed time span and covered articles, with the years 2006 and 2007 being the only exceptions. This highlights the ongoing relevance of airborne data for permafrost related analyses. Data from ALOS was first applied in 2010 and thereupon continuously used. Within the

framework of this review, first studies based on Aqua data were published in 2009 with peaks in publication counts in 2018 and 2019. Initial studies based on Terra data were already published in 2002, with highest publications numbers in 2018 and 2019, as well. Occasional investigations using data from the CORONA satellites can be observed since 2005. Sporadic usage was also identified for DMSP across the observed temporal window. Earliest investigations based on imagery by Envisat took place in 2010, with a peak in publication numbers in 2012. High resolution imagery from GeoEye-1 was first employed in 2013 and most frequently applied in 2018. Images of high resolution and derived from IKONOS was initially exploited in 2003 and was sporadically included since then. Most IKONOS-based investigations were hereby observed for the year 2018. Landsat data was used across the entire observation window, with the years 2000, 2002, 2004, and 2008 being the only exceptions. A steady trend towards an increased usage of Landsat imagery can be reported. Studies that implemented space-borne data derived from the National Oceanic and Atmospheric Administration (NOAA)-6 to -19 satellites were published on a regular basis since 2003. Earliest usage of high resolution QuickBird imagery can be reported for 2005 and a regular application can be seen since 2010. Other high resolution imagery by SPOT was first utilized in 2009, with the highest publication count in 2018. Most investigations based on SAR data by TerraSAR-X were published in 2017 and 2018. Finally, imagery from WorldView was initially implemented in 2014 within the context of studying permafrost related features and processes. Data from WorldView was frequently applied since then and constitutes the most common source of high resolution optical satellite data across all platforms.

Figure 2.16 b) illustrates the cumulative sum of utilized sensor types on an annual basis. An ongoing trend towards increasing annual publication numbers can be observed across all sensor types during the second half of the temporal observation window. Especially the years since 2018 indicate an extraordinary jump in publication numbers. Overall largest increase was identified for optical sensor types. The sensor type with the second strongest growing rate was SAR, although the growth is hereby significantly less compared to optical sensor types. Passive RADAR,thermal sensors and other sensor types indicate overall weak growth rates.

Figure 2.16 c) visualizes the percentage of Sentinel-based investigations compared to other platforms per year. Optical and SAR imagery based on the Sentinel-fleet was first utilized in 2018. A trend towards a growing percentage of studies that include Sentinel data can be observed in recent years. In case of S2, the year 2020 features a slightly lower share across all platforms compared to the previous year. Nonetheless, only studies published within the first two months of 2020 are hereby covered. The actual share of Sentinel data for the whole year 2020 therefore might deviate. Despite

the launch of and S2A in 2015 and S1A in 2014 (European Space Agency, n.d.-b,-h), earliest investigations based on data from these satellites were published not before 2018.
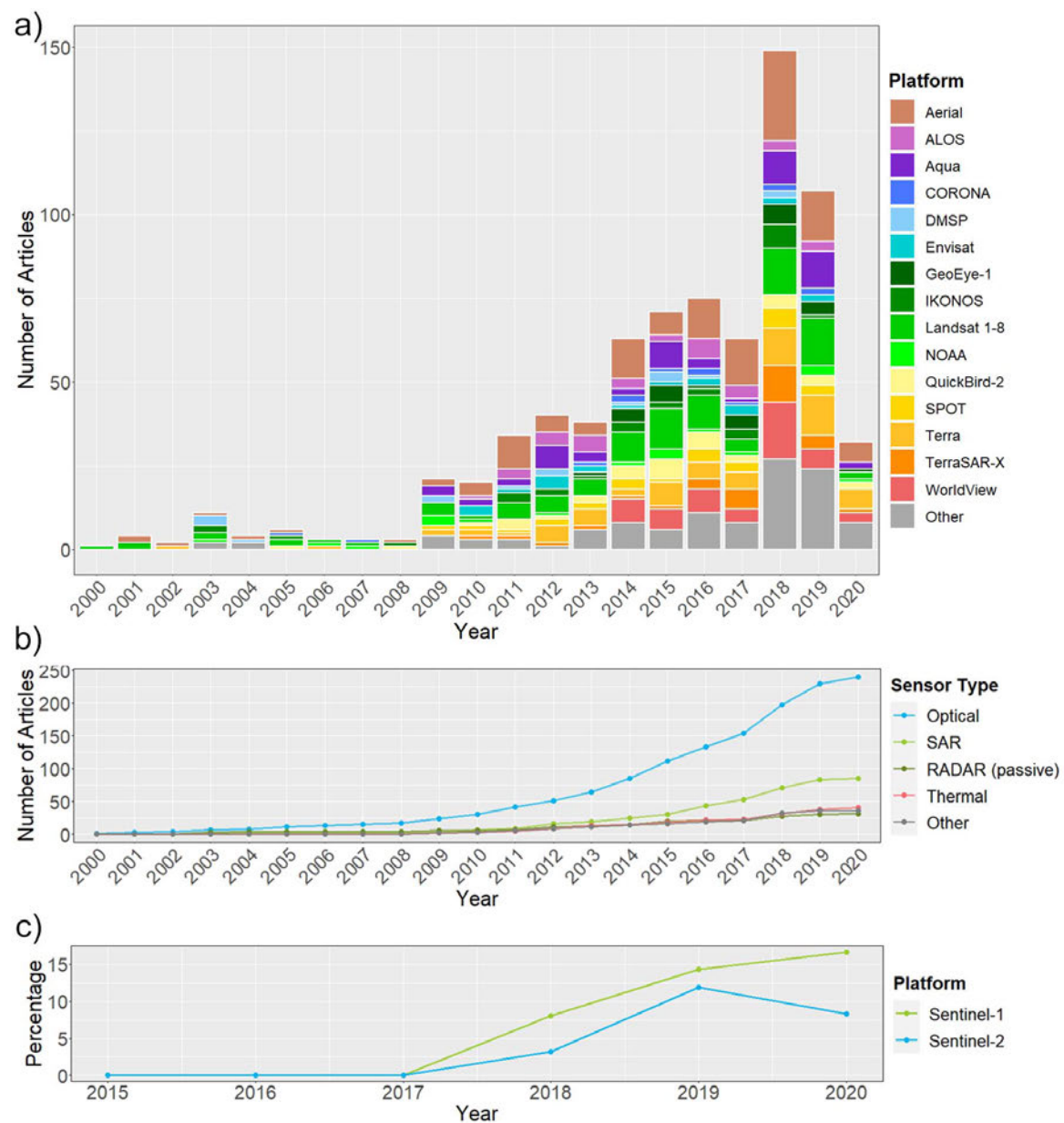
Figure 2.16: (**a**) Temporal development of the top 15 most frequently utilized remote sensing platforms across the reviewed articles over the past two decades. Several articles used data from more than one platform. (**b**) Cumulative sum of applied sensor types over the past twenty years. (**c**) Annual percentage of articles that utilized imagery derived from Sentinel satellites during the years 2015–2020. Modified after Philipp et al. (2021).

Details on the applied sensor combinations across the reviewed articles is illustrated in Figure 2.17. Space-borne and airborne sensors were hereby associated to individual categories. Roughly one third (∼33%; 107 articles) of investigations based their analyses exclusively on optical satellite imagery. The second most common (∼15%;

49 articles) and first actual sensor combination covers optical imagery from both satellite and aerial platforms. Airborne images where hereby commonly used as a historical reference, for investigating small scale features and processes at very high spatial resolution, or to increase the temporal frequency of multi-temporal and time series analysis. The third most frequent combination ($\sim$11%; 37 articles) is again not an actual combination but covers investigations based on purely SAR data. The next most common combination includes satellite-based optical and thermal images ($\sim$5%; 16 articles), followed by passive RADAR-only investigations ($\sim$5%; 15 articles). Several studies also employed other sensor combinations, such as SAR + optical + and airborne optical ($\sim$4%; 13 articles), SAR + optical ($\sim$4%; 12 articles), exclusively thermal imagery ($\sim$3%; 11 articles), as well as SAR and optical aerial imagery ($\sim$3%; 10 articles). Moreover, a total of six studies ($\sim$2%) combined optical imagery from satellite and airborne platforms in addition to airborne LiDAR information. Further 49 articles ($\sim$15%) utilized different sensor combinations as the previously mentioned ones and therefore highlight the possibilities of combining data from various platforms and of different types to effectively investigate permafrost related features and processes.
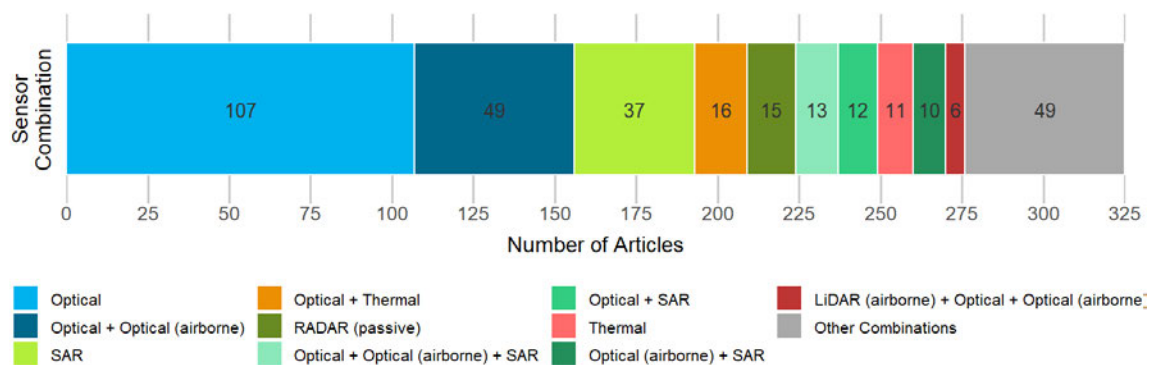
Figure 2.17: Distribution of the top ten most frequently utilized sensor combinations across the reviewed articles. A differentiation between space-borne and airborne sensor types was applied. Modified after Philipp et al. (2021).

2.2.7 Relevant and openly-available Products for Permafrost-related Analyses

Table 2.2 lists diverse and openly available products that are relevant in the context satellite remote sensing of permafrost and its associated features/processes. The international Cooperative Global Air Sampling Network hereby provides information about the atmospheric composition via air flask samples for a variety of greenhouse gases, such as methane, carbon dioxide, and carbon monoxide (NOAA Earth System Research Laboratories, n.d.-a,-b). Datasets on surface water are provided by, e.g.,

Pekel et al. (2016), who introduced an approach for global mapping of surface water on a monthly basis since 1984 and a 30 m spatial resolution by combining three million Landsat images. Another publicly available data set on global surface water at higher temporal frequency but coarser spatial resolution is the Global WaterPack, for which daily MODIS imagery is used to classify water areas at a 250 m resolution (I. Klein et al., 2017). Furthermore, a high resolution and circum-Arctic mapping effort of lakes and ponds at 5 m spatial resolution (or less) was undertaken by Muster et al. (2017) and published via the Permafrost Region Pond and Lake (PeRL) database. Information about coastal change was provided by Lantuit et al. (2012) in form of the previously mentioned Arctic Coastal Dynamics Database (ACD). A total of ∼101.447 km of Arctic coastline was hereby divided into 1.315 segments, with details on the coastal geomorphology, build-up, and erosion rates for each segment (Lantuit et al., 2012). Insights on the duration of snow cover at 500 m spatial resolution and on a daily basis are provided by the Global SnowPack (Dietz et al., 2015). Further information on the daily Snow Water Equivalent (SWE) and Snow Extent (SE) are available via the ESA GlobSnow SWE and GlobSnow SE data sets at spatial resolutions of 20 km and 1 km, respectively (Metsämäki et al., 2015; Larue et al., 2017). Various different land cover products based on satellite data are available. Some of which are the CAVM, GLC2000, GlobeLand30, MODIS land cover, and ESA CCI land cover (Plummer et al., 2017; Friedl et al., 2002; Jun et al., 2014; Bartholome & Belward, 2005; Raynolds et al., 2019; D. A. Walker et al., 2005). Liang et al. (2019) examined differences and similarities of four frequently applied global land cover products in a recent study. The authors reported highest overall accuracy in Arctic regions for the ESA CCI land cover product (63.6%), followed by GlobLand30 (62.2%). The MODIS land cover product and the Global Land Cover by the National Mapping Organization (GLCNMO) revealed accuracies of 29.5% and 48.8%, respectively, and were therefore not recommended as a reference for investigations in Arctic environments (Liang et al., 2019). As mentioned in a review article on mapping land cover in NHL by Bartsch, Höfler, et al. (2016), the most common map to address circumpolar investigations was revealed to be CAVM. Although offering adequate thematic information for various different Arctic inquiries, the missing separation between lichen- and shrub-dominated land cover types, limitations in non-forested regions, and the spatial resolution of 1 km were identified to be major limitation factors (Bartsch, Höfler, et al., 2016). Next to the land cover itself, information about trends in changing land cover is provided by Nitze et al. (2018). The authors hereby applied time series analyses on various multi-spectral indices based on Landsat data across four transects at regional scale within the permafrost domain (Nitze et al., 2018). Information on surface elevation at 30 m spatial resolution and covering the terrestrial area between 56° south and 60° north is provided by the Shuttle

Radar Topography Mission (SRTM) DEM product (Farr et al., 2007). The ALOS Digital Surface Model (DSM) is another product on surface elevation at the same spatial resolution but with a global coverage and generated via stereoscopic observations of optical imagery based on the PRISM sensor (Takaku et al., 2016). In addition, the ArcticDEM elevation product, which is based on optical stereo-imagery from the Worldview-1, 2, and 3 satellites, enables detailed topographic investigations due to its high spatial resolution of 2 m for areas above 60° northern latitude (Morin et al., 2016). Several datasets on soil properties are openly available. One example is hereby the SoilGrids database which offers details on soil texture, organic carbon content, and soil pH value, among other soil properties, at a global scale and 250 m spatial resolution (Hengl et al., 2017). Information on the carbon content for soil depths of 0 3 m is provided by the Northern Circumpolar Soil CarbonDatabase version 2 (NCSCDv2) (Hugelius et al., 2013). Furthermore, the Harmonized World Soil Database (HWSD) offers details on the geographical distribution of 15,000 soil mapping units at a spatial resolution of 30-arc seconds (FAO et al., 2012, 2020). Moreover, the ESA CCI Soil Moisture product presents daily soil moisture observations at a global scale and a spatial resolution of 0.25° based on two active and four passive RADAR satellite sensors (Dorigo et al., 2015). Information on freeze/thaw dynamics are available for the years 1979 2017 via daily passive RADAR satellite observations at a spatial resolution of 25 km and on a global scale within the NASA Making Earth System Data Records for Use in Research Environments (MEaSUREs) program (Y. Kim et al., 2017). The CALM network provides in-situ reference data of near-surface permafrost and active layer thickness for more than 100 sites since 1990 on an annual basis (International Permafrost Association, n.d.-a; J. Brown et al., 2000). Additional borehole measurements are publicly provided by the TSP program (Biskaborn et al., 2015). Finally, information about the distribution of permafrost itself is available via the frequently cited map by J. Brown et al. (2002), which features the geographical distribution of different permafrost zones at a scale of 1:10,000,000. Permafrost zones are hereby categorized as isolated, sporadic, discontinuous, or continuous permafrost regions (J. Brown et al., 2002). In addition, recent modelling efforts by Obu et al. (2019) and Obu et al. (2020) resulted in pan-Arctic and pan-Antarctic maps of the permafrost fraction and MAGT at a spatial resolution of 1 km. Table 2.3 lists a number of databases which host several of the aforementioned data sets.

Table 2.2: Overview of a variety of openly available products related to permafrost and associated features and processes. The column "Temporal Resolution" describes the covered time span and in parenthesis the temporal frequency of available data if multiple scenes are available within the time span. Modified after Philipp et al. (2021).

Name	Spatial Resolution	Temporal Resolution	Reference
Greenhouse Gases			
Cooperative Global Air Sampling Network	in-situ observations	since 1967 (varies)	NOAA Earth System Research Laboratories (n.d.-a)
Surface Water			
Global WaterPack	250 m	since 2003 (daily)	I. Klein et al. (2017)
Global Surface Water	30 m	since 1984 (monthly)	Pekel et al. (2016)
Permafrost Region Pond and Lake (PeRL) database	< 5 m	2002–2013	Muster et al. (2017)
Coastal Dynamics			
Arctic Coastal Dynamics Database	varies	2012	Lantuit et al. (2012)
Snow Cover and Snow Water Equivalent			
Global Snow Pack	500 m	since 2000 (daily)	Dietz et al. (2015)
ESA GlobSnow Snow Water Equivalent (SWE)	20 km	since 1979 (daily)	Metsämäki et al. (2015)
ESA GlobSnow Snow Extent (SE)	1 km	since 1995 (daily)	Larue et al. (2017)
Land Cover			
ESA Climate Change Initiative (CCI) land cover	300 m	1992–2015 (annual)	Plummer et al. (2017)
MODIS land cover	500 m	since 2001 (annual)	Friedl et al. (2002)
GlobeLand30	30 m	2000, 2010	Jun et al. (2014)

(Table continues on the next page ...)

Table 2.2: Continued.

Name	Spatial Resolution	Temporal Resolution	Reference
GLC2000	1 km	2000	Bartholome & Belward (2005)
Circumpolar Arctic Vegetation Map (CAVM) Raster Version	1 km	2003	Raynolds et al. (2019)
Trends of land surface change from Landsat	30 m	1999–2014	Nitze et al. (2018)
Digital Elevation and Surface Models			
ArcticDEM	2 m	2016	Morin et al. (2016)
SRTM	30 m	2000	Farr et al. (2007)
ALOS DSM	30 m	2006–2011	Takaku et al. (2016)
Soil Properties			
SoilGrids250m 2.0	250 m	1905–2016	Poggio & de Souse (2020)
Harmonized World Soil Database	30 arc-seconds	2012	FAO et al. (2012)
Northern Circumpolar Soil Carbon Database version 2 (NCSCDv2)	0.012 degrees	2013	Hugelius et al. (2013)
ESA Climate Change Initiative (CCI) Soil Moisture	0.25 degrees	1978–2019 (daily)	Dorigo et al. (2015)
Freeze/Thaw Dynamics			
MEaSUREs Global Record of Daily Landscape Freeze/Thaw Status	25 km	1979–2017 (daily)	Y. Kim et al. (2017)
Active Layer Thickness			
Circumpolar Active Layer Monitoring (CALM) program	in-situ observations	since 1990 (annual)	J. Brown et al. (2000)
Climate Change Initiative (CCI) Active Layer Thickness (ALT)	927 m	2017–2019 (annual)	Obu et al. (2021a)
Borehole Measurements			

Table 2.2: Continued.

Name	Spatial Resolution	Temporal Resolution	Reference
Thermal State of Permafrost (TSP) program	in-situ observations	2007–2009	Biskaborn et al. (2015)
Permafrost Extent and Ground Temperature Maps			
Circum-Arctic Map of Permafrost and Ground-Ice Conditions, Version 2	Scale of 1:10.000.000	2002	J. Brown et al. (2002)
Permafrost Extent and Ground Temperature Map	1 km	2000–2016	Obu et al. (2019)
Climate Change Initiative (CCI) Permafrost Fraction	927 m	1997–2019 (annual)	Obu et al. (2021b)
Pan-Antarctic map of near-surface permafrost temperatures	1 km	2000–2017	Obu et al. (2020)

(... end of continued table.)

Table 2.3: Overview of diverse databases with permafrost related and openly available data. Modified after Philipp et al. (2021).

Name	Description	Reference
PANGAEA	Data publisher and library for Earth and environmental science.	Diepenbroek et al. (2002)
GTN-P database	Active Layer Thaw Depth & Permafrost Temperatures.	Biskaborn et al. (2015)
The Permafrost Information System (PerSys)	Portal for GlobPermafrost products, related results, and data sets - Including ground and surface temperature, permafrost extent, Freeze/Thaw dynamics and others.	Haas et al. (2017)
National Snow & Ice Data Center	Management and distribution of cryospheric data.	National Snow and Ice Data Center (NSIDC) (2020)

2.3 Discussion on Potentials and future Requirements

Within this review a clear relation between the study country and the first authors institution nationality could be seen. This is likely caused by available local reference data, the location of in-situ field sites, and research funding. Geographical study clusters were identified in the Beiluhe region within the QTP, the Lena Delta, Gydan and Yamal Peninsulas, the Mackenzie Delta, and in the North Slope of Alaska (Figure 2.5). Large parts of the permafrost regions in Russia outside the Gydan/Yamal Peninsulas and the Lena delta feature hardly any satellite earth observation based investigations, despite Russia being the most frequently studied country (Figure 2.3). Similarly, while most investigations in Canada are concentrated in proximity to the Mackenzie Delta, both the Arctic islands and the mainland of the Nunavut territory are for the most part barely covered (Figure 2.5). Significantly fewer studies dedicated their research efforts within the southern Hemisphere, which can be explained by the relatively sparse distribution of permafrost occurrences that are limited to ice-free regions of the South Shetland Islands in the Antarctic or alpine environments, e.g., the Andes (Figure 2.6). Nonetheless, recently published and permafrost-related products for the southern Hemisphere, such as the near-surface permafrost temperature map at a pan-Arctic scale by Obu et al. (2020), may trigger some future studies to focus their work within the southern Hemisphere.

Investigations on high spatial resolution, high temporal frequency, large to circumpolar scales, and covering long time periods are required to assess long-term implications of thawing frozen ground on the atmosphere and land cover. Nevertheless, most articles (62%) exercised their study efforts on local scales, while only 9% of publications considered in this review performed circum-Arctic investigations (Figure 2.13). 60% of studies which dedicated their analyses to quantifying coastal erosion covered an area less than 100 km^2 (Figure 2.14 a). Although roughly half of investigations utilized a time series approach, only 47% of these studies covered temporal observation periods of more than 10 years. Moreover, only 21% of all time series investigations are longer than 20 years (Figure 2.11 & 2.12). Free and openly available tools, such as the recently released geospatial and cloud-based analytic platform Google Earth Engine (GEE), enable processing of large time series and massive amounts of data, even if an individual's computing capacity is restricted (Gorelick et al., 2017). One of the earliest works which utilized the cloud computing capabilities of GEE was published by Nyland et al. (2018), who quantified changes in the land cover within central Siberia via a dense time series analysis of Landsat imagery since 1985 for an area the size of ~60.750 km^2. Nill et al. (2019) dedicated their work on analysing changing spectral properties and land surface temperatures within the Mackenzie

Delta, Canada, by exploiting the processing capabilities of GEE, as well. Cloud-based analysis platforms such as GEE together with the rising spatio-temporal availability of satellite records hereby allow for analysing permafrost-related process and features on continuously growing spatial and temporal scales.

Only a handful of the reviewed articles exploited the potential of DL within the context of investigating permafrost-related processes and features. In addition to the aforementioned study by L. Huang et al. (2020), a successful implementation of DL was demonstrated by Langford et al. (2019), who mapped the distribution of Arctic vegetation for a ∼343 km^2 region in western Alaska. W. Zhang et al. (2020) combined DL with space-borne and airborne imagery for mapping ice-wedge polygons. Another publication by W. Zhang et al. (2018) demonstrated the potential of combining DL with high resolution aerial imagery for classifying individual ice-wedge polygons with an accuracy of 95% for a study region covering 134 km^2 in northern Alaska. A recent study by Bartsch, Pointner, et al. (2020) explored the feasibility of combining DL, space-borne SAR, and optical satellite imagery for mapping Arctic settlements. The authors further performed comparisons between the segmentatio capabilities of DL vs. using Gradient Boosting Machines (GBM). User accuracy scores were hereby higher for the DL approach. Nonetheless, the authors suggest to combine both DL and GBM for best possible results (Bartsch, Pointner, et al., 2020). Based on the promising segmentation capabilities of DL, increasing applications rates of DL for investigations on permafrost related features can be expected in future studies.

"Surface Land Features and Processes" proved to be both the fastest growing and the overall most common category (43% of all foci) among the five categories introduced in this review. The categories "Subsurface Features and Processes" and "Surface Water Features and Processes" indicate a generally similar growing rate and an overall similar distribution (21% and 25% of all foci). Weakest increase in publication numbers and overall fewest articles were associated with the categories "Thermal Features and Processes" and "Atmospheric Features and Processes". Especially "Atmospheric Features and Processes" appears drastically under-represented and makes up only ∼4% of all study foci across the reviewed articles (Figure 2.7). As mentioned by Dlugokencky et al. (2009) and Jackson et al. (2020), current Arctic emission rates are relatively small compared to other latitudes. Nevertheless, emissions of greenhouse gases are expected to increase with a continuous degradation of permafrost in the near future (Jackson et al., 2020; Dlugokencky et al., 2009). This demonstrates the necessity of further satellite-based investigations on permafrost-atmosphere-related processes. AMPAC, as an exemplary new joint community initiative, provides hereby a foundation for future research approaches to tackle this challenging field of study (European Space Agency, n.d.-a, 2020). Thermal capabilities of satellite sensors, especially those of the Landsat

mission, also appear heavily under-utilized (Figure 2.15). Albeit some studies include thermal imagery as a supplementary proxy for investigating subsurface features, only a handful of articles put particular focus on the application possibilities of thermal data. Hachem et al. (2012) and Batbaatar et al. (2020), e.g., extracted valuable insights via the use of thermal imagery. Thus, the potential of thermal analyses may still remain partly unexplored and the application of long-term thermal investigations, as offered, e.g., by the Landsat thermal products, could reveal crucial details within the context of satellite earth observation of permafrost and its related features/processes.

Next to the distribution of frozen ground on land, marine permafrost occurrences constitute another important parameter within the permafrost research domain. Since the Late Pleistocene, a global sea level rise of roughly 120 m has been taken place which consequently resulted in the flooding of permafrost-underlain coastal land areas (Brothers et al., 2012). A potential release of previously stored methane hydrates to the oceans via rising ground temperatures could be the consequence of the flooding of former land areas within the permafrost zone (Taylor, 1991; Rachold et al., 2007). Out of the 325 reviewed articles, not a single study directed their research efforts towards submarine-permafrost. Although numerous articles addressed sea surface properties in the context of permafrost research (e.g. Doxaran et al., 2012; Fichot et al., 2013; Heim et al., 2014; Doxaran et al., 2015; Fouest et al., 2018; Juhls et al., 2019; K. P. Klein et al., 2019), sub-sea permafrost is for the most part not detectable by current satellite remote sensing technology (Angelopoulos et al., 2020), which explains the absence of this topic within the reviewed articles.

Despite rapid advances in satellite technologies (e.g. Sentinel-5P and Merlin) and new methodologies (e.g. DL), many challenges in satellite earth observation of permafrost and its associated processes and features still remain. Although imagery derived from the Landsat mission enables long time series investigations based on regular observations, data availability before the year 2000 is comparatively scarce, especially in the Arctic (Bartsch, Höfler, et al., 2016). Low light intensities, frequent cloudiness, and steep sun angles in Arctic environments constitute additional complications for passive satellite systems (Duncan et al., 2020). As stated in Myers-Smith et al. (2020), polar remote sensing features many and often unique challenges which are frequently understated. SAR data is largely independent from the aforementioned limitations, but comes with its own restrictions (Kääb et al., 2005; Kääb, 2008). The decorrelation between individual SAR scenes as a result of changes in surface properties (e.g. dynamics in vegetation cover, soil moisture, and snow cover extent) limit the feasibility of D-InSAR studies for investigations on surface deformation (Zwieback et al., 2016; Westermann et al., 2014). SAR data of shorter wavelengths (e.g. X-band data) usually offers high spatial resolution, but at the cost of higher noise levels in

long-term observations of surface movements compared to longer wavelength data derived from, e.g., L-band SAR (Short et al., 2011). Also, the generally limited access to high resolution imagery on large spatial and temporal scales is another commonly mentioned restraint, especially in the context of analysing small scale processes and features (Kääb et al., 2005; Bartsch, Höfler, et al., 2016; M. T. Jorgenson & Grosse, 2016).

Although airborne-exclusive studies were excluded from this review, "aerial" still proved to be the most common platform type across all investigated articles (Figure 2.15). Detailed assessment of small scale processes and features, such as thaw slumps, coastal erosion, and patterned ground, requires data of correspondingly high spatial resolution and temporal frequency (M. T. Jorgenson & Grosse, 2016). Given this fact, one can assume that aerial imagery will continue to play a crucial role in near future analyses (S. V. Kokelj & Jorgenson, 2013; Arenson et al., 2016; M. T. Jorgenson & Grosse, 2016). At the same time, this highlights the importance of large scale availability and easy access to space-borne and high resolution images for a broader audience.

Data from optical sensors are most commonly applied across the investigated articles. Optical data also features the strongest growth rate in the number of applications per year across all sensor types. The second most common sensor type and also second fastest growing rate could be observed for SAR (Figure 2.15 & 2.16 b). The accelerated application in the frequency of applied SAR and optical data in recent years may be explained be the openly available data from new satellites, such as Sentine-1/2. At this point, only a small percentage of applied remote sensing data for permafrost-related analyses and within the scope of this review is derived from the Sentinel satellites. In comparison to other long-term satellite observation mission, e.g., Aqua/Terra or Landsat, Sentinel satellites were just recently launched, which may explain the small portion of studies associated with this data. At the same time, the application frequency of Sentinel data was observed to expand significantly during the last couple of years (Figure 2.16 c). The spatio-temporal availability, global coverage, and spatial resolution of Sentinel imagery constitute an attractive data package for future permafrost studies. Furthermore, combining different data types (e.g. SAR & optical) or combining data of the same type but from different platforms (e.g. Landsat-8 & S2) has tremendous potential, as shown by, e.g., Runge & Grosse (2019), who investigated the complimentary use of S2 and Landsat-8 data. Results of their investigations revealed good agreement between the spectral information from the two platforms. Nonetheless, the authors recommend local adjustments to spectral properties rather then using global parameters (Runge & Grosse, 2019).

A variety of openly available products are provided on various platforms, which may act as a reference or as a means for validation (Table 2.2 & 2.3). Nevertheless, there is still room for improvement in terms of accuracy, spatial coverage, spatial resolution, and thematic detail of land cover products (Liang et al., 2019). Thus, there is still a need for a circum-Arctic land cover dataset with high thematic detail, sufficient spatial resolution, and high accuracy (Bartsch, Höfler, et al., 2016). Also, in-situ reference data is commonly distributed in clusters instead of being evenly distributed across the ∼23 million km of permafrost affected terrain, which can be attributed to the difficult to access terrain and general remoteness of the majority of permafrost environments (Grosse et al., 2016).

In this review, a total of 325 articles published in 30 different international journals were investigated. Some relevant studies may have been published in other journals which were not included in this review. Additionally, non-English articles were excluded from the review process. Moreover, the proposed filtering approach may have led to the exclusion of some fitting publications. At the same time, the applied filtering criteria should provide a representative sample of articles related to space born earth observation of permafrost and its related processes and features. Therefore, the proposed review framework is considered to be a reasonable compromise in order to ensure a representative overview of recent trends in this field of study.

2.4 Summary

This chapter summarized trends in satellite earth observation for permafrost related analyses during the past 20 years and based on 325 articles published in 30 international journals. Articles were investigated on the basis of the applied spatial scales, resolutions, and temporal frequencies of satellite data, the spatial distribution of study locations, sensor and platform distribution, as well as the relationship between the first author institution nationality and the study country. Moreover, a variety of public and freely available datasets in the context of permafrost research are listed. The key findings of this review are as follows:

- The total number of published articles more than doubled since the year 2015.

- A clear connection between the first author's institution nationality and the investigated country was observed. 58% of studies in Canada were conducted by Canadian institutions, 80% of research efforts in the United States of America (USA) were performed by American institutions, and almost all (93%) investigations located in China are associated with Chinese institutions.

- 75% of studies sites are located in Canada, USA, China, or Russia.

- Russia appears heavily under-represented among the author countries with only 2% of articles being associated to this country.

- Key study regions were observed to be the Lena Delta and Gydan and Yamal Peninsulas in Russia, the Mackenzie Delta in Canada, the Beiluhe region located on the Qinghai Tibet Plateau (QTP) in China, and the North Slope Borough and its Arctic Coastal Plain in Alaska.

- Large parts of the continuous permafrost domain in the Nunavut territory in Canada and Russia remain largely unexplored from a satellite remote sensing perspective.

- Nearly all (94%) articles investigated the northern Hemisphere. Only a handful of studies were located on the southern Hemisphere, likely due to the restricted permafrost presence in Alpine regions and ice-free areas in the Antarctic.

- 43% of articles investigated land surface processes and features. 25% of investigations were dedicated to surface water processes/features, followed by 21% for subsurface processes/features. Studies on atmospheric and thermal features/processes were the minority with 4% and 7%, respectively.

- Regional differences in study foci were identified. Lake extent dynamics proved to be the most common subject in Canada, USA and Russia, whereas surface movement was the main topic in China.

- Even though 47% of studies employed time series analyses, only 21% of which cover more than 20 years.

- Only 8% of investigations were applied on a circumpolar scale, whereas 62% of articles limited their analysis to local scales.

- With increasing spatial scales, a general tendency towards the application of coarser resolution data was observed.

- Deviations of the applied spatial resolutions and temporal frequencies could be observed for different topics. Thaw slumps, coastal erosion, or surface movements were mostly investigated with high resolution imagery and on local scales, whereas dynamics in soil freezing and thawing were generally studied with coarse resolution data and on larger scales.

- Optical data was the most common data type (55% of all data types), followed by Synthetic Aperture RADAR (SAR) (20% of all data types).

- Aerial was identified to be the most frequent platform (31% of all platforms), although aerial-exclusive studies were already excluded from the review process. Using airborne data for validation, the investigation of small scale processes/features, or as a historical reference are hereby explanations. The most frequent satellite platform proved to be Landsat (27% of all platforms). Data from Sentinel satellites only made up 6% of utilized platforms, however a tendency towards more frequent usage of data from the Sentinel missions in recent years could be observed.

- Several openly available products in the context permafrost research have already been published. Some products, however, still feature insufficient extent, resolution, thematic detail, or accuracy for many permafrost related analyses. Moreover, reference data sets are often concentrated in clusters, instead of being evenly distributed across the Arctic.

The combination of data from different origins and the application of Deep Learning (DL) for segmentation tasks are promising new approaches for future investigations within the context of satellite earth observation of permafrost. Thermal data, especially from Landsat satellites, hereby still remains heavily under-utilized. A high demand for easily accessible and free satellite data of high spatial resolution exists within the permafrost research community. Data of high temporal and spatial resolution allows for monitoring small scale features and processes, such as thaw slumps, patterned ground, or coastal erosion at high detail. In addition, more long-term and large scale analyses are required to fully assess the thermal state of permafrost and the implications of its degradation on the environment and human society. Only a few studies dedicated their research efforts to carbon emissions thus far. New satellite missions such as Sentinel-5P and the Methane Remote Sensing LiDAR Mission (Merlin) are hereby likely to accelerate the publication frequency within this field of study. Moreover, data derived from Landsat will continue to be an important source for lengthy time series investigations. Especially the exploitation of cloud-based processing platforms such as Google Earth Engine (GEE) will thereby make processing of long-term and large scale analyses more accessible. Finally, the available spatial resolutions, spectral coverage, temporal frequency, global coverage, and open data policy of Sentinel imagery will likely lead to more frequent research applications based on data from Sentinel satellites.

Chapter 3

A novel Monitoring Framework for circum-Arctic Quantification of annual Erosion Rates of Permafrost Coasts[*]

The following chapter introduces a novel framework for circum-Arctic quantification of Arctic coastal erosion rates at high spatial resolution and on an annual basis. The presented analysis and products provide detailed information about Arctic coastal change rates at an unprecedented combined spatial scale and resolution. Sentinel-1 (S1) Ground Range Detected (GRD) Synthetic Aperture RADAR (SAR) scenes in Interferometric Wide (IW) swath mode were hereby used as a basis for the analysis. The methodology includes the generation of a high quality Arctic coastline product via a Deep Learning (DL) approach. Nine different U-Net models were thereby combined to create a robust and accurate output dataset covering 161,600 km of Arctic coastline. The DL product served as a reference for the Change Vector Analysis (CVA) based quantification of coastal erosion and build-up rates. The generated products may act as a valuable tool for further investigations in permafrost affected coastal environments.

3.1 Input Data

A variety of different datasets were utilized within the framework of this analysis. The computation of a high quality reference coastline dataset as well as the coastal change investigations were mainly based on S1 Ground Range Detected (GRD) Synthetic Aperture RADAR (SAR) scenes in Interferometric Wide (IW) swath mode (ESA Communications, 2012). In addition, optical imagery from Google Earth (L. Yu

---

[*]This chapter is for the most part based on Philipp et al. (2022) and Philipp et al. (2023).

& Gong, 2012) and S2 (European Space Agency, 2016) were employed for further quality control. In particular, high resolution imagery from CNES/Airbus and Maxar Technologies was accessible via Google Earth. The extent of the study area was partly defined by the coastline dataset from OSM (OpenStreetMap contributors, 2017) and the circum-Arctic CCI fraction of permafrost product by Obu et al. (2021b). Furthermore, the impact of changing tides on the presented data and methods was investigated by utilizing MTL data from the National Oceanic and Atmospheric Administration (NOAA) (2022b) as a reference. Both the daily sea ice concentration based on the ARTIST Sea Ice (ASI) dataset (Spreen et al., 2008) and details on glacier extents via the Global Land Ice Measurements from Space (GLIMS) glacier database (Raup et al., 2007) were incorporated for further quality assurance. Extracted coastal change rates were compared with existing data on coastal build-up and erosion provided by the ACD by Lantuit et al. (2012). Table 3.1 lists further details on the temporal coverage, spatio-temporal resolution and type of applied data within this thesis.

Table 3.1: List of utilized datasets within the framework of this chapter. The column "Temporal Coverage & Resolution" provides information about the temporal window of utilized data. The frequency of available data within this time period is shown in parentheses. Modified after Philipp et al. (2023).

Name	Data Type	Spatial Resolution	Temporal Coverage & Resolution	Reference
Climate Change Initiative (CCI) Permafrost Fraction	Raster	927 m	2017	Obu et al. (2021b)
ARTIST Sea Ice (ASI) Arctic Sea Ice Concentration	Raster	3125 m	2017–2021 (daily)	Spreen et al. (2008)
Sentinel-1 (S1) Ground Range Detected (GRD) Interferometric Wide (IW) swath	Raster	10 m	2017–2021 (up to 6 days)	ESA Communications (2012)
Sentinel-2 (S2) Level-2A Surface Reflectance (SR)	Raster	10 m	2017–2021 (up to 5 days)	European Space Agency (2016)
Google Earth	Raster	varies	2017–2021 (varies)	L. Yu & Gong (2012)

(Table continues on the next page ...)

Table 3.1: Continued.

Name	Data Type	Spatial Resolution	Temporal Coverage & Resolution	Reference
Buoy Mean Tidal Level (MTL) Data	Table	-	2020 (6 minutes)	National Oceanic and Atmospheric Administration (NOAA) (2022b)
OpenStreetMap (OSM)	Vector	-	2022	OpenStreetMap contributors (2017)
Global Land Ice Measurements from Space (GLIMS) glacier database	Vector	-	2022	Raup et al. (2007)
Arctic Coastal Dynamics Database (ACD) Database	Vector	-	2012	Lantuit et al. (2012)
International Hydrographic Organization (IHO) Sea Areas	Vector	-	2018	Flanders Marine Institute (2018)

(... end of continued table.)

3.1.1 Sentinel-1

Optical satellite imagery derived from the Landsat legacy allows for lengthy time series investigations since 1972 (T. Zhang et al., 2004). Recent satellite missions such as the ESA S2 mission, enable land surface investigations with a pixel size of up to 10 m and a temporal resolution of up to 5 days when combining both satellites S2 A/B (European Space Agency, 2016). However, the applicability of optical imagery in the Arctic is heavily limited by the scarce availability of data combined with frequent cloud cover in these regions (T. Zhang et al., 2004; A. M. Trofaier et al., 2017; Bartsch, Höfler, et al., 2016). In contrast, SAR data is largely independent of weather conditions and sun illumination and may therefore surpass present limitations of optical imagery (Kääb et al., 2005; Kääb, 2008). This thesis aims to exploit the uninterrupted monitoring capabilities of SAR data derived from S1 for quantifying changing Arctic permafrost coastlines. In particular, S1 Level-1 GRD SAR data in IW swath mode where thereby utilized, which represents focused SAR imagery that has

been detected, multi-looked, and projected to ground range with the help of both an ellipsoid model and a DEM (ESA Communications, 2012). S1 data was available at 10 m spatial resolution and accessible via the cloud computing platform GEE (Google Developers, 2021).

3.1.2 Optical Satellite Data

As previously mentioned, optical imagery from both the ESA Sentinel mission as well as Google Earth was utilized. The optical satellite data was hereby utilized as an additional reference data set for assessing the quality of the generated DL coastline product, as well as to validate the coastal change rates derived from SAR imagery. High resolution imagery from CNES/Airbus and Maxar Technologies was available in Google Earth. In case of S2, Level-2A SR data with a 10 m spatial resolution and a revisit time of up to 5 days was incorporated (European Space Agency, 2016).

3.1.3 Auxiliary Data

A number of additional auxiliary data was included to successfully perform the analysis on a circum-Arctic scale. First, the OSM Arctic coastline product was used as a reference for both defining the extent of the study area and as a additional training source of the DL based segmentation between sea and land. Quality fluctuations for various areas are regularly observed within the OSM dataset (Barron et al., 2014). Nevertheless, the huge quantity of added training data outweighed these changing levels of quality of the OSM product. The CCI permafrost fraction dataset was also utilized for confining the study area to regions that feature permafrost occurrences. The dataset is available on an annual basis from 1997 2019 (version 3.0) and with a spatial resolution of ∼927 m (Obu et al., 2021b). Information on the Arctic sea ice concentration was included via the ASI dataset, which provides insights on daily sea ice concentration at a spatial resolution of ∼3125 m and is based on data from the AMSR-E passive-microwave radiometer system (Spreen et al., 2008). Details on the sea ice concentration was used as an additional quality layer for assessing the applicability of the proposed data and methods. The GLIMS glacier database was used for further quality control (Raup et al., 2007). Since the focus of this thesis lies on the quantification of coastal change in the form of erosion and build-up, glacier areas were removed to minimize the effects of changing glaciers on the analysis. Additional information on the MTL from four different buoy stations and provided by the National Oceanic and Atmospheric Administration (NOAA) (2022b) was included to study the effects of tidal changes on the SAR investigations. MTL data was thereby available on a six minute basis within the observation period of this thesis. The identified coastal

change rates based on the proposed data and methods were compared with numbers in previously published literature, as well as with change rates available via the ACD by Lantuit et al. (2012). Next to statistics on coastal change per country, change rates were also computed per sea based on the IHO sea areas (Flanders Marine Institute, 2018).

3.2 Methodological Framework

The methodological framework was mainly split into three parts (Figure 3.1). The first part was dedicated to the confinement of the study area and the pre-processing of S1 GRD SAR backscatter images in IW swath mode. Annual (months June September) sd and median composites were thereby computed for each polarisation and covering the years 2017 2021.
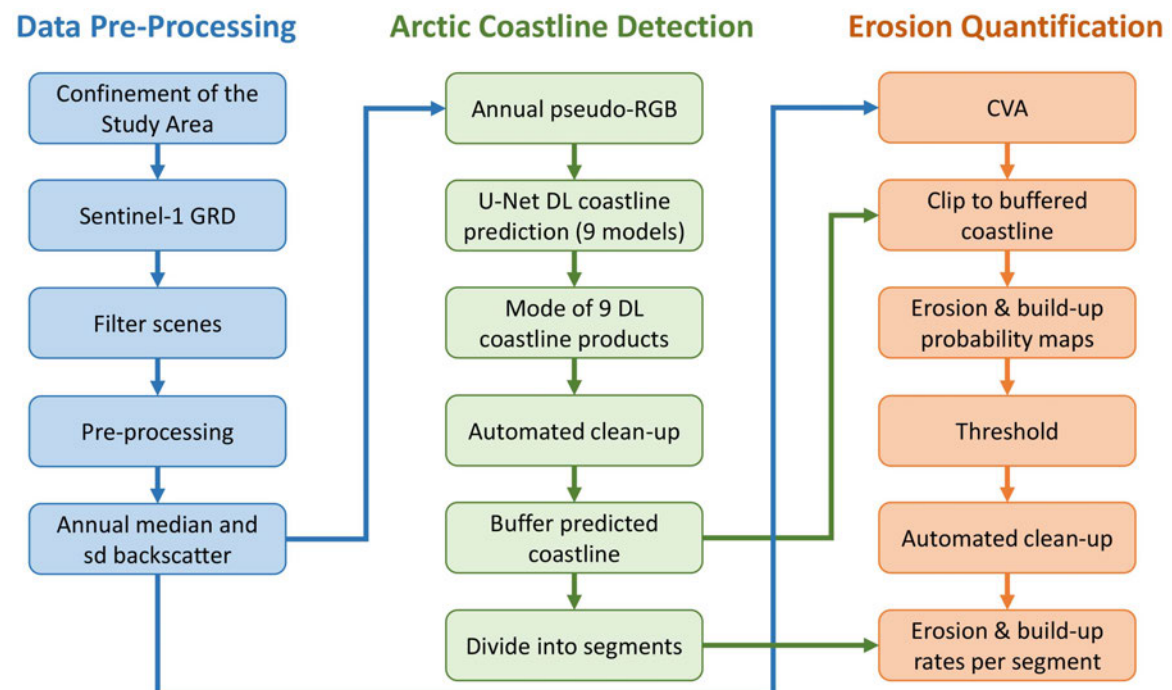
Figure 3.1: Flowchart of the study outline. The analysis was split into three parts. In the first part, the study area was defined. In addition, satellite data was pre-processed and annual Sentinel-1 (S1) composites were computed. The second part was dedicated to generate a high-quality Arctic coastline product via Deep Learning (DL). In the third part, Arctic coastal erosion and build-up rates were quantified via the application of Change Vector Analysis (CVA) in conjunction with the previously computed coastline product which acted as a reference. The following abbreviations are used throughout the flowchart: Ground Range Detected (GRD); standard deviation (sd); Red-Green-Blue (RGB); Deep Learning (DL); and Change Vector Analysis (CVA). Modified after Philipp et al. (2022).

In the second step, a high quality coastline product was generated at a circum-Arctic scale via a DL approach. A total of nine different U-net architectures were hereby trained and combined to generate a robust and accurate output covering 161,600 km of the Arctic coastline. The created coastline product acted as a reference for the third and final step, which was dedicated to quantifying coastal change rates at 10 m spatial resolution by combining the previously computed annual S1 SAR composites with a CVA approach. Next to the coastline and coastal change products, several quality layers were generated to assess the applicability of the proposed methodologies and data across the investigated area. Finally, average coastal change in the form of build-up and erosion were computed for 400 m segments along the 161,000 km of observed coastline. The effect of tidal changes on the analysis was also examined. Particularly for sandy and flat coasts, variations in local tides may significantly affect the precise position of the zone where sea and land meet. Detailed descriptions of each processing step and dataset are provided in the following sections.

3.2.1 Training and Testing Sites

The first task was to define the extent of the study area, which was limited to regions with available S1 GRD backscatter data in IW swath mode. It was further limited to coastal regions in close proximity to the presence of permafrost. The OSM Arctic coastline product acted thereby as a reference for confining the study area. First, the extent of permafrost was defined via the CCI permafrost fraction product for the year 2017 by Obu et al. (2021b). The continuous data was converted into a binary map that differentiates between permafrost presence ($\geq$1% permafrost occurrence) and permafrost absence. Since the dataset is provided at a spatial resolution of $\sim$927 m, a buffer of 20 km around the permafrost presence areas was computed in order to also include smaller islands, which were not contained within the CCI product. Secondly, the spatio-temporal coverage of available S1 GRD imagery in IW swath mode above 30 degrees latitude was assessed. Imagery was filtered to the months June September and until the end of the year 2021 (Figure 3.2). It was further differentiated between images acquired from a descending or an ascending orbit. The most frequent orbit per pixel was extracted and used as a basis for filtering the SAR data before computing the annual composites. In case an equal amount of images were available for both orbits, the ascending orbit was used (Figure 3.2 e). Figure 3.2 f) also illustrates the spatial variations in the first year with available data across the northern Hemisphere. S1 data was accessed, filtered and downloaded via the cloud computing platform GEE. Finally, both the binary permafrost presence map and information about S1 data coverage were used to clip the OSM Arctic coastline product. A buffer of 10 km was computed around the OSM product in order to account for any inaccuracies within

the dataset. The buffered and clipped OSM coastline revealed the final area of interest visualized in Figure 3.3.

The investigated coastline was split into separate training and testing sites. Training and testing were hereby performed on two levels, in case of the DL work-flow. For the first level, a total of 1,038 km of manually digitized Arctic permafrost coastline divided into ten regions which are distributed across the Arctic and covering a combined area of 19,275 km^2 was used. All areas featured significant coastal change rates based on the ACD by Lantuit et al. (2012) and were therefore classified as suitable test regions. The manually digitized sites were further separated into seven training areas and three validation areas, as highlighted in Figure 3.3 by the light-green and dark-green points, respectively. A spatial separation between the testing and training sites was conducted to avoid spatial auto-correlation within the training process. Further details on the center coordinates, covered area, coastal length, country, and region name of each manually digitized site is provided in Table (3.2). Moreover, detailed description of the manual digitization process is given in Section 3.2.6.

The purpose of the second level was to generate additional validation an training data for the DL approach. OSM data was thereby exploited to overcome the challenge of the massive training data requirements by Convolutional Neural Networks (CNN) as well as to cover the wide range of diverse coastal morphologies. OSM is among the largest Volunteered Geographic Information (VGI) projects with more than eight million contributors (OpenStreetMap, n.d.). OSM data is imported and edited by various editors from a variety of sources (Barron et al., 2014). Data quality of available geometries within the OSM dataset heavily depends on the utilized sources, e.g. Global Positioning System (GPS) tracks and airborne imagery (Mooney et al., 2010; Barron et al., 2014). A number of different companies, such as Aerowest, Yahoo!, and Bing, provided, at least temporally, access to airborne imagery as a basis for creating new OSM content (Barron et al., 2014). Despite the tremendous community efforts, the quality of the OSM product is observed to vary across different areas. In addition, while being updated on a regular basis, OSM data may not precisely represent the current state of surface land features, especially for highly dynamic regions, such as Arctic coastal environments. At the same time, it is presumed that the enormous amount of additional data will offset present fluctuations in data quality, particularly when using CNNs. Thus, OSM based land polygons were acquired for all areas outside the manually digitized regions and within the previously defined study area. The land polygons were then turned into binary rasters, where the pixels have a value of 0 for sea area, while the pixels have a value of 1 for terrestrial areas. The binary reference data extracted from OSM was further split into 136 individual tiles, 109 of which were randomly selected for training and the remaining 27 tiles were used for validation.

The distribution of training and validations sites based on OSM is visualized as orange and red lines in Figure 3.3.
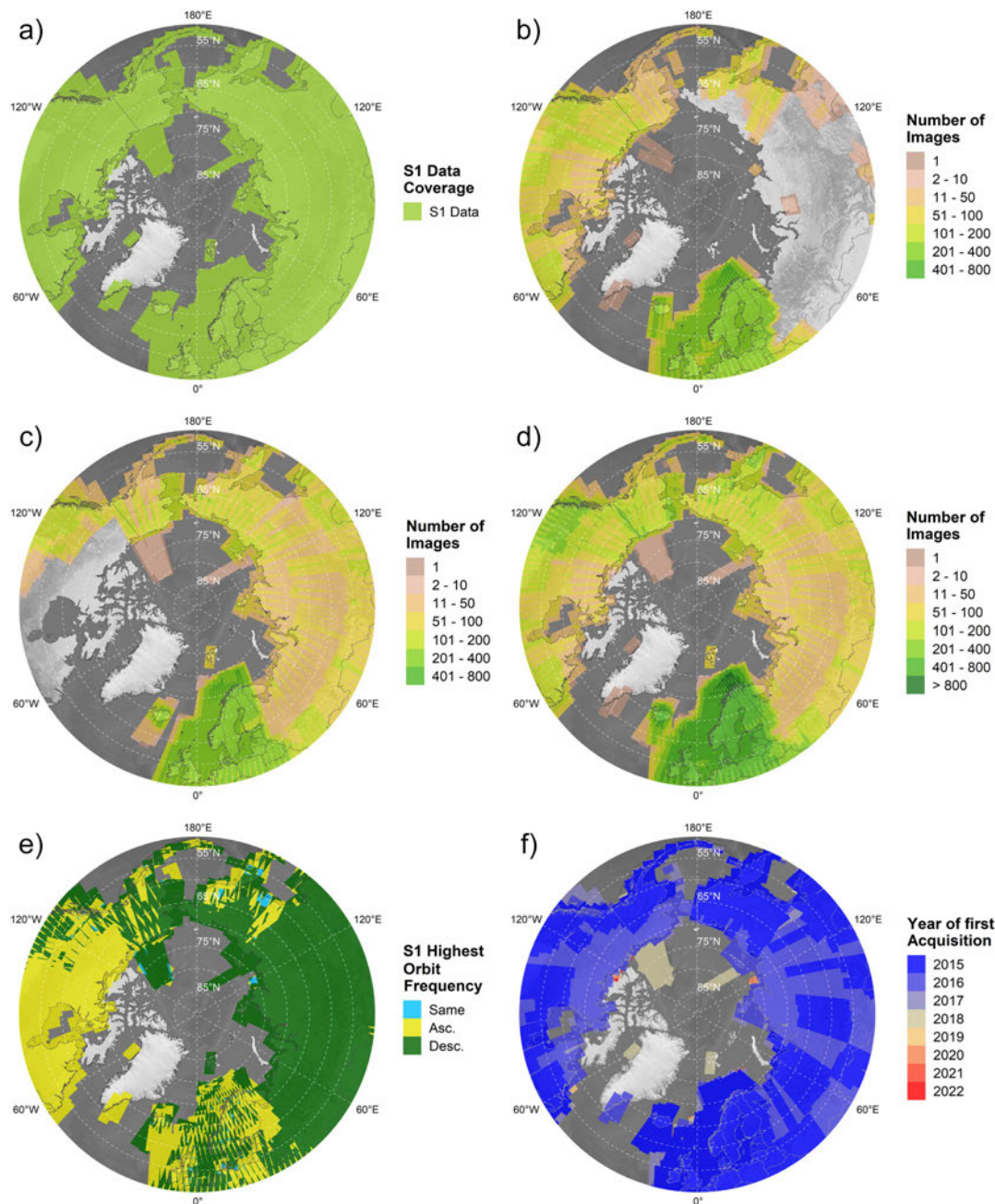
Figure 3.2: Data availability of Sentinel-1 (S1) Ground Range Detected (GRD) Interferometric Wide (IW) swath mode images since launch until the end of 2021 for the months June–September above 50° latitude. (**a**) Total data coverage. (**b**) Number of available images with an Ascending (Asc) orbit. (**c**) Number of available images with a Descending (Desc) orbit. (**d**) Number of available images with Asc and Desc orbits combined. (**e**) The orbit (either Asc, Desc, or same) with the highest number of images per pixel. (**f**) Year of first available data per pixel. A shaded relief by Natural Earth (n.d.) was utilized as a background map. Administrative boundaries are based on the Global Administrative Unit Layers (GAUL) dataset, implemented by the Food and Agriculture Organization of the United Nations (FAO) within the CountrySTAT and Agricultural Market Information System (AMIS) projects. Modified after Philipp et al. (2023).
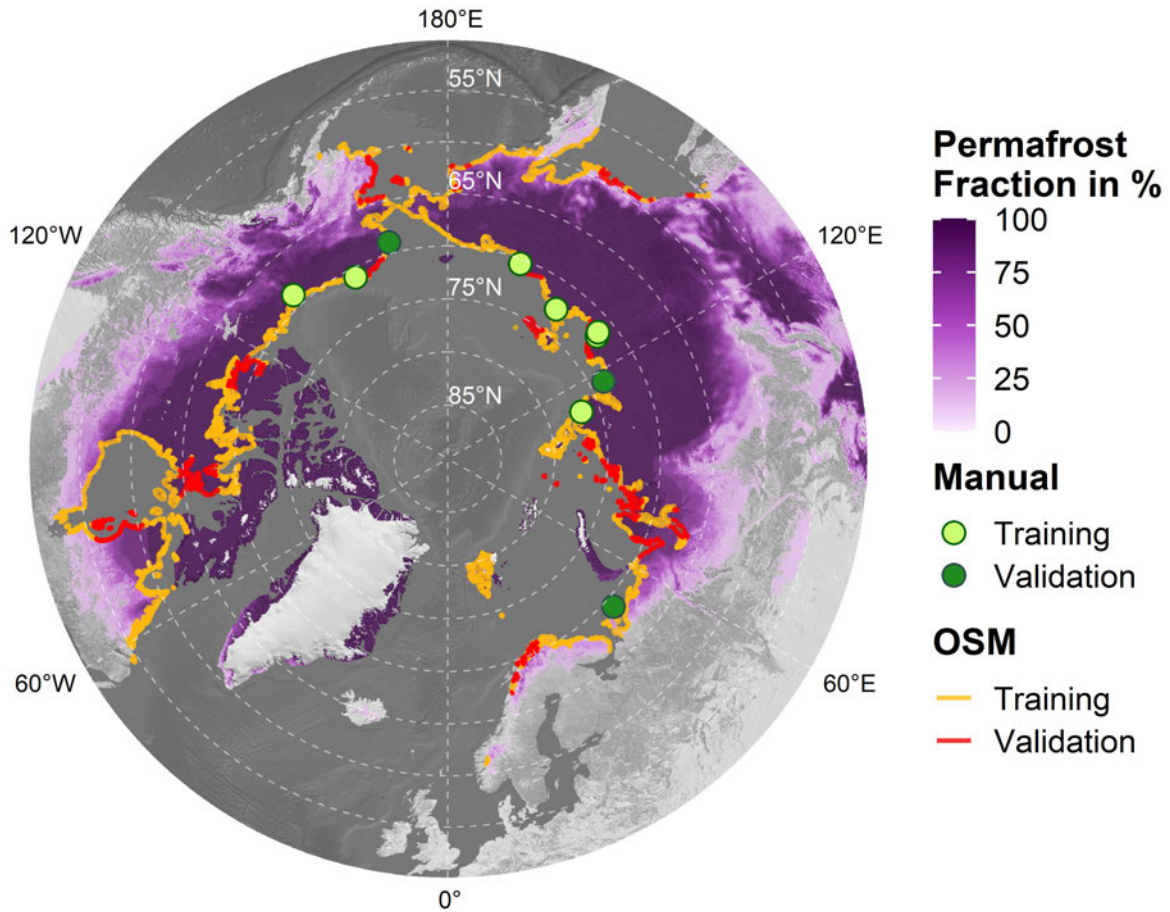
Figure 3.3: Training and validation regions from the manually digitized sites (green points), as well as training and validation regions based on OpenStreetMap (OSM) (orange and red lines). A shaded relief by Natural Earth (n.d.) in combination with the permafrost fraction across the Northern Hemisphere for the year 2017 based on data by Obu et al. (2021b) was used as a background map. All data is visualized in a polar Lambert azimuthal equal area projection. Modified after Philipp et al. (2023).

Table 3.2: List of manually digitized test regions. Information about the region's name, country, length of the present coastline, covered area, and the center coordinates per Area of Interest (AOI) are provided. Validation sites are highlighted in bold text. Modified after Philipp et al. (2022).

No.	Name	Country	Coast Length	Area	Center Coords.
1	**Corwin Bluffs**	**USA**	**67.8 km**	**1631 km^2**	**68.8°N; 165°W**
2	Drew Point–Cape Halkett	USA	142.4 km	1335 km^2	70.9°N; 153°W
3	Shoalwater Bay	Canada	113.7 km	636 km^2	68.8°N; 136.7°W

Table 3.2: Continued.

No.	Name	Country	Coast Length	Area	Center Coords.
4	**Kolgujev**	**Russia**	**49.4 km**	**685 km^2**	**69°N; 48.2°E**
5	Sims Bay	Russia	97.2 km	1280 km^2	76.7°N; 109°E
6	**Mus-Khaya Cape–Mouth of Peshanaya**	**Russia**	**170.2 km**	**3454 km^2**	**73.6°N; 116°E**
7	Bykovsky Peninsula	Russia	115 km	828 km^2	71,9°N; 129.3°E
8	Muostakh Island	Russia	15.7 km	212 km^2	71.6°N; 130°E
9	Bezimyanniy Cape–Eastern Oyagoss Cape	Russia	109 km	2748 km^2	72.6°N; 144°E
10	Mouth of Kurdugina–Malyy Chukochiy Cape	Russia	158.4 km	6476 km^2	70.5°N; 159.8°E

(... end of continued table.)

3.2.2 Pre-Processing of Sentinel-1 Data

As mentioned in section 3.1.1, S1 GRD SAR backscatter data in IW swath mode and with a spatial resolution of 10 m was used as a basis for both the DL approach to generate a high quality Arctic coastline product as well as for the CVA-based coastal change quantification. The data was available in GEE with pixel values representing the backscatter coefficient sigma nought (σ^0) in the unit decibel (dB) (Google Developers, 2021). Imagery between 2017 2021 and covering the months beginning of June until the end of September was considered throughout this analysis. A temporal filtering to the months June September was applied in order to reduce the effects of sea ice presence on individual scenes. The satellite imagery was further filtered to the orbit with the largest amount of available images on a pixel basis (Figure 3.2 e). In case of the manually digitized reference sites (Figure 3.3 green points), available scenes were additionally filtered to the most frequent relative orbit per AOI. Table 3.3 lists the number of available scenes and the associated most frequent relative orbit per AOI and for the years 2017 and 2020. Further pre-processing included the application of a median Moving Window (MV) with a window size of 3×3 on each scene to reduce the amount of speckle. For the purpose of removing speckle, pixel values were temporarily

changed from dB to natural via Equation 3.1 and afterwards converted back to dB via Equation 3.2. As a next step, sd and median backscatter images were computed on an annual basis and separately for each polarisation, vertical-vertical (VV) and vertical-horizontal (VH). Since the median is more robust to outliers than the arithmetic mean, it was chosen as a statistical metric (Mutlu, 2019). The annual SAR composites were subsequently combined into Pseudo-RGB images, by linking the VH-polarised median backscatter to the red channel, the VV-polarised median backscatter to the green channel, and lastly the VV polarised sd backscatter to the blue channel. Each Pseudo-RGB images was further normalized to the 2nd and 98th percentile per channel. An example Pseudo-RGB image, and the individual composites its made out of, is illustrated for a subsection of Cape Halkett, Alaska in Figure 3.4.
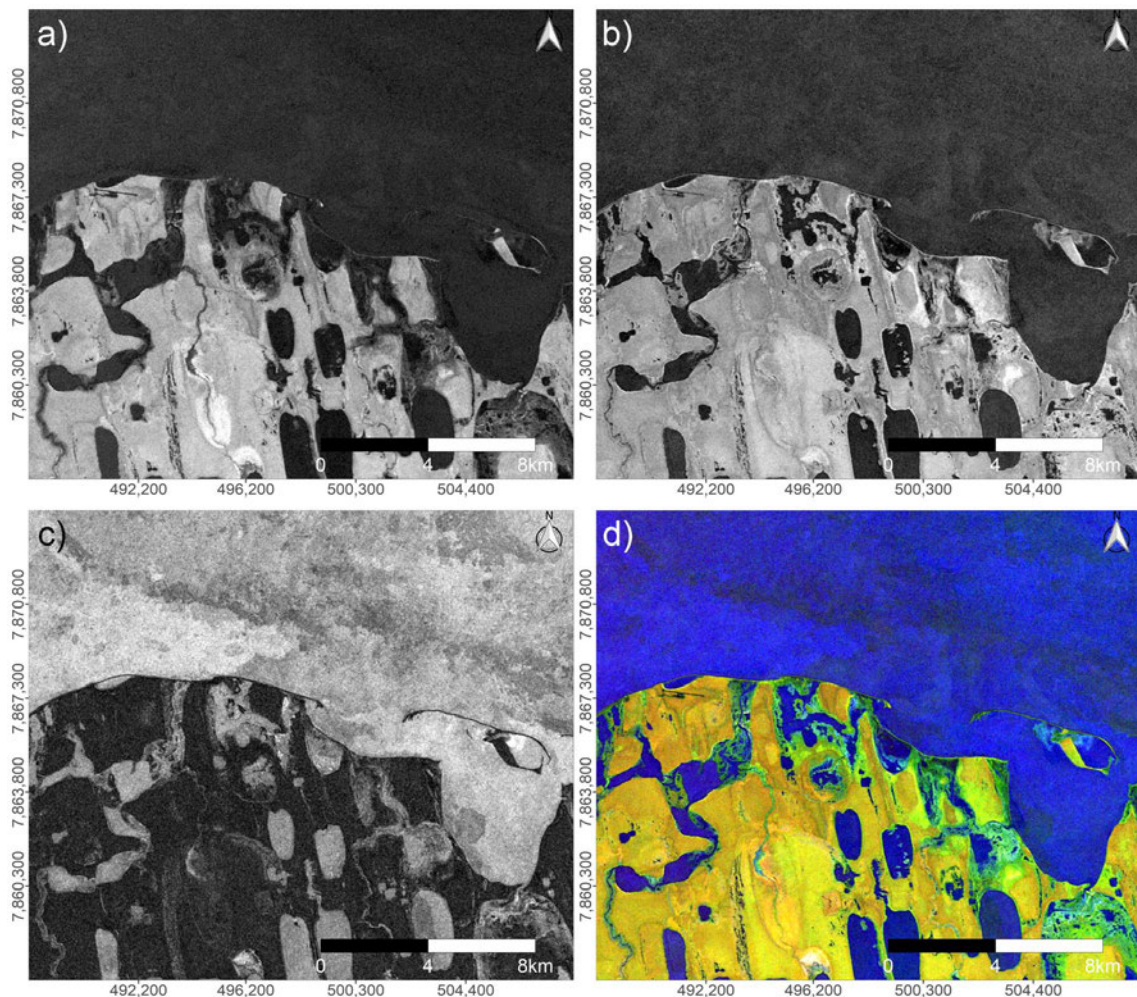
Figure 3.4: Composition of a Pseudo-Red-Green-Blue (RGB) image based on Sentinel-1 (S1) Ground Range Detected (GRD) backscatter data from June–September 2020 for a subsection of the study area Cape Halkett in the United States of America (USA) (Area of Interest (AOI) 02). (**a**) Annual median vertical-horizontal (VH) backscatter, (**b**) annual median vertical-vertical (VV) backscatter, (**c**) annual standard deviation (sd) VV backscatter, and (**d**) the pseudo-RGB composite by combining (**a**–**c**). All data is visualized in a Universal Transverse Mercator (UTM) zone 5 North projection. Modified after Philipp et al. (2022).

Finally, all data was re-projected to a polar Lambert azimuthal equal-area projection for further processing. The generated RGB composites were used as training input for the DL framework. The individual median and sd composites acted as a basis for the CVA. The number of scenes that were accessible per pixel was retrieved as an additional quality layer for both the final DL coastline product and the CVA coastal change quantification. All pre-processing of S1 data was performed in GEE.

$$\sigma^0 = 10^{\frac{\sigma^0_{(db)}}{10}} \tag{3.1}$$

$$\sigma^0(dB) = 10 * \log_{10} \sigma^0 \tag{3.2}$$

Table 3.3: Number of available Sentinel-1 (S1) Ground Range Detected (GRD) Interferometric Wide (IW) swath mode scenes per path direction and year after filtering the data to the months June–September and further filtering the images to the most frequent relative orbit per Area of Interest (AOI). Validation sites are highlighted in bold text. The minus symbol "-" represents no available scenes. Modified after Philipp et al. (2022).

AOI	Year	Rel. Orbit	No. of Scenes
1	**2017**	**88 (Desc.); 153 (Asc.)**	**10 (Desc.); 9 (Asc.)**
	2020	**88 (Desc.); 153 (Asc.)**	**9 (Desc.); 9 (Asc.)**
2	2017	73 (Desc.); 94 (Asc.)	10 (Desc.); 9 (Asc.)
	2020	73 (Desc.); 94 (Asc.)	10 (Desc.); 10 (Asc.)
3	2017	116 (Desc.); 108 (Asc.)	10 (Desc.); 5 (Asc.)
	2020	116 (Desc.); 108 (Asc.)	10 (Desc.); 10 (Asc.)
4	**2017**	**123 (Desc.); - (Asc.)**	**10 (Desc.); - (Asc.)**
	2020	**123 (Desc.); - (Asc.)**	**7 (Desc.); - (Asc.)**
5	2017	48 (Desc.); - (Asc.)	10 (Desc.); - (Asc.)
	2020	48 (Desc.); - (Asc.)	5 (Desc.); - (Asc.)
6	**2017**	**135 (Desc.); - (Asc.)**	**10 (Desc.); - (Asc.)**
	2020	**135 (Desc.); - (Asc.)**	**10 (Desc.); - (Asc.)**
7	2017	149 (Desc.); - (Asc.)	10 (Desc.); - (Asc.)
	2020	149 (Desc.); - (Asc.)	8 (Desc.); - (Asc.)
8	2017	149 (Desc.); - (Asc.)	10 (Desc.); - (Asc.)
	2020	149 (Desc.); - (Asc.)	8 (Desc.); - (Asc.)
9	2017	61 (Desc.); - (Asc.)	10 (Desc.); - (Asc.)
	2020	61 (Desc.); - (Asc.)	9 (Desc.); - (Asc.)
10	2017	31 (Desc.); - (Asc.)	10 (Desc.); - (Asc.)
	2020	31 (Desc.); - (Asc.)	10 (Desc.); - (Asc.)

3.2.3 Pre-Processing of optical Satellite Data

Similar to the S1 satellite scenes, optical imagery derived from S2, Level-2A SR data was filtered to the years 2017 2021 and to the months June September. Filtering the data to summer months was performed in order to reduce the amount of sea ice content in each image to a minimum. Only scenes covering the manually digitized sites were hereby considered. The data was further stripped from cloud- and snow-contaminated pixels by using the associated scene classification product available for each observation (European Space Agency, 2016). Lastly, annual median SR reflectance values were computed on a pixel basis. Working on annual median composites instead of single scenes not only reduced the effects of remaining clouds, sea ice, and snow, but also further reduced the geolocation uncertainty of individual scenes (Schubert et al., 2015, 2017).

3.2.4 Deep Learning for Arctic Coastline Extraction

DL CNNs gained increasing popularity in the past couple of years. It was found that CNNs frequently outperform more traditional Machine Learning (ML) classifiers like support vector machines and random forest (Zhu et al., 2017; R. Li et al., 2018). In comparison to conventional image processing, CNNs were observed to perform particularly better at segmentations tasks between land and water, and are therefore considered a valuable tool for identifying coastlines (D. Cheng et al., 2016; R. Li et al., 2018). One of the primary objectives of this thesis is to take advantage of the DL segmentation capabilities for the creation of a circum-Arctic and high-quality coastline product. In order to achieve this goal, CNN-based U-Net architectures were incorporated which were reported to be very effective in accurately identifying coastlines based on SAR data (e.g. Baumhoer et al., 2019, 2020, 2021; Heidler et al., 2021). A detailed explanation of the structure and functionality of a U-Net can be found in the original paper by Ronneberger et al. (2015). A brief description of the CNN-based U-Net structure and associated hyper-parameters employed in this work will be provided from here onwards.

A U-Net comprises an encoder in the form of a contracting path, which extracts the context of a given scene, as well as a decoder in the form of an expanding path, which enables the precise localisation of the extracted features (Ronneberger et al., 2015). A number of filters (also called kernels) are applied on the input image within the contracting path, which emphasize specific features. The filters have a size of 3×3 pixels and scan the image via a MV method with a stride of 1 pixel and return the dot product for each position. By adding a frame of zero pixel values around the

image (also called padding), shrinking in y- and x-direction is avoided throughout the convolution process. The weights for the aforementioned kernels are randomly initialized and are modified while the model is trained. A Rectified Linear Unit (ReLU) activation function (Equation 3.3) is subsequently applied on the generated feature map after running the kernel across the image. Negative pixel values are thereby replaced with 0. As a next step, MaxPooling is performed on the feature map. The process of MaxPooling hereby describes the application of another MV, but this time the highest value for a given window is extracted. The window size is 2×2 pixels and a stride of 2 pixels is used. During MaxPooling, the size of the feature map in x- and y-dimensions is reduced, which leads to lower computational requirements in further processing steps. The mentioned procedure is continuously performed numerous times with a growing number of applied filters during each step. As a result, a growing number of feature maps are generated, while at the same the image size is drastically reduced in x- and y-direction. During the condensing of the present information in the form of features, the localisation of the extracted information is gradually lost. Information on the spatial distribution of identified features is subsequently restored during the expanding path. Here, the generated feature maps are up-sampled and concatenated with the features of the corresponding level in the contracting path. A repetition of this process is performed until the x-y-dimensions of the up-sampled feature stack are equal to the x-y-dimensions of the input image. Lastly, a final convolution combined with a Sigmoid activation function (Equation 3.4) is applied on the feature stack, which results in a probability map where pixel values range from 0 1. A schematic overview of a U-Net architecture is illustrated in Figure 3.5.

$$y = max(0, x) \tag{3.3}$$

$$\sigma(x) = \frac{1}{1 + e^{-x}} \tag{3.4}$$

3.2.4.1 Training the U-Net Models

In order to perform a high-quality and circum-Arctic segmentation between terrestrial area (including inland lakes and rivers) and sea area, nine different U-Net architectures were trained, and the model outputs combined. The following model architectures were utilized within the framework of this thesis: SE-ResNeXt50 (J. Hu et al., 2018), ResNeXt50 (S. Xie et al., 2017), DenseNet121 (G. Huang et al., 2017), Inception-ResNet v2 (Szegedy et al., 2017), Inception v3 (Szegedy et al., 2016), VGG19, (Simonyan & Zisserman, 2014), VGG16 (Simonyan & Zisserman, 2014), ResNet34 (He et al., 2016), and ResNet50 (He et al., 2016). All models were hereby accessible

with pre-trained encoder weights via the ImageNet database. The ImageNet database comprises ≈14 Mio. images associated to over 20,000 classes (Russakovsky et al., 2015).
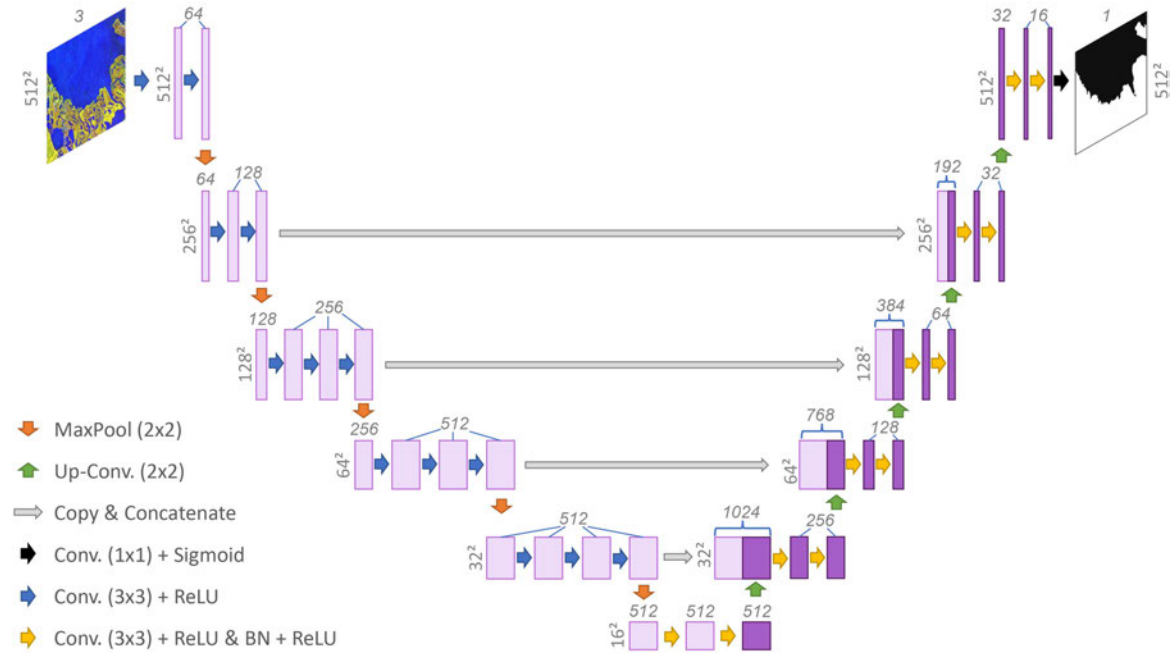
Figure 3.5: Schematic illustration of a VGG16 U-Net architecture. The vertical numbers at the side of each feature block describe the size in x–y-dimensions. The numbers in italic above each block describe the amount of feature maps (layers). Feature maps inside the down-sampling path of the (pre-trained) encoder are illustrated in light purple colour, whereas feature maps within the up-sampling path of the decoder are visualized in dark purple colour. The following abbreviations are used: Batch Normalization (BN), Convolution (Conv), and Rectified Linear Unit (ReLU). Modified after Philipp et al. (2022).

Further training of the presented models was performed in two phases. In the first phase, additional training of models was based on reference data from the manually digitized sites. Input images were separated into tiles with x-y-dimensions of 512×512 pixels. Augmentation in the form of rotating the tiles by 90, 180, and 270 degrees, as well as flipping the images was applied to further increase the amount of reference data. As a results, 49,096 tiles were available for further model training within the first phase. Out of the 49,096 tiles, 32,606 tiles were used for actual training, while 16,490 tiles from the independent validation sites were deployed for validation. Different hyper-parameter settings were tested for best-possible model output results. A batch size of 8, binary accuracy as an accuracy metric, a Root Mean Square Propagation (RMSprop) optimizer with a learning rate of 0.001, and a binary cross-entropy loss function were identified as the most suitable parameter settings. By choosing binary cross-entropy (also called log loss) as a loss function, the negative log of the predicted probability of a certain class is taken, as shown in Equation 3.5 (Bishop & Nasrabadi, 2006). As a

result, the loss value grows exponentially as the estimated probability for the actual class gets closer to zero. Thus, heavy penalties are associated with large differences between the actual probability and the estimated probability of a given class. All models were trained for a total of 30 epochs. The number of epochs indicates how frequently the full dataset is shown to the network for adjusting its weights. The representative trained model per network architecture was thereby chosen based on the epoch that featured the highest binary validation accuracy.

$$CE = -\frac{1}{n}\sum_{i=1}^{n} y_i \cdot \log(p_i) + (1 - y_i) \cdot \log(1 - p_i) \tag{3.5}$$

where:

CE	$=$	Binary cross entropy;
n	$=$	Total number of observations;
i	$=$	Current observation;
y	$=$	Current label $\in \{0,1\}$;
p	$=$	Probability of belonging to label 1.

For the second phase, each of the nine representative models was further trained based on reference data from the OSM sites. No augmentation was applied on the reference images based on OSM. Identical to the images from the manually digitized sites, reference data from OSM was also converted into separate tiles with a size of 512×512 pixels each. The total number of tiles was thereby 307,056, 237,460 of which were used for training and the remaining 67,760 tiles were used for validation. Identical parameter settings as specified in the first training phase were applied for training the networks in the second phase. Once again, the representative trained model per network architecture was chosen based on the epoch that featured the highest binary validation accuracy.

Probability maps were then produced using the fully trained networks for the whole investigated area, with values ranging from 0 1 for each 512 by 512 pixel tile. In order to separate terrestrial area (including inland lakes and rivers) from sea area, a threshold of 0.5 was applied on each probability tile from each network. Thus, nine binary classifications, one from each trained network, were available per tile. The mode value per pixel was subsequently extracted based on the individual binary classifications to generate the most representative output across all models. Additionally, the level of agreement between all network outputs was extracted on a pixel basis via Equation 3.6. This information was utilized as a quality layer for the DL coastline product. Lowest possible agreement of 0.11 is present if only 5 out of 9 models predicted the same class, whereas an agreement of 1 is achieved if all models predicted the same class.

$$model_{agreement} = \frac{n_{mode} - \frac{n_{models}}{n_{classes}}}{n_{models} - \frac{n_{models}}{n_{classes}}} \tag{3.6}$$

where:

n_{mode}	=	Number of occurrences of the mode value;
n_{models}	=	Total number of models;
$n_{classes}$	=	Total number of classes

3.2.4.2 Deep Learning post-Processing

Final touch-ups comprised the closing of holes with sizes that are smaller ≈ 3 km^2 as well as removing objects smaller than ≈ 0.2 km^2. The final combined DL coastline product was revealed by vectorizing the border line between the terrestrial area and sea area. Minor local adjustments were applied to the coastline product during a manual screening of the generated product. The generated DL coastline was further compared with openly accessible and circumpolar coastline products, namely the Circumpolar Arctic Vegetation Map (CAVM) coastline dataset (D. A. Walker et al., 2005), the Global Self-consistent, Hierarchical, High-resolution Geography Database (GSHHG) product (Wessel & Smith, 1996), and OpenStreetMap (OSM) (OpenStreetMap contributors, 2017).

3.2.5 Coastal Change Quantification via Change Vector Analysis

As demonstrated in Figure 3.4, the sd and median backscatter behave inversely for terrestrial and sea areas. Generally, higher sd values are observed over water vs. land, whereas a higher median backscatter is shown over land compared to water. This behaviour was subsequently utilized to study changes between water and land in Arctic coastal environments through the application of CVA. CVA constitutes a frequently applied technique for detecting changes between individual scenes and provides further information not only on the direction, but also the magnitude of present change (Wegmann et al., 2016). Moreover, and contrary to traditional post-classification change analyses, CVA prevents the aggregation of uncertainties in individual classification, which are used for detecting change (J. Chen et al., 2010). Due to the mentioned advantages of CVA, the technique was combined with the previously generated S1 backscatter composites to quantify annual change rates of Arctic permafrost coasts on a circumpolar scale.

3.2.5.1 Magnitude of Change

The previously generated annual sd and median backscatter images, as described in section 3.2.2, were used as input data for the CVA on coastal change. Specifically, SAR composites for the year 2017 2021 were incorporated. In case no SAR data was available in 2017 for a specific region, S1 composites covering the year 2018 were used. As mentioned in the previous section, an inverse behaviour of the sd and median backscatter was observed over land vs. water areas. If the sd backscatter between the two observed years increased, while the median backscatter decreased, it was assumed as an erosion-related transition from land to water. If a transition in the opposite direction was detected, it was considered as build-up. The extracted magnitude of change from CVA refers to the Euclidean distance of the two positions of one pixel based on different dates in a two-dimensional Euclidean plane (Equation 3.7) (D. Cohen et al., 2004). The extracted magnitude of change data was re-scaled to a value range between 0 1. Alongside to the magnitude of change itself, the number of available SAR scenes per pixel and per year was investigated and provided in the form of a quality layer to assess the applicability of the CVA based coastal change investigation.

$$d_{(x,y)} = \sqrt{(x_i - y_i)^2 + (x_j + y_j)^2} \tag{3.7}$$

where:

d = Euclidean distance;
x = Date 1 (e.g. the year 2017);
y = Date 2 (e.g. the year 2021);
i = Band 1 (in this study: VV standard deviation backscatter);
j = Band 2 (in this study: VV median backscatter)

3.2.5.2 Change Vector Analysis post-Processing

The DL coastline product was utilized as a reference for defining the area in which coastal change was quantified. The DL coastline was buffered by 200 m towards the sea and a buffer of 50 m was added towards the land area. The additional buffer towards terrestrial area was added in order to make up for any potential errors and inaccuracies within the DL coastline product. The CVA-based magnitude of change data was subsequently clipped to the buffered coastline. Therefore, the analysis was limited to exclusively quantify change along the coastline. As the magnitude of change maps present continuous numbers (range 0 1), a suitable threshold needed to be identified for differentiating between noise and actual change. For this reason, and as mentioned in section 3.2.3, high resolution imagery from Google Earth together with

optical data from S2 were combined with the investigated S1 composites to manually outline changes along the coastline within the manual test regions. The manually digitized areas of change were used as a reference to identify ideal threshold-values for erosion and build-up. More details and examples for the manual delineation of coastal change rates are provided in the upcoming section 3.2.6. Most suitable threshold values of 0.6 and 0.35 were hereby identified for build-up and erosion, respectively. Further post processing included the application of a mode MV with a size of 3×3 in order to minimize the remaining noise within the thresholded change maps. In addition, the distance of each cluster of build-up and erosion to the DL coastline was computed. In case a change-cluster featured a distance of 100 m or larger it was regarded as noise within the sea and therefore discarded. Also, glacier polygons from the GLIMS glacier database (Raup et al., 2007; GLIMS Consortium, 2005) were buffered by 500 m and the resulting area was subsequently removed from the CVA coastal change quantification. Thus, the impact of glacier movements on the proposed framework was reduced to a minimum. The next step of CVA post processing covered the removal of areas which featured less than ten scenes in either the "before" year (2017/2018) and/or the "after" year (2021). Within the framework of the proposed data and methods, it is presumed that a higher number of available satellite scenes in general results in more reliable change quantification. The application extent of the CVA was further confined to areas that are sea-ice-free for more than half of the days within the observation window June September. The ASI database was thereby used as a reference for daily sea-ice concentration data (Spreen et al., 2008). A pixel was classified as affected by sea-ice if 20% or more ice concentration was present. As a last step, average erosion and build-up rates alongside the DL coastline product and within 200 m and 400 m segments were separately extracted. A rectangular polygon with a size of 400×400 m (40×40 pixels) was thereby generated (in case of the 400 m segments) around the center point located on the coastline for each segment. The number of change pixels (separately for erosion and build-up) within the polygon of each segment was extracted and the average change rates within this segment was calculated via Equation 3.8.

$$change_{seg} = length_{window} * \frac{n_{change}}{n_{total}} \tag{3.8}$$

where:

$change_{seg}$	=	Average change (either erosion or build-up) per segment in meters;
$length_{window}$	=	Length of the rectangular observation window in meters;
n_{change}	=	Number of pixels that indicate change (either erosion or build-up);
n_{total}	=	Total number of pixels in the observed window

Although various examples for a successful application of CVA in quantifying land cover change were already published (e.g. Malila, 1980; Siwe & Koch, 2008; Vorovencii, 2014; Flores & Yool, 2007; Perbet et al., 2019; C. Huang et al., 2016; Dewi et al., 2017; Landmann et al., 2013), this study represents the first attempt in measuring coastal change rates within Arctic permafrost environments and on a circumpolar scale by combining CVA with S1 SAR data.

3.2.6 Validation and Quality Control

Both the CVA coastal change investigation and the DL coastline product underwent extensive validation. Manually digitized coastlines were utilized as reference data to extract accuracy metrics of the generated DL output and the CVA products. In addition, quality layers, such as the duration of sea-ice coverage, the number of available scenes, and the level of agreement between individual model outputs are provided per pixel. Lastly, the effects of variations in tide levels on the shoreline identification was further examined.

3.2.6.1 Deep Learning Coastline Extraction

By splitting the reference data from both the manually digitized sites and the OSM sites into separate training and validation areas, spatial-autocorrelation between the train and test sets could be avoided and therefore ensured, that accuracy metrics were not inflated. 1038 km of manually digitized reference coastline for ten different sites across the Arctic were generated for training the individual U-Net models and for validation purposes (Figure 3.6). Binary accuracy and loss information were extracted per model and per epoch, as well as separately after training on the manually digitized sites and after further training with OSM sites. Differences between the predicted coastline and the manually digitized reference coastline, which is based on annual composites of S1, S2, and high resolution imagery from Google Earth, was utilized for accuracy assessment of the final DL product. Additionally, accuracy metrics within a buffer of 500 m around the manually digitized coastline were extracted based on the final binary output classifications, after combining the results of each model. It was hereby differentiated between accuracy metrics for training and validation sites. Overall accuracy values are expected to be relatively high across an entire scene, since the output product represents a binary classification.
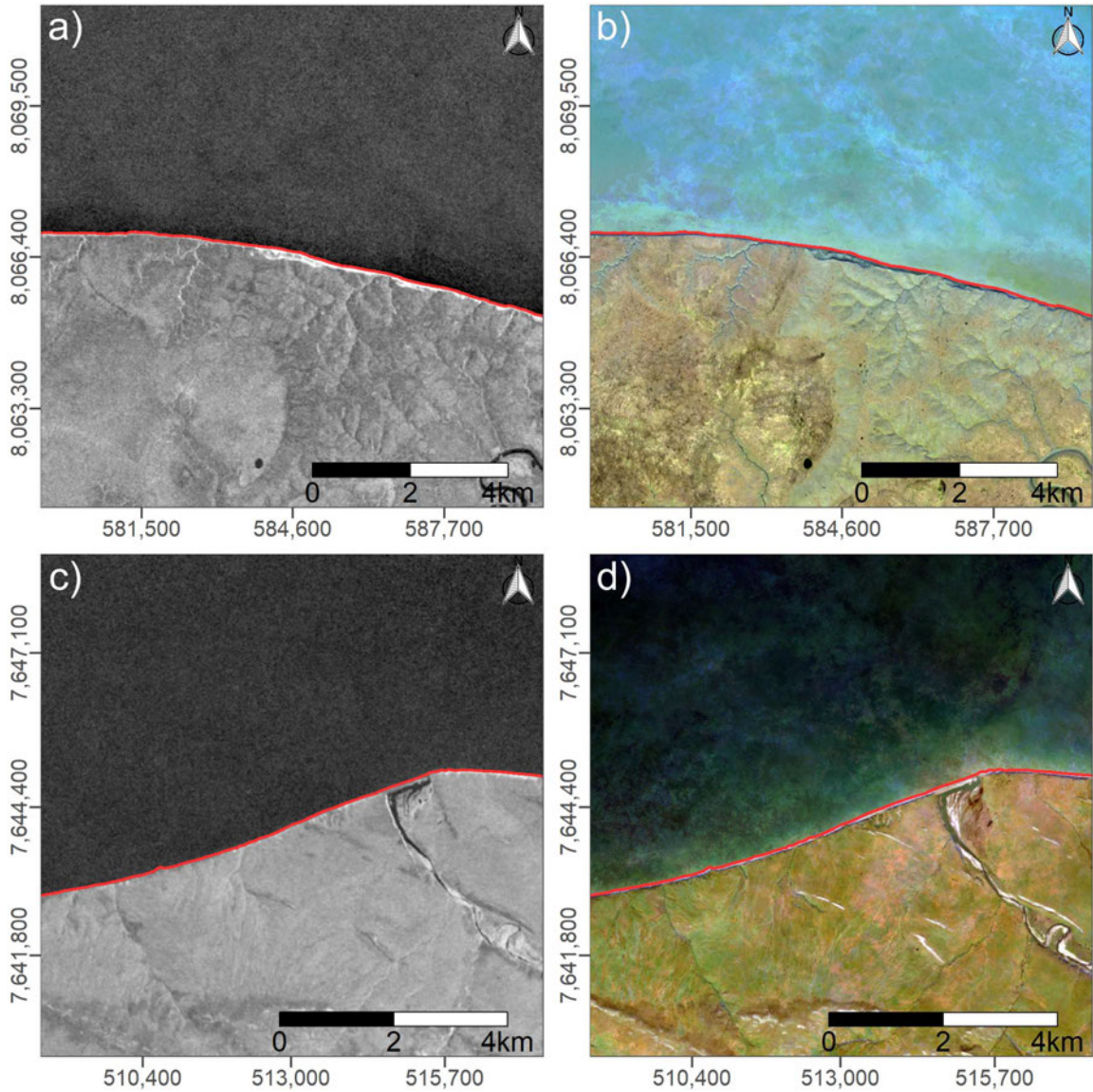
Figure 3.6: Subsections of the two regions of interest, Bezimyanniy Cape in Russia (Area of Interest (AOI) 09) (**a**, **b**), and Corwin Bluffs in the United States of America (USA) (AOI 01) (**c**, **d**). Median images covering the months June–September in the year 2020 from Sentinel-1 (S1) in vertical-vertical (VV) polarization (**a**, **c**) and Sentinel-2 (S2) in Red-Green-Blue (RGB) (**b**, **d**) are shown together with the manually digitized reference coastline (red line). All data is projected and visualized in the respective local Universal Transverse Mercator (UTM) zone. Modified after Philipp et al. (2022).

Because the focus lies on the position of the transition zone between land and sea, further accuracy statistics were derived for the area in proximity (500 m) to the coastline. Frequently used accuracy metrics, namely the F_1-score, recall, precision, and overall accuracy were employed to assess the quality of the final DL-based binary classification maps. Precision is hereby an appropriate metric for evaluating false positives, since it measures the ratio of accurate positive predictions to all positive predictions (Powers, 2020). Recall captures the ratio between the true positive

predictions vs. all positives, whether correctly predicted or not, and is thereby a suitable metric for assessing real positives (Fawcett, 2006). The F_1-score measures the harmonic mean between the recall and the precision and is therefore a balance of both metrics (Taha & Hanbury, 2015). In addition to the accuracy assessment, a variety of pixel-wise quality layers are provided alongside the DL coastline product, including the number of available scenes for generating the S1 annual composites, the number of days within the observation period that feature over 20% sea-ice concentration per pixel based on the ASI database (Spreen et al., 2008), and the level of agreement across the individual output products from each of the nine models.

3.2.6.2 Change Vector Analysis on Coastal Change

The identification of the most suited threshold for converting the continuous magnitude of change maps into binary information for build-up and erosion is crucial. Annual composites from S1, S2, and Imagery from Google Earth were employed to manually digitize coastal changes between 2017 and 2020 across the manual test sites (Figure 3.7). Areas with strong coastal change rates as well as stable coastlines were hereby included as a reference in order to avoid under- or overestimations of the CVA-based products. Different thresholds were applied and the deviations to the manually digitized erosion and build-up rates extracted to determine the most suitable threshold values. Differences between the thresholded change maps and the reference data were thereby used as a metric for assessing the quality of the CVA-based coastal change products. Additionally, and similar to the DL product, a variety of associated quality layers are provided to assess the applicability and quality of the generated coastal change rates. The duration of sea-ice presence and the number of available S1 SAR images per pixel are thereby included for each of the investigated years. The number of sea ice days with more than 20% ice concentration per pixel for the years 2017 and 2021 are illustrated in Figure 3.8. Furthermore, details about the spatial distribution of glacier extents based on the GLIMS glacier database (GLIMS Consortium, 2005) acted as another quality layer. The previously generated magnitude of change maps themselves are also a quality layer, which can be further utilized for differentiating between actual change and noise as well as for the application of user-defined threshold values.
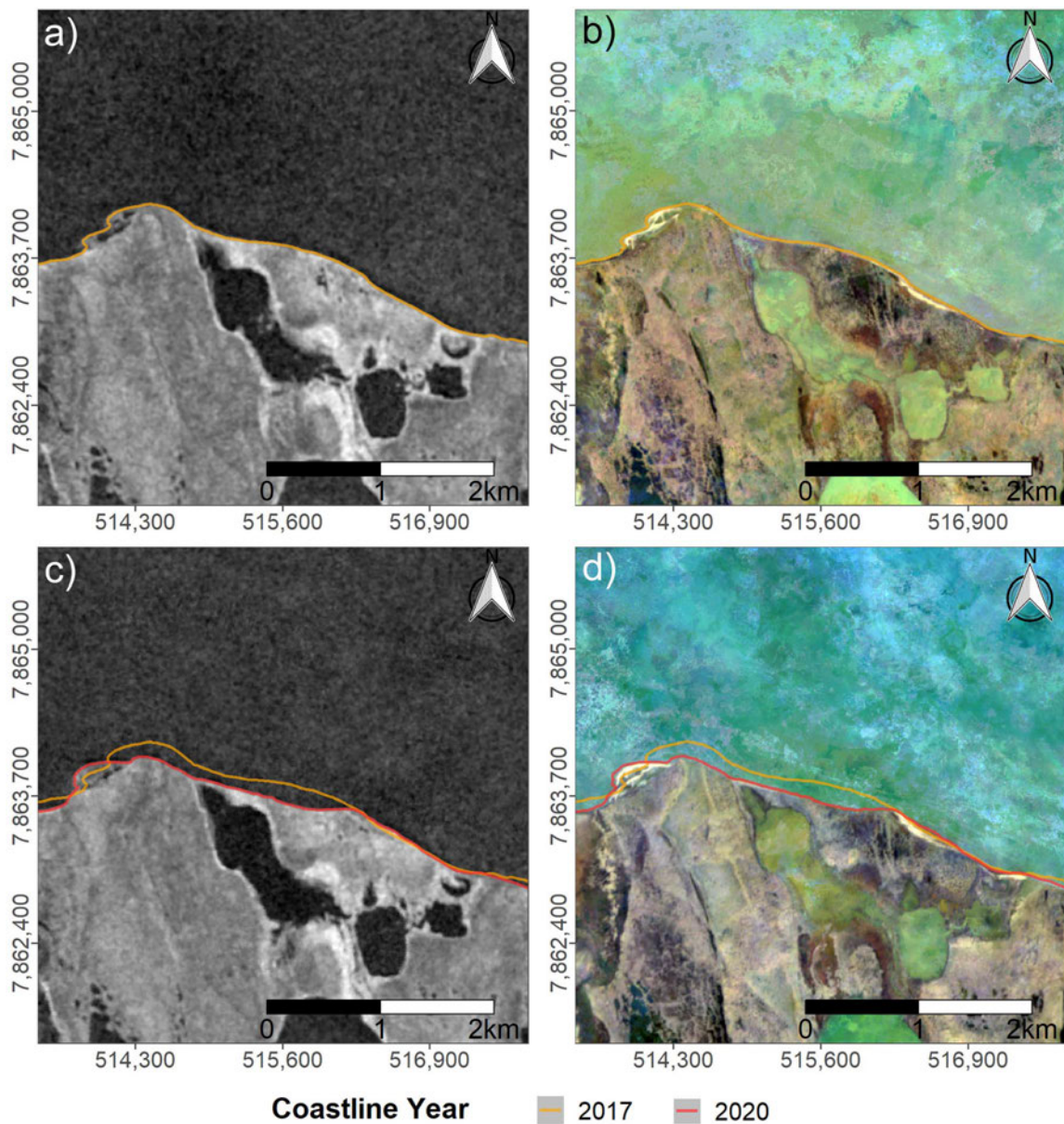
Figure 3.7: Example of the erosion reference data for a subsection of Cape Halkett in the United States of America (USA) (Area of Interest (AOI) 02) in the year 2017 (**a**, **b**) and 2020 (**c**, **d**). Median images for the months June–September from Sentinel-1 (S1) in vertical-vertical (VV) polarization (**a**, **c**) and Sentinel-2 (S2) in Red-Green-Blue (RGB) (**b**, **d**) are shown together with the manually digitized reference coastlines for the years 2017 (orange line) and 2020 (red line). All data is visualized in a Universal Transverse Mercator (UTM) zone 5 North projection. Modified after Philipp et al. (2022).
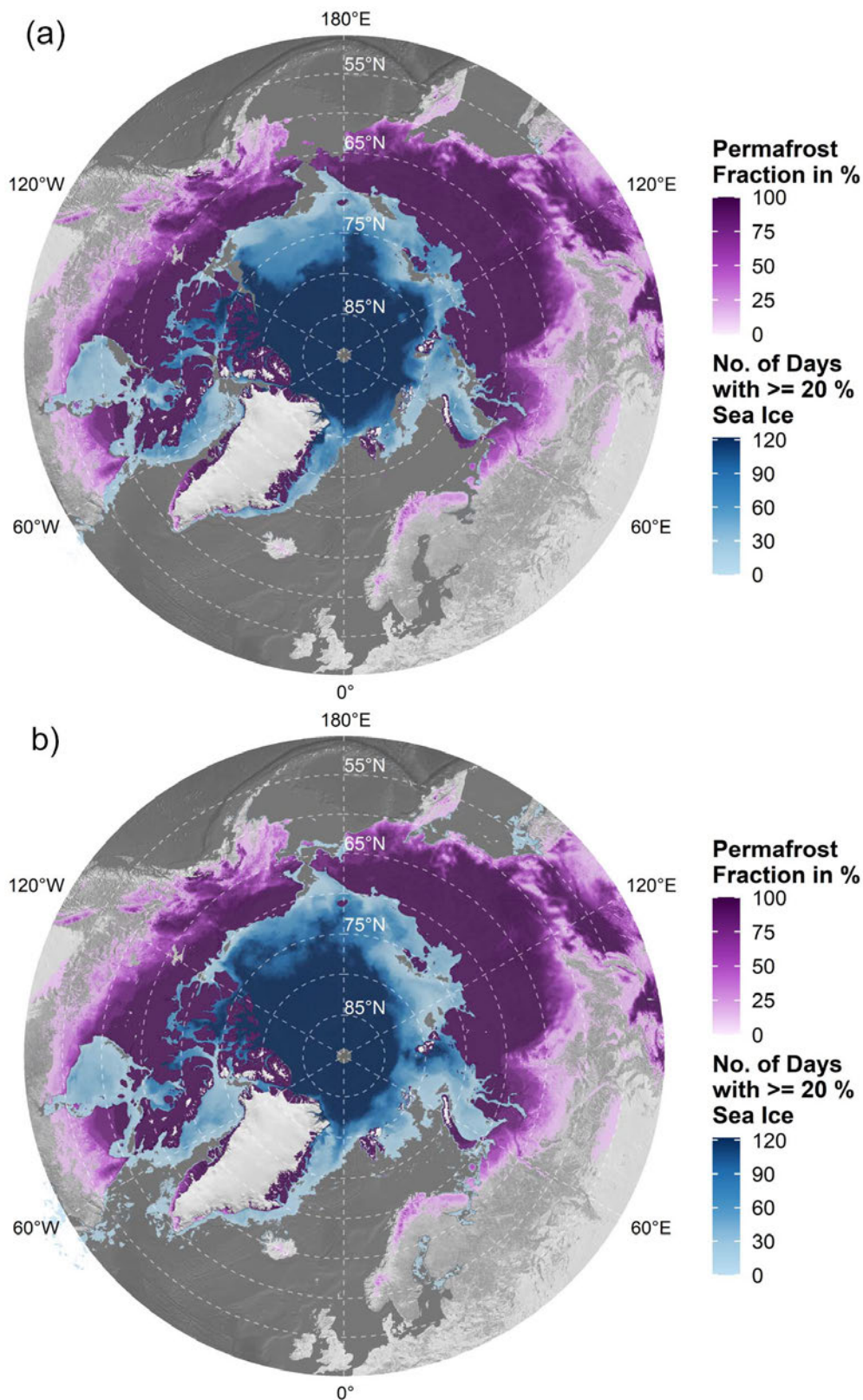
Figure 3.8: Spatial variation of the number of days with at least 20 % sea ice between the months June–September for the years 2017 (**a**) and 2021 (**b**). Sea ice concentration data is based on the ARTIST Sea Ice (ASI) database (Spreen et al., 2008). A shaded relief by Natural Earth (n.d.) in combination with the permafrost fraction across the Northern Hemisphere for the year 2017 based on data by Obu et al. (2021b) was used as a background map. Modified after Philipp et al. (2023).

3.2.6.3 Influence of tidal Changes

Changes in local tide levels may cause the exact position of the Arctic coastline to fluctuate within the observation window June September. For this reason, working on temporal composites instead of single observations likely provides a more representative positioning of the coastline, especially for regions with flat and sandy coasts. At the same time, the quality of the composite may vary depending on the number of available images and local tidal levels at satellite acquisition times. Therefore, six-minutely MTL data derived from four buoy stations covering the same temporal observation frame as the Pseudo-RGB satellite imagery (June September 2020) were accessed via the National Oceanic and Atmospheric Administration (NOAA) (2022b). Data from the following stations, 9497645 Prudhoe Bay, 9491094 Red Dog Dock, 9468756 Nome, and 9468333 Unalakleet were accessed. Figure 3.9 illustrates the geographical distribution of the four buoy stations across Alaska.
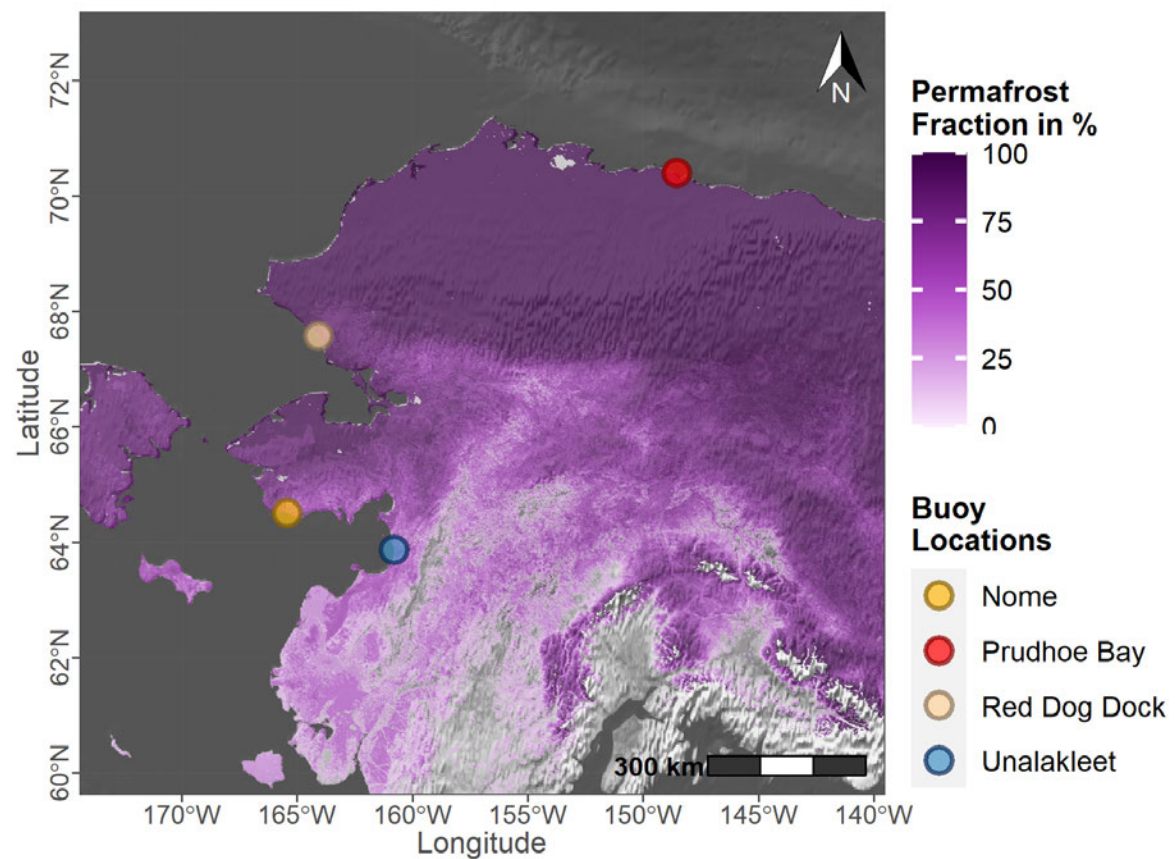
Figure 3.9: Spatial distribution of the buoy stations 9468756 Nome, 9468333 Unalakleet, 9497645 Prudhoe Bay, and 9491094 Red Dog Dock provided by the National Oceanic and Atmospheric Administration (NOAA) (2022b). A shaded relief by Natural Earth (n.d.) in combination with the permafrost fraction across the Northern Hemisphere for the year 2017 based on data by Obu et al. (2021b) was used as a background map. Modified after Philipp et al. (2023).

The MTL represents the arithmetic mean of mean low water and mean high water (National Oceanic and Atmospheric Administration (NOAA), 2022a). Local MTL was extracted for the acquisition times and dates of available S1 GRD SAR data in IW swath mode over each buoy location. For each buoy location, the average MTL at satellite acquisition dates was compared with the overall average MTL from the whole buoy data set within the temporal observation window. It was confirmed that buoy data and satellite acquisition dates were formatted in the same time zone (Greenwich Mean Time (GMT)). A close average MTL from S1 acquisition to the overall average MTL was assumed to indicate that the annual satellite composite is highly representative in terms of its visualized transition zone between land and water.

3.3 Results

The following section presents the results of both the DL work-flow for generating a high-quality Arctic coastline product as well as the CVA-based quantification of coastal change rates. First, details on the DL model performance, segmentation results, and a comparison between the DL coastline product and other openly available Arctic coastline data sets is provided. Secondly, accuracy metrics and statistics of coastal erosion and build-up are provided. Lastly, the effects of tidal changes on the generated composites are highlighted.

3.3.1 Deep Learning

Results of the deep learning framework are described in detail from here on out. The overall performance of individual models, effects of different hyper-parameter settings, the level of agreement on the output between different models, accuracy statistics of the final binary segmentation maps and statistics on the quality of the extracted coastline are provided in the following sections. Moreover, the quality of the generated coastline was compared to other publicly available coastline products.

3.3.1.1 Model Performance

As mentioned in section 3.2.4.1, different hyper-parameters and their effects on model performance were tested. Specifically, the two optimizers "Adam" and "RMSprop", as well as the two loss functions "binary cross-entropy" and "mean absolute error" were compared. Details on the accuracy and loss values for each optimizer and loss-function combination applied on the two models ResNet34 and VGG16 are provided in Table 3.4. Statistics hereby represent the epoch with the

highest validation accuracy over a 30 epoch training period per model/optimizer/loss-function combination. In case of the model ResNet34, both highest training accuracy (0.9991) and validation accuracy (0.998) could be achieved with a combined use of RMSprop and binary cross-entropy. The same behaviour was also observed for the model VGG16, where highest training accuracy (0.9991) and validation accuracy (0.9979) were also achieved by combining the RMSprop optimizer with the binary cross-entropy loss-function. This highlights the reasoning for choosing RMSprop and binary cross-entropy as hyper-parameters within the DL framework.

Table 3.4: Statistics of the hyper-parameter testing after training on the manually digitized sites. Hyper-parameters were tested on the models VGG16 and ResNet34. The two optimizers Adam and Root Mean Square Propagation (RMSprop), and the two loss functions binary cross-entropy and mean absolute error were compared. Statistics for the epoch with the highest validation accuracy are listed for each model and hyper-parameter combination. Numbers are rounded to the fourth decimal place.

		Model: ResNet34				
Optimizer	**Loss Function**	**Epoch**	**Train. Acc.**	**Train. Loss**	**Val. Acc.**	**Val. Loss**
Adam	binary cross-entropy	25	0.9934	0.0204	0.9966	0.013
Adam	mean absolute error	16	0.9866	0.0134	0.9967	0.0043
RMSprop	binary cross-entropy	29	0.9991	0.003	0.998	0.0087
RMSprop	mean absolute error	17	0.9964	0.0036	0.9971	0.0034

		Model: VGG16				
Optimizer	**Loss Function**	**Epoch**	**Train. Acc.**	**Train. Loss**	**Val. Acc.**	**Val. Loss**
Adam	binary cross-entropy	6	0.9911	0.0262	0.9973	0.0203
Adam	mean absolute error	8	0.9897	0.0104	0.9977	0.0025
RMSprop	binary cross-entropy	22	0.9991	0.003	0.9979	0.0085
RMSprop	mean absolute error	20	0.9978	0.0022	0.9966	0.0103

Accuracy values per epoch after training with SAR composites from the manually digitized sites are visualized for each model and separately for training and validation data in Figure 3.10. Training accuracy was hereby already relatively high (>0.9) after the first one or two epochs and was close to 1 after the first couple of epochs across all models. Validation accuracy featured stronger fluctuations within the first couple of epochs but generally also featured accuracy values close to 1 in later training epochs. Figure 3.11 illustrates the dynamics of loss values during training on the manual sites. Similarly to the accuracy values, stronger variations were observed for the validation data in contrast to the training data. Loss vales for all models and both training and validation sites were generally close to 0 after the first couple of epochs. Table 3.5 provides details on accuracy and loss statistics for the epoch with the highest validation accuracy per model. All models were trained for at least 14 epochs before reaching the highest validation accuracy after training on the manually digitized sites. Validation accuracies per model after the first training phase ranged between 0.9957 (Inception v3) and 0.998 (VGG19 and ResNet34) with an average validation accuracy of 0.9973. Training accuracies from 0.9977 (ResNet50 and DenseNet121) to 0.9998 (SE-ResNeXt50) were observed with an average training accuracy of 0.9989. Validation loss ranged from 0.0075 (VGG19) to 0.0167 (Inception v3) with an average loss of 0.0106. Training loss values between 0.0005 (SE-ResNeXt50) to 0.0091 (DenseNet121) and an average training loss of 0.0039 were identified.

A slightly different behaviour was observed for the training process based on reference data from the OSM sites compared to the first training phase. Since the models were already pre-trained not only on the ImageNet database, but also on data from the manually digitized sites, accuracy measures for both training and validation stayed continuously very high and close to 1 during the entire training procedure (Figure 3.12). On the other hand, loss values were observed to continuously slightly decrease in case of training data, but tend to moderately increase in case of validation data throughout the second training phase (Figure 3.13). The epoch which led to the highest validation accuracy after training on OSM data therefore strongly varied across the individual models. The earliest epoch of 4 was observed for ResNet34, whereas the models VGG16 and Inception v3 achieved highest validation accuracy during the 29th epoch of the second training phase. Final validation accuracies per model after the second training phase ranged between 0.9785 (Inception v3) and 0.9805 (ResNeXt50) with an average validation accuracy of 0.9792. Training accuracies from 0.9838 (ResNet34) to 0.9952 (Inception v3) were observed with an average training accuracy of 0.991. Validation loss ranged from 0.0696 (ResNet34) to 0.1508 (Inception v3) with an average loss of 0.1051. Training loss values between 0.0121 (Inception v3) to 0.0488 (ResNet34) and an average training loss of 0.0253 were identified. Detailed

statistics on accuracy and loss rates are provided in Table 3.5.
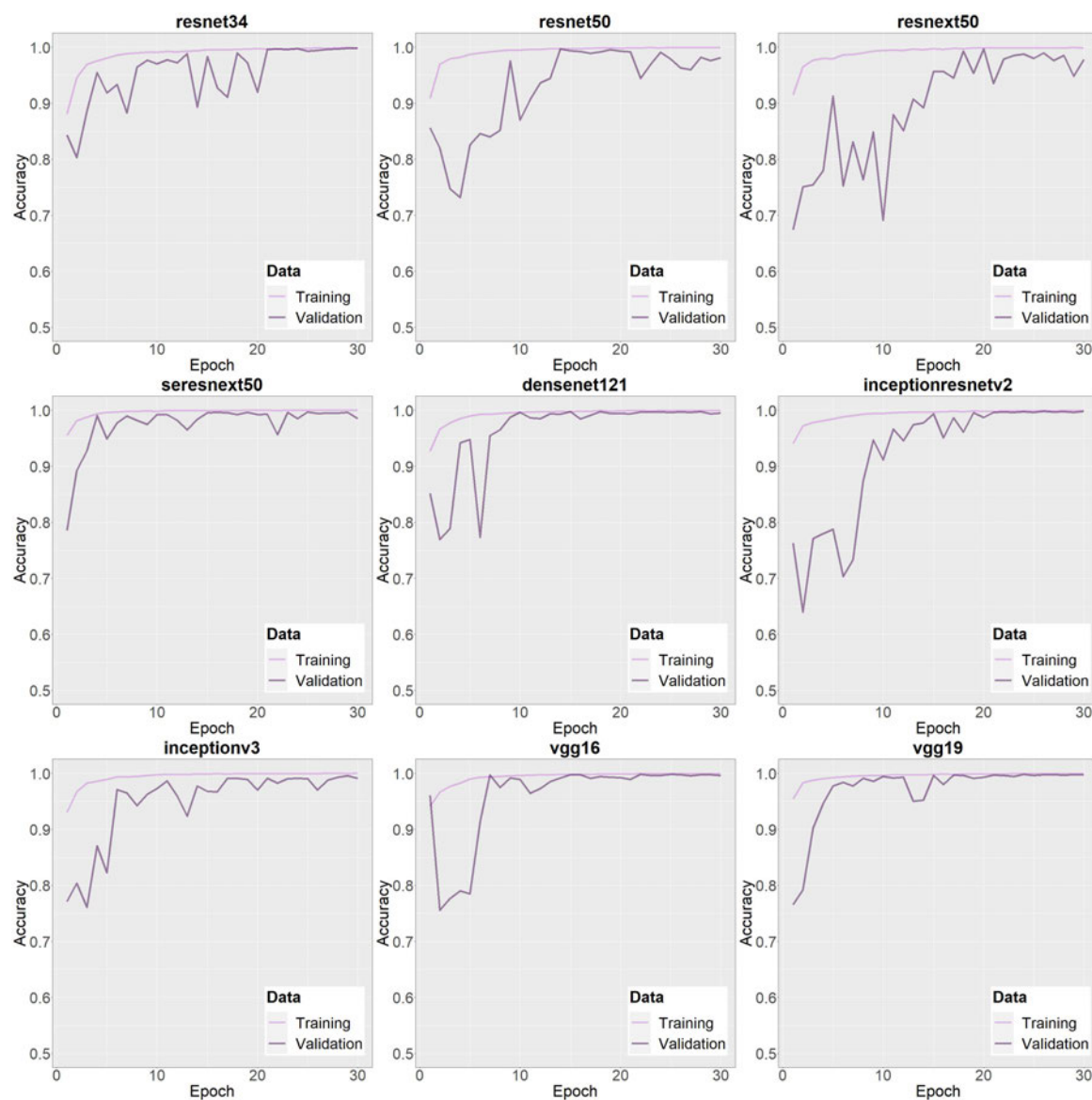
Figure 3.10: Training and validation accuracies per model and epoch after training the networks on the manually digitized sites. Each model was trained for 30 epochs. A batch size of 8, a binary cross-entropy loss function, a Root Mean Square Propagation (RMSprop) optimizer with a learning rate of 0.001, and binary accuracy as an accuracy metric were used for training.
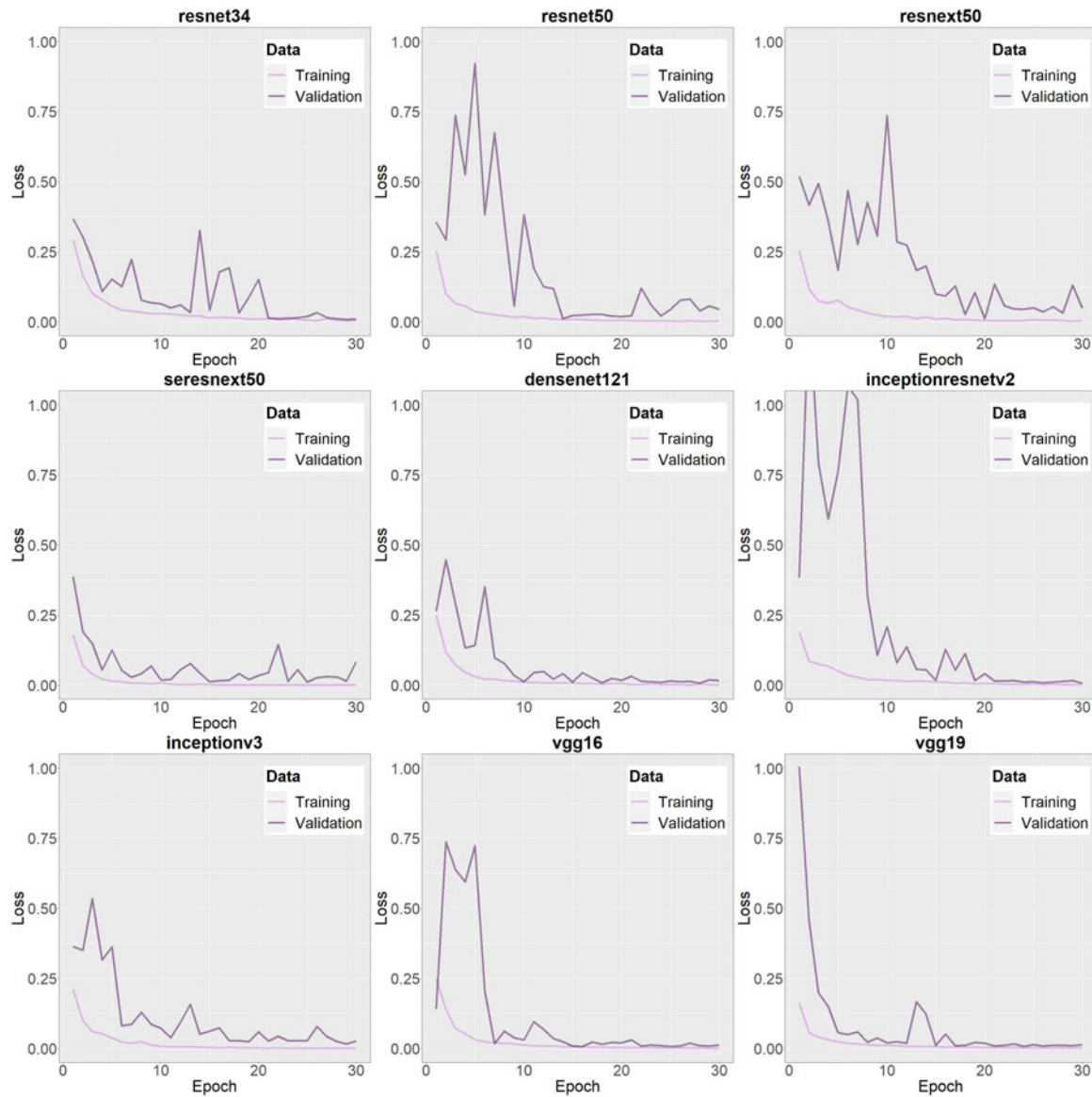
Figure 3.11: Training and validation loss per model and epoch after training the networks on the manually digitized sites. Each model was trained for 30 epochs. A batch size of 8, a binary cross-entropy loss function, a Root Mean Square Propagation (RMSprop) optimizer with a learning rate of 0.001, and binary accuracy as an accuracy metric were used for training.
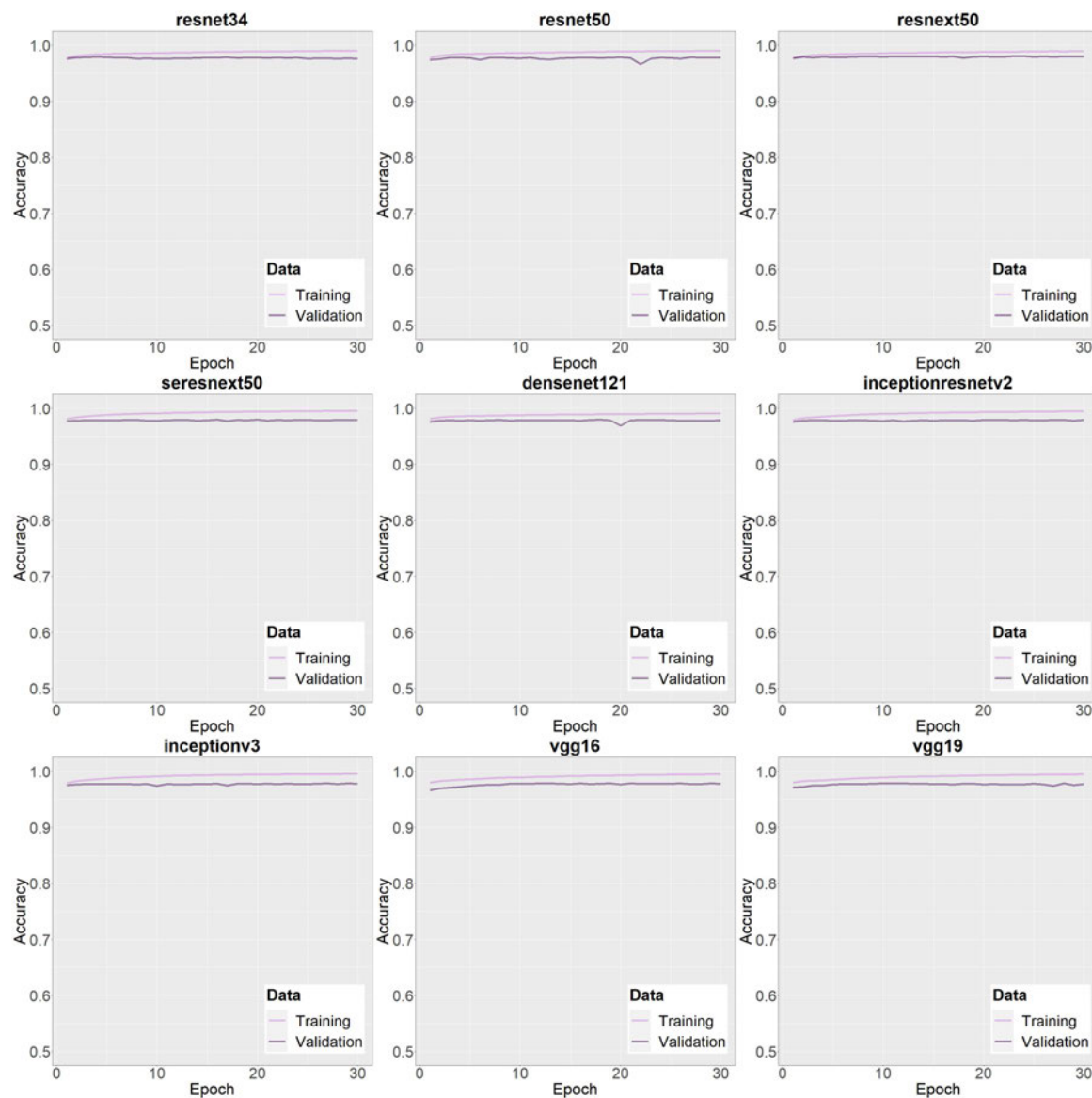
Figure 3.12: Training and validation accuracies per model and epoch after additional training of the networks on the OpenStreetMap (OSM) sites. Each model was trained for 30 epochs. A batch size of 8, a binary cross-entropy loss function, a Root Mean Square Propagation (RMSprop) optimizer with a learning rate of 0.001, and binary accuracy as an accuracy metric were used for training.
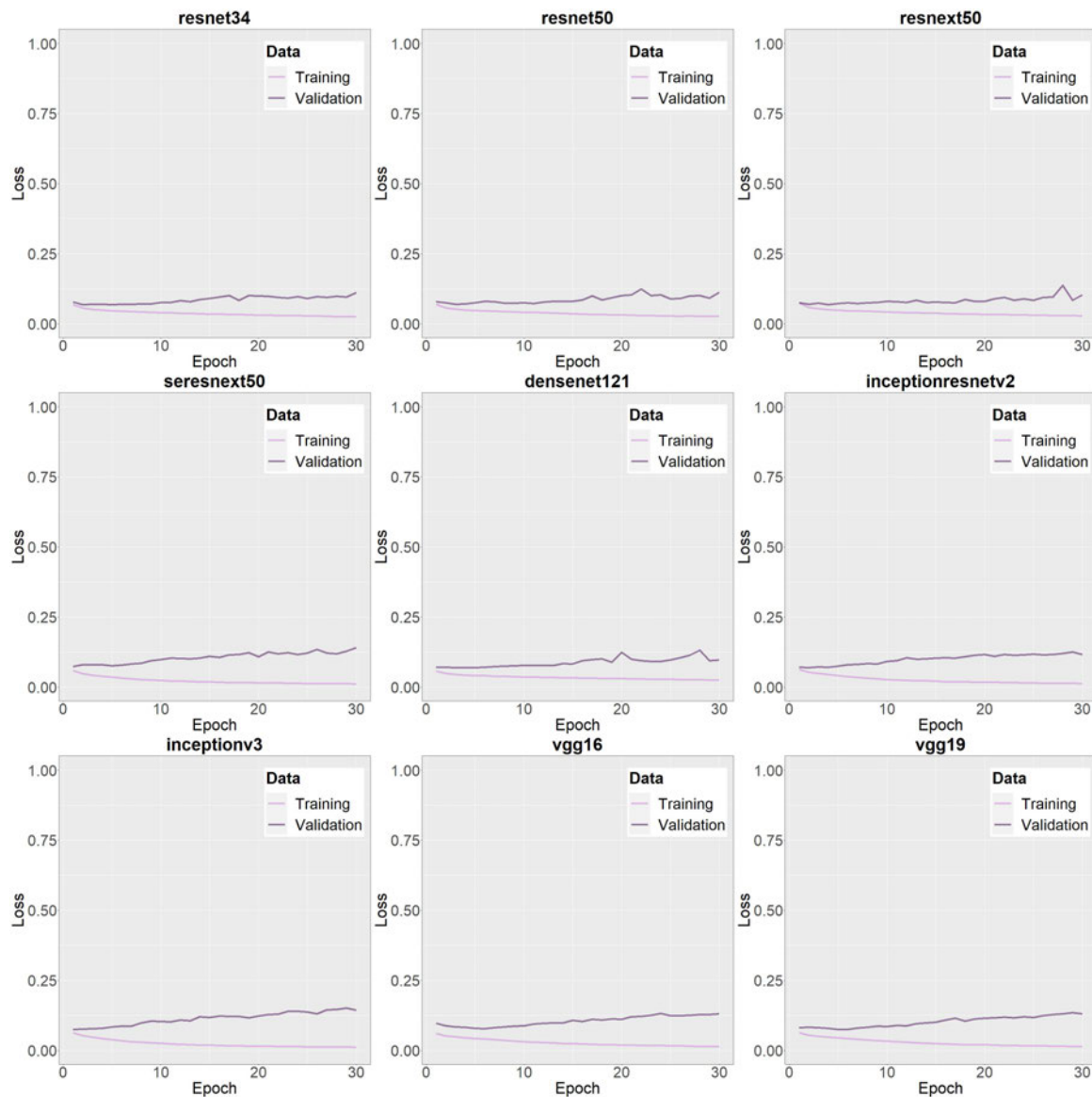
Figure 3.13: Training and validation loss per model and epoch after additional training of the networks on the OpenStreetMap (OSM) sites. Each model was trained for 30 epochs. A batch size of 8, a binary cross-entropy loss function, a Root Mean Square Propagation (RMSprop) optimizer with a learning rate of 0.001, and binary accuracy as an accuracy metric were used for training.

Table 3.5: Accuracy statistics and epochs per model after training on the manually digitized sites and after additional training on the OpenStreetMap (OSM) sites. The epoch with the highest validation accuracy was chosen as the representative output for each model. Accuracy and loss values were rounded to the fourth decimal place. Modified after Philipp et al. (2022) and Philipp et al. (2023).

Manually Digitized Sites					
Model	**Epoch**	**Training Acc.**	**Training Loss**	**Validation Acc.**	**Validation Loss**
ResNet34	29	0.9991	0.003	0.998	0.0087
ResNet50	14	0.9977	0.0082	0.9969	0.0116
Inception v3	29	0.9997	0.001	0.9957	0.0167
Inception-ResNet v2	26	0.9992	0.0025	0.9979	0.0081
ResNeXt	20	0.9986	0.0053	0.9967	0.0113
DenseNet121	15	0.9977	0.0091	0.9976	0.0111
SE-ResNeXt50	25	0.9998	0.0005	0.9964	0.0117
VGG16	22	0.9991	0.003	0.9979	0.0085
VGG19	24	0.9993	0.0027	0.998	0.0075
OpenStreetMap (OSM) Sites					
Model	**Epoch**	**Training Acc.**	**Training Loss**	**Validation Acc.**	**Validation Loss**
ResNet34	4	0.9838	0.0488	0.9790	0.0696
ResNet50	27	0.9900	0.0276	0.9787	0.1000
Inception v3	29	0.9952	0.0121	0.9785	0.1508
Inception-ResNet v2	20	0.9933	0.0175	0.9796	0.1160
ResNeXt	23	0.9885	0.0323	0.9805	0.0844
DenseNet121	18	0.9894	0.0311	0.9796	0.1003
SE-ResNeXt50	20	0.9941	0.0155	0.9799	0.1080
VGG16	29	0.9945	0.0143	0.9787	0.1283
VGG19	12	0.9900	0.0289	0.9787	0.0881

Table 3.6 lists accuracy statistics of the combined binary classification map within a 500 m buffer around the reference coastline after training on the manual sites. Accuracy statistics within the 500 m buffer are thereby slightly lower compared to the full scenes as listed in Table 3.5, but overall still very high. Overall accuracy values across all manual sites ranged from 0.965 and 0.992, with an average overall accuracy of 0.974 within the mentioned buffer. Recall values between 0.936 and 0.995, and an average recall of 0.976 was observed for sea areas. Terrestrial areas featured recall values from 0.944 to 0.998, with an average value of 0.972. Precision scores between 0.953 and 0.999, and an average precision score of 0.974 were observed for sea

areas. Precision values from 0.945 to 0.995, with an average precision of 0.974 could be identified for terrestrial regions. Finally, F_1-scores ranging from 0.963 to 0.993, and an average F_1-score of 0.975 were observed for the sea class. The terrestrial class featured F_1-scores between 0.964 and 0.991, while the average F_1-score proved to be 0.973.

Further accuracy statistics after additional training on the OSM sites and within a 500 m buffer are provided in Table 3.7. Overall accuracy scores for the final combined binary classification map after post-processing proved to be 0.95 for training areas and 0.97 for validation areas in case of the manually digitized sites. Comparable high values were identified for the F_1-score, recall, and precision for both land and marine locations, as well as both training and validation sites of the manually digitized areas. Overall accuracy values for OSM sites of 0.95 and 0.94 were observed for training and validation areas, respectively. Again, similarly good agreement between the reference data and the predicted binary classification is reflected in the F_1-score, recall, and precision values for both training and validation sites.

Table 3.6: Accuracy statistics within a 500 m buffer around the manually digitized reference coastline after training on the manually digitized sites. Recall, precision, and F_1-scores are given for both classes, terrestrial area (including inland rivers and lakes) and sea per AOI. Validation sites are highlighted in bold text. Accuracy measures are rounded to the third decimal place. Modified after Philipp et al. (2022).

AOI	Overall Acc.	Label	Recall	Precision	F1
1	**0.992**	**Terrestrial**	**0.988**	**0.995**	**0.991**
		Sea	**0.995**	**0.988**	**0.992**
2	0.972	Terrestrial	0.944	0.99	0.967
		Sea	0.993	0.958	0.975
3	0.967	Terrestrial	0.993	0.947	0.97
		Sea	0.936	0.992	0.963
4	**0.982**	**Terrestrial**	**0.969**	**0.995**	**0.982**
		Sea	**0.995**	**0.971**	**0.983**
5	0.969	Terrestrial	0.948	0.987	0.967
		Sea	0.988	0.953	0.97
6	**0.965**	**Terrestrial**	**0.957**	**0.972**	**0.964**
		Sea	**0.973**	**0.958**	**0.965**
7	0.977	Terrestrial	0.973	0.977	0.975
		Sea	0.981	0.977	0.979

(Table continues on the next page ...)

Table 3.6: Continued.

AOI	Overall Acc.	Label	Recall	Precision	F1
8	0.99	Terrestrial	0.998	0.965	0.981
		Sea	0.987	0.999	0.993
9	0.964	Terrestrial	0.983	0.945	0.964
		Sea	0.945	0.983	0.963
10	0.986	Terrestrial	0.996	0.977	0.986
		Sea	0.976	0.996	0.986

(... end of continued table.)

Table 3.7: Accuracy statistics within a 500 m buffer around the manually digitized reference coastline (Manual) as well as the OpenStreetMap (OSM) coastline for the final combined binary classification product after training on the OSM sites and post-processing. Recall, precision, and F_1-scores are shown for both classes, terrestrial area (including inland lakes and rivers) and sea. Accuracy measures are rounded to the second decimal place. Modified after Philipp et al. (2023).

Manually Digitized Sites					
Area	**Overall Acc.**	**Label**	**Recall**	**Precision**	**F1**
Training	0.95	Terrestrial	0.93	0.97	0.95
		Sea	0.97	0.93	0.95
Validation	0.97	Terrestrial	0.96	0.98	0.97
		Sea	0.98	0.96	0.97
OpenStreetMap (OSM) Sites					
Area	**Overall Acc.**	**Label**	**Recall**	**Precision**	**F1**
Training	0.95	Terrestrial	0.97	0.92	0.94
		Sea	0.93	0.97	0.95
Validation	0.94	Terrestrial	0.99	0.90	0.94
		Sea	0.91	0.99	0.95

3.3.1.2 Circum-Arctic Coastline Extraction

The total length of the final extracted DL coastline product is ≈161,600 km. S1 pseudo-RGB backscatter composites, the associated binary classification result after combining the outputs of all nine trained networks, as well as the extracted coastline are visualized for four different Arctic regions in Figure 3.14.
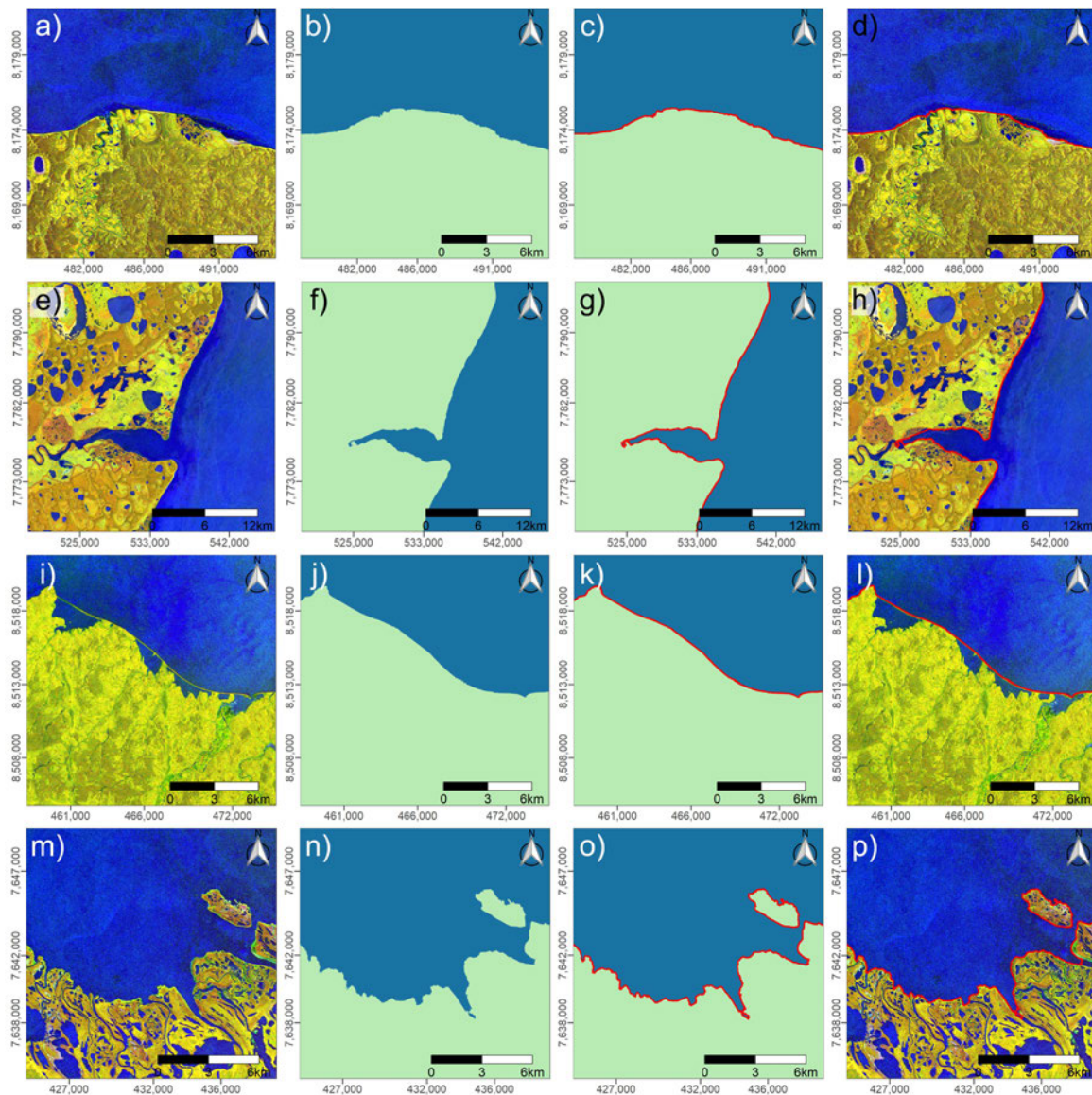
Figure 3.14: Subsets of annual Sentinel-1 (S1) pseudo-Red-Green-Blue (RGB) images (**a**, **e**, **i**, **m**), the associated Deep Learning (DL)-based binary classification maps (**b**, **f**, **j**, **n**), and the derived coastlines (**c**, **g**, **k**, **o**) for four different regions, including Mus-Khaya Cape–Mouth of Peshanaya in Russia (Area of Interest (AOI) 06) (**a**–**d**), Mouth of Kurdugina–Malyy Chukochiy Cape in Russia (AOI 10) (**e**–**h**), Sims Bay in Russia (AOI 05) (**i**–**l**), and Shoalwater Bay in Canada (AOI 03) (**m**–**p**). All data is projected and visualized in their respective Universal Transverse Mercator (UTM) zone. Modified after Philipp et al. (2022).

Average deviation of ± 8.7 m and ± 131.2 m were observed to the reference coastline of the manually digitized sites and OSM sites, respectively. The median deviation proved to be ± 6.3 m in case of the manual sites and ± 29.6 m in case of the OSM sites. sd values of ± 8.5 m (manual sites) and ± 404.8 m (OSM sites) were observed. Minimum deviation was 0 m for both reference data sets. A strong discrepancy between the maximum deviation for manual sites (± 50 m) and OSM sites (± 8989.3 m) could be measured. Lastly, 2nd and 98th percentile values of ± 0.2 m and ± 36.9 m were

identified within the manual sites, while the 2nd and 98th percentiles were ±1.1 m and ±1402.5 m for the OSM sites. Table 3.8 lists statistics on the deviation between the reference coastline of the manually digitized sites and the generated DL coastline product, as well as statistics for three other openly available and circumpolar coastline data sets. The DL-based product hereby featured significantly lower deviations to the reference compared to the other listed products. Out of the three products CAVM, GSHHG, and OSM, best performance was observed for OSM, which featured a median deviation of ±40.1 m and an average distance to the reference line of ±331 m. At the same time, the highest sd of ±768.7 m, strongest maximum deviation of ±5525.6 m, and the largest 98th percentile of ±3215.6 m was also observed for the OSM dataset. Second lowest median (±386.8 m) and average (±563 m) deviations were identified for the GSHHG product. CAVM featured the weakest accuracy in terms of average and median deviation to the reference coastline, with ±707.7 m and ±584.6 m, respectively. Figure 3.16 further illustrates differences in quality of the mentioned coastline products for the area Drew Point Cape Halkett in Alaska. The figure reflects the average deviation of each coastline product as listed in Table 3.8. While the DL coastline product runs, for the most part, smoothly along the reference coastline, the other three products feature partly strong deviations to the reference across the entire area. Boxplots of the distance values to the manually digitized reference coastline for each of the mentioned products is visualized in Figure 3.16. Figure 3.17 further illustrates the distance between the manually digitized reference coastline and the generated DL coastline product based on points located every 200 m along the coastline. The two regions Drew Point Cape Halkett in Alaska (Figure 3.17 a,b) and Sims Bay in Russia (Figure 3.17 c,d) are shown. The majority of points indicate distances of less than 10 m. All statistics on the deviation of coastline products to the reference line are based on reference points every 200 m along the respective coastline.

An exemplary annual S1 Pseudo-RGB composite over Shoalwater Bay in Canada, together with the level of agreement across the output products from the individual networks, and the derived binary classification and extracted coastline are visualized in Figure 3.18. A high level of agreement among the implemented models is observed over large parts of the sea and terrestrial area. Areas of stronger disagreement between the models are hereby identified for large river deltas, large lake areas, and the exact location of the transition zone between land and water (Figure 3.18 b). This confusion among the individual models can partly also be depicted in the final combined binary classification map, that features partly noisy transitions between the two classes, especially for larger river deltas (Figure 3.18 c).
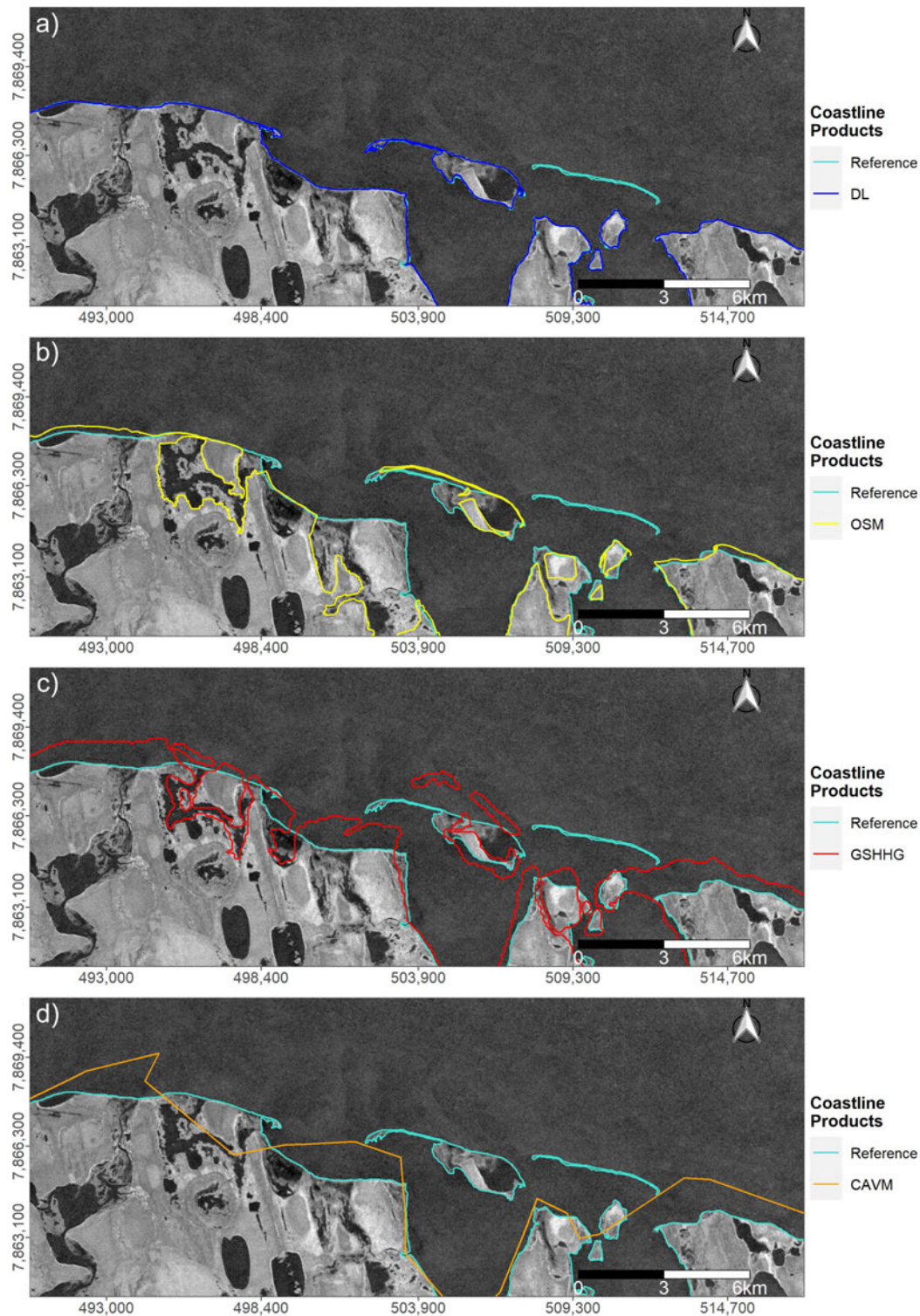
Figure 3.15: Comparison of different coastline products to the reference line for Drew Point–Cape Halkett, United States of America (USA) (Area of Interest (AOI) 02). (**a**) Deep Learning (DL) coastline product, (**b**) OpenStreetMap (OSM) coastline, (**c**) Global Self-consistent, Hierarchical, High-resolution Geography Database (GSHHG) coastline, (**d**) and the Circumpolar Arctic Vegetation Map (CAVM) coastline are displayed. A Sentinel-1 (S1) annual median backscatter image for the year 2020 (months June–September) in vertical-vertical (VV) polarization is utilized as a background image. All data is visualized in a Universal Transverse Mercator (UTM) zone 5 North projection. Modified after Philipp et al. (2022).
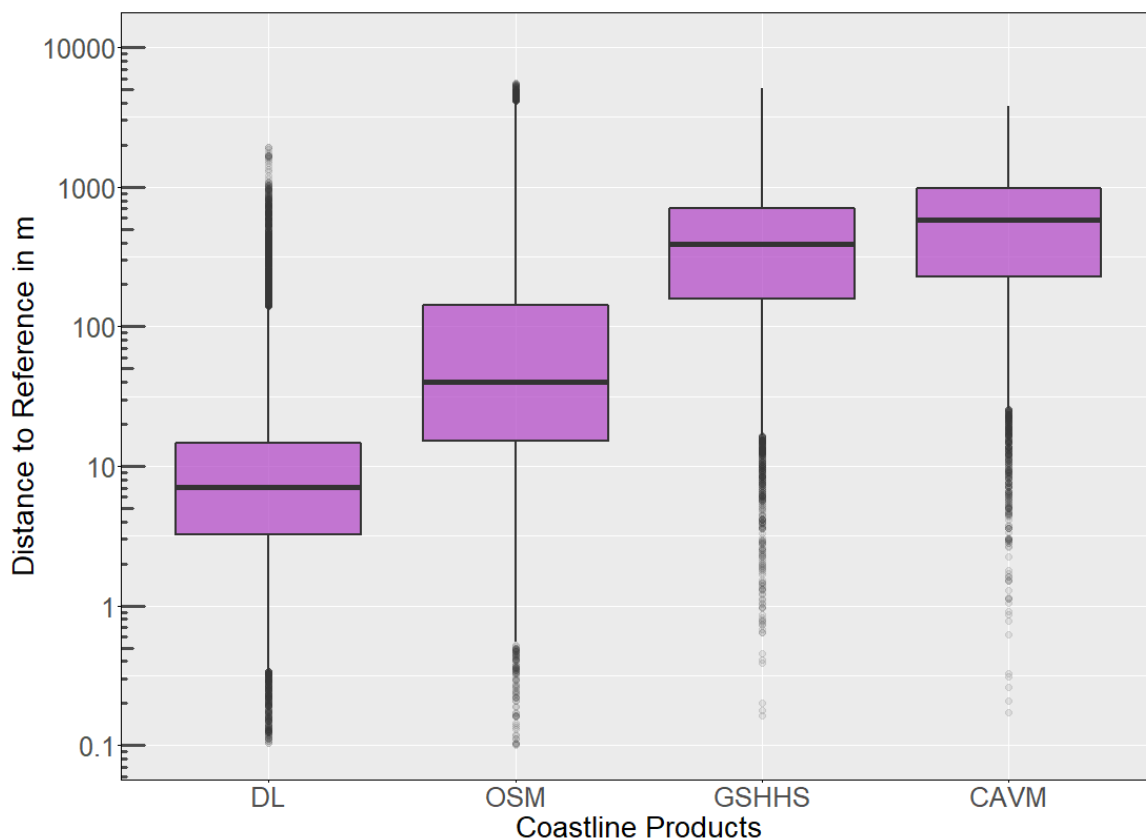
Figure 3.16: Boxplots of the deviation between different coastline products to the reference line across the manually digitized sites, including the Deep Learning (DL) coastline product, the OpenStreetMap (OSM) coastline, the Global Self-consistent, Hierarchical, High-resolution Geography Database (GSHHG) coastline, and the Circumpolar Arctic Vegetation Map (CAVM) coastline. Numbers are based on reference points every 200 m along the coastline products. The y-axis is visualized in a logarithmic scale.

Table 3.8: The deviation of four different coastline products to the reference coastline of the manually digitized sites. Numbers are based on reference points every 200 m along the coastline products. Listed coastlines are the Deep Learning (DL)-based coastline product after training on both the manually digitized sites and OpenStreetMap (OSM) sites, the Circumpolar Arctic Vegetation Map (CAVM) coastline product, the OSM coastline, and the Global Self-consistent, Hierarchical, High-resolution Geography Database (GSHHG) coastline. Various statistics are shown, including the arithmetic mean, median, minimum (Min), maximum (Max), standard deviation (sd), and the 2nd (P02) and 98th (P98) percentiles. Modified after Philipp et al. (2022).

Name	Mean	Median	Min	Max	SD	P02	P98
DL	8.7 m	6.3 m	0 m	50 m	8.5 m	0.2 m	36.9 m
OSM	331 m	40.1 m	0 m	5525.6 m	768.7 m	1.1 m	3215.6 m
GSHHG	563 m	386.8 m	0.2 m	5098.4 m	614.4 m	12.9 m	2527.6 m
CAVM	707.2 m	584.6 m	0 m	3773.8 m	642.6 m	12.9 m	2828.3 m

Figure 3.19 illustrates the number of available S1 GRD SAR images in IW swath mode during the observation period June September 2020, which were used for the computation of the final DL coastline product. In the figure, data availability over Alaska vs. a section in Central Siberia is contrasted. Overall higher data quantity along the coastline can be observed across Alaska compared to Russia.

A full overview of the DL coastline extent is provided in Figure 3.20. Next to the extent of the DL coastline itself (Figure 3.20 a), zoom-in plots on the two regions Drew Point in Alaska (Figure 3.20 b,c) and an area in the Canadian Archipelago (Figure 3.20 d,e) are visualized. The coverage of the Canadian Arctic Archipelago by the DL coastline product is severely constrained due to a shortage of available S1 GRD data in IW swath mode in this region during the observation period June September 2020. Greenland, as well as the Franz Josef Land archipelago, Yuzhny Island, and Severny Island in Russia were fully excluded, since there was no data available within the temporal observation window. The zoom-in plots on Drew Point in Alaska (Figure 3.20 b,c) highlight the accuracy of the DL-based coastline in comparison to the OSM product for the depicted region. On the other hand, several small islands were excluded during the post-processing of the DL product, which are still present in the OSM dataset, as seen in sub-Figures 3.20 d) & e).
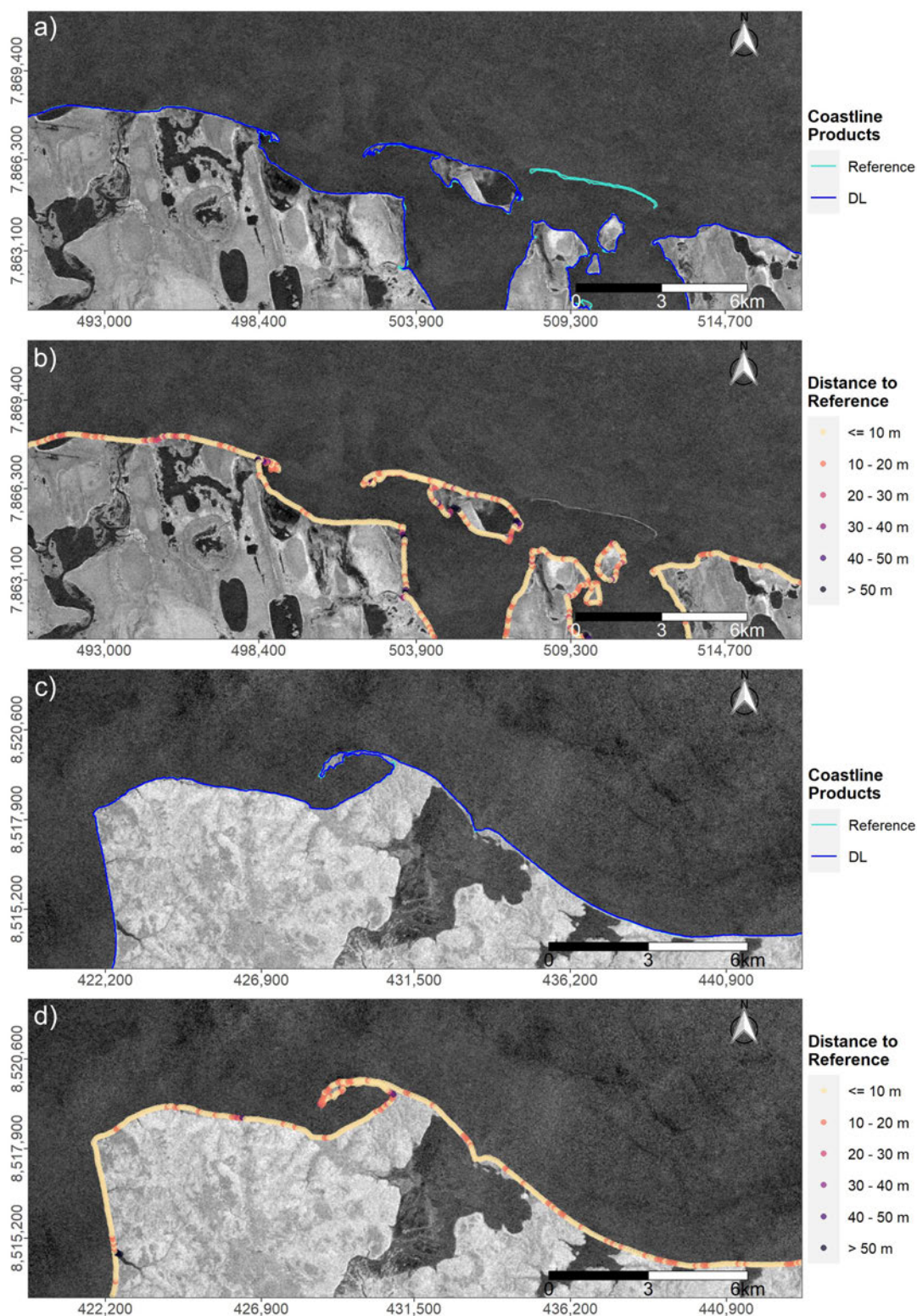
Figure 3.17: Comparison between the location of the Deep Learning (DL)-based predicted coastline (dark blue line) and the reference coastline (turquoise line) (**a**, **c**) as well as the distance of the Deep Learning (DL) line to the reference line (**b**, **d**) for Drew Point–Cape Halkett, United States of America (USA) (Area of Interest (AOI) 02) (**a**, **b**) and Sims Bay, Russia (AOI 05) (**c**, **d**). A Sentinel-1 (S1) annual median backscatter image for the year 2020 (months June–September) in vertical-vertical (VV) polarization is utilized as a background image. All data is projected and visualized in their respective Universal Transverse Mercator (UTM) zone. Modified after Philipp et al. (2022).
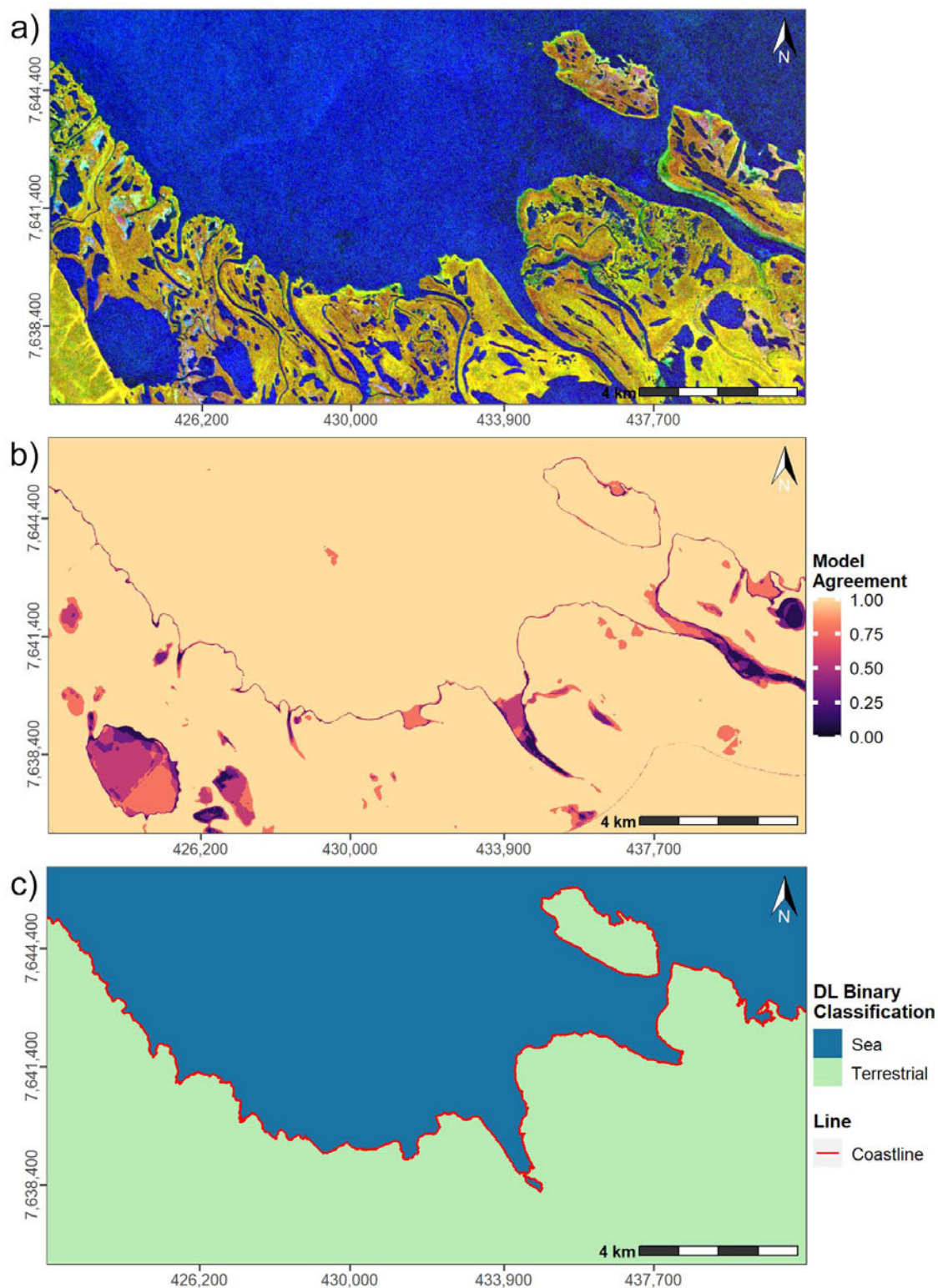
Figure 3.18: (**a**) Sentinel-1 (S1) Pseudo-Red-Green-Blue (RGB) composite covering the months June–September in 2020. (**b**) The level of agreement between the nine individual classifications from different U-Net architectures. (**c**) Final binary segmentation map derived from the mode of nine individual classifications from different U-Net models. The two classes represent sea area (dark-blue colour) and terrestrial area, including inland lakes and rivers (light-green colour). All images display a section of Shoalwater Bay in Canada and are visualized in a Universal Transverse Mercator (UTM) zone 8 projection. Modified after Philipp et al. (2023).
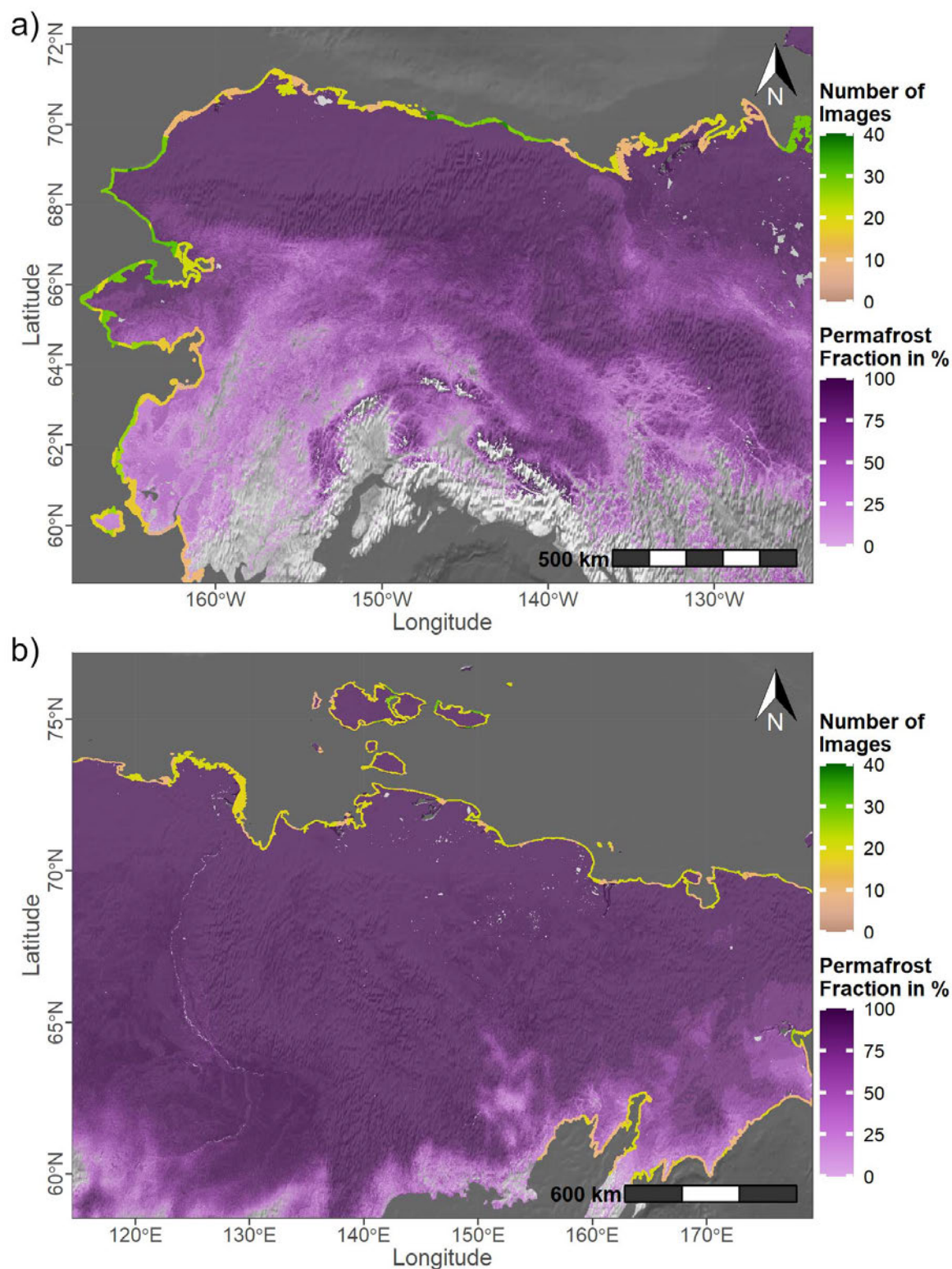
Figure 3.19: The amount of available Sentinel-1 (S1) Ground Range Detected (GRD) scenes in Interferometric Wide (IW) swath mode for coastal regions across Alaska (**a**) and Northern Siberia (**b**) within the time span June–September 2020. The number of images serve hereby as a quality layer for the Deep Learning (DL) coastline product. A shaded relief by Natural Earth (n.d.) in combination with the permafrost fraction across the Northern Hemisphere for the year 2017 based on data by Obu et al. (2021b) was used as a background map. Modified after Philipp et al. (2023).
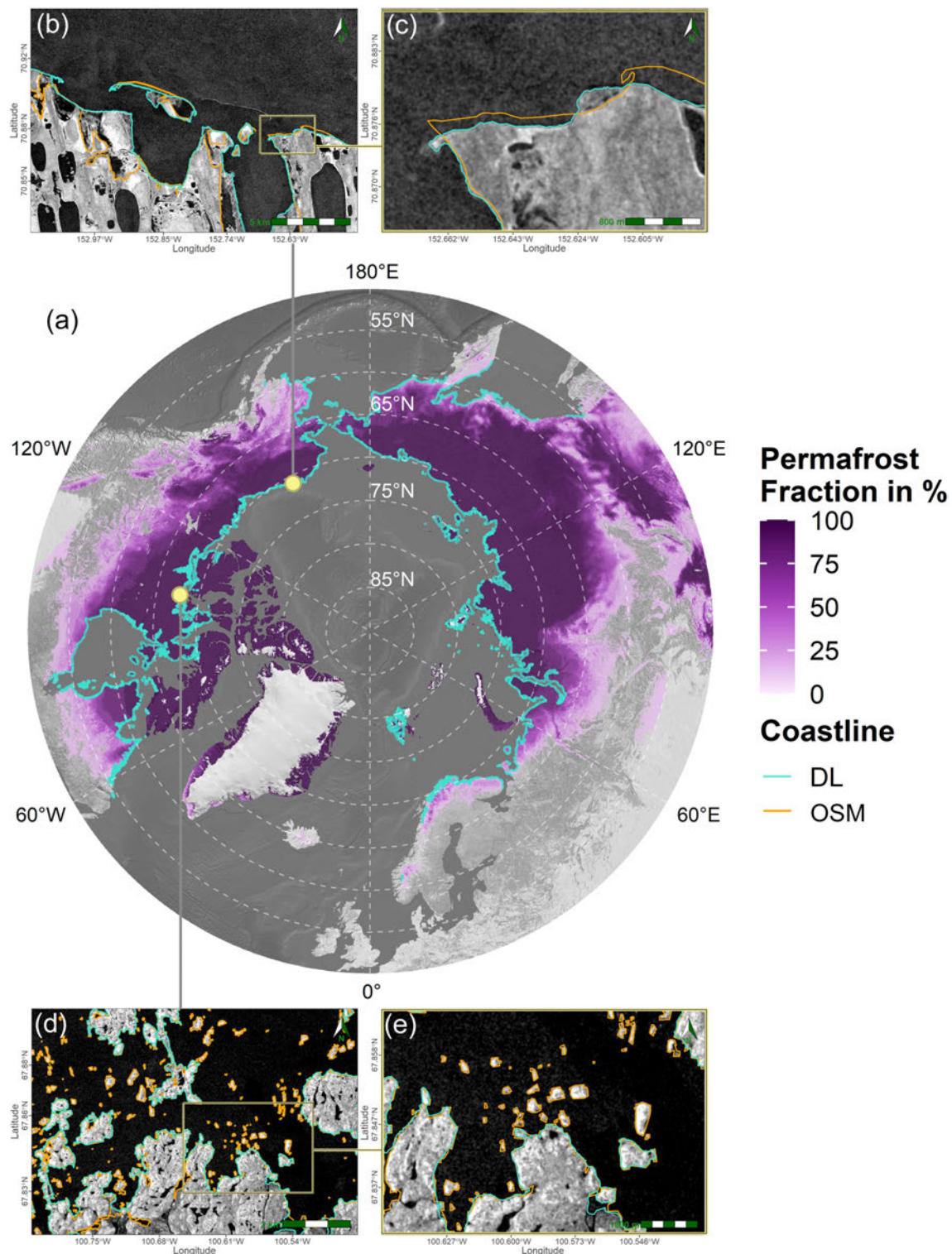
Figure 3.20: Circum-Arctic overview (**a**) with exemplary zoom-ins (**b**–**e**) on the final Deep Learning (DL) coastline product (turquoise line) and the OpenStreetMap (OSM) coastline (orange line). The two example regions Drew Point in Alaska (**b**, **c**), and an area in the Canadian Archipelago (**d**, **e**) are visualized. A Sentinel-1 (S1) annual median backscatter image for the year 2020 (months June–September) in vertical-vertical (VV) polarization is utilized as a background image for (**b**–**e**). A shaded relief by Natural Earth (n.d.) in combination with the permafrost fraction across the Northern Hemisphere for the year 2017 based on data by Obu et al. (2021b) was used as a background map for (**a**). Modified after Philipp et al. (2023).

3.3.2 Coastal Erosion and Build-up

The best thresholds were identified to be 0.6 for detecting build-up and 0.35 for detecting erosion when comparing the CVA probability of the change to the manually digitized coasts for the years 2017 and 2020. An average deviation of -10.3 m can be reported between the thresholded CVA magnitude of change maps and the reference data. Furthermore, an r^2 value of 0.92 and a sd of ± 12.9 m between the predicted and actual change was observed.

CVA probability of change maps and the threshold-applied coastal change for subsections of the two regions Shoalwater Bay in Canada (AOI 03) and Drew Point Cape Halkett in the USA (AOI 02) are visualized in Figure 3.21. Although areas of coastal erosion and build-up can already be identified in the probability of change maps (Figure 3.21 a,c), a significant amount of noise in the form of low probability of change pixels scattered throughout the sea are observable. After applying the previously mentioned thresholds, most of the noise for both build-up and erosion could be removed, while the actual areas of change were retained (Figure 3.21 b,d).

Table 3.9 provides detailed information about the average and maximum build-up and erosion rates between 2017 2020 for each of the manually digitized sites. Maximum erosion of up to 160.3 m and a total average erosion of 4.4 m was observed within the mentioned time span. An average build-up rate of 1.9 m across all manually digitized sites and a maximum build-up of 166.7 m can be reported. Both the strongest average (22 m) and maximum (160.3 m) erosion were identified for Drew Point Cape Halkett in the USA. Second highest erosion rates were observed for Shoalwater Bay in Canada (average: 10.3 m, max: 70 m). Figure 3.22 further illustrates average coastal erosion rates for 200 m segments within the temporal observation window 2017 2020 for a subsection of Shoalwater Bay in Canada (AOI 03). On the other hand, Bezimyanniy Cape Eastern Oyagoss Cape in Russia featured strongest maximum (166.7 m) and average (8.7 m) build-up, followed by Sims Bay in Russia with an average build-up of 1.4 m and a maximum build-up rate of 58 m.

Average annual erosion rates from 2017 2018 based on 20 km segments are visualized for the entire circum-Arctic study area in Figure 3.23. Coastal erosion rates are illustrated for areas with less than 50% sea-ice cover and more than ten available S1 GRD SAR scenes in IW swath mode from June September per year. Less than 1% of segments indicate annual average erosion of more than 50 m. Annual erosion rates between 20-50 m were observed for 1.3% of segments. 2.4% featured annual erosion rates of 10 20 m, while erosion numbers from 5 10 m were observed for 3.8% of segments. Significantly more areas (12.8% of segments) featured erosion rates between

1 5 m. A total of 35% of segments were observed to feature erosion of less than 1 m, while 44.3% did not indicate any erosion at all. In addition to the circumpolar overview (Figure 3.23 a), zoom-in plots for a coastal area in Alaska (Figure 3.23 b d) and a sandy delta in Russia (Figure 3.23 e g) are provided. For each zoomed-in area, the median backscatter in VV polarisation covering the months June September are illustrated separately for both years 2017 and 2021. Moreover, the eroded coastline within this time span is highlighted in red colour. The exemplary delta in Russia (Figure 3.23 e g) illustrates how the CVA algorithm classifies changes in sandy deposits as coastal erosion.
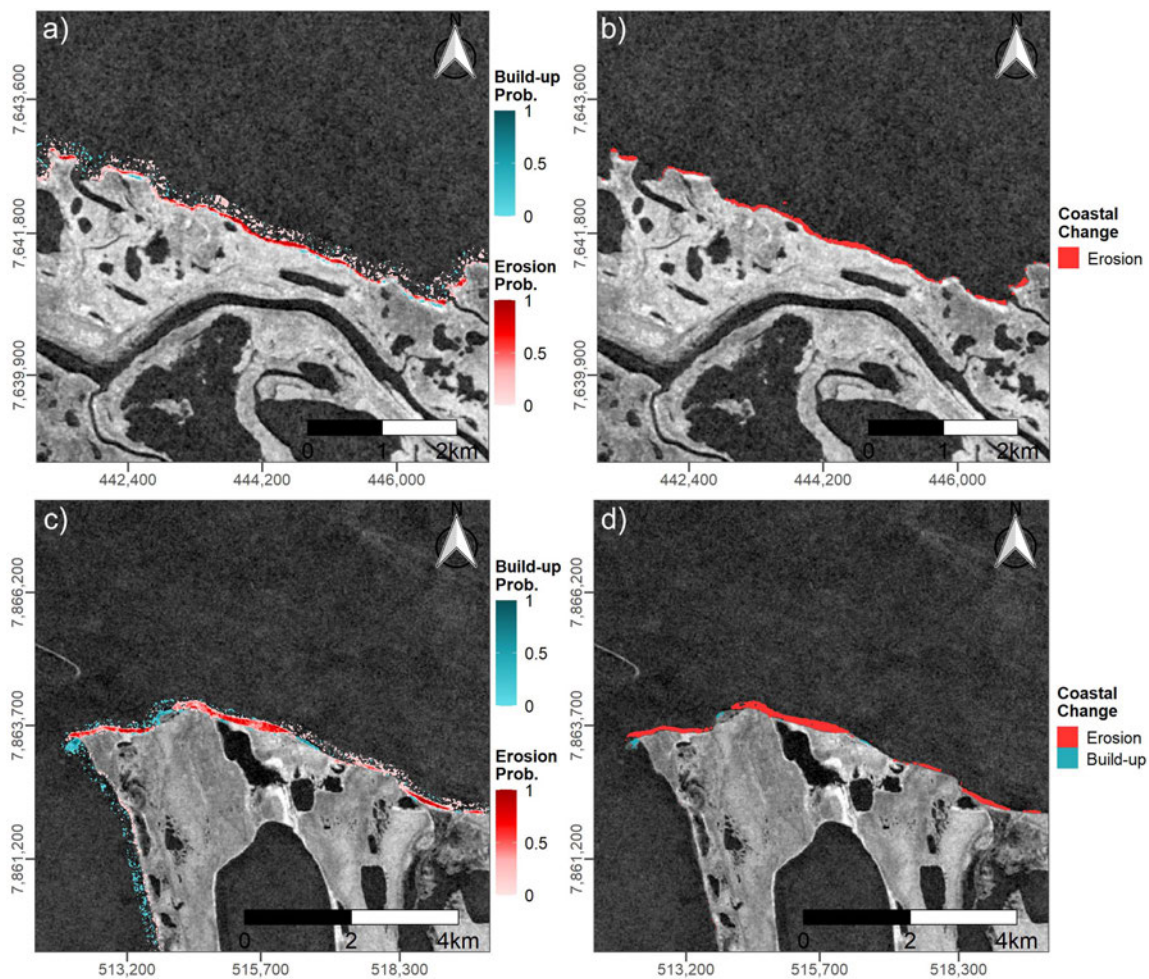
Figure 3.21: Probability maps of build-up and erosion rates between 2017 and 2020 for subsets of Shoalwater Bay, Canada (Area of Interest (AOI) 03) (**a**), and Cape Halkett, United States of America (USA) (AOI 02) (**c**), together with their respective and threshold applied maps of coastal change (**b, d**). A threshold of 0.6 for the build-up and 0.35 for the erosion was applied (**b, d**). All data is projected and visualized in their respective Universal Transverse Mercator (UTM) zone. Modified after Philipp et al. (2022).

Table 3.11 lists statistics on annual build-up and erosion rates per country and based on 400 m segments. Numbers for the countries Canada, Norway (Svalbard

and Jan Mayen), Norway (Scandinavian Peninsula), Russia, and the USA (Alaska) are provided. The USA (Alaska) featured overall strongest average annual erosion (0.75 m), followed by an average erosion of 0.62 m in Russia. In contrast, the lowest average erosion rate of 0.01 m was identified for Norway (Scandinavian Peninsula). Norway also featured the weakest average build-up rate (0 m). On the other hand, average build-up rate was highest in Svalbard and Jan Mayen with 0.07 m per year. Highest overall annual erosion rate per segment was identified in Russia with 67 m, followed by 62.5 m in Alaska. Russia also featured the maximum annual build-up rate per segment with 53.25 m, followed by 52.67 m in Svalbard and Jan Mayen. Alaska featured both the highest sd and 98th percentile values in erosion of 3.45 m and 10.25 m, respectively. Build-up statistics in the form of the 98th percentile were 0 across all countries. The highest sd of build-up per segment was observed in Svalbard and Jan Mayen (1.62 m).

Table 3.9: Average and maximum rates of build-up and erosion between 2017 and 2020 per Area of Interest (AOI). The numbers are based on average values for 200 m segments along the coastline. Highest build-up rates were observed for Bezimyanniy Cape–Eastern Oyagoss Cape in Russia (AOI 09), whereas Drew Point–Cape Halkett, United States of America (USA) (AOI 02) features strongest erosion rates. Modified after Philipp et al. (2022).

AOI	Build-Up		Erosion Rates	
	Mean	**Max**	**Mean**	**Max**
1	0 m	0 m	0.2 m	10.3 m
2	4 m	79 m	22 m	160.3 m
3	0 m	2 m	10.3 m	70 m
4	0.2 m	10.2 m	0.5 m	7.6 m
5	1.4 m	58 m	0.7 m	30 m
6	0 m	0.5 m	1.4 m	62 m
7	0.1 m	14 m	0.6 m	13.6 m
8	0.5 m	7.2 m	1.1 m	26.2 m
9	8.7 m	166.7 m	1.3 m	20.5 m
10	1 m	36 m	0.9 m	40.5 m
All:	1.9 m	166.7 m	4.4 m	160.3 m

Next to statistics on a country basis, numbers are also provided for different seas based on the IHO Sea Areas dataset in Table 3.10. With 1.12 m per year, the Beaufort Sea featured overall strongest average erosion, followed by 0.91 m in the East Siberian Sea. Highest average annual build-up was identified for the Sea of Okhotsk

(0.09 m), followed by 0.07 m for the Laptev Sea. Highest overall annual erosion rate per segment was observed for the Bering Sea (62.5 m) and the Barents Sea (67 m). On the other hand, the Laptev Sea and the Barents Sea featured highest annual build-up per segment with 53.25 m and 52.67 m, respectively. In case of annual erosion, highest 98th percentile values were observed in the East Siberian Sea (9.5 m) and the Bering Sea (9.75 m). In case of annual build-up, 98th percentile values were for the most part 0 m, with the exception of the East Siberian Sea (0.25 m), the Hudson Strait (0.25 m), and the Arctic Ocean (0.33 m). Highest sd in annual erosion was observed for the Bering Sea (3.26 m) and the Barents Sea (3.63 m). In contrast, highest sd in annual build-up was identified for the Barents Sea (0.97 m) and the Laptev Sea (1.17 m). Numbers in both Tables 3.11 and 3.10 are based on average annual erosion and build-up rates within 400 m segments. For this reason, numbers are rounded to the second decimal place. Nevertheless, the actual accuracy for a pixel-wise comparison can only be as good as the pixel size of the input data, which is 10 m. Across the entire investigated Arctic coastline, 12.24% of segments showed an average annual erosion rate of 3.8 m and a combined annual land loss of 17.83 km^2, whereas 1.05% of segments showed an average yearly build-up rate of 2.3 m and a combined annual build-up area of 1.02 km^2.
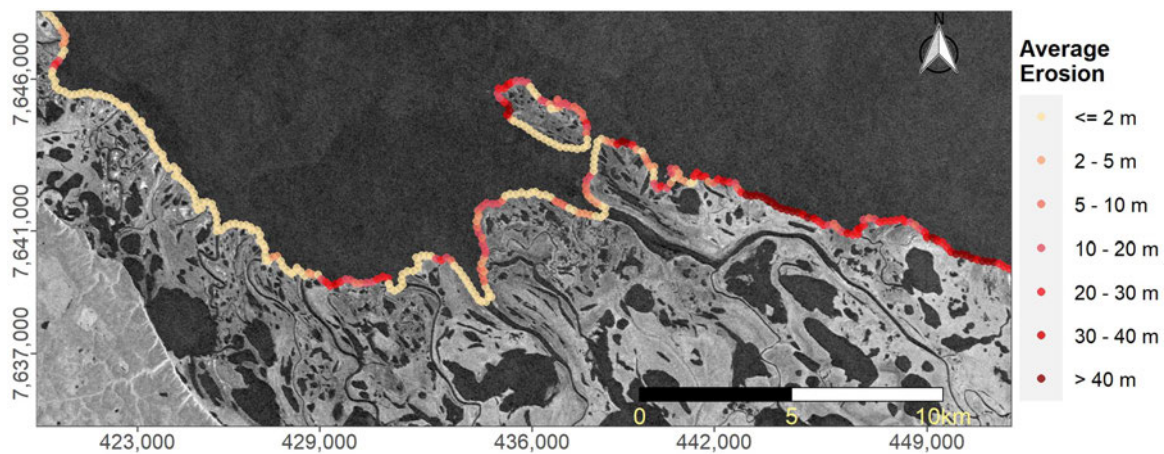
Figure 3.22: Average erosion rates between the years 2017 and 2020 for 200 m segments along a section of Shoalwater Bay, Canada (Area of Interest (AOI) 03). A Sentinel-1 (S1) median backscatter image in vertical-vertical (VV) polarisation of the year 2020 (months June–September) is used as a background image. All data is visualized in a Universal Transverse Mercator (UTM) zone 8 North projection. Modified after Philipp et al. (2022).
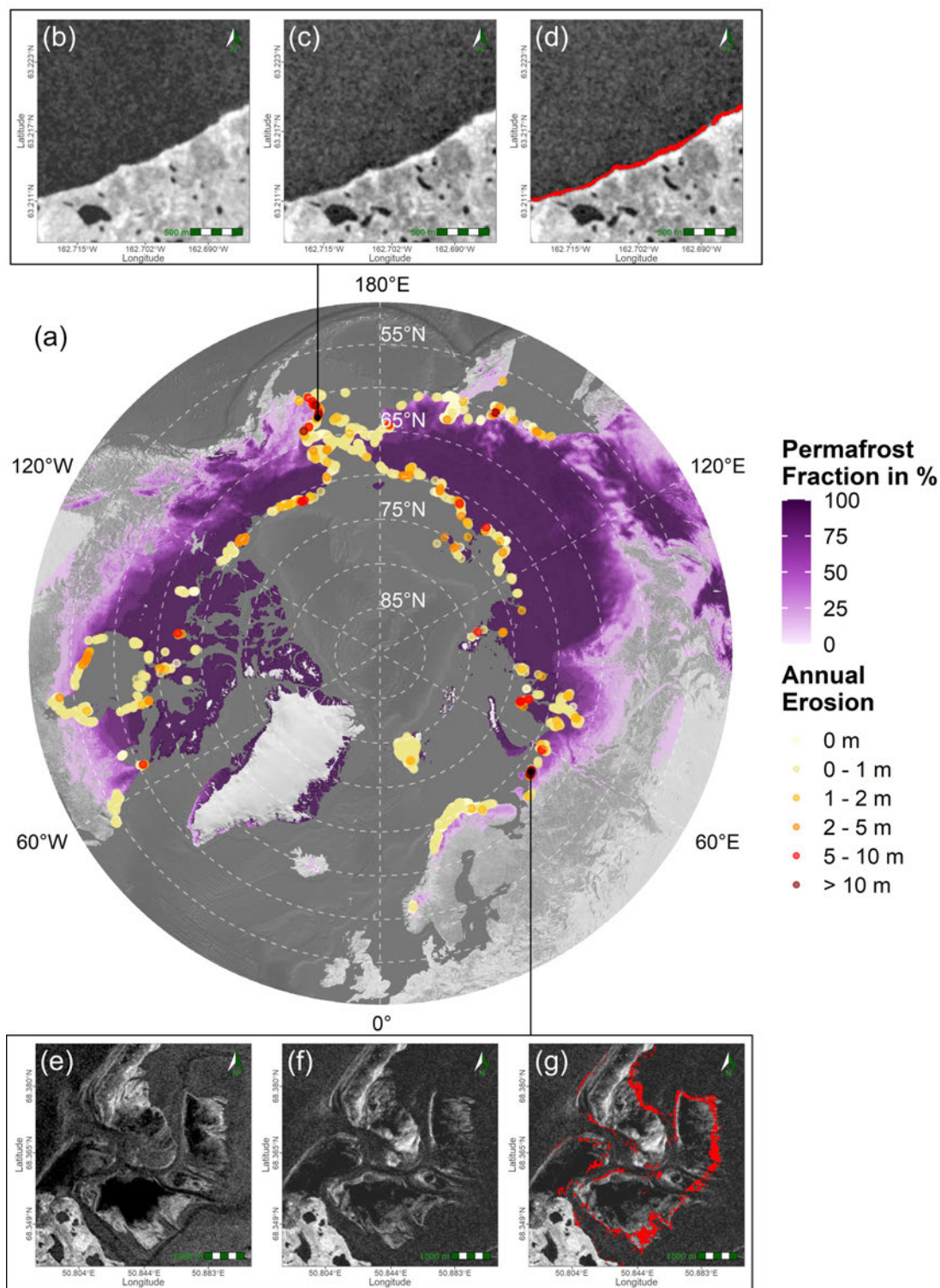
Figure 3.23: Circum-Arctic overview (**a**) and exemplary zoom-ins (**b**–**g**) on the Change Vector Analysis (CVA) based Arctic coastal erosion. Annual average erosion rates for 20 km segments are shown in (**a**). The Sentinel-1 (S1) annual (months June–September) median backscatter in vertical-vertical (VV) polarisation is shown for the years 2017 (**b**, **e**), 2021 (**c**, **f**), and again for the year 2021 with the CVA based erosion highlighted in red colour (**d**, **g**). The two zoom-ins cover a sandy delta in Russia (**e**–**g**) and a coastal area in Alaska (**c**–**f**). A shaded relief by Natural Earth (n.d.) in combination with the permafrost fraction across the Northern Hemisphere for the year 2017 based on data by Obu et al. (2021b) was used as a background map for (**a**). Modified after Philipp et al. (2023).

Table 3.10: Change Vector Analysis (CVA) derived annual build-up and erosion statistics based on 400 m segments per sea after the International Hydrographic Organization (IHO) sea areas. The average, maximum, 98th percentile, and the standard deviation (sd) are listed per sea. Build-up statistics are written in parentheses. Modified after Philipp et al. (2023).

Sea	Mean	Max	P98	SD
Arctic Ocean	0.05 m (0.01 m)	3.67 m (1 m)	0.74 m (0.33 m)	0.31 m (0.1 m)
Barents Sea	0.69 m (0.03 m)	67 m (52.67 m)	11.75 m (0 m)	3.63 m (0.97 m)
Beaufort Sea	1.12 m (0.02 m)	46 m (14.75 m)	11.5 m (0 m)	3.38 m (0.35 m)
Bering Sea	0.65 m (0.02 m)	62.5 m (19 m)	9.75 m (0 m)	3.26 m (0.28 m)
Chukchi Sea	0.19 m (0.01 m)	26 m (11.25 m)	2.52 m (0 m)	1.06 m (0.21 m)
Davis Strait	0.73 m (0 m)	38.75 m (0 m)	10 m (0 m)	3.03 m (0 m)
East Siberian Sea	0.91 m (0.03 m)	33.25 m (10 m)	9.5 m (0.25 m)	2.66 m (0.34 m)
Greenland Sea	0.09 m (0.02 m)	39.33 m (12.67 m)	0.67 m (0 m)	1.08 m (0.37 m)
Hudson Bay	0.22 m (0.02 m)	40 m (18.25 m)	2.5 m (0 m)	1.43 m (0.37 m)
Hudson Strait	0.5 m (0.05 m)	39 m (17.50 m)	7.75 m (0.25 m)	2.33 m (0.64 m)
Labrador Sea	0.05 m (0 m)	13 m (2.25 m)	0.5 m (0 m)	0.38 m (0.02 m)
Laptev Sea	0.25 m (0.07 m)	42 m (53.25 m)	2.75 m (0 m)	1.83 m (1.17 m)
Kara Sea	0.59 m (0.02 m)	51.75 m (5.5 m)	7.25 m (0 m)	2.77 m (0.22 m)
Norwegian Sea	0.01 m (0 m)	18 m (5 m)	0 m (0 m)	0.26 m (0.08 m)
Sea of Okhotsk	0.56 m (0.09 m)	43.75 m (23.75 m)	8.75 m (0 m)	2.89 m (0.93 m)
The Northwestern Passages	0.22 m (0 m)	28.25 m (3.50 m)	3 m (0 m)	1.31 m (0.09 m)

Table 3.11: Change Vector Analysis (CVA) derived annual build-up and erosion statistics based on 400 m segments per country. The average, maximum, 98th percentile, and the standard deviation (sd) are listed per country. Build-up statistics are written in parentheses. Modified after Philipp et al. (2023).

Country	Mean	Max	P98	SD
Canada	0.24 m (0.01 m)	40 m (18.25 m)	3.25 m (0 m)	1.42 m (0.27 m)
Norway (Svalbard and Jan Mayen)	0.09 m (0.07 m)	39.33 m (52.67 m)	1 m (0 m)	1.01 m (1.62 m)
Norway (Scandinavian Peninsula)	0.01 m (0 m)	18 m (5 m)	0 m (0 m)	0.21 m (0.08 m)
Russia	0.62 m (0.04 m)	67 m (53.25 m)	8.75 m (0 m)	3.01 m (0.65 m)
United States (Alaska)	0.75 m (0.01 m)	62.5 m (14.75 m)	10.25 m (0 m)	3.45 m (0.25 m)

Further comparisons were made between the generated coastal change rates based on the proposed methods and data and the ACD. The comparisons were limited to the 36.8% of segments in the ACD that overlap with the investigated coastline of this thesis. Thus, a total of 484 segments from the ACD were compared with results from this thesis. Erosion and build-up rates derived from the CVA framework were combined and average rates of coastal change based on the proposed methods and data were extracted for each segment of the ACD. A deviation of less than 0.5 m in coastal change were observed for 69.4% of segments. Differences between 0.5 1 m could be observed for 3% of segments. A further 9.9% of segments indicated differences between 1 2 m, while deviations larger than 2 m were observed for only 7.6% of segments. Figure 3.24 visualizes the retreat rates of the mentioned coastal segments as published in the Soil Atlas of the Northern Circumpolar Region (A. Jones et al., 2009).

Figure 3.24: Reference data on the retreat rates of coastal segments in the Arctic Ocean. Original figure taken from the Soil Atlas of the Northern Circumpolar Region (A. Jones et al., 2009).

3.3.3 Effects of changing tidal Levels

Changes in the MTL from four different buoy stations during the observation period June September 2020 is illustrated in Figure 3.25. Six-minutely MTL data from the buoy stations 9468756 Nome (Figure 3.25 a), 9468333 Unalakleet (Figure 3.25 b), 9497645 Prudhoe Bay (Figure 3.25 c), and 9491094 Red Dog Dock (Figure 3.25 d) are shown. The blue dots represent the S1 acquisition date-times over each region. The dashed blue line represents the average MTL at S1 acquisition date-times. The grey dashed line, on the other hand, illustrates the overall average MTL across the whole buoy data set. Despite variations in the MTL of up to 2.4 m across the observed regions and time frame, average MTL levels from S1 acquisition date-times are generally similar to the overall average MTL levels based on the full buoy data set per region. Observed deviations were thereby 0.09 m for Nome, 0.23 m for Unalakleet, 0.04 for Prudhoe Bay, and 0.02 m for Red Dog Dock. The amount available S1 images were 20 for Nome, 16 for Unalakleet, 22 for Prudhoe Bay, and 39 for Red Dog Dock. Thus, a larger deviation can be observed for lower quantities of available SAR scenes.
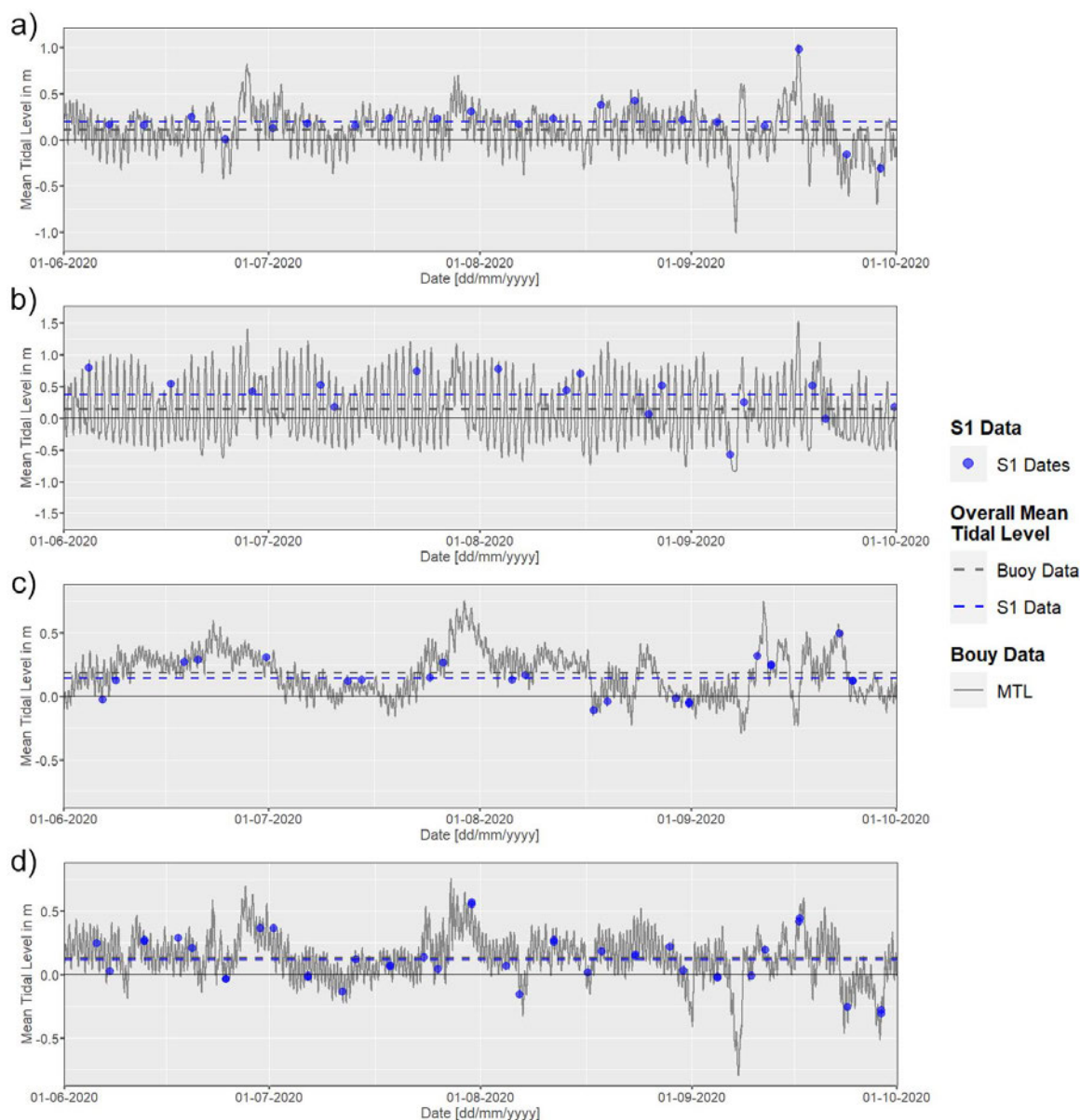
Figure 3.25: Mean Tidal Level (MTL) in meters based on buoy data from June 1st–September 30th 2020. The temporal frequency of measurements is hereby six minutes. Data from the stations 9468756 Nome (**a**), 9468333 Unalakleet (**b**), 9497645 Prudhoe Bay (**c**), and 9491094 Red Dog Dock (**d**) is shown. Buoy data was accessed via the National Oceanic and Atmospheric Administration (NOAA) (2022b). The blue points represent the MTL at Sentinel-1 (S1) acquisition times for each respective region. The dashed lines represent the overall MTL from June–September based on the tidal levels at the S1 acquisition times (blue line), and the full buoy data set (grey line). Modified after Philipp et al. (2023).

3.4 Discussion

This study proposed a novel circum-Arctic monitoring strategy for assessing the annual rates of erosion and build-up of permafrost coastlines. A high-quality Arctic shoreline product was created using DL CNNs and S1 GRD C-Band SAR data in IW

swath mode. Furthermore, S1 backscatter imagery in combination with CVA allowed for the quantification of coastal change with high spatial resolution and on an annual basis. The following section discusses the findings of the proposed data and methods. The applicability of SAR data, DL, and CVA in Arctic coastal environments is further reflected. In addition, identified coastal change rates are compared with numbers published in previous literature. Furthermore, limitations and future potentials for the proposed framework are provided.

3.4.1 Backscatter Behaviour over Land and Sea

The applicability of S1 backscatter data for analysing coastal erosion is limited by ambiguities in the scattering behaviour of single SAR images (Bartsch, Ley, et al., 2020). Nevertheless, the amount of speckle and other noise factors could be significantly reduced by working on annual (June September) backscatter composites, instead of using single observations. Combining multiple images into one composite further reduced the geolocation uncertainty which may be present in single scenes (Schubert et al., 2015, 2017). As this study aimed to investigate coastal changes at a spatial resolution of 10 m, reducing any noise and uncertainty factors is crucial in order to accurately measure coastal change.

Median backscatter over land was observed to be generally higher compared to the backscatter signal over water. In contrast, a higher sd in the backscatter were identified over water vs. terrestrial areas within the temporal window June September (Figure 3.4). Rough terrain leads to diffuse scattering behaviour and therefore higher backscatter intensities, whereas water areas are associated with the specular reflection of the SAR signal and therefore with generally lower backscatter values (Ulaby et al., 1982; Richards et al., 2009). This discrepancy in backscatter characteristics is reflected in the median backscatter images. At the same time, the water surface in the sea is characterized by different wave actions and therefore also not perfectly flat. Wind-driven capillary waves are hereby a type of wave, that relies on the tension of the water's surface (Richards et al., 2009). Gravity waves, on the other hand, are subject to gravitational forces and act as the counterpart to mass disturbances caused by wind-driven waves (Richards et al., 2009; Lighthill & Lighthill, 2001). Each SAR scene detects a unique wave constellation in the sea for a given region, and therefore a unique backscatter signal. This variability in the texture of the surface water results in higher sd backscatter values compared to the relatively stable terrestrial surface texture within the temporal observation window. In addition to the variation in the texture of the surface water, a higher sd over water can also be attributed to the logarithmic transformation (Equation 3.2) that has been applied to the SAR GRD

backscatter images. The closer the values are to 0 in the power scale unit the larger the variation after logarithmic transformation to dB scale. Since values over water are observed to be generally lower compared to values over terrestrial areas, variations over water areas appear amplified when working with backscatter coefficient sigma nought (σ^0) in the unit dB.

3.4.2 Deep Learning for terrestrial-Sea Segmentation

The inverse behaviour of the median and the sd backscatter could be exploited for the creation of a high quality DL coastline product by using annual pseudo-RGB SAR composites as training data (Figure 3.4). Nine different U-Net architectures were employed for the segmentation between sea and terrestrial area (including inland rivers and lakes). One limitation of applying CNNs is the identification of the optimal network depth required for a specific task (Zhou, Siddiquee, et al., 2019). While a traditional approach in machine learning requires the selection of relevant input features by the user (also called feature engineering) for best possible model performance (Heaton, 2016), a CNN is capable of identifying relevant features within the input data by itself (LeCun et al., 2015). Still, the selection of a network of appropriate depth and architecture to successfully assess and solve the complexity of a given task remains challenging (Zhou, Siddiquee, et al., 2019). By merging the results of nine different U-Net models, which feature various architectures and depths, a representative and reliable prediction per pixel is achieved. Another common limitation of CNN-based algorithms is the vast amounts of data required for training the network (C. Tang et al., 2020). Several measures were taken to overcome this limitation. First, pre-trained models were used, which were trained on the ImageNet database (14 Mio. images). Second, augmentation was applied to images derived from the manually digitized sites, which increased the amount of reference data for these areas seven-fold. Lastly, OSM data was utilized as an additional source of reference data for further network training. Despite the frequently communicated fluctuations in data quality of OSM, the massive amount of additional training material outweighed the variations in quality of the data. In comparison to linear regression models, Neural Networks are identified to be more resistant to errors (Bansal et al., 1993). Despite being exposed to one-third erroneous training data, CNNs are reported to achieve accuracies of 90% (Rozhnova, 2021). Some authors even observed moderate performance gains by adding small amounts of errors ranging from 5 15% during the training process of the Neural Network (B. Klein & Rossin, 1999).

Minimum training accuracies across all models of ≥ 0.9838 and validation accuracies of ≥ 0.9785 were observed after training on both the manually digitized sites and the

OSM sites, which indicates a largely successful segmentation between terrestrial area and sea across all models (Table 3.5). Similarly high accuracy statistics were also observed within a 500 m buffer around the reference coastline, in which overall accuracy values of ≥ 0.944 were observed for both training and validation sites. There were no significant differences in the accuracy metrics between the validation and training sites. A median deviation of ± 6.3 was measured between the final DL-based coastline product and the reference line across the manually digitized sites. In case of the OSM sites, a median deviation of ± 29.6 m was identified. The greater discrepancy between the DL coastline product and the reference data from OSM sites can be attributed to the previously mentioned fluctuations in OSM data quality and the greater variety of coastline types represented by OSM. While the DL product outperformed the OSM data set in many regions by providing more accurate and up-to-date information, OSM retained many small islands (<0.2 km^2) that were excluded during post-processing in the DL product. Moreover, OSM provides a larger data coverage due to the limited availability of S1 data for generating the DL product in some Arctic regions. Fewer excluded islands might result from lowering the minimum threshold for object removal, but at the cost of increasing noise levels.

Uncertainties in the segmentation were observed for flat, sandy shores, where it is challenging to clearly distinguish between the sea and the land. River deltas constitute another source of uncertainty, as the networks have trouble in some cases to separate the end of a river and the beginning of a river's mouth. Despite being exposed to challenging environments and limited data availability, the proposed framework was still capable in generating a high quality circum-Arctic coastline product. All U-Net models showed good performance in the differentiating between sea area and inland waters, including rivers and lakes. The left-over lakes after combining the output results of each network could be removed by applying a closing holes algorithm. The manually digitized reference coastline is based on information from high resolution Google Earth imagery, as well as S1 and S2 satellite data. Combining over 1000 km of manually referenced coastline based on high resolution (≥ 10 m) data with additional reference data based on OSM was classified as a reasonable approach in the context of generating a circum-Arctic product.

The generated DL coastline product featured a median accuracy of ± 6.3 to the manually digitized reference data and therefore outperformed other coastline products, which are openly available on a circum-Arctic scale (Table 3.8). The coastline product from CAVM is based on the Digital Chart of the World (DCW) dataset, which was released in 1992 at a spatial scale of 1:1,000,000 (Langaas, 1995). It was one of the most complete world databases at the time, but it hasn't been updated since 1992. Furthermore, the initial DCW coastline product was further simplified by, e.g., the

combination of two lines in proximity (500 m) to each other, and by removing islands that are smaller than 49 km² (Alaska Geobotany Center, 2012). The GSHHG dataset which was formerly known as the Global Self-consistent, Hierarchical, High-resolution Shorelines (GSHHS), received its last update in 2017 and is based on the Atlas of the Cryosphere (AC), the CIA World Data Bank II (WDBII), and the World Vector Shorelines (WVS) dataset (Bennett, 2010). As previously stated, OSM constitutes a non-commercial project that is community driven (Bennett, 2010). Since OSM featured the highest mean and median accuracy out of the three mentioned publicly available datasets (Table 3.8), it was chosen as an additional training source for the DL work-flow. At the same time, largest maximum and standard deviation values were also observed for the OSM dataset, which reflects its varying quality across different regions. The proposed framework of generating a S1 and DL-based coastline product, provides both high resolution and up-to-date information about the coastal position on a circum-Arctic scale.

Good agreement between the overall average MTL based on six-minutely buoy data and the average MTL based on S1 acquisition times can be reported for the observation period June September 2020 (Figure 3.25). It was also observed, that a larger amount of available satellite scenes for a given region led to smaller deviations between the total average MTL and the average MTL at satellite acquisition times. Nonetheless, comparisons with a higher amount and spatially more distributed buoy data are needed for thorough investigations on the impact of tidal changes on the generated satellite composites. Still, the observed results highlight the impact of the satellite data availability on the quality of the generated coastline product. Especially flat and sandy coasts are hereby of concern, where changes in the tidal level may have a significant impact on the location of the transition zone between land and the sea. The number of available S1 GRD scenes in IW swath mode are therefore a valuable proxy for assessing the quality of the output products for a given region (Figure 3.19).

3.4.3 Feasibility of Change Vector Analysis on Coastal Change

The inverse behaviour of the sd and median backscatter for terrestrial vs. sea areas was also employed in the analysis on coastal change via a CVA approach. In addition to avoiding an accumulation of errors from individual input classifications, CVA tends to be less computationally demanding and more flexible when compared to detecting changes via a post-classification method (J. Chen et al., 2010; C. Huang et al., 2016). Threshold values of 0.6 for build-up and 0.35 for erosion were identified as most suitable based on the manually digitized reference sites. A deviation of -10.3 m was measured between the reference data and the CVA change maps after applying

the aforementioned threshold values. Thus, actual coastal change rates are likely underestimated by a small margin for the sake of keeping the amount of left-over noise after post-processing as low as possible. Nevertheless, depending on the amount of available satellite data and coastal type, a different threshold might be better suited for a specific region. The magnitude of change information is thereby a valuably quality layer to manually adjust the threshold value for a given area (Figure 3.21).

An overall maximum annual erosion rate of up to 62.5 m based on segments covering 400 m of coastline was identified in Russia, while the overall average erosion rate on a country basis was highest in the USA (Alaska) with 0.75 m per year. Both weakest build-up and erosion were identified in Norway. The mostly lithified coasts, which are less vulnerable to erosion processes, are thereby likely the reason (Lantuit et al., 2012). Highest average build-up rates per year were observed in Svalbard and Jan Mayen. Movements of small glaciers, which were not covered by the GLIMS database, might hereby explain these numbers. Furthermore, accumulations of sandy deposits along the coastline are another source of build-up across the Arctic coastline.

Overall good agreement between the CVA-based erosion rates and numbers published in previous literature can be reported. B. M. Jones et al. (2018) and J. Wang et al. (2022) identified erosion along Drew Point in Alaska at rates of 30.8 51.4 m and 6.7 22.6 m per year, respectively. This matches the findings from the proposed methods and data in this thesis, which suggest annual erosion rates of 20 50 m for the same area. Annual erosion of 12.5 15 m were observed for the Bell Bluff site on Herschel Island in Canada based on the CVA approach. Fittingly, Obu, Lantuit, Grosse, et al. (2017) also observed maximum retreat rates of the same shoreline ranging from 10 17 m and covering the temporal window 2012 2013. The authors further observed erosion rates of 0 1 m along Kay Point near Herschel Island (Obu, Lantuit, Grosse, et al., 2017). In accordance with this finding, the CVA approach also suggests no erosion for the same region. Irrgang et al. (2018) identified average erosion rates of 0.7±0.2 m per year for a section of Yukon coast in Canada with a length of 210 km by utilizing both high resolution satellite data and historical aerial imagery, covering a time-span from the 1950s to the year 2011. Erosion rates in the same order of magnitude (0.5 m per year) were observed via the proposed data and methods in this thesis. Relatively small coastal retreat rates of <1 m per year were observed for the west coast of the Buor Khaya Peninsula in Russia by Günther et al. (2013), which matches with numbers of this study. Further comparisons between the CVA-based coastal change rates and numbers present in the ACD suggest good agreement (deviations <0.5 m) for two-thirds of the overlapping segments. Overall strongest coastal erosion was observed for the Beaufort Sea in both the ACD and the CVA products. Deviations between coastal change rates proposed in the ACD and

coastal change rates generated by CVA can be attributed to uncertainties in both products, differences in the spatial resolution of applied reference data, and differences in observed temporal examination periods.

3.4.4 Limitations and future Potentials

The presented data and methods constitute a potent approach in quantifying annual coastal build-up and erosion rates at high spatial resolution. Nevertheless, the quality and applicability of the proposed framework strongly depends on the available frequency of S1 GRD SAR backscatter data in IW swath mode, which differs across space and time (European Space Agency, n.d.-e; Alaska Satellite Facility, n.d.). Spatial variations in the data availability is visualized in Figure 3.2. While Europe features a relatively high data frequency, the Canadian archipelago and large portions of Russia are associated with poor S1 data coverage. Due to an anomaly on-board the S1B satellite, data is currently generated by S1A only since December 23rd 2021 (European Space Agency, n.d.-d). As a consequence, data availability is further limited until the launch of S1C, which might impair the quality of current observations. Moreover, SAR-specific challenges, such as ambiguities in the backscatter behaviour and geometric distortions in SAR images in the form of foreshortening, layover, and shadow, may further limit the applicability of the proposed framework for some locations. At the same time, large parts of uncertainties in the geolocation, noise from backscatter ambiguities, and the effects of changing tidal levels were minimized by using annual composites instead of individual scenes as a foundation of the analyses. Several quality layers are provided on a per-pixel-basis, including the absence or presence of glaciers, the level of agreement between the individual model output classifications (Figure 3.18), the number of sea ice days (Figure 3.8), and the amount of available S1 GRD SAR scenes in IW swath mode. The mentioned quality layers may thereby contribute as valuable proxies for assessing the quality and applicability of the proposed data, methods, and output products.

Investigations on Arctic coastal change rates were limited to areas that feature eleven or more scenes and less than 50% sea-ice days during the months June September. This way, the amount of noise could be further reduced, while at the same time restricting the analysis to 42,992 km ($\approx$27%) of the original 161,600 km of observed Arctic coastline within the permafrost domain. It is noteworthy to further mention that quantifying coastal change is only meaningful if the change rates between two observed years are larger then the pixel size of the input data, which is 10 m in case of the applied S1 GRD data in IW swath mode. The aforementioned threshold values for the CVA approach led to best results across the manually digitized reference sites.

However, the ideal threshold value may deviate across different regions depending on the S1 data availability, sea ice duration, and present coastal type. In particular, areas with low data frequency and long sea-ice durations may require adjustments to the threshold values for optimal results. As previously mentioned, the magnitude of change layer is hereby a powerful proxy for manual adjustments of threshold values for a potential improvement in the change detection. The analysis of lengthier time series will be possible with future data. In this context, temporal observation windows for generating SAR composites could be extended over two years, especially for areas with limited data availability. Nevertheless, larger temporal observation windows also lead to greater variations across the individual scenes for creating the composite. The intersection between the observed coastal erosion rates with information about the ground ice content, lithification stage of the coastline, and other geomorphological parameters, as present in the ACD by Lantuit et al. (2012), could further deepen our knowledge and help us to understand the mechanics of Arctic coastal erosion of permafrost coasts. Lantuit et al. (2008) hereby highlighted the influence of ground ice content on the coastal retreat rates. The authors identified a weak but statistically significant correlation ($r = 0.48$ and $\alpha = 0.01$) when performing a linear regression analysis between the ground ice content and the coastal retreat rates based on 545 coast segments of the ACD database across the Arctic. The authors further observed a similar but slightly lower correlation value when comparing annual volume loss rates with ground ice content ($r = 0.41$). It was emphasized that, despite the statistical analyses indicating only a subtle correlation, ground ice plays a significant role as a primary contributor to the erosion process, since the process of eroding Arctic coastlines is influenced by multiple factors (Lantuit et al., 2008). Also worth mentioning are the potential effects of rising sea levels (Shadrick et al., 2022) and the Fennoscandian land uplift (Ekman, 1996) on the present methods and data for long-term investigations. More detailed focus should be put on these topics in future analyses to fully asses their impact on the proposed framework. Lastly, even though the suggested approaches and data were only implemented and validated in the Arctic permafrost region, there is a strong likelihood that the proposed coastal monitoring strategy can be adapted to other latitudes.

This thesis focused on the potential of S1 GRD SAR backscatter data in IW swath mode for monitoring Arctic coastal environments. However, the combination of the S1 imagery with SAR data from other satellite missions could be a potent approach in future analyses. Moreover, the combination of SAR and optical data constitutes another promising technique in increasing both the data quantity and amount of information per pixel. Especially data from the Landsat legacy and S2 satellites are thereby attractive data sources, as they provide fairly high spatial resolutions and

observation frequencies. On the one hand S2 satellites provide data of higher spatial resolution then Landsat satellites. On the other hand, significantly longer time series observations are possible with Landsat data. Figure 3.26 visualizes annual (June September) median RGB composites for all years with available Level 2, Collection 2, Tier 1 surface reflectance data from the satellites Landsat 4, 5, 7, and 8 over Drew Point in Alaska. Images were masked from snow/ice and cloud/cloud shadows based on the associated quality layer per scene (Department of the Interior - U.S. Geological Survey, 2022). First images that cover this were taken in 1985, although images are not available for all years from this point on forward. Several composites feature artefacts from insufficient cloud and snow/ice masking, as well as pixels with missing data after masking. Moreover, the failure of the Scan Line Corrector (SLC) of the Enhanced Thematic Mapper Plus (ETM+) sensor on-board Landsat-7 in 2003 (Alexandridis et al., 2013) is visible in the form of stripes within the median composites. Figure 3.27 visualizes annual (June September) median RGB composites for available S2 Level-2A surface reflectance data over the same region. The images were also removed from clouds and snow by using the associated scene classification layers (European Space Agency, 2016). However, all annual S2 composites feature artefacts within the sea in the form of remaining sea ice content which were not covered by the associated scene classifications. Figure 3.28 illustrates Pseudo-RGB backscatter composites for all years with available data. Annual Pseudo-RGB composites were created identically as described in section 3.2.2. Compared to optical imagery, no data gaps or large scale artefacts can be identified. Since composites are made from scenes from different relative orbits, some delineations of individual scenes with different extents can partly be recognized. A comparison between the three mentioned datasets is visualized in Figure 3.29. The zoom-ins (Figure 3.29 d f) highlight the differences in the spatial resolution. The exact delineation of the coastline is more clearly visible in case of S1 and S2 in contrast to the Landsat 8 median composite. Remaining artefacts from insufficient cloud and sea-ice masking are potential limitation factors for a successful application of optical imagery. Therefore, additional efforts in cloud and sea-ice masking are necessary to achieve best possible results. At the same time, sea-ice will likely continue to be a challenging factor for both optical and SAR data, especially for areas with long sea-ice durations. Nonetheless, the combination of data from different satellites constitutes a promising approach in improving on the quality and extent of the proposed coastal monitoring framework.

Figure 3.26: Annual median (June–September) Red-Green-Blue (RGB) images of Drew Point, Alaska derived from the Landsat Level 2, Collection 2, Tier 1 surface reflectance data. Imagery from the satellites Landsat 4, 5, 7, and 8 were used to compute the annual median composites. Black pixels represent areas with no data after cloud-, cloud shadow-, and snow/ice-masking. All data is visualized in a Universal Transverse Mercator (UTM) Zone 5 North projection. The number in the upper left corner of each image represents the displayed year.
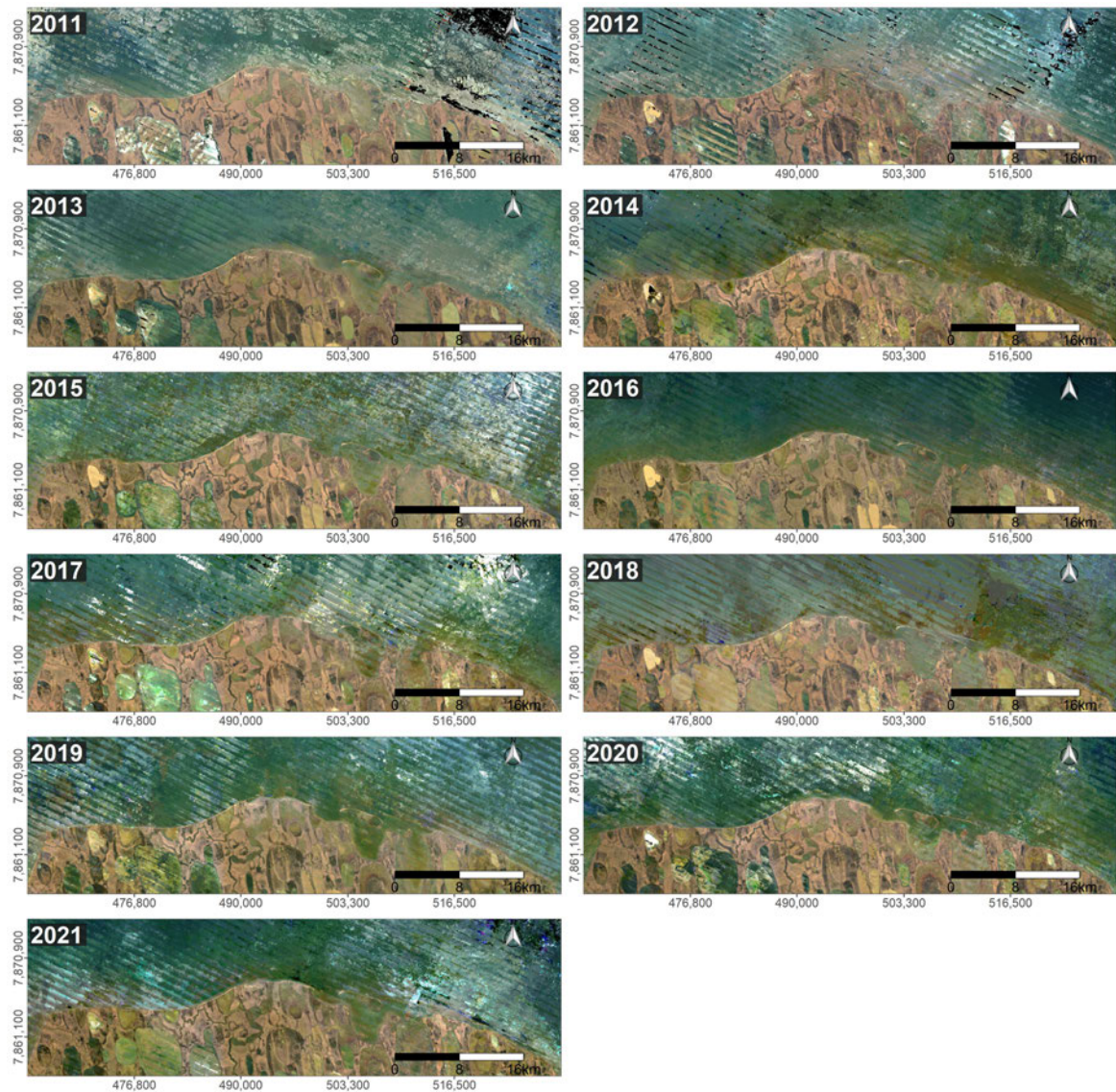
Figure 3.26: Continued.

A comparison between the three mentioned datasets is visualized in Figure 3.29. The zoom-ins (Figure 3.29 d f) highlight the differences in the spatial resolution. The exact delineation of the coastline is more clearly visible in case of S1 and S2 in contrast to the Landsat 8 median composite. Remaining artefacts from insufficient cloud and sea-ice masking are potential limitation factors for a successful application of optical imagery. Therefore, additional efforts in cloud and sea-ice masking are necessary to achieve best possible results. At the same time, sea-ice will likely continue to be a challenging factor for both optical and SAR data, especially for areas with long sea-ice durations. Nonetheless, the combination of data from different satellites constitutes a promising approach in improving on the quality and extent of the proposed coastal monitoring framework.

Figure 3.27: Annual median (June–September) Red-Green-Blue (RGB) images of Drew Point, Alaska derived from Sentinel-2 (S2) Level-2A reflectance data. All data is visualized in a Universal Transverse Mercator (UTM) Zone 5 North projection. The number in the upper left corner of each image represents the displayed year.
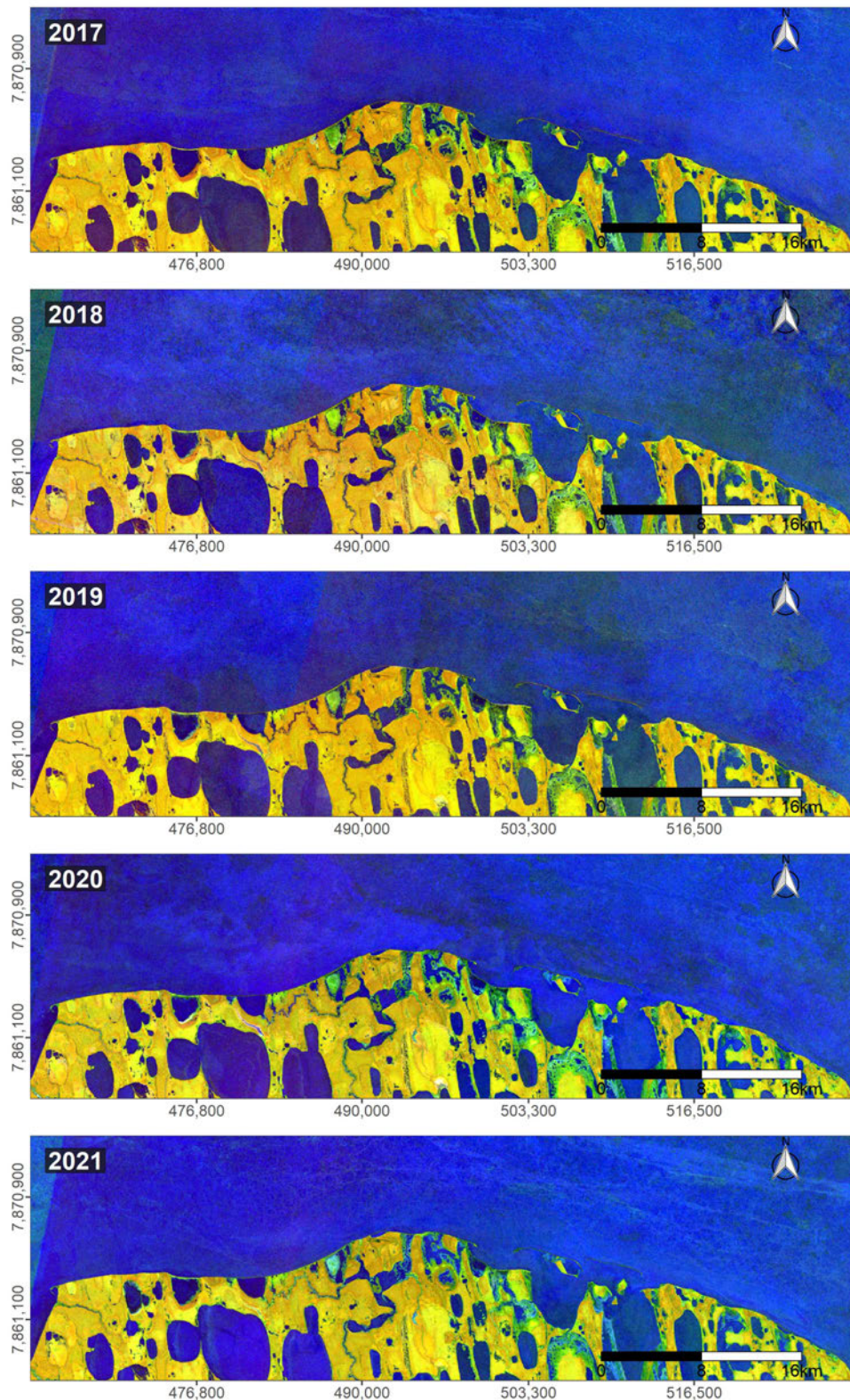
Figure 3.28: Annual median (June–September) Pseudo Red-Green-Blue (RGB) images of Drew Point, Alaska derived from Sentinel-1 (S1) Ground Range Detected (GRD) backscatter data in Interferometric Wide (IW) swath mode. Pseudo-RGB images consist of vertical-horizontal (VH) (red channel), median vertical-vertical (VV) (green channel), and standard deviation (sd) VV (blue channel) backscatter. All data is visualized in a Universal Transverse Mercator (UTM) Zone 5 North projection. The number in the upper left corner of each image represents the displayed year.
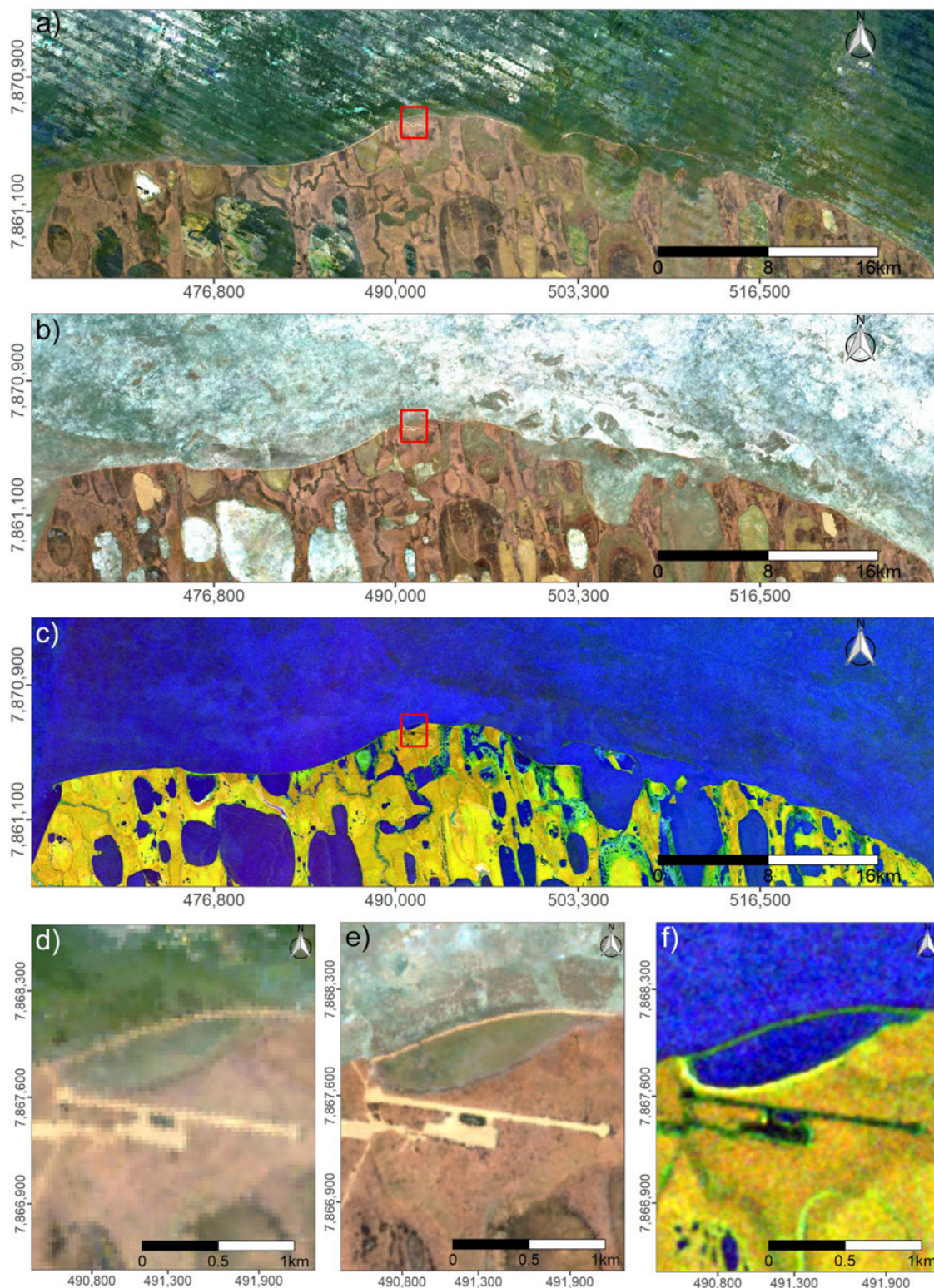
Figure 3.29: Median Red-Green-Blue (RGB) images (June–September 2020) of Drew Point, Alaska based on optical Landsat 8 (**a**, **d**), Sentinel-2 (S2) (**b**, **e**), and Synthetic Aperture RADAR (SAR) Sentinel-1 (S1) (**c**, **f**) imagery. A true colour visualization is shown for Landsat-8 (**a**, **d**) and S2 (**b**, **e**). S1 data (**c**, **f**) is illustrated in Pseudo-RGB using median vertical-horizontal (VH) (red channel), median vertical-vertical (VV) (green channel), and standard deviation (sd) VV (blue channel) backscatter. The red rectangle in sub-figures **a**–**c** represents the zoom-in areas visualized by sub-figures **d**–**f**. All data is visualized in a Universal Transverse Mercator (UTM) Zone 5 North projection.

Amplified erosion rates for Arctic permafrost coasts are frequently reported in recent years and erosion rates are further expected to continuously increase in future years (Günther et al., 2013; B. M. Jones et al., 2018, 2009; Irrgang et al., 2022). An interdisciplinary and coordinated effort of the local population, stakeholders, policymakers, and scientists alike are necessary to tackle the challenge of rapidly changing coastlines (Irrgang et al., 2022). Within this context, the presented DL circum-Arctic coastline product and CVA-based coastal change quantification may provide a valuable contribution towards addressing this issue.

3.5 Summary

This chapter introduced a novel framework for quantifying annual build-up and erosion rates of permafrost coasts on a circum-Arctic scale and with a spatial resolution of 10 m by combining Deep Learning (DL) and Change Vector Analysis (CVA) with Sentinel-1 (S1) Ground Range Detected (GRD) Synthetic Aperture RADAR (SAR) backscatter images in Interferometric Wide (IW) swath mode. Annual composites in the form of standard deviation (sd) and median backscatter were implemented for the computation of a DL-based circum-Artic coastline product, covering 161,000 km of coastline. The annual composites further served as a basis for the detection of coastal changes via CVA. The following main conclusions can be drawn:

- Higher median backscatter was observed over land compared to water, whereas the sd backscatter proved to be higher over water and lower over land. Therefore, a change from high median to high sd backscatter can be classified as a transition from terrestrial area to water and thus, erosion.

- The inverse behaviour of the sd and median backscatter could be successfully implemented for the generation of both a DL-based high quality Arctic coastline product and the quantification of coastal change via CVA.

- OpenStreetMap (OSM) proved to be a valuable asset for additional training of the Convolutional Neural Networks (CNN) U-Net architectures, despite variations in its data quality.

- The combination of nine different U-Net architectures allowed for the generation of a high quality coastline product covering 161,600 km of Arctic permafrost coastline. The median deviation to 1038 km of manually digitized reference coastline proved to be ±6.3 m.

- A good level of agreement between the overall average Mean Tidal Level (MTL) from six-minutely buoy data and the average MTL based on the respective S1

acquisition times for each buoy location can be reported. The lower the number of available S1 scenes, the higher the deviation between the average MTL at S1 acquisition times and the actual average MTL.

- The quality of the output products from the proposed data and methods strongly depend on the local sea ice duration, the present coastal type, and the number of available satellite scenes for a given region.

- Strongest average erosion on a country basis was observed for the United States of America (USA) (Alaska) with 0.75 m per year, followed by Russia with 0.62 m per year. The weakest average erosion per country and per year of was observed in Norway with 0.01 m. Maximum annual erosion rates based on 400 m coastal segments were identified in Russia (67 m), followed by Alaska (62.5 m). Out of all seas, the Beaufort Sea was associated with the highest average erosion of 1.12 m per year. Numbers are thereby based on all segments within a country/sea, even if no coastal change is present.

- Over the entire investigated Arctic coastline, 12.24% demonstrated an average annual erosion rate of 3.8 m and a combined annual eroded land area of 17.83 km^2, whereas 1.05% of the coastline indicated an average yearly build-up rate of 2.3 m and a combined area of 1.02 km^2 in annual build-up.

- Several quality layers, including the presence and absence of glaciers, the level of agreement between individual output classifications of different DL models, the sea-ice duration, and the number of available S1 GRD scenes in IW swath mode are available on a per-pixel basis and may be used as valuable proxies for the evaluation of the product quality and applicability of the presented data and methods.

The proposed methods and data proved to be very effective in both generating a high-quality and circum-Arctic coastline product and for quantifying annual change rates of Arctic permafrost coastlines. The framework may also be transferred to different latitudes for investigating coastal changes. The output products might also be employed to estimate carbon emissions and determine the quantity of lost frozen ground due to the erosion of permafrost coastlines. The CVA-based magnitude of change maps, the related quality layers, and the final circum-Arctic DL coastline will all be made publicly available through the German Aerospace Center (DLR) Earth Observation Center (EOC) Geoservice.

Chapter 4

Estimating Permafrost and Carbon Loss based on Arctic coastal Erosion—An experimental Framework

The following chapter proposes a first experimental approach for estimating the amount of permafrost loss and carbon release as a consequence of eroding permafrost coastlines. The previously extracted information on circum-Arctic coastal erosion rates via S1 backscatter data and CVA was combined with information on surface elevation, permafrost fraction, Active Layer Thickness (ALT), and soil Organic Carbon Stocks (OCS) for quantifying the loss of permafrost and carbon release.

4.1 Input Data

A variety of different datasets were involved for both the quantification of permafrost loss and the release of formerly stored soil organic carbon contents as a consequence of eroding coastlines within the permafrost domain. The previously generated annual and circum-Arctic erosion rates covering the years 2017 2021, as described in detail in the chapter 3, were used as a basis for this experimental framework. Information on the duration of sea ice cover via the ASI dataset (Spreen et al., 2008), and the glacier coverage based on the GLIMS dataset (Raup et al., 2007) were utilized for further restringing the extent of the analysis. In addition to the erosion rates themselves, information on the surface elevation was incorporated via the ArcticDEM Version 3 Mosaic DEM (Porter et al., 2018), and the Copernicus GLO-30 DEM (European Space Agency, Sinergise, 2021). Details on the permafrost presence was available in the form of the Climate Change Initiative (CCI) permafrost fraction dataset by Obu et al. (2021b). Information on the Active Layer Thickness (ALT) was

included via the CCI Active Layer Thickness (ALT) data by Obu et al. (2021a). Lastly, information on the soil organic carbon content was accessed via the SoilGrids250m 2.0 - Soil OCS dataset (Poggio & de Souse, 2020) and used as a basis for the quantification of carbon emissions. Details on each implemented dataset, including the data type, spatial resolution, and the temporal frequency are listed in Table 4.1.

Table 4.1: List of utilized datasets within the framework of this chapter. The column "Temporal Coverage & Resolution" provides information about the temporal window of used data. The frequency of available data within this time span is in shown in parentheses.

Name	Data Type	Spatial Resolution	Temporal Coverage & Resolution	Reference
ArcticDEM Version 3 Mosaic	Raster	2 m	2016	Porter et al. (2018)
ARTIST Sea Ice (ASI) Arctic Sea Ice Concentration	Raster	3125 m	2017–2021 (daily)	Spreen et al. (2008)
Circum-Arctic erosion rates per 200 m segment	Vector	-	2017–2021	Philipp et al. (2023)
Climate Change Initiative (CCI) Active Layer Thickness (ALT)	Raster	927 m	2017–2019 (annual)	Obu et al. (2021a)
Climate Change Initiative (CCI) Permafrost Fraction	Raster	927 m	2017–2019 (annual)	Obu et al. (2021b)
Copernicus GLO-30 Digital Elevation Model (DEM)	Raster	30 m	2011–2015	European Space Agency, Sinergise (2021)
Global Land Ice Measurements from Space (GLIMS) glacier database	Vector	-	2022	Raup et al. (2007)
Sentinel-1 (S1) Ground Range Detected (GRD) Interferometric Wide (IW) swath	Raster	10 m	2017–2021 (up to 6 days)	ESA Communications (2012)
SoilGrids250m 2.0 - Soil Organic Carbon Stocks (OCS)	Raster	250 m	1905–2016	Poggio & de Souse (2020)

4.1.1 Permafrost Extent

The CCI permafrost fraction dataset (version 3.0) is available on an annual basis from 1997 2019 and with a spatial resolution of ∼927 m (Obu et al., 2021b). The data is generated via the TTOP model, which constitutes an equilibrium state model, and is further based on satellite-derived land surface temperature information, land cover data from the ESA CCI Landcover project, and ERA-Interim climate reanalysis data (Obu et al., 2019). Figure 1.1 illustrates the permafrost fraction across the Northern Hemisphere for the year 2017.

4.1.2 Active Layer Thickness

Identical to the CCI permafrost fraction dataset, information on the ALT was available at the same spatio-temporal resolution, temporal coverage, and also based on satellite-derived land surface temperature data as well as ERA-Interim climate reanalysis data (Obu et al., 2021a). Figure 4.1 illustrates the average ALT from 2017 2019 across the Northern Hemisphere. Although the dataset is originally available as continuous data type, it was converted to a discrete scale for visualization purposes. Actual analysis was conducted with the original continuous data type.
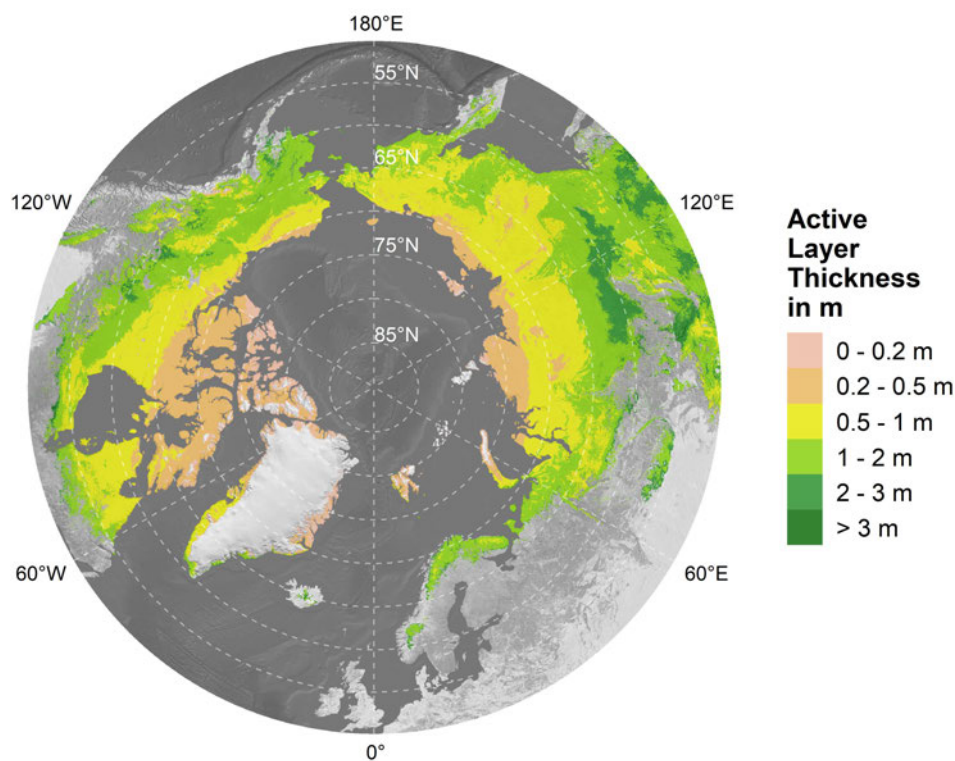
Figure 4.1: The average Active Layer Thickness (ALT) between 2017–2019 across the Northern Hemisphere based on data by Obu et al. (2021a). The continuous data was converted to a discrete scale for this visualization. A shaded relief by Natural Earth (n.d.) was used as a background map.

4.1.3 Digital Elevation Models

The ArcticDEM mosaic constitutes a high resolution DEM made up from pairs of optical stereo satellite imagery of sub-meter (0.32 0.5 m) resolution derived from WorldView-1 3 and GeoEye-1 (Polar Geospatial Center, 2023). The data was accessed in GEE which provides individual stripes within the temporal window 2009 2017, while the mosaic is a collection of strips that have been feathered and blended to reduce artefacts and voids (Google Developers, n.d.-b,-a). The Copernicus DEM GLO-30, on the other hand, is a global DEM with a spatial resolution of 30 m and based on the "WorldDEM", which in turn was generated via RADAR data from the TanDEM-X mission with acquisition times between 2011 2015 (European Space Agency, Sinergise, 2021). Mainly high resolution surface elevation data from the ArcticDEM product was used for estimating volume loss. For areas with no available ArcticDEM data, the Copernicus GLO30 DEM was used, instead. Figure 4.2 highlights the regions with available ArcticDEM data, and areas where surface elevation information from the GLO30 product was utilized.
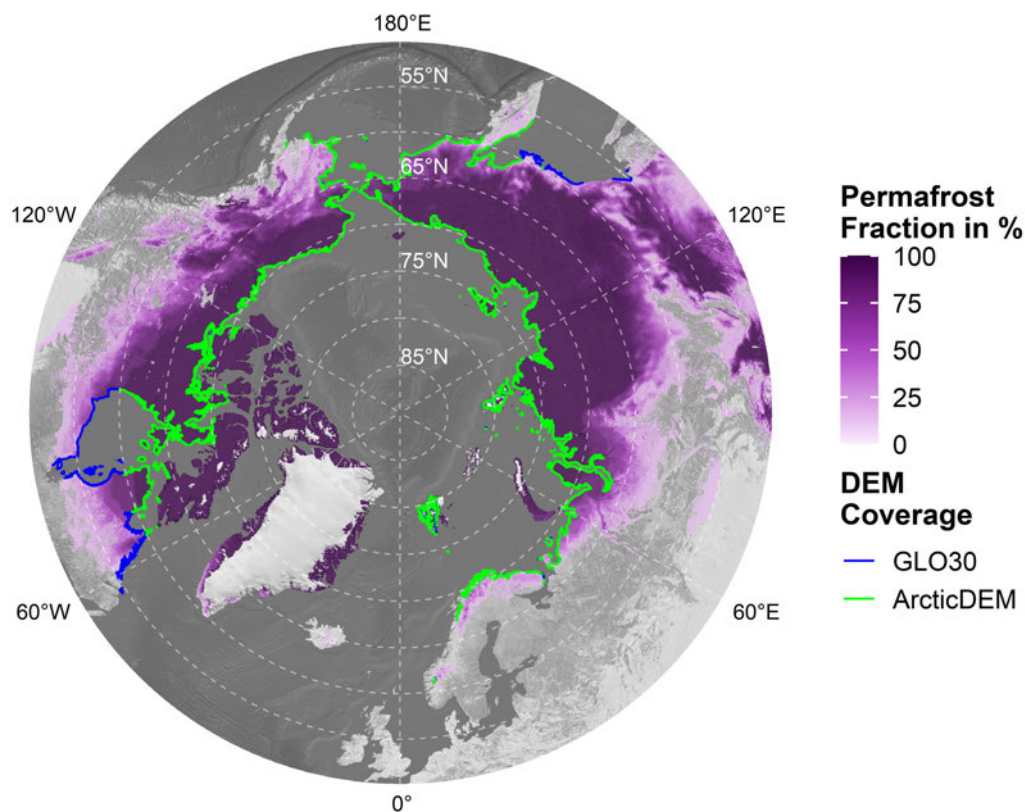
Figure 4.2: Areas of the Deep Learning (DL) coastline product covered by the ArcticDEM (green line). The Copernicus GLO-30 Digital Elevation Model (DEM) was used for the remaining coastline sections (blue line) which are not covered by the ArcticDEM. A shaded relief by Natural Earth (n.d.) in combination with the permafrost fraction across the Northern Hemisphere for the year 2017 based on data by Obu et al. (2021b) was used as a background map.

Figure 4.3 further visualizes the ArcticDEM for Drew Point in Alaska, together with the corresponding S1 Pseudo-RGB image and a binary map that highlights areas below and above sea level. Large parts of the terrestrial area in the visualized scene are associated with elevation numbers below sea level.
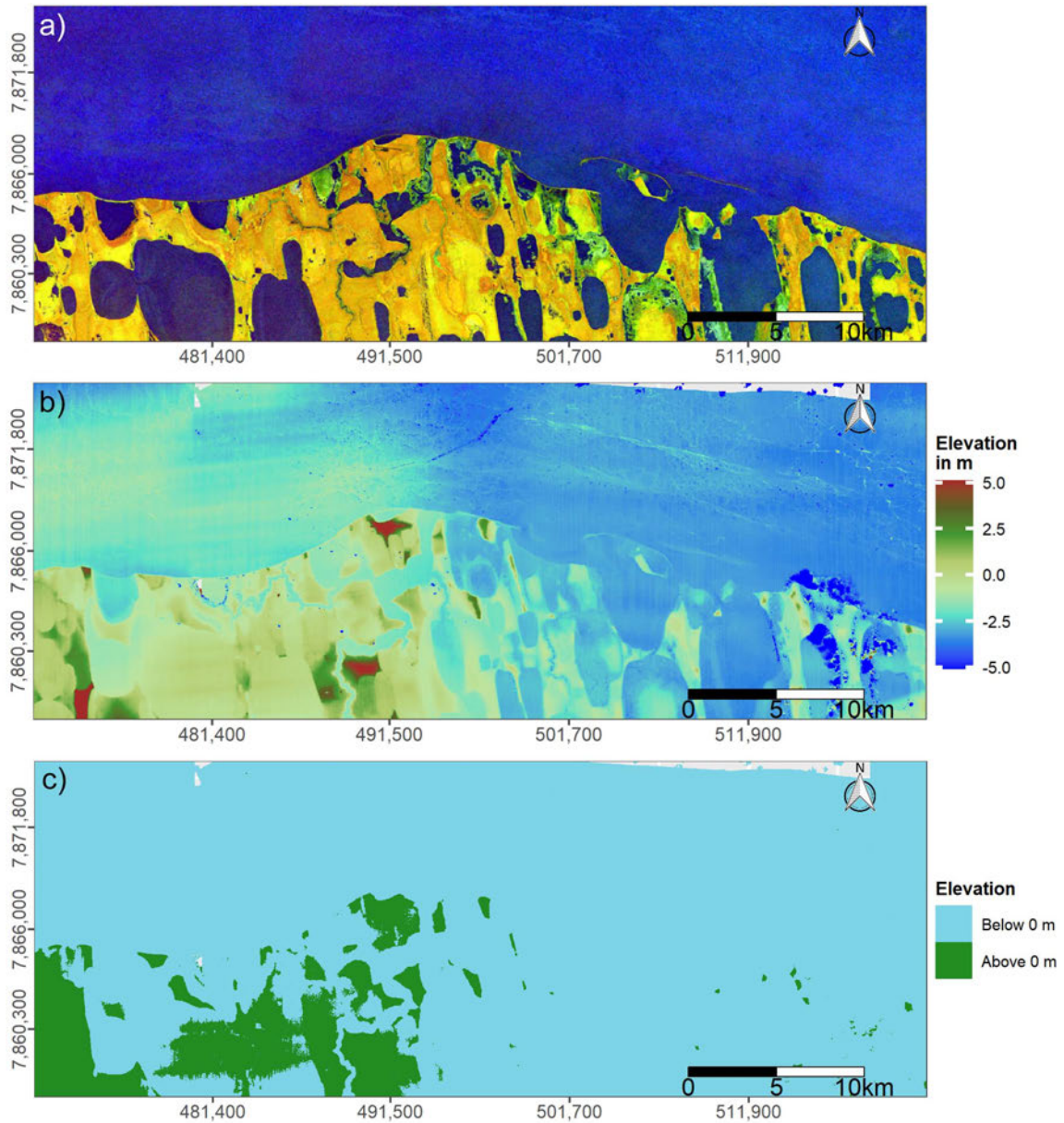
Figure 4.3: (**a**) Sentinel-1 (S1) Pseudo-Red-Green-Blue (RGB) composite covering the months June–September in 2017. (**b**) Surface elevation based on the ArcticDEM version 3 Digital Elevation Model (DEM) with a 2 m spatial resolution. (**c**) Binary map that differentiates between areas above and below sea level based on the ArcticDEM elevation data.

4.1.4 Soil Carbon

Data on soil OCS in the unit tonnes per hectare for depths of 0 30 cm were accessed via the SoilGrids250m 2.0 product, which provides global information on soil organic carbon content at a spatial resolution of 250 m (Poggio & de Souse, 2020). The data set was generated based on reference data from $\approx$240,000 locations distributed across the entire world and more than 200 additional environmental covariates that provide details on the hydrology, geology, climate, morphology, terrain, and the vegetation cover (Poggio et al., 2021). Figure 4.4 illustrates the OCS in the unit tonnes per hectare across the northern hemisphere. Although the data set is provided in the form of a continuous data type, it was converted to a discrete scale for visualization purposes. Actual analysis was conducted with the original continuous data type.
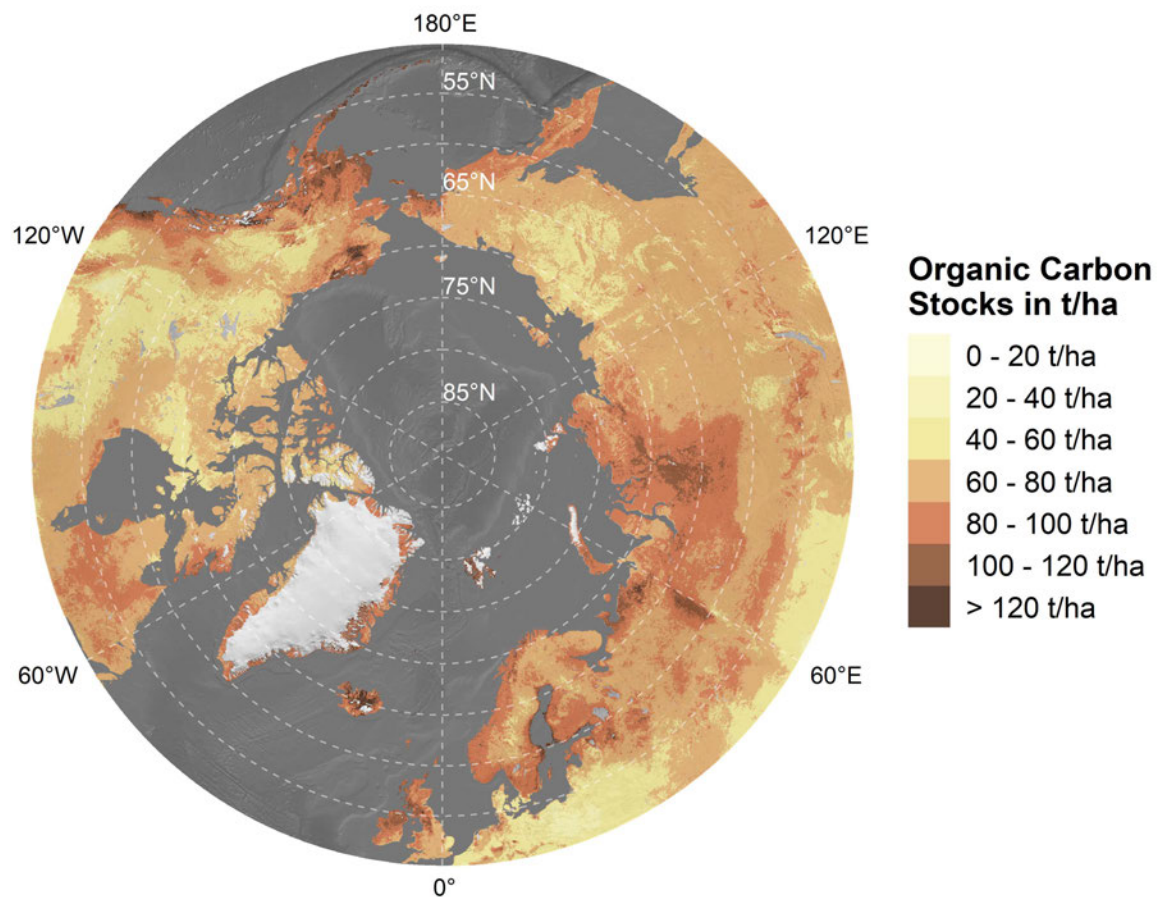
Figure 4.4: Soil Organic Carbon Stocks (OCS) in the unit tonnes per hectare for soil depths of 0–30 cm across the Northern Hemisphere based on data by Poggio & de Souse (2020). The continuous data was converted to a discrete scale for this visualization. A shaded relief by Natural Earth (n.d.) was used as a background map.

4.1.5 Arctic coastal Erosion Rates

S1 GRD SAR scenes in IW swath mode at a spatial resolution of 10 m were utilized in combination with a CVA approach to quantify coastal erosion rates (Chapter 3). As mentioned in the previous chapter, analyses on Arctic coastal change was limited to areas in proximity to permafrost based on the CCI permafrost fraction by Obu et al. (2021b), and with more than ten available S1 scenes per year. A further limitation on the investigation extent was applied based on the number of sea ice days (less than 50% during the observation period June September) via the ASI Arctic sea ice concentration. Lastly, areas in proximity (500 m) to glaciers based on the Global Land Ice Measurements from Space (GLIMS) were excluded from the analysis. Thus, erosion rates across a total of 42,992 km of Arctic permafrost coastline served as a basis for the quantification of permafrost loss and carbon release. The remaining coastline and associated erosion rates are visualized in Figure 3.23.

4.2 Methodology

Average erosion rates between 2017 2021 based on 200 m segments were utilized as a reference. Details on how the average erosion per segment was computed is described in detail in Section 3.2.5.2 and Equation 3.8. For each segment, a center point on the coastline was generated and the average erosion was added as a property. Each segment point was subsequently intersected with raster data on the permafrost fraction, ALT, soil OCS, and surface elevation. In case of the permafrost fraction and ALT, data was available on an annual basis for the years 2017 2019 within the observation time span of the coastal erosion (2017 2021). The average permafrost fraction and ALT per pixel across the three available years was computed in order to have the most representative value within the observed temporal window. Furthermore, since both data sets are available at relatively coarse spatial resolution of ≈927 m, the pixel value from the pixel whose center was closest to each segment point and where the pixel value was not masked was extracted. The extracted pixel value was interpreted as the representative value for this segment. The same procedure was also applied for extracting the soil OCS value per segment. In case of surface elevation data, a slightly different approach was applied. As visualized in Figure 4.3, terrestrial areas in proximity to the coastline are often associated with elevation values below 0. This issue was frequently observed, especially for areas with flat terrain near the shoreline. In order to still be able to investigate volumetric land loss, the difference between surface elevation values of the local terrestrial area and the local sea area was computed. To achieve this, a buffer with a size of 100 m was computed around each segment point. Within this buffer, all pixel values were extracted and the 5th and

95th percentile values were interpreted as the representative values for the local sea level and local terrestrial elevation, respectively. By using the 5th and 95th percentiles instead of the min and max values, outliers could be avoided. The difference between the 5th and 95th percentiles of elevation values within each buffered segment point was ultimately interpreted as the elevation of the local shoreline for each segment. Finally, the volume of lost permafrost in m^3 and the amount of released carbon stocks in tonnes were estimated via Equations 4.1 and 4.3, respectively. For the calculation of carbon loss, the percentage of the depth limit of measured OCS (30 cm) which is covered by the elevation difference between local sea and terrestrial area is also considered via Formula 4.2. The equation is used to convert the ratio between the elevation difference and the OCS depth limit to 1 if it is greater than 1. Otherwise, if the ratio is smaller than 1, the original ratio value [0;1] will be left unchanged. As information about OCS was only available for maximum soil depths of 0 30 cm, the quantification of carbon release was limited to the this soil depth, even if the elevation difference was greater than 30 cm.

$$v_{perma} = (diff_{ele} - alt) * ero_{seg} * len_{seg} * frac_{perma} \qquad (4.1)$$

where:

v_{perma}	$=$	Volume loss of permafrost in m^3;
$diff_{ele}$	$=$	Elevation difference between terrestrial area and sea area in m;
alt	$=$	Active layer thickness in m;
ero_{seg}	$=$	Average annual erosion per coastal segment in m;
len_{seg}	$=$	Length of the coastal segment in m;
$frac_{perma}$	$=$	Fraction of permafrost in percent [0;1]

$$perc_{depth} = min(\frac{diff_{ele}}{depth_{ocs}}, 1) \qquad (4.2)$$

$$v_{carbon} = ocs * perc_{depth} * ero_{seg} * len_{seg} \qquad (4.3)$$

where:

v_{carbon}	$=$	Volume of released carbon in tonnes;
ocs	$=$	Soil organic carbon content in tonnes per m^2 for depths of 0–30 cm;
$perc_{depth}$	$=$	Percentage of covered OCS depth by $diff_{ele}$ [0;1];
$depth_{ocs}$	$=$	Depth limit of the measured OCS in m;

4.3 Results

The following section present the results of the experimental framework for both the quantification of lost permafrost volume and carbon releases due to the erosion of Arctic coastlines. First, details on the permafrost loss on a country basis are provided. Next, estimated carbon releases are highlighted per country.

4.3.1 Permafrost Loss

Strongest average annual loss of permafrost volume per 200 m segment was observed in Alaska with 129.68 m^3, followed by Russia (108.56 m^3) and Svalbard & Jan Mayen (105.97 m^3). Lowest average annual permafrost volume loss per segment was observed in Norway (Scandinavian Peninsula) with 0.49 m^3. However, the majority of permafrost in these regions is limited to mountain areas and do not represent coastal permafrost. The coarse resolution (927 m) of the permafrost fraction reference dataset can be linked to this misleading observation. The highest maximum annual volume loss per segment was identified in Alaska with 217,817.72 m^3, followed by Svalbard & Jan Mayen (157,847.94 m^3). The two countries also featured highest sd values in annual permafrost volume loss. The overall highest amount of lost permafrost as a consequence of Arctic coastal erosion can be reported for Russia (7,891,167.72 m^3), followed by Alaska (4,583,853.16 m^3). The country with the lowest total amount of lost permafrost was predicted to be Norway (Scandinavian Peninsula) with 15,124.38 m^3. The total amount of estimated permafrost volume loss is estimated to be 16,409,376 m^3 per year. Table 4.2 provides further details on the average, maximum, sd and total loss of permafrost per year and per country.

4.3.2 Carbon Loss

The average amount of annually released carbon stocks based on 200 m segments and caused by coastal erosion ranges between 0.01 t (Norway - Scandinavian Peninsula) and 1.39 t (Alaska). The maximum amount of annually lost carbon stocks per segment was observed in Alaska (142.50 t), followed by Russia (131.32 t). Both countries also feature the highest sd values in carbon releases per year. Overall highest total carbon loss per year can be reported for Russia (62,405.59 t) and Alaska (49,117.99 t). The country with the lowest total amount of annual carbon releases was identified to be Norway (Scandinavian Peninsula) with 262 t. The overall total amount of annual carbon releases across all countries and as a consequence of eroding permafrost coastlines was predicted to be 127,234.30 t. Table 4.3 lists statistics in the form of the average, max, sd, and total annual carbon release in tonnes per country and based on

200 m coastline segments.

Table 4.2: Statistics on the coastal erosion-based annual volume loss of permafrost per country in the unit cubic meters. Numbers are based on 200 m segments and the observation period 2017–2021. Statistical measures in the form of the arithmetic mean, maximum, and the standard deviation (sd) per 200 m segment together with the total volume of annually lost permafrost is provided per country.

Country	Mean	Max	SD	Total
Canada	43.37 m^3	58,195.57 m^3	731.32 m^3	2,945,976.73 m^3
Norway (Svalbard and Jan Mayen)	105.97 m^3	157,847.94 m^3	2,606.48 m^3	973,253.95 m^3
Norway (Scandinavian Peninsula)	0.49 m^3	1,832.20 m^3	20.78 m^3	15,124.38 m^3
Russia	108.56 m^3	96,114.55 m^3	1,243.67 m^3	7,891,167.72 m^3
United States (Alaska)	129.68 m^3	217,817.72 m^3	2,501.92 m^3	4,583,853.16 m^3
Total				**16,409,376 m^3**

Table 4.3: Statistics on the coastal erosion-based annual release of soil Organic Carbon Stocks (OCS) per country in the unit tonnes. Numbers are based on 200 m segments and the observation period 2017–2021. Statistical measures in the form of the arithmetic mean, maximum, and the standard deviation (sd) per 200 m segment together with the total amount of annually released soil OCS is provided per country.

Country	Mean	Max	SD	Total
Canada	0.20 t	69.75 t	1.48 t	13,864.06 t
Norway (Svalbard and Jan Mayen)	0.17 t	73.16 t	1.91 t	1,584.70 t
Norway (Scandinavian Peninsula)	0.01 t	31.68 t	0.28 t	262.00 t
Russia	0.86 t	131.32 t	4.65 t	62,405.59 t
United States (Alaska)	1.39 t	142.50 t	6.89 t	49,117.99 t
Total				**127,234.30 t**

4.4 Discussion

A variety of different data sources were utilized in this experimental framework for estimating the annual volume of lost permafrost and released organic carbon content due to coastal erosion. However, various uncertainties are also associated with the proposed approach and data. While data on Arctic coastal erosion was generated at a high spatial resolution of 10 m (Chapter 3), information on the soil carbon content, permafrost fraction, and ALT was available at relatively course spatial resolutions. Pixel sizes were 250 m in case of soil carbon and ≈927 m in case of permafrost fraction and ALT (Table 4.1). Although the analysis was down-scaled from an erosion-based pixel level (10 m) to coastal segments with a length of 200 m, the spatial resolutions of the aforementioned environmental datasets were still lower than the size of one segment. Thus, the attributed pixel value to one segment covers a larger area than the segment itself, which is a major source of uncertainty. Moreover, strong variations in permafrost temperatures and ALT are reported even on smaller scales (Y. Zhang et al., 2021), which means that the low resolution data may not accurately depict the local properties of the permafrost fraction and thickness of the active layer. The quality of the ALT product is communicated to strongly vary across space, with lower accuracy in particular for areas where ground stratigraphic measurements are erroneous (Bartsch et al., 2021). Uncertainties in the data quality are also present for the soil OCS information. As mentioned by Poggio et al. (2021), the importance of more in-situ soil observations, particularly in areas of high-latitude, was underlined by the spatial uncertainty at the global scale. Estimations on carbon loss are further limited to depths of 0 30 cm, as the available data was restricted to this soil depth.

In case of elevation data by the ArcticDEM and the Copernicus GLO-30 DEM, spatial resolutions were higher than the size of one segment. However, data on surface elevation in coastal environments were observed to come with its own challenges. As visualized in Figure 4.3, partly strong variations in the surface elevation data were observed within the sea area in proximity to the coastline. Moreover, terrestrial areas were often associated with negative elevation values, especially for flat terrestrial regions near the coastline. Thus, working with absolute elevation values in coastal areas was not feasible. As a compromise, the 5th and 95th percentiles in surface elevation numbers within one segment were interpreted as the representative local elevations of the sea and terrestrial area, respectively. The difference in the two values was therefore assigned as the local elevation of the shoreline. Working with the 5th and 95th percentiles instead of the minimum and maximum values thereby minimized the risk of introducing outliers. In some regions, however, the sea area was completely masked out and no information on the local surface elevation of the sea was available.

In this case, the pixel with the lowest elevation of terrestrial area was assumed to be the representative elevation of the sea level for this segment, which constitutes another source of uncertainty. Also, only the area above the (local) sea level was considered for estimated volume loss of permafrost. Sub-sea permafrost loss was not considered in this experimental framework.

The analysis was limited to areas with more than ten available S1 GRD backscatter scenes in IW mode for both years 2017 and 2021. The investigated extent was further restricted to areas with less than 50% sea ice days during the observation period June September in order to reduce the amount of noise in the CVA analysis to a minimum. Furthermore, and as mentioned in Section 3.2.4.2, islands smaller than ≈ 0.2 km^2 were excluded from the analysis. Thus, large parts of the Arctic permafrost coastline were not considered in this experimental framework. Glaciers were also excluded from the analysis via the GLIMS glacier database, which minimized the impact of changing glaciers on the proposed data and methods. However, remaining smaller glaciers, which were not covered by the GLIMS glacier database, can have a significant impact on the statistics on the volume of lost permafrost and released carbon content.

Present uncertainties in the form of variations in data quality, the partly low spatial resolution of available data, the limitation of the carbon analysis to soil depths of 0 30 cm, the restriction of the quantification of permafrost loss to areas above (local) sea level, and the previously mentioned uncertainties of the proposed methods and data for quantifying Arctic coastal erosion (Section 3.4) are all limiting factors to this experimental approach. At the same time, this experimental investigation demonstrates the potential of SAR satellite-based coastal erosion quantification for circum-Arctic monitoring of permafrost loss and carbon releases. Nevertheless, extensive in-situ validation and higher resolution auxiliary data is needed for quality assessment and the computation of more realistic estimates. Due to the mentioned uncertainties in input data, methodologies, and missing large scale validation, the proposed framework should be interpreted as a first experimental outline. The generated statistics on the volume of lost permafrost and released carbon content should further be treated with caution.

4.5 Summary

This chapter introduced an experimental framework for quantifying the coastal erosion-based loss of permafrost and carbon releases. Various different data sources were incorporated in this framework, including information about the permafrost

fraction, active layer thickness, soil Organic Carbon Stocks (OCS), surface elevation, number of sea-ice days, glacier presence, and the previously generated circum-Arctic coastal erosion rates derived from Sentinel-1 (S1) Ground Range Detected (GRD) backscatter imagery in Interferometric Wide (IW) swath mode. The following main conclusions can be drawn:

- Strongest average annual loss of permafrost volume per 200 m segment was observed in Alaska (129.68 m^3) and Russia (108.56 m^3). Russia also featured the overall highest amount (7,891,167.72 m^3) of annually lost permafrost due to Arctic coastal erosion, followed by Alaska (4,583,853.16 m^3). The total amount of lost permafrost across the entire investigated Arctic coastline was observed to be 16,409,376 m^3 per year.

- Highest average amount of annually released carbon stocks based on 200 m segments and caused by coastal erosion was observed in Alaska (1.39 t). Overall highest annual carbon loss per year and on a regional scale can be reported for Russia (62,405.59 t), followed by Alaska (49,117.99 t). The total amount of annual carbon releases as a consequence of eroding permafrost coasts across the entire investigated Arctic coastline were estimated to be 127,234.30 t.

- While the proposed data and methods provide a valuable first insight in circum-Arctic permafrost and carbon loss, many uncertainties in both the data and the methodology are present.

- Information on soil carbon, permafrost fraction, and Active Layer Thickness (ALT) is only available at a relatively course spatial resolutions on a circum-Arctic scale. Spatial variations in the data quality are thereby a further challenge.

- Surface elevation data in Arctic coastal environments is associated with many artefacts in some areas, which limits the precise estimation of volume loss. Moreover, high resolution data on surface elevation is only available for areas above the (local) sea level. No sub-sea volumetric changes were investigated.

- Some terrestrial regions in proximity to the coastline were associated with values below the sea level within the available surface elevation data. The 5th and 95th percentiles in surface elevation numbers within one segment were therefore interpreted as the representative local elevations of the sea and terrestrial area. However, some regions were fully masked from water areas, which leads to an increased uncertainty in estimating the actual shoreline surface elevation.

- Glaciers were excluded from the analysis via the Global Land Ice Measurements from Space (GLIMS) glacier database. However, small remaining glaciers,

which are not covered by the GLIMS database, can have a significant effect on volumetric estimations for erosion-based permafrost loss.

- Estimations on carbon loss were restricted to depths of 0 30 cm, as the available data on soil OCS was limited to this soil depth.

- Data on coastal erosion was not available for the entire Arctic coastline, but was limited to areas with more than ten S1 GRD scenes in IW mode for both years 2017 and 2021, and further limited to areas with less than 50% sea-ice duration within the observation time-frame June September. Thus, absolute volume estimations on carbon release and permafrost loss are not representing the entire Arctic coastline.

- Extensive and large scale in-situ validation is necessary to further assess and improve on the quality of the proposed data and methods.

The suggested framework should be viewed as a first experimental outline due to the acknowledged uncertainties in the input data, techniques, and missing large scale validation. Caution should be exercised when interpreting the generated numbers on the amount of permafrost loss and the released carbon content as presented in this chapter.

Chapter 5

Synthesis and Outlook

This chapter provides a synthesis of the conclusive findings of this dissertation. Section 5.1 gives a short summary and discussion of the results with respect to the initially set-up research questions in Section 1.2. Section 5.2 subsequently focuses on future challenges and opportunities in the context of quantifying the effects of permafrost degradation in Arctic coastal environments via satellite earth observation.

5.1 Summary and conclusive Findings

In the introduction (Chapter 1), the importance of permafrost and the consequences of its degradation for both the environment but also human society were presented. The need for continuous and large scale observations of permafrost-related features and processes was also stressed. In particular, the effects of degrading permafrost in coastal environments was highlighted. Within this context, SAR-based satellite earth observation was introduced as a promising data source for closing existing gaps on the continuous and automated quantification of circum-Arctic coastal erosion rates at a high spatial resolution.

Within this dissertation, current trends in satellite earth observation for permafrost related analyses during the past two decades were investigated. In addition, a novel monitoring framework for circum-Arctic quantification of annual erosion of permafrost coasts based on S1 SAR backscatter data, DL, and CVA was proposed. Lastly, an experimental outline for intersecting circum-Arctic coastal erosion with the amount of lost permafrost and released carbon stocks was presented. In this context, initial research questions were defined in Section 1.2 and addressed in the Chapters 2, 3, and 4. The following paragraphs provide a short summary of the answers on each research question:

> ## Research Questions 1
>
> - *How does the publication frequency for studies that investigate permafrost-related features and processes via space-borne data change over time?*
> - *How are the study areas distributed across the permafrost domain? What are the study hotspots?*
> - *What environmental foci are studied the most and what foci are studied the least?*
> - *What spatio-temporal resolutions were applied to address different environmental topics?*
> - *What satellite platforms and data types are frequently applied?*
> - *What are existing research gaps in the context of satellite-based analyses of permafrost related processes and features and how can they be addressed?*

This paragraph focuses on the results which are related to the first block of research questions. Based on the 325 investigated articles during the review process of this thesis, a clear trend towards higher publication numbers per year could be observed during the past two decades and within the context of satellite earth observation of permafrost related analysis. A particular rise in study numbers was observed during the last decade, where the total number of publications more than doubled since the year 2015. Nearly all (94%) study areas were located on the northern Hemisphere, where Gydan and Yamal Peninsuals and the Lena Delta in Russia, the Mackenzie Delta in Canada, the Beiluhe region within the Tibet Plateau in China, and the North Slope Borough and its Arctic Coastal Plain in Alaska were identified as key study regions. The heavy focus on the northern Hemisphere can be explained by the restricted permafrost presence on the southern Hemisphere, which is for the most part limited to Alpine regions and ice-free areas in the Antarctic. The majority (43%) of studied environmental foci were related to land surface processes and features, followed by 25% of investigations covering surface water processes and features. 21% of studies were associated with subsurface processes and features, whereas only 7% were linked to thermal processes/features. Merely 4% of studies were connected to atmospheric processes/features. Variations in the distribution of the most common study foci were observed across different regions. While surface movement was the main focus of studies located in China, the most frequent topic in the USA, Canada, and Russia proved to be dynamics in lake extents. Although almost half (47%) of articles applied a time series analysis (ten or more time steps), only 21% of which covered a time span of more than 20 years. A mere 8% of articles applied their analysis on a circumpolar scale, while the majority of studies (62%) restricted their investigations to local scales. Furthermore,

while roughly half (52%) of local studies were using high resolution imagery (<10 m), about three quarters (74%) of circum-Arctic studies relied on low resolution data (>1000 m). Optical data was the most frequently applied data type with 55% of all data types, followed by 20% SAR data. Despite the exclusion of aerial-only studies, the type "aerial" still proved to be the most frequently used platform (31% of all platforms), followed by satellites within the Landsat legacy (27% of all platforms). The sentinel satellites only made up 6% of all incorporated platforms, but a strong tendency towards increased exploitation of data from these platforms was observed in recent years. Several research gaps in the context of satellite earth observation for permafrost related analyses were identified. First, many openly available products related to permafrost feature insufficient accuracy, spatial resolution, thematic detail, and/or extent for large scale investigations. Also reference data is often concentrated around key study regions, while large parts of the continuous permafrost zone feature little to no reference data. More frequent and a more spatially homogeneous distribution of reference data could improve future models and analyses. While first investigations on applying a DL framework showed promising results, only a handful of studies explored the potential of DL in the context permafrost. In terms of environmental foci, very little attention was so far directed towards investigations on thermal topics and atmospheric features and processes within the context permafrost. Thermal data from the Landsat satellites appears hereby heavily under-utilized. An increased application of thermal data from the Landsat mission could potentially contribute to an enhanced understanding of the thermal state of permafrost. Moreover, new satellite missions such as Merlin and Sentinel-5P are attractive data sources for future investigations on atmospheric effects of permafrost degradation. Even though Arctic regions feature unfavourable environmental conditions for optical remote sensing (low light intensities, cloud cover, etc.), it still proved to be the most commonly applied data type. SAR data, which is largely independent on these environmental factors, therefore appears under-represented and, at the same time, constitutes an attractive data source for many use-cases in future Arctic investigations. The previously mentioned lack of large to circum-Arctic scale studies, especially based on medium-high high resolution data, was identified as another research gap. Also, long-term (>20 years) time series investigations were sparsely applied. Cloud-based computing platforms, such as GEE, will thereby likely accelerate both analyses on larger scales and facilitate long-term time series studies.

Research Questions 2

- *Is the application of S1 SAR backscatter data feasible for monitoring coastal change in Arctic environments?*

- *How can space-borne remote sensing in combination with AI be integrated to generate a high quality Arctic coastline product for permafrost environments? What are the challenges and how can they be overcome?*

- *How can CVA be combined with S1 SAR backscatter data to contribute in monitoring Arctic coastal change rates?*

- *Can the proposed data and methods be transferred to quantify coastal change in different latitudinal regions? What needs to be considered?*

This paragraph focuses on the results which are related to the second block of research questions. Results for both the generation of a high-quality circum-Arctic coastline product and the CVA-based coastal change analysis based on S1 backscatter imagery proved the feasibility of C-band SAR backscatter data for monitoring Arctic coastal environments. Working on annual (June September) composites instead of single scenes thereby reduced the amount of noise and geolocation uncertainty. The median deviation of the DL-based coastline product to the manually digitized reference data was observed to be ±6.3 m. Extracted coastal change rates featured an average deviation of −10.3 m and an r^2 value of 0.92 to the manually digitized reference data. Thus, both products featured satisfactory accuracy which underlines the feasibility of SAR data as a basis for these tasks. An inverse behaviour of the median and sd backscatter signal could be observed over land vs. sea areas. This inverse behaviour was exploited for both the computation of the DL-based high-quality coastline product, as well as the CVA analysis on coastal change. Median and sd backscatter data were combined to pseudo-RGB images and fed as input data for training the U-Net based CNN architectures. A common limitation of CNNs is the vast amount of training data required to achieve an adequate model performance. This limitation could be largely overcome by (1) using pre-trained networks based on the ImageNet database (≈14 Mio. images), (2) by increasing the amount of training data through augmentation, as well as (3) by incorporating further training data derived from OSM as an addition to the manually reference training sites. Another challenge of working with CNNs is finding a suitable model architecture for the task at hand. By combining the segmentation results of nine individually trained models with varying architecture types and depths, a representative output segmentation product could be generated. The CVA approach also took advantage of the inverse behaviour in sd and median backscatter. The sd backscatter was observed to be higher over water and lower over land, whereas

the median backscatter acted inversely. Thus, the magnitude of change between the median and sd backscatter across two different years could be computed on a pixel basis and interpreted as either coastal erosion (rising sd, declining median) or coastal build-up (rising median, declining sd). Suitable thresholds for the resulting magnitude of change maps were derived based on reference data from the manually digitized sites. As previously mentioned, an r^2 value of 0.92 and an average deviation of -10.3 m between the generated coastal change product and the reference data was observed. The proposed data and methods could be successfully applied in Arctic environments, although the quality of the products heavily depends on the amount of available data and the local sea-ice concentration. Since the data and methods are not bound to Arctic properties, they feature a high potential in transferability to other latitudes. In case of the DL approach for generating a high-quality coastline product, a considerable amount of additional training data from the target regions is recommended. The networks were thus far only trained with data from Arctic coastal environments. In order to also achieve satisfactory results for the numerous types of coastal environments outside the Arctic, additional training of the networks is advised. The proposed threshold values for the CVA-based magnitude of change maps are based on Arctic-only environments, as well. Thus, different threshold values might be appropriate for different latitudes. Moreover, the amount of available images per pixel is an important quality layer and it is therefore advised to also include this information for analyses in other geographical regions.

Research Questions 3

- *What are the relevant environmental parameters to estimate permafrost loss and carbon release associated to coastal erosion? What products for these parameters are openly available?*

- *What challenges are present when quantifying permafrost and carbon loss based on the utilized data and methods? How can they be overcome?*

This paragraph focuses on the results which are related to the third block of research questions. In order to quantify the loss of permafrost and the release of previously stored soil organic carbon contents as a result of eroding coastlines, a range of different datasets were used. The previously generated annual and circum-Arctic erosion rates were utilized as a basis for this experimental framework. In addition, details on permafrost occurrences and ALT were incorporated via the CCI permafrost fraction and CCI ALT data sets. Furthermore, surface elevation data from the ArcticDEM Version 3 Mosaic DEM and the Copernicus GLO-30 DEM acted as a reference for the volumetric estimations. Data from the GLO-30 DEM were used for

areas where no data from the ArcticDEM was available. The GLIMS glacier database was used to remove glaciers from the analysis. Lastly, details on the stored carbon content in Arctic soils was accessed via the SoilGrids250m 2.0 - Soil OCS dataset. Although the suggested data and applied methods offer a useful initial impression on circum-Arctic permafrost and carbon loss, there are several uncertainties in both the methodology and the data. First, data on different environmental parameters are available at different spatial resolutions. Especially the permafrost fraction, ALT and soil OCS is provided with relatively coarse pixel sizes, making a pixel-wise analysis at the original resolution (10 m) of the S1 GRD data in IW swath mode difficult. As a compromise, numbers were computed for 200 m coastal segments. Moreover, spatial variations in data quality are reported for all data sets. While the spatial resolution of applied surface elevation data was feasible, many artefacts were observed in Arctic coastal environments. Flat terrain in proximity to coastlines were often associated with elevation values below 0 m. In order to estimate the local heights of the shoreline, the 5th and 95th percentile values of surface elevation within one coastal segment were interpreted as the representative local sea and terrestrial elevation levels. For some regions, however, the sea area was fully masked, which further complicated estimations on coastal elevations above the sea level. Furthermore, although glaciers were masked out based on the GLIMS glacier database, small remaining glaciers may have a significant effect on the volume estimations of lost permafrost. Also, the estimated release of carbon stocks is limited to carbon content in soil depths of 0 30 cm, as available in the SoilGrids250m 2.0 dataset. Therefore, the proposed framework should be viewed as a first experimental outline in quantifying permafrost loss and carbon releases as a consequence of eroding coastlines. Extensive and large scale validation is needed for further verification of the estimated volume losses. In order to generate more representative numbers on permafrost and carbon loss, data on permafrost fraction, soil carbon, and ALT of higher spatial resolution is required. Also, information on carbon stocks for deeper soil depths are required for more realistic estimations on the release of carbon.

5.2 Future Challenges and Opportunities

This thesis presented a novel and potent approach in generating a high-quality Arctic coastline product as well as quantifying annual coastal change rates on a circum-Arctic scale and at a high spatial resolution. The applicability of the proposed data and methods, however, strongly depends on the number of available satellite images. The recent failure of the S1B satellite constitutes a further challenge due to a restricted data availability until the launch of S1C. While large parts of noise, geolocation

uncertainty, and backscatter ambiguities could be removed by working on annual backscatter composites, some SAR specific challenges, such as geometric distortions (foreshortening, layover, and shadow), may still impair the quality of the output products in some regions. Analyses on Arctic coastal change were limited to areas with more than ten satellite observations and less than 50% sea-ice cover duration per year. Therefore, the analysis was restricted to 27% of the entire observed Arctic coastline. As a continuous satellite mission, S1 provides high potential especially for future analysis. Longer time series investigations allow for the quantification of coastal change rates also for coastal environments, where annual erosion/build-up rates are relatively small. By increasing the temporal observation window, annual erosion rates less the size of one pixel (10 m) will eventually also become quantifiable. Moreover, by having lengthier time series data, temporal windows for the computation of single composites could be extended from one year to two or more years. This is especially valuable for areas with poor data availability. At the same time, the variation in surface information within one composite also increases with larger temporal observation windows. Also, available S1 scenes were separated by their associated orbit direction (ascending or descending). Both the DL-based high-quality coastline product and the CVA-based coastal change analysis were based on data from the most frequent orbit direction (ascending or descending) per pixel. However, a combination of both orbit directions would greatly improve the overall amount of data per pixel and could therefore not only improve the quality of the analysis, but also the extent of the coastal change investigation. At the same time, the impact of combining scenes from different orbit directions on the product quality should be further investigated.

While this thesis focused on utilizing SAR data derived from S1, combining SAR imagery from different satellite sources constitutes a promising approach for future analyses. In addition, combining different data types, e.g. SAR and optical data could be another potent technique in increasing not only the temporal frequency of observations, but also the diversity of available information per pixel. S2 and Landsat here thereby particularly attractive sources of data due to the spatio-temporal resolution of available imagery. While Landsat allows for longer time-series observations, S2 features higher spatial resolution. At the same time, frequent cloud cover, sea-ice contamination, and data gaps are remaining challenges when working with optical datasets in Arctic environments (Figures 3.26 & 3.27). Nonetheless, combining data from various satellites represents a viable strategy for enhancing the accuracy and extent of the suggested coastal monitoring framework.

A global application of the proposed coastal observation framework seems plausible, as the presented methods are not restricted to specific properties of Arctic environments. However, and as mentioned earlier, additional training of the CNNs and further

investigations of suitable threshold values in case of the CVA-based magnitude of change maps for other regions are advised. Moreover, intersecting the extracted erosion rates with high resolution geomorphological parameters, such as lithification stage or ground ice content, may further help to improve our understanding of underlying mechanics and drivers of coastal erosion. For accurate estimates of permafrost loss and carbon release, environmental data of higher resolution are necessary. Additionally, carbon content of deeper soil depths are required. Lastly, extensive validation of the permafrost fraction, ALT, soil OCS and extracted erosion rates are highly recommended for future investigations on the loss of permafrost and carbon release related to Arctic coastal erosion. The degradation of permafrost has many effects on the environment but also on human infrastructure and society. Widespread Arctic coastal erosion and the associated release of previously stored organic carbon stocks are hereby significant challenges we are currently facing and will likely continue to face in the future. The proposed DL circum-Arctic coastline product and CVA-based coastal change quantification may thereby constitute a relevant and important basis to address this challenge.

Bibliography

Abbott, B. W., Jones, J. B., Schuur, E. A., Chapin III, F. S., Bowden, W. B., Bret-Harte, M. S., ... others (2016). Biomass offsets little or none of permafrost carbon release from soils, streams, and wildfire: an expert assessment. *Environmental Research Letters*, *11*(3), 034014.

Abis, B., & Brovkin, V. (2017). Environmental conditions for alternative tree-cover states in high latitudes. *Biogeosciences*, *14*(3), 511 527.

Alaska Geobotany Center. (2012). *Circumpolar Arctic Coastline and Treeline Boundary.* http://www.arcticatlas.org/maps/themes/cp/cpcoast. (Accessed on 10 February 2022)

Alaska Satellite Facility. (n.d.). *Sentinel-1 Acquisition Maps.* https://asf.alaska.edu/data-sets/sar-data-sets/sentinel-1/sentinel-1-acquisition-maps/. (Accessed on 10 February 2022)

Alexander, M. A., Scott, J. D., Friedland, K. D., Mills, K. E., Nye, J. A., Pershing, A. J., & Thomas, A. C. (2018). Projected sea surface temperatures over the 21st century: Changes in the mean, variability and extremes for large marine ecosystem regions of Northern Oceans. *Elementa: Science of the Anthropocene*, *6*.

Alexandridis, T. K., Cherif, I., Kalogeropoulos, C., Monachou, S., Eskridge, K., & Silleos, N. (2013). Rapid error assessment for quantitative estimations from Landsat 7 gap-filled images. *Remote Sensing Letters*, *4*(9), 920 928.

Alfred-Wegener-Institute. (n.d.-a). *Changing Arctic Carbon cycle in the cOastal Ocean Near-shore - CACOON.* https://www.awi.de/forschung/geowissenschaften/permafrostforschung/projekte/cacoon.html. (Accessed: February 26th 2021)

Alfred-Wegener-Institute. (n.d.-b). *Modular Observation Solutions for Earth Systems MOSES.* https://www.awi.de/en/science/geosciences/permafrost-research/projects/moses.html. (Accessed: February 26th 2021)

Alfred-Wegener-Institute. (n.d.-c). *PETA-CARB: Rapid Permafrost Thaw in a Warming Arctic and Impacts on the Soil Organic Carbon Pool.* https://www.awi.de/en/science/junior-groups/peta-carb.html. (Accessed: February 26th 2021)

Allison, I., Barry, R. G., & Goodison, B. E. (2001). *Climate and cryosphere (CliC) project science and co-ordination plan: version 1* (Vol. 114). Joint Planning Staff for WCRP, World Meteorological Organization.

Bibliography

André, C., Ottlé, C., Royer, A., & Maignan, F. (2015). Land surface temperature retrieval over circumpolar Arctic using SSM/I SSMIS and MODIS data. *Remote Sensing of Environment*, *162*, 1 10.

Andresen, C. G., & Lougheed, V. L. (2015). Disappearing Arctic tundra ponds: Fine-scale analysis of surface hydrology in drained thaw lake basins over a 65 year period (1948 2013). *Journal of Geophysical Research: Biogeosciences*, *120*(3), 466 479.

Angelopoulos, M., Overduin, P. P., Miesner, F., Grigoriev, M. N., & Vasiliev, A. A. (2020). Recent advances in the study of Arctic submarine permafrost. *Permafrost and Periglacial Processes*, *31*(3), 442 453.

Anthony, K. W., Daanen, R., Anthony, P., von Deimling, T. S., Ping, C.-L., Chanton, J. P., & Grosse, G. (2016). Methane emissions proportional to permafrost carbon thawed in Arctic lakes since the 1950s. *Nature Geoscience*, *9*(9), 679 682.

Anthony, K. W., von Deimling, T. S., Nitze, I., Frolking, S., Emond, A., Daanen, R., . . . Grosse, G. (2018). 21st-century modeled permafrost carbon emissions accelerated by abrupt thaw beneath lakes. *Nature communications*, *9*(1), 1 11.

Antonova, S., Beck, I., Marx, S., Anders, K., Boike, J., & Höfle, B. (2019). *PermaSAR: Entwicklung einer Methode zur Detektion von Subsidenz in Permafrostgebieten mit D-InSAR: Schlussbericht.* TIB.

Antonova, S., Kääb, A., Heim, B., Langer, M., & Boike, J. (2016). Spatio-temporal variability of X-band radar backscatter and coherence over the Lena River Delta, Siberia. *Remote Sensing of Environment*, *182*, 169 191.

Antonova, S., Sudhaus, H., Strozzi, T., Zwieback, S., Kääb, A., Heim, B., . . . Boike, J. (2018). Thaw subsidence of a yedoma landscape in northern Siberia, measured in situ and estimated from TerraSAR-X interferometry. *Remote Sensing*, *10*(4), 494.

Arctic Development and Adaptation to Permafrost in Transition (ADAPT). (n.d.). *Permafrost 101.* `https://science.cen.ulaval.ca/adapt/communications/permafrost101.php`. (Accessed: Januar 6th 2023)

ArcticNet. (n.d.-a). *ArcticNET - About us.* `https://arcticnet.ulaval.ca/vision-and-mission/about-us`. (Accessed: November 16th 2020)

ArcticNet. (n.d.-b). *ArcticNet annual report 2019 / 2020.* `https://arcticnet.ulaval.ca//pdf/media/arcticnet-ra-19-20-ang.pdf`. (Accessed: October 28th 2020)

Arenson, L. U., & Jakob, M. (2015). Periglacial geohazard risks and ground temperature increases. In *Engineering geology for society and territory-volume 1* (pp. 233 237). Springer.

Arenson, L. U., Kääb, A., & O'Sullivan, A. (2016). Detection and analysis of ground deformation in permafrost environments. *Permafrost and Periglacial Processes*, *27*(4), 339 351.

Bai, X., Yang, J., Tao, B., & Ren, W. (2018). Spatio-Temporal Variations of Soil Active Layer Thickness in Chinese Boreal Forests from 2000 to 2015. *Remote Sensing*, *10*(8), 1225.

Balser, A. W., Jones, J. B., & Gens, R. (2014). Timing of retrogressive thaw slump initiation in the Noatak Basin, northwest Alaska, USA. *Journal of Geophysical Research: Earth Surface*, *119*(5), 1106 1120.

Bansal, A., Kauffman, R. J., & Weitz, R. R. (1993). Comparing the modeling performance of regression and neural networks as data quality varies: A business value approach. *Journal of Management Information Systems*, *10*(1), 11 32.

Barnhart, K., Overeem, I., & Anderson, R. (2014, 09). The effect of changing sea ice on the physical vulnerability of Arctic coasts. *The Cryosphere*, *8*(5), 1777 1799. doi: 10.5194/tc-8-1777-2014

Barnhart, K. R., Miller, C. R., Overeem, I., & Kay, J. E. (2016). Mapping the future expansion of Arctic open water. *Nature Climate Change*, *6*(3), 280 285.

Barron, C., Neis, P., & Zipf, A. (2014). A comprehensive framework for intrinsic OpenStreetMap quality analysis. *Transactions in GIS*, *18*(6), 877 895.

Bartholome, E., & Belward, A. S. (2005). GLC2000: a new approach to global land cover mapping from Earth observation data. *International Journal of Remote Sensing*, *26*(9), 1959 1977.

Bartsch, A., Balzter, H., & George, C. (2009). The influence of regional surface soil moisture anomalies on forest fires in Siberia observed from satellites. *Environmental Research Letters*, *4*(4), 045021.

Bartsch, A., Grosse, G., Kääb, A., Westermann, S., Strozzi, T., Wiesmann, A., . . . Goler, R. (2016). GlobPermafrost How space-based Earth observation supports understanding of permafrost. In *Proceedings of the esa living planet symposium, prague, czech republic* (pp. 9 13).

Bartsch, A., Höfler, A., Kroisleitner, C., & Trofaier, A. M. (2016). Land cover mapping in northern high latitude permafrost regions with satellite data: Achievements and remaining challenges. *Remote Sensing*, *8*(12), 979.

Bartsch, A., Leibman, M., Strozzi, T., Khomutov, A., Widhalm, B., Babkina, E., . . . Bergstedt, H. (2019). Seasonal progression of ground displacement identified with satellite radar interferometry and the impact of unusually warm conditions on permafrost at the Yamal Peninsula in 2016. *Remote Sensing*, *11*(16), 1865.

Bartsch, A., Ley, S., Nitze, I., Pointner, G., & Vieira, G. (2020). Feasibility study for the application of Synthetic Aperture Radar for coastal erosion rate quantification across the Arctic. *Frontiers in Environmental Science*, *8*, 143.

Bartsch, A., Obu, J., Westermann, S., & Strozzi, T. (2021). *CCI+ Phase 1 New ECVS Permafrost D4.3 PRODUCT USER GUIDE (PUG) Version 3.0.* `https://climate.esa.int/media/documents/CCI_PERMA_PUG_v3.0.pdf`. (Accessed: January 14th 2023)

Bartsch, A., Pointner, G., Ingeman-Nielsen, T., & Lu, W. (2020). Towards Circumpolar Mapping of Arctic Settlements and Infrastructure Based on Sentinel-1 and Sentinel-2. *Remote Sensing*, *12*(15), 2368.

Bartsch, A., Pointner, G., Leibman, M. O., Dvornikov, Y. A., Khomutov, A. V., & Trofaier, A. M. (2017). Circumpolar mapping of ground-fast lake ice. *Frontiers in Earth Science*, *5*, 12.

Batbaatar, J., Gillespie, A. R., Sletten, R. S., Mushkin, A., Amit, R., Liaudat, D. T., ... Petrie, G. (2020). Toward the Detection of Permafrost Using Land-Surface Temperature Mapping. *Remote Sensing*, *12*(4), 695.

Baumhoer, C. A., Dietz, A. J., Kneisel, C., & Kuenzer, C. (2019). Automated extraction of antarctic glacier and ice shelf fronts from sentinel-1 imagery using deep learning. *Remote Sensing*, *11*(21), 2529.

Baumhoer, C. A., Dietz, A. J., Kneisel, C., Paeth, H., & Kuenzer, C. (2020). Driving Forces of Circum-Antarctic Glacier and Ice Shelf Front Retreat over the Last Two Decades. *The Cryosphere Discussions*, *2020*, 1 30.

Baumhoer, C. A., Dietz, A. J., Kneisel, C., Paeth, H., & Kuenzer, C. (2021). Environmental drivers of circum-Antarctic glacier and ice shelf front retreat over the last two decades. *The Cryosphere*, *15*(5), 2357 2381.

Beck, I., Ludwig, R., Bernier, M., Lévesque, E., & Boike, J. (2015). Assessing permafrost degradation and land cover changes (1986 2009) using remote sensing data over Umiujaq, sub-arctic Québec. *Permafrost and Periglacial Processes*, *26*(2), 129 141.

Beighley, R., Eggert, K., Wilson, C., Rowland, J., & Lee, H. (2015). A hydrologic routing model suitable for climate-scale simulations of arctic rivers: application to the Mackenzie River Basin. *Hydrological Processes*, *29*(12), 2751 2768.

Belshe, E., Schuur, E., & Grosse, G. (2013). Quantification of upland thermokarst features with high resolution remote sensing. *Environmental Research Letters*, *8*(3), 035016.

Bennett, J. (2010). *OpenStreetMap: Be your own cartographer*. Packt Publishing Ltd.

Bernard-Grand'Maison, C., & Pollard, W. (2018). An estimate of ice wedge volume for a High Arctic polar desert environment, Fosheim Peninsula, Ellesmere Island. *The Cryosphere*, *12*(11), 3589 3604.

Bernhardt, H., Reiss, D., Hiesinger, H., Hauber, E., & Johnsson, A. (2017). Debris flow recurrence periods and multi-temporal observations of colluvial fan evolution in central Spitsbergen (Svalbard). *Geomorphology*, *296*, 132 141.

Bertone, A., Zucca, F., Marin, C., Notarnicola, C., Cuozzo, G., Krainer, K., ... Seppi, R. (2019). An unsupervised method to detect rock glacier activity by using Sentinel-1 SAR interferometric coherence: a regional-scale study in the eastern European Alps. *Remote Sensing*, *11*(14), 1711.

Bibi, S., Wang, L., Li, X., Zhang, X., & Chen, D. (2019). Response of groundwater storage and recharge in the Qaidam Basin (Tibetan Plateau) to climate variations from 2002 to 2016. *Journal of Geophysical Research: Atmospheres*, *124*(17-18), 9918 9934.

Bishop, C. M., & Nasrabadi, N. M. (2006). *Pattern recognition and machine learning* (Vol. 4). Springer.

Biskaborn, B. K., Lanckman, J.-P., Lantuit, H., Elger, K., Dmitry, S., William, C., & Vladimir, R. (2015). The new database of the Global Terrestrial Network for Permafrost (GTN-P). *Earth System Science Data*, *7*, 245 259.

Bockheim, J. G. (2014). Distribution, properties and origin of viscous-flow features in the McMurdo Dry Valleys, Antarctica. *Geomorphology*, *204*, 114 122.

Bohn, T. J., Melton, J. R., Ito, A., Kleinen, T., Spahni, R., Stocker, B., ... others (2015). WETCHIMP-WSL: intercomparison of wetland methane emissions models over West Siberia. *Biogeosciences*, *12*(11), 3321 3349.

Boike, J., Grau, T., Heim, B., Günther, F., Langer, M., Muster, S., ... Lange, S. (2016). Satellite-derived changes in the permafrost landscape of central Yakutia, 2000 2011: Wetting, drying, and fires. *Global and Planetary Change*, *139*, 116 127.

Boyle, S. A., Kennedy, C. M., Torres, J., Colman, K., Pérez-Estigarribia, P. E., & Noé, U. (2014). High-resolution satellite imagery is an important yet underutilized resource in conservation biology. *PLoS One*, *9*(1), e86908.

Brenning, A. (2009). Benchmarking classifiers to optimally integrate terrain analysis and multispectral remote sensing in automatic rock glacier detection. *Remote Sensing of Environment*, *113*(1), 239 247.

Brenning, A., Long, S., & Fieguth, P. (2012). Detecting rock glacier flow structures using Gabor filters and IKONOS imagery. *Remote Sensing of environment*, *125*, 227 237.

Brenning, A., Peña, M., Long, S., & Soliman, A. (2012). Thermal remote sensing of ice-debris landforms using ASTER: an example from the Chilean Andes. *The Cryosphere*, *6*(2), 367.

Broderick, D. E., Frey, K. E., Rogan, J., Alexander, H. D., & Zimov, N. S. (2015). Estimating upper soil horizon carbon stocks in a permafrost watershed of Northeast Siberia by integrating field measurements with Landsat-5 TM and WorldView-2 satellite data. *GIScience & Remote Sensing*, *52*(2), 131 157.

Brooker, A., Fraser, R. H., Olthof, I., Kokelj, S. V., & Lacelle, D. (2014). Mapping the activity and evolution of retrogressive thaw slumps by tasselled cap trend analysis of a Landsat satellite image stack. *Permafrost and Periglacial Processes*, *25*(4), 243 256.

Brothers, L. L., Hart, P. E., & Ruppel, C. D. (2012). Minimum distribution of subsea ice-bearing permafrost on the US Beaufort Sea continental shelf. *Geophysical research letters*, *39*(15).

Brown, D., Jorgenson, M. T., Kielland, K., Verbyla, D. L., Prakash, A., & Koch, J. C. (2016). Landscape effects of wildfire on permafrost distribution in interior Alaska derived from remote sensing. *Remote Sensing*, *8*(8), 654.

Brown, J., Ferrians, O., Heginbottom, J., & Melnikov, E. (2002). Circum-Arctic map of permafrost and ground-ice conditions, version 2. *Boulder, Colorado USA, National Snow and Ice Data Center*. (doi: `https://doi.org/10.7265/skbg-kf16`)

Brown, J., Hinkel, K. M., & Nelson, F. (2000). The circumpolar active layer monitoring (CALM) program: research designs and initial results. *Polar Geography*, *24*(3), 166 258.

Brown, R. D., & Robinson, D. A. (2011). Northern Hemisphere spring snow cover variability and change over 1922-2010 including an assessment of uncertainty. *The Cryosphere*, *5*(1), 219.

Cao, B., Zhang, T., Wu, Q., Sheng, Y., Zhao, L., & Zou, D. (2019). Permafrost zonation index map and statistics over the Qinghai Tibet Plateau based on field evidence. *Permafrost and Periglacial Processes*, *30*(3), 178 194.

Carpino, O. A., Berg, A. A., Quinton, W. L., & Adams, J. R. (2018). Climate change and permafrost thaw-induced boreal forest loss in northwestern Canada. *Environmental Research Letters*, *13*(8), 084018.

Carroll, M. L., & Loboda, T. V. (2018). The sign, magnitude and potential drivers of change in surface water extent in Canadian tundra. *Environmental Research Letters*, *13*(4), 045009.

Central Institute for Meteorology and Geodynamics Section Climate Change Impacts. (n.d.). *COLD Yamal - COmbining remote sensing and field studies for assessment of Landform Dynamics and permafrost state on Yamal.* `http://cold.zgis.net/`. (Accessed: October 28th 2020)

Chang, L., & Hanssen, R. F. (2015). Detection of permafrost sensitivity of the Qinghai Tibet railway using satellite radar interferometry. *International journal of remote sensing*, *36*(3), 691 700.

Chasmer, L., & Hopkinson, C. (2017). Threshold loss of discontinuous permafrost and landscape evolution. *Global change biology*, *23*(7), 2672 2686.

Chasmer, L., Hopkinson, C., Veness, T., Quinton, W., & Baltzer, J. (2014). A decision-tree classification for low-lying complex land cover types within the zone of discontinuous permafrost. *Remote Sensing of Environment*, *143*, 73 84.

Chasmer, L., Quinton, W., Hopkinson, C., Petrone, R., & Whittington, P. (2011). Vegetation canopy and radiation controls on permafrost plateau evolution within the discontinuous permafrost zone, Northwest Territories, Canada. *Permafrost and Periglacial Processes*, *22*(3), 199 213.

Chen, F., Lin, H., Li, Z., Chen, Q., & Zhou, J. (2012). Interaction between permafrost and infrastructure along the Qinghai Tibet Railway detected via jointly analysis of C-and L-band small baseline SAR interferometry. *Remote sensing of environment*, *123*, 532 540.

Chen, F., Lin, H., Zhou, W., Hong, T., & Wang, G. (2013). Surface deformation detected by ALOS PALSAR small baseline SAR interferometry over permafrost en-

vironment of Beiluhe section, Tibet Plateau, China. *Remote sensing of environment*, *138*, 10 18.

Chen, J., Chen, X., Cui, X., & Chen, J. (2010). Change vector analysis in posterior probability space: A new method for land cover change detection. *IEEE Geoscience and Remote Sensing Letters*, *8*(2), 317 321.

Chen, J., Günther, F., Grosse, G., Liu, L., & Lin, H. (2018). Sentinel-1 InSAR Measurements of Elevation Changes over Yedoma Uplands on Sobo-Sise Island, Lena Delta. *Remote Sensing*, *10*(7), 1152.

Chen, W., Zhang, Y., Cihlar, J., Smith, S. L., & Riseborough, D. W. (2003). Changes in soil temperature and active layer thickness during the twentieth century in a region in western Canada. *Journal of Geophysical Research: Atmospheres*, *108*(D22).

Cheng, D., Meng, G., Cheng, G., & Pan, C. (2016). SeNet: Structured edge network for sea land segmentation. *IEEE Geoscience and Remote Sensing Letters*, *14*(2), 247 251.

Cheng, G. (2005). Permafrost studies in the Qinghai Tibet plateau for road construction. *Journal of Cold Regions Engineering*, *19*(1), 19 29.

Chimitdorzhiev, T. N., Dagurov, P. N., Bykov, M. E., Dmitriev, A. V., & Kirbizhekova, I. I. (2016). Comparison of ALOS PALSAR interferometry and field geodetic leveling for marshy soil thaw/freeze monitoring, case study from the Baikal lake region, Russia. *Journal of Applied Remote Sensing*, *10*(1), 016006.

Clarivate Analytics. (n.d.). *Web of Science.* `https://apps.webofknowledge.com/`. (Accessed: September 13th 2020)

Climate and Cryosphere (CliC). (n.d.). *About CliC.* `http://www.climate-cryosphere.org/about`. (Accessed: November 16th 2020)

Coch, C., Ramage, J., Lamoureux, S., Meyer, H., Knoblauch, C., & Lantuit, H. (2020). Spatial variability of dissolved organic carbon, solutes, and suspended sediment in disturbed Low Arctic coastal watersheds. *Journal of Geophysical Research: Biogeosciences*, *125*(2), e2019JG005505.

Cohen, D., Lee, T. B., & Sklar, D. (2004). *Precalculus: A Problems-Oriented Approach.* Cengage Learning.

Cohen, J., Screen, J. A., Furtado, J. C., Barlow, M., Whittleston, D., Coumou, D., . . . others (2014). Recent Arctic amplification and extreme mid-latitude weather. *Nature geoscience*, *7*(9), 627 637.

Connon, R. F., Quinton, W. L., Craig, J. R., & Hayashi, M. (2014). Changing hydrologic connectivity due to permafrost thaw in the lower Liard River valley, NWT, Canada. *Hydrological Processes*, *28*(14), 4163 4178.

Couture, N. J., Irrgang, A., Pollard, W., Lantuit, H., & Fritz, M. (2018). Coastal erosion of permafrost soils along the Yukon Coastal Plain and fluxes of organic carbon to the Canadian Beaufort Sea. *Journal of Geophysical Research: Biogeosciences*, *123*(2), 406 422.

Crawford, A., Stroeve, J., Smith, A., & Jahn, A. (2021). Arctic open-water periods are projected to lengthen dramatically by 2100. *Communications Earth & Environment*, *2*(1), 1 10.

Crowell, S. M., Randolph Kawa, S., Browell, E. V., Hammerling, D. M., Moore, B., Schaefer, K., & Doney, S. C. (2018). On the ability of space-based passive and active remote sensing observations of CO2 to detect flux perturbations to the carbon cycle. *Journal of Geophysical Research: Atmospheres*, *123*(2), 1460 1477.

Cunliffe, A. M., Tanski, G., Radosavljevic, B., Palmer, W. F., Sachs, T., Lantuit, H., . . . Myers-Smith, I. H. (2019). Rapid retreat of permafrost coastline observed with aerial drone photogrammetry. *The Cryosphere*, *13*, 1513 1528.

Curasi, S. R., Loranty, M. M., & Natali, S. M. (2016). Water track distribution and effects on carbon dioxide flux in an eastern Siberian upland tundra landscape. *Environmental Research Letters*, *11*(4), 045002.

Davidson, S. J., Santos, M. J., Sloan, V. L., Watts, J. D., Phoenix, G. K., Oechel, W. C., & Zona, D. (2016). Mapping Arctic tundra vegetation communities using field spectroscopy and multispectral satellite data in North Alaska, USA. *Remote Sensing*, *8*(12), 978.

Department of Remote Sensing - University of Würzburg. (2023). *Permafrost Research.* `https://permafrost.remote-sensing.org/`. (Accessed: January 14th 2023)

Department of the Interior - U.S. Geological Survey. (2022). *Landsat 8-9 Collection 2 (C2) Level 2 Science Product (L2SP) Guide.* `https://d9-wret.s3.us-west-2.amazonaws.com/assets/palladium/production/s3fs-public/media/files/LSDS-1619_Landsat-8-9-C2-L2-ScienceProductGuide-v4.pdf`. (Accessed: January 14th 2023)

Dewi, R. S., Bijker, W., & Stein, A. (2017). Change vector analysis to monitor the changes in fuzzy shorelines. *Remote sensing*, *9*(2), 147.

Diepenbroek, M., Grobe, H., Reinke, M., Schindler, U., Schlitzer, R., Sieger, R., & Wefer, G. (2002). PANGAEA an information system for environmental sciences. *Computers & Geosciences*, *28*(10), 1201 1210.

Dietz, A. J., Kuenzer, C., & Dech, S. (2015). Global SnowPack: a new set of snow cover parameters for studying status and dynamics of the planetary snow cover extent. *Remote sensing letters*, *6*(11), 844 853.

Dini, B., Daout, S., Manconi, A., & Loew, S. (2019). Classification of slope processes based on multitemporal DInSAR analyses in the Himalaya of NW Bhutan. *Remote Sensing of Environment*, *233*, 111408.

Dlugokencky, E. J., Bruhwiler, L., White, J., Emmons, L., Novelli, P. C., Montzka, S. A., . . . others (2009). Observational constraints on recent increases in the atmospheric CH4 burden. *Geophysical Research Letters*, *36*(18).

Dorigo, W., Gruber, A., De Jeu, R., Wagner, W., Stacke, T., Loew, A., . . . others (2015). Evaluation of the ESA CCI soil moisture product using ground-based observations. *Remote Sensing of Environment*, *162*, 380 395.

Doxaran, D., Devred, E., & Babin, M. (2015). A 50% increase in the mass of terrestrial particles delivered by the Mackenzie River into the Beaufort Sea (Canadian Arctic Ocean) over the last 10 years. *Biogeosciences*, *12*(11), 3551 3565.

Doxaran, D., Ehn, J., Bélanger, S., Matsuoka, A., Hooker, S., & Babin, M. (2012). Optical characterisation of suspended particles in the Mackenzie River plume (Canadian Arctic Ocean) and implications for ocean colour remote sensing. *Biogeosciences*, *9*(8), 3213 3229.

Duan, L., Man, X., Kurylyk, B. L., Cai, T., & Li, Q. (2017). Distinguishing streamflow trends caused by changes in climate, forest cover, and permafrost in a large watershed in northeastern China. *Hydrological Processes*, *31*(10), 1938 1951.

Duguay, C. R., Zhang, T., Leverington, D. W., & Romanovsky, V. E. (2005). Satellite remote sensing of permafrost and seasonally frozen ground. *GEOPHYSICAL MONOGRAPH-AMERICAN GEOPHYSICAL UNION*, *163*, 91.

Dulamsuren, C., Klinge, M., Degener, J., Khishigjargal, M., Chenlemuge, T., Bat-Enerel, B., ... others (2016). Carbon pool densities and a first estimate of the total carbon pool in the Mongolian forest-steppe. *Global Change Biology*, *22*(2), 830 844.

Duncan, B. N., Ott, L. E., Abshire, J. B., Brucker, L., Carroll, M. L., Carton, J., ... others (2020). Space-Based Observations for Understanding Changes in the Arctic-Boreal Zone. *Reviews of Geophysics*, *58*(1), e2019RG000652.

Dupeyrat, L., Hurault, B., Costard, F., Marmo, C., & Gautier, E. (2018). Satellite image analysis and frozen cylinder experiments on thermal erosion of periglacial fluvial islands. *Permafrost and Periglacial Processes*, *29*(2), 100 111.

Dvornikov, Y., Leibman, M., Heim, B., Bartsch, A., Herzschuh, U., Skorospekhova, T., ... others (2018). Terrestrial CDOM in lakes of Yamal peninsula: connection to lake and lake catchment properties. *Remote Sensing*, *10*(2), 167.

Eckerstorfer, M., Malnes, E., & Christiansen, H. (2017). Freeze/thaw conditions at periglacial landforms in Kapp Linné, Svalbard, investigated using field observations, in situ, and radar satellite monitoring. *Geomorphology*, *293*, 433 447.

Ehret, G., Bousquet, P., Pierangelo, C., Alpers, M., Millet, B., Abshire, J. B., ... others (2017). MERLIN: A French-German space lidar mission dedicated to atmospheric methane. *Remote Sensing*, *9*(10), 1052.

Ekman, M. (1996). A consistent map of the postglacial uplift of Fennoscandia. *Terra Nova*, *8*(2), 158 165.

Elder, C. D., Thompson, D. R., Thorpe, A. K., Hanke, P., Walter Anthony, K. M., & Miller, C. E. (2020). Airborne mapping reveals emergent power law of arctic methane emissions. *Geophysical Research Letters*, *47*(3), e2019GL085707.

Engram, M., Arp, C. D., Jones, B. M., Ajadi, O. A., & Meyer, F. J. (2018). Analyzing floating and bedfast lake ice regimes across Arctic Alaska using 25 years of spaceborne SAR imagery. *Remote sensing of environment*, *209*, 660 676.

Epstein, H. E., Raynolds, M. K., Walker, D. A., Bhatt, U. S., Tucker, C. J., & Pinzon, J. E. (2012). Dynamics of aboveground phytomass of the circumpolar Arctic tundra during the past three decades. *Environmental Research Letters*, *7*(1), 015506.

Eriksen, H. Ø., Lauknes, T. R., Larsen, Y., Corner, G. D., Bergh, S. G., Dehls, J., & Kierulf, H. P. (2017). Visualizing and interpreting surface displacement patterns on unstable slopes using multi-geometry satellite SAR interferometry (2D InSAR). *Remote Sensing of Environment*, *191*, 297 312.

ESA Communications. (2012). *Sentinel-1: ESA's Radar Observatory Mission for GMES Operational Services.* `https://sentinel.esa.int/documents/247904/349449/S1_SP-1322_1.pdf`. (Accessed on 14 January 2022)

Eshqi Molan, Y., Kim, J.-W., Lu, Z., Wylie, B., & Zhu, Z. (2018). Modeling wildfire-induced permafrost deformation in an alaskan boreal forest using InSAR observations. *Remote Sensing*, *10*(3), 405.

Etzelmüller, B., Heggem, E. S. F., Sharkhuu, N., Frauenfelder, R., Kääb, A., & Goulden, C. (2006). Mountain permafrost distribution modelling using a multi-criteria approach in the Hövsgöl area, northern Mongolia. *Permafrost and Periglacial Processes*, *17*(2), 91 104.

Etzelmüller, B., Ødegård, R. S., Berthling, I., & Sollid, J. L. (2001). Terrain parameters and remote sensing data in the analysis of permafrost distribution and periglacial processes: principles and examples from southern Norway. *Permafrost and Periglacial Processes*, *12*(1), 79 92.

European Space Agency. (n.d.-a). *Arctic Methane and Permafrost Challenge (AMPC).* `https://eo4society.esa.int/communities/scientists/arctic-methane-and-permafrost/`. (Accessed: November 28th 2020)

European Space Agency. (n.d.-b). *Copernicus: Sentinel-1 - The SAR Imaging Constellation for Land and Ocean Services.* `https://directory.eoportal.org/web/eoportal/satellite-missions/c-missions/copernicus-sentinel-1`. (Accessed: September 1st 2020)

European Space Agency. (n.d.-c). *GlobPermafrost- A Service for Global Permafrost Monitoring.* `http://due.esrin.esa.int/page_project161.php`. (Accessed: November 16th 2020)

European Space Agency. (n.d.-d). *Mission ends for Copernicus Sentinel-1B satellite.* `https://www.esa.int/Applications/Observing_the_Earth/Copernicus/Sentinel-1/Mission_ends_for_Copernicus_Sentinel-1B_satellite`. (Accessed on 29 November 2022)

European Space Agency. (n.d.-e). *Observation Scenario Archive.* `https://sentinels.copernicus.eu/web/sentinel/missions/sentinel-1/observation-scenario/archive`. (Accessed on 10 February 2022)

European Space Agency. (n.d.-f). *Permafrost - Information System on Permafrost.* `http://due.esrin.esa.int/page_project116.php`. (Accessed: November 16th 2020)

European Space Agency. (n.d.-g). *Permafrost is a phenomenon of the subsurface thermal state and is defined as ground at or below the freezing point of water for two or more years.* `https://climate.esa.int/en/projects/permafrost/about/`. (Accessed: September 11th 2020)

European Space Agency. (n.d.-h). *Sentinel-2 Mission Details.* `https://earth.esa.int/web/guest/missions/esa-operational-eo-missions/sentinel-2`. (Accessed: September 1st 2020)

European Space Agency. (2016). *Sentinel-2 User Handbook.* `https://sentinels.copernicus.eu/documents/247904/685211/Sentinel-2_User_Handbook`. (Accessed on 14 January 2022)

European Space Agency. (2020). *A NASA and ESA collaborative community initiative on Arctic methane and permafrost.* `https://eo4society.esa.int/2020/09/01/a-nasa-and-esa-collaborative-community-initiative-on-arctic-methane-and-permafrost/`. (Accessed: November 28th 2020)

European Space Agency, Sinergise. (2021). *Copernicus Global Digital Elevation Model. Distributed by OpenTopography.* `https://doi.org/10.5069/G9028PQB`. NERC EDS Centre for Environmental Data Analysis. (Accessed: November 14th 2022)

Euskirchen, E., McGUIRE, A. D., Kicklighter, D. W., Zhuang, Q., Clein, J. S., Dargaville, R., . . . others (2006). Importance of recent shifts in soil thermal dynamics on growing season length, productivity, and carbon sequestration in terrestrial high-latitude ecosystems. *Global Change Biology*, *12*(4), 731 750.

Evans, S. G., Ge, S., Voss, C. I., & Molotch, N. P. (2018). The role of frozen soil in groundwater discharge predictions for warming alpine watersheds. *Water Resources Research*, *54*(3), 1599 1615.

FAO, IIASA, ISRIC, ISSCAS, & JRC. (2012). *Harmonized World Soil Database (version 1.2). FAO, Rome, Italy and IIASA, Laxenburg, Austria.* `http://webarchive.iiasa.ac.at/Research/LUC/External-World-soil-database/HTML/HWSD_Data.html?sb=4`. (Accessed: September 11th 2020)

FAO, IIASA, ISRIC, ISSCAS, & JRC. (2020). *Harmonized World Soil Database v 1.2.* `http://www.fao.org/soils-portal/soil-survey/soil-maps-and-databases/harmonized-world-soil-database-v12/en/`. (Accessed: September 11th 2020)

Farquharson, L., Mann, D. H., Grosse, G., Jones, B. M., & Romanovsky, V. (2016). Spatial distribution of thermokarst terrain in Arctic Alaska. *Geomorphology*, *273*, 116 133.

Farquharson, L. M., Mann, D., Swanson, D., Jones, B., Buzard, R., & Jordan, J. (2018). Temporal and spatial variability in coastline response to declining sea-ice in northwest Alaska. *Marine Geology*, *404*, 71 83.

Farquharson, L. M., Romanovsky, V. E., Cable, W. L., Walker, D. A., Kokelj, S. V., & Nicolsky, D. (2019). Climate change drives widespread and rapid thermokarst development in very cold permafrost in the Canadian High Arctic. *Geophysical Research Letters*, *46*(12), 6681 6689.

Farr, T. G., Rosen, P. A., Caro, E., Crippen, R., Duren, R., Hensley, S., . . . others (2007). The shuttle radar topography mission. *Reviews of Geophysics*, *45*(2).

Fawcett, T. (2006). An introduction to ROC analysis. *Pattern recognition letters*, *27*(8), 861 874.

Fichot, C. G., Kaiser, K., Hooker, S. B., Amon, R. M., Babin, M., Bélanger, S., . . . Benner, R. (2013). Pan-Arctic distributions of continental runoff in the Arctic Ocean. *Scientific reports*, *3*(1), 1 6.

Finger Higgens, R., Chipman, J., Lutz, D., Culler, L., Virginia, R., & Ogden, L. (2019). Changing lake dynamics indicate a drier Arctic in Western Greenland. *Journal of Geophysical Research: Biogeosciences*, *124*(4), 870 883.

Flanders Marine Institute. (2018). *IHO Sea Areas, version 3.* `https://www .marineregions.org/`. doi: 10.7265/N5V98602

Flessa, H., Rodionov, A., Guggenberger, G., Fuchs, H., Magdon, P., Shibistova, O., . . . Blodau, C. (2008). Landscape controls of CH4 fluxes in a catchment of the forest tundra ecotone in northern Siberia. *Global Change Biology*, *14*(9), 2040 2056.

Flores, S. E., & Yool, S. R. (2007). Sensitivity of change vector analysis to land cover change in an arid ecosystem. *International Journal of Remote Sensing*, *28*(5), 1069 1088.

Forbes, B. C., Fauria, M. M., & Zetterberg, P. (2010). Russian Arctic warming and 'greening'are closely tracked by tundra shrub willows. *Global Change Biology*, *16*(5), 1542 1554.

Forkel, M., Migliavacca, M., Thonicke, K., Reichstein, M., Schaphoff, S., Weber, U., & Carvalhais, N. (2015). Codominant water control on global interannual variability and trends in land surface phenology and greenness. *Global change biology*, *21*(9), 3414 3435.

Forkel, M., Thonicke, K., Beer, C., Cramer, W., Bartalev, S., & Schmullius, C. (2012). Extreme fire events are related to previous-year surface moisture conditions in permafrost-underlain larch forests of Siberia. *Environmental Research Letters*, *7*(4), 044021.

Fouest, V. L., Matsuoka, A., Manizza, M., Shernetsky, M., Tremblay, B., & Babin, M. (2018). Towards an assessment of riverine dissolved organic carbon in surface waters of the western Arctic Ocean based on remote sensing and biogeochemical modeling. *Biogeosciences*, *15*(5), 1335 1346.

Fraser, R. H., Kokelj, S. V., Lantz, T. C., McFarlane-Winchester, M., Olthof, I., & Lacelle, D. (2018). Climate sensitivity of high Arctic permafrost terrain demonstrated by widespread ice-wedge thermokarst on Banks Island. *Remote Sensing*, *10*(6), 954.

Fraser, R. H., Olthof, I., Kokelj, S. V., Lantz, T. C., Lacelle, D., Brooker, A., . . . Schwarz, S. (2014). Detecting landscape changes in high latitude environments using landsat trend analysis: 1. Visualization. *Remote Sensing*, *6*(11), 11533 11557.

Freitas, P., Vieira, G., Canário, J., Folhas, D., & Vincent, W. F. (2019). Identification of a Threshold Minimum Area for Reflectance Retrieval from Thermokarst Lakes and Ponds Using Full-Pixel Data from Sentinel-2. *Remote Sensing*, *11*(6), 657.

Friedl, M. A., McIver, D. K., Hodges, J. C., Zhang, X. Y., Muchoney, D., Strahler, A. H., . . . others (2002). Global land cover mapping from MODIS: algorithms and early results. *Remote sensing of Environment*, *83*(1-2), 287 302.

Fritz, M., Vonk, J. E., & Lantuit, H. (2017). Collapsing arctic coastlines. *Nature Climate Change*, *7*(1), 6 7.

Frohn, R. C., Hinkel, K. M., & Eisner, W. R. (2005). Satellite remote sensing classification of thaw lakes and drained thaw lake basins on the North Slope of Alaska. *Remote sensing of environment*, *97*(1), 116 126.

Frost, G. V., Christopherson, T., Jorgenson, M. T., Liljedahl, A. K., Macander, M. J., Walker, D. A., & Wells, A. F. (2018). Regional patterns and asynchronous onset of ice-wedge degradation since the Mid-20th Century in Arctic Alaska. *Remote Sensing*, *10*(8), 1312.

Frost, G. V., & Epstein, H. E. (2014). Tall shrub and tree expansion in Siberian tundra ecotones since the 1960s. *Global change biology*, *20*(4), 1264 1277.

Frost, G. V., Epstein, H. E., & Walker, D. A. (2014). Regional and landscape-scale variability of Landsat-observed vegetation dynamics in northwest Siberian tundra. *Environmental Research Letters*, *9*(2), 025004.

Fuchs, M., Grosse, G., Strauss, J., Günther, F., Grigoriev, M., Maximov, G. M., & Hugelius, G. (2018). Carbon and nitrogen pools in thermokarst-affected permafrost landscapes in Arctic Siberia. *Biogeosciences*, *15*(3), 953 971.

Gagarin, L., Wu, Q., Melnikov, A., Volgusheva, N., Tananaev, N., Jin, H., . . . Zhizhin, V. (2020). Morphometric Analysis of Groundwater Icings: Intercomparison of Estimation Techniques. *Remote Sensing*, *12*(4), 692.

Gallerman, T., Haas, U., Teipel, U., von Poschinger, A., Wagner, B., Mahr, M., & Bäse, F. (2017). *Permafrost Messstation am Zugspitzgipfel: Ergebnisse und Modellberechnungen.* Bayerisches Landesamt für Umwelt.

Gangodagamage, C., Rowland, J. C., Hubbard, S. S., Brumby, S. P., Liljedahl, A. K., Wainwright, H., . . . others (2014). Extrapolating active layer thickness measurements across Arctic polygonal terrain using LiDAR and NDVI data sets. *Water resources research*, *50*(8), 6339 6357.

Gao, L., Liao, J., & Shen, G. (2013). Monitoring lake-level changes in the Qinghai Tibetan Plateau using radar altimeter data (2002 2012). *Journal of Applied Remote Sensing*, *7*(1), 073470.

German Aerospace Centre (DLR). (n.d.). *MERLIN - Die deutsch-französische Klimamission.* `https://www.dlr.de/rd/en/desktopdefault.aspx/tabid-2440/3586_read-31672/`. (Accessed: February 20th 2021)

Gibson, C. M., Chasmer, L. E., Thompson, D. K., Quinton, W. L., Flannigan, M. D., & Olefeldt, D. (2018). Wildfire as a major driver of recent permafrost thaw in boreal peatlands. *Nature communications*, *9*(1), 1 9.

Gisnås, K., Etzelmüller, B., Farbrot, H., Schuler, T., & Westermann, S. (2013). CryoGRID 1.0: Permafrost distribution in Norway estimated by a spatial numerical model. *Permafrost and Periglacial Processes*, *24*(1), 2 19.

GLIMS Consortium. (2005). *GLIMS Glacier Database, Version 1.* `https://nsidc.org/data/NSIDC-0272/versions/1`. NASA National Snow and Ice Data Center Distributed Active Archive Center. doi: 10.7265/N5V98602

Godin, E., Osinski, G. R., Harrison, T. N., Pontefract, A., & Zanetti, M. (2019). Geomorphology of Gullies at Thomas Lee Inlet, Devon Island, Canadian High Arctic. *Permafrost and Periglacial Processes*, *30*(1), 19 34.

Gong, W., Darrow, M. M., Meyer, F. J., & Daanen, R. P. (2019). Reconstructing movement history of frozen debris lobes in northern Alaska using satellite radar interferometry. *Remote Sensing of Environment*, *221*, 722 740.

Google Developers. (n.d.-a). *ArcticDEM Mosaic.* `https://developers.google.com/earth-engine/datasets/catalog/UMN_PGC_ArcticDEM_V3_2m_mosaic#description`. (Accessed: January 14th 2023)

Google Developers. (n.d.-b). *ArcticDEM Strips.* `https://developers.google.com/earth-engine/datasets/catalog/UMN_PGC_ArcticDEM_V3_2m#citations`. (Accessed: January 14th 2023)

Google Developers. (2021). *Sentinel-1 Algorithms.* `https://developers.google.com/earth-engine/guides/sentinel1`. (Accessed on 14 January 2022)

Gorelick, N., Hancher, M., Dixon, M., Ilyushchenko, S., Thau, D., & Moore, R. (2017). Google Earth Engine: Planetary-scale geospatial analysis for everyone. *Remote sensing of Environment*, *202*, 18 27.

Griffin, C. G., Frey, K. E., Rogan, J., & Holmes, R. M. (2011). Spatial and interannual variability of dissolved organic matter in the Kolyma River, East Siberia, observed using satellite imagery. *Journal of geophysical research: Biogeosciences*, *116*(G3).

Griffin, D., Zhao, X., McLinden, C. A., Boersma, F., Bourassa, A., Dammers, E., … others (2019). High-resolution mapping of nitrogen dioxide with TROPOMI: First results and validation over the Canadian oil sands. *Geophysical Research Letters*, *46*(2), 1049 1060.

Grosse, G., Goetz, S., McGuire, A. D., Romanovsky, V. E., & Schuur, E. A. (2016). Changing permafrost in a warming world and feedbacks to the Earth system. *Environmental Research Letters*, *11*(4), 040201.

Grosse, G., Schirrmeister, L., Kunitsky, V. V., & Hubberten, H.-W. (2005). The use of CORONA images in remote sensing of periglacial geomorphology: an illustration from the NE Siberian coast. *Permafrost and periglacial processes*, *16*(2), 163 172.

Grosse, G., Schirrmeister, L., Siegert, C., Kunitsky, V. V., Slagoda, E. A., Andreev, A. A., & Dereviagyn, A. Y. (2007). Geological and geomorphological evolution of a

sedimentary periglacial landscape in Northeast Siberia during the Late Quaternary. *Geomorphology*, *86*(1-2), 25 51.

Gruber, S., & Hoelzle, M. (2001). Statistical modelling of mountain permafrost distribution: local calibration and incorporation of remotely sensed data. *Permafrost and Periglacial Processes*, *12*(1), 69 77.

Günther, F., Overduin, P. P., Sandakov, A. V., Grosse, G., & Grigoriev, M. N. (2013). Short- and long-term thermo-erosion of ice-rich permafrost coasts in the Laptev Sea region. *Biogeosciences*, *10*(6), 4297 4318.

Günther, F., Overduin, P. P., Yakshina, I. A., Opel, T., Baranskaya, A. V., & Grigoriev, M. N. (2015). Observing Muostakh disappear: permafrost thaw subsidence and erosion of a ground-ice-rich island in response to arctic summer warming and sea ice reduction. *The Cryosphere*, *9*(1), 151 178.

Haas, A., Grosse, G., Heim, B., Schäfer-Neth, C., Laboor, S., Nitze, I., . . . Seifert, F.-M. (2017). PerSYS Permafrost Information System Web-GIS: Visualization of permafrost-related Remote Sensing products for ESA GlobPermafrost. In *2nd asian conference on permafrost, hokkaido university, sapporo.*

Hachem, S., Allard, M., & Duguay, C. (2009). Using the MODIS land surface temperature product for mapping permafrost: an application to Northern Quebec and Labrador, Canada. *Permafrost and Periglacial Processes*, *20*(4), 407 416.

Hachem, S., Duguay, C., & Allard, M. (2012). Comparison of MODIS-derived land surface temperatures with ground surface and air temperature measurements in continuous permafrost terrain. *The Cryosphere*, *6*(1), 51.

Hakkinen, S., Proshutinsky, A., & Ashik, I. (2008). Sea ice drift in the Arctic since the 1950s. *Geophysical Research Letters*, *35*(19).

Hammerling, D. M., Kawa, S. R., Schaefer, K., Doney, S., & Michalak, A. M. (2015). Detectability of CO2 flux signals by a space-based lidar mission. *Journal of Geophysical Research: Atmospheres*, *120*(5), 1794 1807.

Hao, J., Wu, T., Wu, X., Hu, G., Zou, D., Zhu, X., . . . others (2019). Investigation of a small landslide in the Qinghai-Tibet Plateau by InSAR and absolute deformation model. *Remote Sensing*, *11*(18), 2126.

Haq, M. A., & Baral, P. (2019). Study of permafrost distribution in Sikkim Himalayas using Sentinel-2 satellite images and logistic regression modelling. *Geomorphology*, *333*, 123 136.

Hartley, I. P., Hill, T. C., Wade, T. J., Clement, R. J., Moncrieff, J. B., Prieto-Blanco, A., . . . others (2015). Quantifying landscape-level methane fluxes in subarctic Finland using a multiscale approach. *Global change biology*, *21*(10), 3712 3725.

Hayman, G., Bartsch, A., Prigent, C., Aires, F., Buchwitz, M., Burrows, J., . . . others (2010). *Wetland extent and methane dynamics: An overview of the ESA ALANIS-methane project.*

He, K., Zhang, X., Ren, S., & Sun, J. (2016). Deep residual learning for image recognition. In *Proceedings of the ieee conference on computer vision and pattern recognition* (pp. 770 778).

Heaton, J. (2016). An empirical analysis of feature engineering for predictive modeling. In *Southeastcon 2016* (pp. 1 6).

Heidler, K., Mou, L., Baumhoer, C., Dietz, A., & Zhu, X. X. (2021). HED-UNet: Combined Segmentation and Edge Detection for Monitoring the Antarctic Coastline. *IEEE Transactions on Geoscience and Remote Sensing*.

Heim, B., Abramova, E., Doerffer, R., Günther, F., Hölemann, J., Kraberg, A., . . . others (2014). Ocean colour remote sensing in the southern Laptev Sea: evaluation and applications. *Biogeosciences*, *11*(15), 4191 4210.

Heim, B., Bartsch, A., Elger, K., Lantuit, H., Boike, J., Muster, S., . . . others (2011). ESA DUE Permafrost: An Earth observation (EO) permafrost monitoring system. *EARSeL eProceedings*, *10*(2), 73 82.

Helbig, M., Wischnewski, K., Kljun, N., Chasmer, L. E., Quinton, W. L., Detto, M., & Sonnentag, O. (2016). Regional atmospheric cooling and wetting effect of permafrost thaw-induced boreal forest loss. *Global Change Biology*, *22*(12), 4048 4066.

Hengl, T., Mendes de Jesus, J., Heuvelink, G. B., Ruiperez Gonzalez, M., Kilibarda, M., Blagotić, A., . . . others (2017). SoilGrids250m: Global gridded soil information based on machine learning. *PLoS one*, *12*(2), e0169748.

Herzschuh, U., Pestryakova, L. A., Savelieva, L. A., Heinecke, L., Böhmer, T., Biskaborn, B. K., . . . Birks, H. J. B. (2013). Siberian larch forests and the ion content of thaw lakes form a geochemically functional entity. *Nature Communications*, *4*(1), 1 8.

Hinkel, K., Eisner, W., & Kim, C. (2017). Detection of tundra trail damage near Barrow, Alaska using remote imagery. *Geomorphology*, *293*, 360 367.

Hinkel, K. M., Frohn, R., Nelson, F., Eisner, W., & Beck, R. (2005). Morphometric and spatial analysis of thaw lakes and drained thaw lake basins in the western Arctic Coastal Plain, Alaska. *Permafrost and Periglacial Processes*, *16*(4), 327 341.

Hinzman, L. D., Bettez, N. D., Bolton, W. R., Chapin, F. S., Dyurgerov, M. B., Fastie, C. L., . . . others (2005). Evidence and implications of recent climate change in northern Alaska and other arctic regions. *Climatic change*, *72*(3), 251 298.

Hjort, J., Karjalainen, O., Aalto, J., Westermann, S., Romanovsky, V. E., Nelson, F. E., . . . Luoto, M. (2018). Degrading permafrost puts Arctic infrastructure at risk by mid-century. *Nature communications*, *9*(1), 1 9.

Högström, E., Heim, B., Bartsch, A., Bergstedt, H., & Pointner, G. (2018). Evaluation of a MetOp ASCAT-Derived Surface Soil Moisture Product in Tundra Environments. *Journal of Geophysical Research: Earth Surface*, *123*(12), 3190 3205.

Holloway, J. E., Lamoureux, S. F., Montross, S. N., & Lafrenière, M. J. (2016). Climate and terrain characteristics linked to mud ejection occurrence in the Canadian High Arctic. *Permafrost and Periglacial Processes*, *27*(2), 204 218.

Hu, H., Landgraf, J., Detmers, R., Borsdorff, T., Aan de Brugh, J., Aben, I., . . . Hasekamp, O. (2018). Toward global mapping of methane with TROPOMI: First results and intersatellite comparison to GOSAT. *Geophysical Research Letters*, *45*(8), 3682 3689.

Hu, J., Shen, L., & Sun, G. (2018). Squeeze-and-excitation networks. In *Proceedings of the ieee conference on computer vision and pattern recognition* (pp. 7132 7141).

Hu, J., Wang, Q., Li, Z., Zhao, R., & Sun, Q. (2016). Investigating the ground deformation and source model of the Yangbajing geothermal field in Tibet, China with the WLS InSAR technique. *Remote Sensing*, *8*(3), 191.

Hu, T., Zhao, T., Zhao, K., & Shi, J. (2019). A continuous global record of near-surface soil freeze/thaw status from AMSR-E and AMSR2 data. *International Journal of Remote Sensing*, *40*(18), 6993 7016.

Huang, C., Zan, X., Yang, X., & Zhang, S. (2016). Surface water change detection using change vector analysis. In *2016 ieee international geoscience and remote sensing symposium (igarss)* (pp. 2834 2837).

Huang, G., Liu, Z., Van Der Maaten, L., & Weinberger, K. Q. (2017). Densely connected convolutional networks. In *Proceedings of the ieee conference on computer vision and pattern recognition* (pp. 4700 4708).

Huang, L., Luo, J., Lin, Z., Niu, F., & Liu, L. (2020). Using deep learning to map retrogressive thaw slumps in the Beiluhe region (Tibetan Plateau) from CubeSat images. *Remote Sensing of Environment*, *237*, 111534.

Hugelius, G., Bockheim, J. G., Camill, P., Elberling, B., Grosse, G., Harden, J. W., . . . others (2013). A new data set for estimating organic carbon storage to 3 m depth in soils of the northern circumpolar permafrost region. *Earth System Science Data (Online)*, *5*(2).

Hugelius, G., Kuhry, P., Tarnocai, C., & Virtanen, T. (2010). Soil organic carbon pools in a periglacial landscape: a case study from the central Canadian Arctic. *Permafrost and Periglacial Processes*, *21*(1), 16 29.

Humlum, O., Instanes, A., & Sollid, J. L. (2003). Permafrost in Svalbard: a review of research history, climatic background and engineering challenges. *Polar research*, *22*(2), 191 215.

International Permafrost Association. (n.d.-a). *Circumpolar Active Layer Monitoring Network (CALM).* https://ipa.arcticportal.org/products/gtn-p/calm. (Accessed: September 14th 2020)

International Permafrost Association. (n.d.-b). *Thermal State of Permafrost (TSP).* https://ipa.arcticportal.org/products/gtn-p/tsp. (Accessed: November 16th 2020)

International Permafrost Association; Arctic Portal; Alfred-Wegener-Institut. (n.d.). *About GTN-P.* https://gtnp.arcticportal.org/about-the-gtnp. (Accessed: November 16th 2020)

Irrgang, A. M., Bendixen, M., Farquharson, L. M., Baranskaya, A. V., Erikson, L. H., Gibbs, A. E., . . . others (2022). Drivers, dynamics and impacts of changing Arctic coasts. *Nature Reviews Earth & Environment*, *3*(1), 39 54.

Irrgang, A. M., Lantuit, H., Manson, G. K., Günther, F., Grosse, G., & Overduin, P. P. (2018). Variability in rates of coastal change along the Yukon coast, 1951 to 2015. *Journal of Geophysical Research: Earth Surface*, *123*(4), 779 800.

Isaev, V., Koshurnikov, A., Pogorelov, A., Amangurov, R., Podchasov, O., Sergeev, D., . . . Kioka, A. (2019). Cliff retreat of permafrost coast in south-west Baydaratskaya Bay, Kara Sea, during 2005 2016. *Permafrost and Periglacial Processes*, *30*(1), 35 47.

Iwahana, G., Harada, K., Uchida, M., Tsuyuzaki, S., Saito, K., Narita, K., . . . Hinzman, L. D. (2016). Geomorphological and geochemistry changes in permafrost after the 2002 tundra wildfire in Kougarok, Seward Peninsula, Alaska. *Journal of Geophysical Research: Earth Surface*, *121*(9), 1697 1715.

Iwahana, G., Uchida, M., Liu, L., Gong, W., Meyer, F. J., Guritz, R., . . . Hinzman, L. (2016). InSAR detection and field evidence for thermokarst after a tundra wildfire, using ALOS-PALSAR. *Remote Sensing*, *8*(3), 218.

Jackson, R. B., Saunois, M., Bousquet, P., Canadell, J. G., Poulter, B., Stavert, A. R., . . . Tsuruta, A. (2020). Increasing anthropogenic methane emissions arise equally from agricultural and fossil fuel sources. *Environmental Research Letters*, *15*(7), 071002.

Jagdhuber, T., Stockamp, J., Hajnsek, I., & Ludwig, R. (2014). Identification of soil freezing and thawing states using SAR polarimetry at C-band. *Remote Sensing*, *6*(3), 2008 2023.

Janke, J. R., Ng, S., & Bellisario, A. (2017). An inventory and estimate of water stored in firn fields, glaciers, debris-covered glaciers, and rock glaciers in the Aconcagua River Basin, Chile. *Geomorphology*, *296*, 142 152.

Jepsen, S. M., Walvoord, M. A., Voss, C. I., & Rover, J. (2016). Effect of permafrost thaw on the dynamics of lakes recharged by ice-jam floods: case study of Yukon Flats, Alaska. *Hydrological Processes*, *30*(11), 1782 1795.

Jia, Y., Kim, J.-W., Shum, C., Lu, Z., Ding, X., Zhang, L., . . . others (2017). Characterization of active layer thickening rate over the northern Qinghai-Tibetan plateau permafrost region using ALOS interferometric synthetic aperture radar data, 2007 2009. *Remote Sensing*, *9*(1), 84.

Jones, A., Stolbovay, V., Tarnocai, C., Broll, G., Spaargaren, O., Montanarella, L., et al. (2009). *Soil atlas of the northern circumpolar region.* European Commission.

Jones, B. M., Arp, C. D., Jorgenson, M. T., Hinkel, K. M., Schmutz, J. A., & Flint, P. L. (2009). Increase in the rate and uniformity of coastline erosion in Arctic Alaska. *Geophysical Research Letters*, *36*(3).

Jones, B. M., Baughman, C. A., Romanovsky, V. E., Parsekian, A. D., Babcock, E. L., Stephani, E., ... Berg, E. E. (2016). Presence of rapidly degrading permafrost plateaus in south-central Alaska. *The Cryosphere*, *10*(6), 2673 2692.

Jones, B. M., Farquharson, L. M., Baughman, C. A., Buzard, R. M., Arp, C. D., Grosse, G., ... others (2018). A decade of remotely sensed observations highlight complex processes linked to coastal permafrost bluff erosion in the Arctic. *Environmental Research Letters*, *13*(11), 115001.

Jones, B. M., Grosse, G., Arp, C., Jones, M., Anthony, K. W., & Romanovsky, V. (2011). Modern thermokarst lake dynamics in the continuous permafrost zone, northern Seward Peninsula, Alaska. *Journal of Geophysical Research: Biogeosciences*, *116*(G2).

Jones, B. M., Grosse, G., Arp, C. D., Miller, E., Liu, L., Hayes, D. J., & Larsen, C. F. (2015). Recent Arctic tundra fire initiates widespread thermokarst development. *Scientific reports*, *5*(1), 1 13.

Jones, B. M., Irrgang, A. M., Farquharson, L. M., Lantuit, H., Whalen, D., Ogorodov, S., ... others (2020). Coastal Permafrost Erosion. *Arctic report card*, *15*.

Jones, M. C., Grosse, G., Jones, B. M., & Walter Anthony, K. (2012). Peat accumulation in drained thermokarst lake basins in continuous, ice-rich permafrost, northern Seward Peninsula, Alaska. *Journal of Geophysical Research: Biogeosciences*, *117*(G2).

Jones, M. K. W., Pollard, W. H., & Jones, B. M. (2019). Rapid initialization of retrogressive thaw slumps in the Canadian high Arctic and their response to climate and terrain factors. *Environmental Research Letters*, *14*(5), 055006.

Jørgensen, C. J., Johansen, K. M. L., Westergaard-Nielsen, A., & Elberling, B. (2015). Net regional methane sink in High Arctic soils of northeast Greenland. *Nature Geoscience*, *8*(1), 20 23.

Jorgenson, J. C., Jorgenson, M. T., Boldenow, M. L., & Orndahl, K. M. (2018). Landscape change detected over a half century in the Arctic National Wildlife Refuge using high-resolution aerial imagery. *Remote Sensing*, *10*(8), 1305.

Jorgenson, M., & Osterkamp, T. E. (2005). Response of boreal ecosystems to varying modes of permafrost degradation. *Canadian Journal of Forest Research*, *35*(9), 2100 2111.

Jorgenson, M. T., Frost, G. V., & Dissing, D. (2018). Drivers of landscape changes in coastal ecosystems on the Yukon-Kuskokwim Delta, Alaska. *Remote Sensing*, *10*(8), 1280.

Jorgenson, M. T., & Grosse, G. (2016). Remote sensing of landscape change in permafrost regions. *Permafrost and periglacial processes*, *27*(4), 324 338.

Jorgenson, M. T., Harden, J., Kanevskiy, M., O'Donnell, J., Wickland, K., Ewing, S., ... others (2013). Reorganization of vegetation, hydrology and soil carbon after permafrost degradation across heterogeneous boreal landscapes. *Environmental Research Letters*, *8*(3), 035017.

Juhls, B., Overduin, P. P., Hölemann, J., Hieronymi, M., Matsuoka, A., Heim, B., & Fischer, J. (2019). Dissolved organic matter at the fluvial marine transition in the Laptev Sea using in situ data and ocean colour remote sensing. *Biogeosciences*, *16*(13), 2693 2713.

Jun, C., Ban, Y., & Li, S. (2014). Open access to Earth land-cover map. *Nature*, *514*(7523), 434 434.

Juszak, I., Erb, A. M., Maximov, T. C., & Schaepman-Strub, G. (2014). Arctic shrub effects on NDVI, summer albedo and soil shading. *Remote Sensing of Environment*, *153*, 79 89.

Kääb, A. (2002). Monitoring high-mountain terrain deformation from repeated air-and spaceborne optical data: examples using digital aerial imagery and ASTER data. *ISPRS Journal of Photogrammetry and remote sensing*, *57*(1-2), 39 52.

Kääb, A. (2008). Remote sensing of permafrost-related problems and hazards. *Permafrost and periglacial processes*, *19*(2), 107 136.

Kääb, A., Huggel, C., Fischer, L., Guex, S., Paul, F., Roer, I., . . . Weidmann, Y. (2005). Remote sensing of glacier- and permafrost-related hazards in high mountains: an overview. *Natural Hazards and Earth System Sciences*, *5*(4), 527 554. Retrieved from `https://nhess.copernicus.org/articles/5/527/2005/` doi: 10.5194/nhess-5-527-2005

Karlsson, J. M., Lyon, S. W., & Destouni, G. (2014). Temporal behavior of lake size-distribution in a thawing permafrost landscape in northwestern Siberia. *Remote sensing*, *6*(1), 621 636.

Kartoziia, A. (2019). Assessment of the ice wedge polygon current state by means of UAV imagery analysis (Samoylov Island, the Lena Delta). *Remote Sensing*, *11*(13), 1627.

Kasprzak, M., Łopuch, M., Głowacki, T., & Milczarek, W. (2020). Evolution of Near-Shore Outwash Fans and Permafrost Spreading Under Their Surface: A Case Study from Svalbard. *Remote Sensing*, *12*(3), 482.

Kenyi, L. W., & Kaufmann, V. (2003). Estimation of rock glacier surface deformation using SAR interferometry data. *IEEE Transactions on Geoscience and Remote Sensing*, *41*(6), 1512 1515.

Kharuk, V. I., Ranson, K. J., Im, S. T., & Il'ya, A. P. (2015). Climate-induced larch growth response within the central Siberian permafrost zone. *Environmental Research Letters*, *10*(12), 125009.

Kharuk, V. I., Shushpanov, A. S., Im, S. T., & Ranson, K. J. (2016). Climate-induced landsliding within the larch dominant permafrost zone of central Siberia. *Environmental research letters*, *11*(4), 045004.

Kim, E., & England, A. (2003). A yearlong comparison of plot-scale and satellite footprint-scale 19 and 37 GHz brightness of the Alaskan North Slope. *Journal of Geophysical Research: Atmospheres*, *108*(D13).

Kim, Y., Kimball, J. S., Glassy, J. M., & Du, J. (2017). An extended global Earth system data record on daily landscape freeze thaw status determined from satellite passive microwave remote sensing. *Earth System Science Data*, *9*, 133 147.

Kim, Y., Kimball, J. S., Robinson, D., & Derksen, C. (2015). New satellite climate data records indicate strong coupling between recent frozen season changes and snow cover over high northern latitudes. *Environmental Research Letters*, *10*(8), 084004.

Kim, Y., Kimball, J. S., Zhang, K., & McDonald, K. C. (2012). Satellite detection of increasing Northern Hemisphere non-frozen seasons from 1979 to 2008: Implications for regional vegetation growth. *Remote Sensing of Environment*, *121*, 472 487.

Kizyakov, A., Khomutov, A., Zimin, M., Khairullin, R., Babkina, E., Dvornikov, Y., & Leibman, M. (2018). Microrelief associated with gas emission craters: Remote-sensing and field-based study. *Remote Sensing*, *10*(5), 677.

Kizyakov, A., Zimin, M., Sonyushkin, A., Dvornikov, Y., Khomutov, A., & Leibman, M. (2017). Comparison of gas emission crater geomorphodynamics on Yamal and Gydan Peninsulas (Russia), based on repeat very-high-resolution stereopairs. *Remote Sensing*, *9*(10), 1023.

Klein, B., & Rossin, D. (1999). Data quality in neural network models: effect of error rate and magnitude of error on predictive accuracy. *Omega*, *27*(5), 569 582.

Klein, I., Gessner, U., Dietz, A. J., & Kuenzer, C. (2017). Global WaterPack A 250 m resolution dataset revealing the daily dynamics of global inland water bodies. *Remote sensing of environment*, *198*, 345 362.

Klein, K. P., Lantuit, H., Heim, B., Fell, F., Doxaran, D., & Irrgang, A. M. (2019). Long-term high-resolution sediment and sea surface temperature spatial patterns in Arctic nearshore waters retrieved using 30-year landsat archive imagery. *Remote Sensing*, *11*(23), 2791.

Kleinen, T., & Brovkin, V. (2018). Pathway-dependent fate of permafrost region carbon. *Environmental Research Letters*, *13*(9), 094001.

Klinge, M., Dulamsuren, C., Erasmi, S., Karger, D. N., & Hauck, M. (2018). Climate effects on vegetation vitality at the treeline of boreal forests of Mongolia. *Biogeosciences*, *15*(5), 1319 1333.

Kohnert, K., Juhls, B., Muster, S., Antonova, S., Serafimovich, A., Metzger, S., . . . Sachs, T. (2018). Toward understanding the contribution of waterbodies to the methane emissions of a permafrost landscape on a regional scale   A case study from the Mackenzie delta, Canada. *Global change biology*, *24*(9), 3976 3989.

Kokelj, S., Tunnicliffe, J., Lacelle, D., Lantz, T., Chin, K., & Fraser, R. (2015). Increased precipitation drives mega slump development and destabilization of ice-rich permafrost terrain, northwestern Canada. *Global and Planetary Change*, *129*, 56 68.

Kokelj, S. V., & Jorgenson, M. (2013). Advances in thermokarst research. *Permafrost and Periglacial Processes*, *24*(2), 108 119.

KoPf. (n.d.). *KoPf Carbon in permafrost.* `http://www.kopf-permafrost.de/index.php?id=36`. (Accessed: February 26th 2021)

Koven, C. D., Lawrence, D. M., & Riley, W. J. (2015). Permafrost carbon- climate feedback is sensitive to deep soil carbon decomposability but not deep soil nitrogen dynamics. *Proceedings of the National Academy of Sciences*, *112*(12), 3752 3757.

Koven, C. D., Schuur, E., Schädel, C., Bohn, T., Burke, E., Chen, G., . . . others (2015). A simplified, data-constrained approach to estimate the permafrost carbon climate feedback. *Philosophical Transactions of the Royal Society A: Mathematical, Physical and Engineering Sciences*, *373*(2054), 20140423.

Kremer, M., Lewkowicz, A. G., Bonnaventure, P. P., & Sawada, M. C. (2011). Utility of classification and regression tree analyses and vegetation in mountain permafrost models, Yukon, Canada. *Permafrost and Periglacial Processes*, *22*(2), 163 178.

Kroisleitner, C., Bartsch, A., & Bergstedt, H. (2018). Circumpolar patterns of potential mean annual ground temperature based on surface state obtained from microwave satellite data. *The Cryosphere*, *12*(7), 2349 2370.

Kupilik, M., Witmer, F. D., MacLeod, E.-A., Wang, C., & Ravens, T. (2018). Gaussian Process Regression for Arctic Coastal Erosion Forecasting. *IEEE Transactions on Geoscience and Remote Sensing*, *57*(3), 1256 1264.

Landerer, F. W., Dickey, J. O., & Güntner, A. (2010). Terrestrial water budget of the Eurasian pan-Arctic from GRACE satellite measurements during 2003 2009. *Journal of Geophysical Research: Atmospheres*, *115*(D23).

Landmann, T., Schramm, M., Huettich, C., & Dech, S. (2013). MODIS-based change vector analysis for assessing wetland dynamics in Southern Africa. *Remote Sensing Letters*, *4*(2), 104 113.

Langaas, S. (1995). *Completeness of the Digital Chart of the World (DCW) database.* UNEP/GRID-Arendal.

Langer, M., Westermann, S., & Boike, J. (2010). Spatial and temporal variations of summer surface temperatures of wet polygonal tundra in Siberia-implications for MODIS LST based permafrost monitoring. *Remote Sensing of Environment*, *114*(9), 2059 2069.

Langer, M., Westermann, S., Heikenfeld, M., Dorn, W., & Boike, J. (2013). Satellite-based modeling of permafrost temperatures in a tundra lowland landscape. *Remote Sensing of Environment*, *135*, 12 24.

Langford, Z. L., Kumar, J., Hoffman, F. M., Breen, A. L., & Iversen, C. M. (2019). Arctic vegetation mapping using unsupervised training datasets and convolutional neural networks. *Remote Sensing*, *11*(1), 69.

Lantuit, H. (2019, 09). Nunataryuk - Permafrost Thaw and the changing Arctic coast, science for socioeconomic adaptation. In *5th yes congress.*

Lantuit, H., Overduin, P. P., Couture, N., & Ødegård, R. (2008). Sensitivity of coastal erosion to ground ice contents: an arctic-wide study based on the acd classification

of arctic coasts. In *Proceedings of the 9 international conference on permafrost*th (pp. 1025 1029).

Lantuit, H., Overduin, P. P., Couture, N., Wetterich, S., Aré, F., Atkinson, D., . . . others (2012). The Arctic coastal dynamics database: a new classification scheme and statistics on Arctic permafrost coastlines. *Estuaries and Coasts*, *35*(2), 383 400.

Lantuit, H., & Pollard, W. (2008). Fifty years of coastal erosion and retrogressive thaw slump activity on Herschel Island, southern Beaufort Sea, Yukon Territory, Canada. *Geomorphology*, *95*(1-2), 84 102.

Lantz, T., & Turner, K. (2015). Changes in lake area in response to thermokarst processes and climate in Old Crow Flats, Yukon. *Journal of Geophysical Research: Biogeosciences*, *120*(3), 513 524.

Lara, M. J., Chipman, M. L., & Hu, F. S. (2019). Automated detection of thermoerosion in permafrost ecosystems using temporally dense Landsat image stacks. *Remote Sensing of Environment*, *221*, 462 473.

Lara, M. J., Genet, H., McGuire, A. D., Euskirchen, E. S., Zhang, Y., Brown, D. R., . . . Bolton, W. R. (2016). Thermokarst rates intensify due to climate change and forest fragmentation in an Alaskan boreal forest lowland. *Global Change Biology*, *22*(2), 816 829.

Lara, M. J., Nitze, I., Grosse, G., Martin, P., & McGuire, A. D. (2018). Reduced arctic tundra productivity linked with landform and climate change interactions. *Scientific Reports*, *8*(1), 1 10.

Larue, F., Royer, A., De Sève, D., Langlois, A., Roy, A., & Brucker, L. (2017). Validation of GlobSnow-2 snow water equivalent over Eastern Canada. *Remote Sensing of Environment*, *194*, 264 277.

LeCun, Y., Bengio, Y., & Hinton, G. (2015). Deep learning. *nature*, *521*(7553), 436 444.

Li, C., Lu, H., Leung, L. R., Yang, K., Li, H., Wang, W., . . . Chen, Y. (2019). Improving land surface temperature simulation in CoLM over the Tibetan Plateau through fractional vegetation cover derived from a remotely sensed clumping index and model-simulated leaf area index. *Journal of Geophysical Research: Atmospheres*, *124*(5), 2620 2642.

Li, R., Liu, W., Yang, L., Sun, S., Hu, W., Zhang, F., & Li, W. (2018). DeepUNet: A deep fully convolutional network for pixel-level sea-land segmentation. *IEEE Journal of Selected Topics in Applied Earth Observations and Remote Sensing*, *11*(11), 3954 3962.

Li, X., Jin, H., He, R., Huang, Y., Wang, H., Luo, D., . . . others (2019). Effects of forest fires on the permafrost environment in the northern Da Xing'anling (Hinggan) mountains, Northeast China. *Permafrost and Periglacial Processes*, *30*(3), 163 177.

Li, X., Jin, R., Pan, X., Zhang, T., & Guo, J. (2012). Changes in the near-surface soil freeze thaw cycle on the Qinghai-Tibetan Plateau. *International Journal of Applied Earth Observation and Geoinformation*, *17*, 33 42.

Liang, L., Liu, Q., Liu, G., Li, H., & Huang, C. (2019). Accuracy Evaluation and Consistency Analysis of Four Global Land Cover Products in the Arctic Region. *Remote Sensing*, *11*(12), 1396.

Lighthill, M. J., & Lighthill, J. (2001). *Waves in fluids.* Cambridge university press.

Liljedahl, A. K., Boike, J., Daanen, R. P., Fedorov, A. N., Frost, G. V., Grosse, G., ... others (2016). Pan-Arctic ice-wedge degradation in warming permafrost and its influence on tundra hydrology. *Nature Geoscience*, *9*(4), 312 318.

Liu, J., Chen, J., & Cihlar, J. (2003). Mapping evapotranspiration based on remote sensing: An application to Canada's landmass. *Water resources research*, *39*(7).

Liu, J., Wang, S., Yu, S., Yang, D., & Zhang, L. (2009). Climate warming and growth of high-elevation inland lakes on the Tibetan Plateau. *Global and Planetary Change*, *67*(3-4), 209 217.

Liu, L., Schaefer, K., Chen, A., Gusmeroli, A., Zebker, H., & Zhang, T. (2015). Remote sensing measurements of thermokarst subsidence using InSAR. *Journal of Geophysical Research: Earth Surface*, *120*(9), 1935 1948.

Liu, L., Schaefer, K., Gusmeroli, A., Grosse, G., Jones, B. M., Zhang, T., ... Zebker, H. A. (2014). Seasonal thaw settlement at drained thermokarst lake basins, Arctic Alaska. *Cryosphere*, *8*, 815 826.

Liu, L., Zhang, T., & Wahr, J. (2010). InSAR measurements of surface deformation over permafrost on the North Slope of Alaska. *Journal of Geophysical Research: Earth Surface*, *115*(F3).

López-Martínez, J., Serrano, E., Schmid, T., Mink, S., & Linés, C. (2012). Periglacial processes and landforms in the South Shetland Islands (northern Antarctic Peninsula region). *Geomorphology*, *155*, 62 79.

Loranty, M. M., Natali, S. M., Berner, L. T., Goetz, S. J., Holmes, R. M., Davydov, S. P., ... Zimov, S. A. (2014). Siberian tundra ecosystem vegetation and carbon stocks four decades after wildfire. *Journal of Geophysical Research: Biogeosciences*, *119*(11), 2144 2154.

Lorente, A., Borsdorff, T., Butz, A., Hasekamp, O., Schneider, A., Wu, L., ... others (2021). Methane retrieved from TROPOMI: improvement of the data product and validation of the first 2 years of measurements. *Atmospheric Measurement Techniques*, *14*(1), 665 684.

Lousada, M., Pina, P., Vieira, G., Bandeira, L., & Mora, C. (2018). Evaluation of the use of very high resolution aerial imagery for accurate ice-wedge polygon mapping (Adventdalen, Svalbard). *Science of the Total Environment*, *615*, 1574 1583.

Lu, X., & Zhuang, Q. (2011). Areal changes of land ecosystems in the Alaskan Yukon River Basin from 1984 to 2008. *Environmental Research Letters*, *6*(3), 034012.

Luo, J., Niu, F., Lin, Z., Liu, M., & Yin, G. (2019). Recent acceleration of thaw slumping in permafrost terrain of Qinghai-Tibet Plateau: An example from the Beiluhe Region. *Geomorphology*, *341*, 79 85.

Luo, J., Yin, G., Niu, F., Lin, Z., & Liu, M. (2019). High spatial resolution modeling of climate change impacts on permafrost thermal conditions for the Beiluhe Basin, Qinghai-Tibet Plateau. *Remote Sensing*, *11*(11), 1294.

Lyons, E. A., Sheng, Y., Smith, L. C., Li, J., Hinkel, K. M., Lenters, J. D., & Wang, J. (2013). Quantifying sources of error in multitemporal multisensor lake mapping. *International Journal of Remote Sensing*, *34*(22), 7887 7905.

Lyu, Z., & Zhuang, Q. (2018). Quantifying the effects of snowpack on soil thermal and carbon dynamics of the Arctic terrestrial ecosystems. *Journal of Geophysical Research: Biogeosciences*, *123*(4), 1197 1212.

Mahoney, A. R., Eicken, H., Gaylord, A. G., & Gens, R. (2014). Landfast sea ice extent in the Chukchi and Beaufort Seas: The annual cycle and decadal variability. *Cold Regions Science and Technology*, *103*, 41 56.

Mair, V., Zischg, A. P., Lang, K., Tonidandel, D., Krainer, K., Kellerer-Pirklbauer, A., . . . Böckli, L. (2011). *PermaNET, Permafrost Long-term Monitoring Network.* International Research Society INTERPRAEVENT.

Malila, W. A. (1980). Change vector analysis: an approach for detecting forest changes with Landsat. In *Lars symposia* (p. 385).

Mao, D., Wang, Z., Yang, H., Li, H., Thompson, J. R., Li, L., . . . Wu, J. (2018). Impacts of climate change on Tibetan lakes: Patterns and processes. *Remote Sensing*, *10*(3), 358.

Marchand, N., Royer, A., Krinner, G., Roy, A., Langlois, A., & Vargel, C. (2018). Snow-Covered Soil Temperature Retrieval in Canadian Arctic Permafrost Areas, Using a Land Surface Scheme Informed with Satellite Remote Sensing Data. *Remote Sensing*, *10*(11), 1703.

Marconcini, M., Fernandez-Prieto, D., Pinnock, S., Hayman, G., Helbert, J., & de Leeuw, G. (2010). ALANIS: A Joint ESA-Ileaps Atmosphere-Land Interaction Study over Boreal Eurasia. *iLEAPS Newsletter*, *10*, 28 33.

Meng, Y., Lan, H., Li, L., Wu, Y., & Li, Q. (2015). Characteristics of surface deformation detected by X-band SAR Interferometry over Sichuan-Tibet grid connection project area, China. *Remote Sensing*, *7*(9), 12265 12281.

Meredith, M., Sommerkorn, M., Cassotta, S., Derksen, C., Ekaykin, A., Hollowed, A., . . . others (2019). Chapter 3: Polar Regions. In Pörtner, H.O., Roberts, D.C., Masson-Delmotte, V., Zhai, P., Tignor, M., Poloczanska, E., Mintenbeck, K., Nicolai, M., Okem, A., Petzold, J., Rama, B., Weyer, N. (Eds.) IPCC Special Report on the Ocean and Cryosphere in a Changing Climate. *IPCC Intergovernmental Panel on Climate Change (IPCC).*

Mętrak, M., Szwarczewski, P., Bińka, K., Rojan, E., Karasiński, J., Górecki, G., & Suska-Malawska, M. (2019). Late Holocene development of Lake Rangkul (Eastern Pamir, Tajikistan) and its response to regional climatic changes. *Palaeogeography, Palaeoclimatology, Palaeoecology*, *521*, 99 113.

Metsämäki, S., Pulliainen, J., Salminen, M., Luojus, K., Wiesmann, A., Solberg, R., ... Ripper, E. (2015). Introduction to GlobSnow Snow Extent products with considerations for accuracy assessment. *Remote Sensing of Environment*, *156*, 96 108.

Michaelides, R. J., Schaefer, K., Zebker, H. A., Parsekian, A., Liu, L., Chen, J., ... Schaefer, S. R. (2019). Inference of the impact of wildfire on permafrost and active layer thickness in a discontinuous permafrost region using the remotely sensed active layer thickness (ReSALT) algorithm. *Environmental Research Letters*, *14*(3), 035007.

Mikola, J., Virtanen, T., Linkosalmi, M., Vähä, E., Nyman, J., Postanogova, O., ... others (2018). Spatial variation and linkages of soil and vegetation in the Siberian Arctic tundra coupling field observations with remote sensing data. *Biogeosciences*, *15*(9), 2781 2801.

Miller, C., Griffith, P., Goetz, S., Hoy, E., Pinto, N., McCubbin, I., ... others (2019). An overview of ABoVE airborne campaign data acquisitions and science opportunities. *Environmental Research Letters*, *14*(8), 080201.

Mink, S., López-Martínez, J., Maestro, A., Garrote, J., Ortega, J. A., Serrano, E., ... Schmid, T. (2014). Insights into deglaciation of the largest ice-free area in the South Shetland Islands (Antarctica) from quantitative analysis of the drainage system. *Geomorphology*, *225*, 4 24.

Miranda, V., Pina, P., Heleno, S., Vieira, G., Mora, C., & Schaefer, C. E. (2020). Monitoring recent changes of vegetation in Fildes Peninsula (King George Island, Antarctica) through satellite imagery guided by UAV surveys. *Science of The Total Environment*, *704*, 135295.

Mohammadimanesh, F., Salehi, B., Mahdianpari, M., English, J., Chamberland, J., & Alasset, P.-J. (2019). Monitoring surface changes in discontinuous permafrost terrain using small baseline SAR interferometry, object-based classification, and geological features: a case study from Mayo, Yukon Territory, Canada. *GIScience & Remote Sensing*, *56*(4), 485 510.

Monnier, S., Kinnard, C., Surazakov, A., & Bossy, W. (2014). Geomorphology, internal structure, and successive development of a glacier foreland in the semiarid Chilean Andes (Cerro Tapado, upper Elqui Valley, 30°08' S., 69°55' W.). *Geomorphology*, *207*, 126 140.

Mooney, P., Corcoran, P., & Winstanley, A. C. (2010). Towards quality metrics for OpenStreetMap. In *Proceedings of the 18th sigspatial international conference on advances in geographic information systems* (pp. 514 517).

Morgenstern, A., Grosse, G., Günther, F., Fedorova, I., & Schirrmeister, L. (2011). Spatial analyses of thermokarst lakes and basins in Yedoma landscapes of the Lena Delta. *The Cryosphere Discussions*, *5*, 1495 1545.

Morgenstern, A., Ulrich, M., Günther, F., Roessler, S., Fedorova, I. V., Rudaya, N. A., ... Schirrmeister, L. (2013). Evolution of thermokarst in East Siberian ice-rich permafrost: A case study. *Geomorphology*, *201*, 363 379.

Morin, P., Porter, C., Cloutier, M., Howat, I., Noh, M.-J., Willis, M., ... Peterman, K. (2016). ArcticDEM; a publically available, high resolution elevation model of the Arctic. *EGUGA*, EPSC2016 8396.

Morse, P., & Wolfe, S. (2015). Geological and meteorological controls on icing (aufeis) dynamics (1985 to 2014) in subarctic Canada. *Journal of Geophysical Research: Earth Surface*, *120*(9), 1670 1686.

Moura, P. A., Francelino, M. R., Schaefer, C. E. G., Simas, F. N., & de Mendonça, B. A. (2012). Distribution and characterization of soils and landform relationships in Byers Peninsula, Livingston Island, Maritime Antarctica. *Geomorphology*, *155*, 45 54.

Muskett, R. R., & Romanovsky, V. E. (2009). Groundwater storage changes in arctic permafrost watersheds from GRACE and in situ measurements. *Environmental Research Letters*, *4*(4), 045009.

Muskett, R. R., & Romanovsky, V. E. (2011). Alaskan permafrost groundwater storage changes derived from GRACE and ground measurements. *Remote Sensing*, *3*(2), 378 397.

Muster, S., Heim, B., Abnizova, A., & Boike, J. (2013). Water body distributions across scales: A remote sensing based comparison of three arctic tundra wetlands. *Remote Sensing*, *5*(4), 1498 1523.

Muster, S., Langer, M., Abnizova, A., Young, K. L., & Boike, J. (2015). Spatio-temporal sensitivity of MODIS land surface temperature anomalies indicates high potential for large-scale land cover change detection in Arctic permafrost landscapes. *Remote sensing of environment*, *168*, 1 12.

Muster, S., Riley, W. J., Roth, K., Langer, M., Cresto Aleina, F., Koven, C. D., ... others (2019). Size distributions of Arctic waterbodies reveal consistent relations in their statistical moments in space and time. *Frontiers in Earth Science*, *7*, 5.

Muster, S., Roth, K., Langer, M., Lange, S., Cresto Aleina, F., Bartsch, A., ... others (2017). PeRL: A circum-Arctic permafrost region pond and lake database. *Earth System Science Data*, *9*(1), 317 348.

Mutlu, E. (2019). *What is Robustness in Statistics? A Brief Intro to Robust Estimators.* https://towardsdatascience.com/what-is-robustness-in-statistics-a-brief-intro-to-robust-estimators-e926d74d1609. (Accessed: April 11th 2021)

Myers-Smith, I. H., Kerby, J. T., Phoenix, G. K., Bjerke, J. W., Epstein, H. E., Assmann, J. J., ... others (2020). Complexity revealed in the greening of the Arctic. *Nature Climate Change*, *10*(2), 106 117.

Naeimi, V., Paulik, C., Bartsch, A., Wagner, W., Kidd, R., Park, S.-E., ... Boike, J. (2012). ASCAT Surface State Flag (SSF): Extracting information on surface freeze/thaw conditions from backscatter data using an empirical threshold-analysis algorithm. *IEEE Transactions on Geoscience and Remote Sensing*, *50*(7), 2566 2582.

Nagai, H., Fujita, K., Nuimura, T., & Sakai, A. (2013). Southwest-facing slopes control the formation of debris-covered glaciers in the Bhutan Himalaya. *The Cryosphere*, *7*(4), 1303 1314.

Nagy, B., Ignéczi, Á., Kovács, J., Szalai, Z., & Mari, L. (2019). Shallow ground temperature measurements on the highest volcano on Earth, Mt. Ojos del Salado, Arid Andes, Chile. *Permafrost and Periglacial Processes*, *30*(1), 3 18.

Nassar, R., Sioris, C. E., Jones, D. B., & McConnell, J. C. (2014). Satellite observations of CO2 from a highly elliptical orbit for studies of the Arctic and boreal carbon cycle. *Journal of Geophysical Research: Atmospheres*, *119*(5), 2654 2673.

National Aeronautics and Space Administration (NASA). (n.d.). *Earth Expeditions: ABoVE.* `https://www.nasa.gov/content/earth-expeditions-above`. (Accessed: November 16th 2020)

National Oceanic and Atmospheric Administration (NOAA). (2022a). *Tidal Datums - NOAA Tides, and Currents.* `https://tidesandcurrents.noaa.gov/datum_options.html`. (Accessed on 14 October 2022)

National Oceanic and Atmospheric Administration (NOAA). (2022b). *Water Levels - NOAA Tides, and Currents.* `https://tidesandcurrents.noaa.gov/stations.html?type=Water+Levels`. (Accessed on 14 October 2022)

National Research Council. (2014). *Opportunities to use remote sensing in understanding permafrost and related ecological characteristics: Report of a workshop.* National Academies Press.

National Snow and Ice Data Center (NSIDC). (2020). *National Snow and Ice Data Center.* `https://nsidc.org/`. (Accessed: September 25th 2020)

Natural Earth. (n.d.). *Natural Earth I with Shaded Relief and Water.* `https://www.naturalearthdata.com/downloads/10m-raster-data/10m-natural-earth-1/`. (Accessed: August 28th 2020)

Necsoiu, M., Dinwiddie, C. L., Walter, G. R., Larsen, A., & Stothoff, S. A. (2013). Multi-temporal image analysis of historical aerial photographs and recent satellite imagery reveals evolution of water body surface area and polygonal terrain morphology in Kobuk Valley National Park, Alaska. *Environmental Research Letters*, *8*(2), 025007.

Necsoiu, M., Onaca, A., Wigginton, S., & Urdea, P. (2016). Rock glacier dynamics in Southern Carpathian Mountains from high-resolution optical and multi-temporal SAR satellite imagery. *Remote sensing of environment*, *177*, 21 36.

Nguyen, T.-N., Burn, C. R., King, D. J., & Smith, S. (2009). Estimating the extent of near-surface permafrost using remote sensing, Mackenzie Delta, Northwest Territories. *Permafrost and Periglacial Processes*, *20*(2), 141 153.

Nielsen, D. M., Pieper, P., Barkhordarian, A., Overduin, P., Ilyina, T., Brovkin, V., . . . Dobrynin, M. (2022). Increase in Arctic coastal erosion and its sensitivity to warming in the twenty-first century. *Nature Climate Change*, *12*(3), 263 270.

Nill, L., Ullmann, T., Kneisel, C., Sobiech-Wolf, J., & Baumhauer, R. (2019). Assessing Spatiotemporal Variations of Landsat Land Surface Temperature and Multispectral

Indices in the Arctic Mackenzie Delta Region between 1985 and 2018. *Remote Sensing*, *11*(19), 2329.

Nitze, I., & Grosse, G. (2016). Detection of landscape dynamics in the Arctic Lena Delta with temporally dense Landsat time-series stacks. *Remote Sensing of Environment*, *181*, 27 41.

Nitze, I., Grosse, G., Jones, B. M., Arp, C. D., Ulrich, M., Fedorov, A., & Veremeeva, A. (2017). Landsat-based trend analysis of lake dynamics across northern permafrost regions. *Remote Sensing*, *9*(7), 640.

Nitze, I., Grosse, G., Jones, B. M., Romanovsky, V. E., & Boike, J. (2018). Remote sensing quantifies widespread abundance of permafrost region disturbances across the Arctic and Subarctic. *Nature communications*, *9*(1), 1 11.

Niu, F., Yin, G., Luo, J., Lin, Z., & Liu, M. (2018). Permafrost distribution along the Qinghai-Tibet Engineering Corridor, China using high-resolution statistical mapping and modeling integrated with remote sensing and GIS. *Remote Sensing*, *10*(2), 215.

NOAA Earth System Research Laboratories. (n.d.-a). *Cooperative Air Sampling Network.* `https://www.esrl.noaa.gov/gmd/ccgg/flask.html`. (Accessed: October 28th 2020)

NOAA Earth System Research Laboratories. (n.d.-b). *NOAA Cooperative Global Air Sampling Network - Greenhouse Gases.* `https://www.esrl.noaa.gov/gmd/obop/mlo/programs/esrl/ccg/ccg.html`. (Accessed: October 28th 2020)

Novikova, A., Belova, N., Baranskaya, A., Aleksyutina, D., Maslakov, A., Zelenin, E., . . . Ogorodov, S. (2018). Dynamics of permafrost coasts of Baydaratskaya Bay (Kara Sea) based on multi-temporal remote sensing data. *Remote Sensing*, *10*(9), 1481.

NUNATARYUK. (n.d.). *NUNATARYUK - The Project.* `https://nunataryuk.org/about`. (Accessed: November 16th 2020)

Nyland, K. E., Gunn, G. E., Shiklomanov, N. I., Engstrom, R. N., & Streletskiy, D. A. (2018). Land cover change in the lower Yenisei River using dense stacking of landsat imagery in Google Earth Engine. *Remote Sensing*, *10*(8), 1226.

Obu, J., Lantuit, H., Grosse, G., Günther, F., Sachs, T., Helm, V., & Fritz, M. (2017). Coastal erosion and mass wasting along the Canadian Beaufort Sea based on annual airborne LiDAR elevation data. *Geomorphology*, *293*, 331 346.

Obu, J., Lantuit, H., Myers-Smith, I., Heim, B., Wolter, J., & Fritz, M. (2017). Effect of terrain characteristics on soil organic carbon and total nitrogen stocks in soils of Herschel Island, Western Canadian Arctic. *Permafrost and Periglacial Processes*, *28*(1), 92 107.

Obu, J., Westermann, S., Barboux, C., Bartsch, A., Delaloye, R., Grosse, G., . . . Wiesmann, A. (2021a). *ESA Permafrost Climate Change Initiative (Permafrost_cci): Permafrost active layer thickness for the Northern Hemisphere, v3.0.* NERC EDS Centre for Environmental Data Analysis. (Accessed: September 11th 2022) doi: doi:10.5285/67a3f8c8dc914ef99f7f08eb0d997e23

Obu, J., Westermann, S., Barboux, C., Bartsch, A., Delaloye, R., Grosse, G., ... Wiesmann, A. (2021b). *ESA Permafrost Climate Change Initiative (Permafrost_cci): Permafrost extent for the Northern Hemisphere, v3.0.* NERC EDS Centre for Environmental Data Analysis. (Accessed: September 11th 2022) doi: doi:10.5285/6e2091cb0c8b4106921b63cd5357c97c

Obu, J., Westermann, S., Bartsch, A., Berdnikov, N., Christiansen, H. H., Dashtseren, A., ... others (2019). Northern Hemisphere permafrost map based on TTOP modelling for 2000 2016 at 1 km2 scale. *Earth-Science Reviews*, *193*, 299 316.

Obu, J., Westermann, S., Vieira, G., Abramov, A., Balks, M. R., Bartsch, A., ... Ramos, M. (2020). Pan-Antarctic map of near-surface permafrost temperatures at 1 km 2 scale. *The Cryosphere*, *14*(2), 497 519.

Oelke, C., & Zhang, T. (2004). A model study of circum-Arctic soil temperatures. *Permafrost and Periglacial Processes*, *15*(2), 103 121.

Oelke, C., Zhang, T., Serreze, M. C., & Armstrong, R. L. (2003). Regional-scale modeling of soil freeze/thaw over the Arctic drainage basin. *Journal of Geophysical Research: Atmospheres*, *108*(D10).

Olthof, I., Fraser, R. H., & Schmitt, C. (2015). Landsat-based mapping of thermokarst lake dynamics on the Tuktoyaktuk Coastal Plain, Northwest Territories, Canada since 1985. *Remote Sensing of Environment*, *168*, 194 204.

OpenStreetMap. (n.d.). *Contributors.* `https://wiki.openstreetmap.org/wiki/Contributors#Denmark`. (Accessed on 22 January 2023)

OpenStreetMap contributors. (2017). *Planet dump retrieved from `https://planet.osm.org`.* `https://www.openstreetmap.org`.

Oppenheimer, M., Glavovic, B., Hinkel, J., van de Wal, R., Magnan, A. K., Abd-Elgawad, A., ... others (2019). Sea level rise and implications for low lying islands, coasts and communities. *IPCC Special Report on the Ocean and Cryosphere in a Changing Climate (in press).*

Ou, C., LaRocque, A., Leblon, B., Zhang, Y., Webster, K., & McLaughlin, J. (2016). Modelling and mapping permafrost at high spatial resolution using Landsat and Radarsat-2 images in Northern Ontario, Canada: Part 2 regional mapping. *International Journal of Remote Sensing*, *37*(12), 2751 2779.

Ou, C., Leblon, B., Zhang, Y., LaRocque, A., Webster, K., & McLaughlin, J. (2016). Modelling and mapping permafrost at high spatial resolution using Landsat and Radarsat images in northern Ontario, Canada: Part 1 model calibration. *International Journal of Remote Sensing*, *37*(12), 2727 2750.

Overduin, P. P., Strzelecki, M. C., Grigoriev, M. N., Couture, N., Lantuit, H., St-Hilaire-Gravel, D., ... Wetterich, S. (2014). Coastal changes in the Arctic. *Geological Society, London, Special Publications*, *388*(1), 103 129.

PAGE21. (n.d.). *PAGE21 - Changing Permafrost in the Arctic and its Global Effects in the 21st Century.* `https://www.page21.eu/`. (Accessed: October 28th 2020)

Paltan, H., Dash, J., & Edwards, M. (2015). A refined mapping of Arctic lakes using Landsat imagery. *International Journal of Remote Sensing*, *36*(23), 5970 5982.

Panda, S., Prakash, A., Jorgenson, M., & Solie, D. (2012). Near-surface permafrost distribution mapping using logistic regression and remote sensing in Interior Alaska. *GIScience & Remote Sensing*, *49*(3), 346 363.

Panda, S. K., Prakash, A., Solie, D. N., Romanovsky, V. E., & Jorgenson, M. T. (2010). Remote sensing and field-based mapping of permafrost distribution along the Alaska Highway corridor, interior Alaska. *Permafrost and Periglacial Processes*, *21*(3), 271 281.

Park, H., Kim, Y., & Kimball, J. S. (2016). Widespread permafrost vulnerability and soil active layer increases over the high northern latitudes inferred from satellite remote sensing and process model assessments. *Remote Sensing of Environment*, *175*, 349 358.

Park, S.-E., Bartsch, A., Sabel, D., Wagner, W., Naeimi, V., & Yamaguchi, Y. (2011). Monitoring freeze/thaw cycles using ENVISAT ASAR Global Mode. *Remote Sensing of Environment*, *115*(12), 3457 3467.

Pastick, N. J., Jorgenson, M. T., Goetz, S. J., Jones, B. M., Wylie, B. K., Minsley, B. J., . . . Jorgenson, J. C. (2019). Spatiotemporal remote sensing of ecosystem change and causation across Alaska. *Global change biology*, *25*(3), 1171 1189.

Pastick, N. J., Jorgenson, M. T., Wylie, B. K., Minsley, B. J., Ji, L., Walvoord, M. A., . . . Rose, J. R. (2013). Extending airborne electromagnetic surveys for regional active layer and permafrost mapping with remote sensing and ancillary data, Yukon Flats Ecoregion, Central Alaska. *Permafrost and Periglacial Processes*, *24*(3), 184 199.

Pastick, N. J., Jorgenson, M. T., Wylie, B. K., Nield, S. J., Johnson, K. D., & Finley, A. O. (2015). Distribution of near-surface permafrost in Alaska: Estimates of present and future conditions. *Remote Sensing of Environment*, *168*, 301 315.

Pastick, N. J., Jorgenson, M. T., Wylie, B. K., Rose, J. R., Rigge, M., & Walvoord, M. A. (2014). Spatial variability and landscape controls of near-surface permafrost within the Alaskan Yukon River basin. *Journal of Geophysical Research: Biogeosciences*, *119*(6), 1244 1265.

Pearson, R. G., Phillips, S. J., Loranty, M. M., Beck, P. S., Damoulas, T., Knight, S. J., & Goetz, S. J. (2013). Shifts in Arctic vegetation and associated feedbacks under climate change. *Nature climate change*, *3*(7), 673 677.

Pekel, J.-F., Cottam, A., Gorelick, N., & Belward, A. S. (2016). High-resolution mapping of global surface water and its long-term changes. *Nature*, *540*(7633), 418 422.

Perbet, P., Fortin, M., Ville, A., & Béland, M. (2019). Near real-time deforestation detection in Malaysia and Indonesia using change vector analysis with three sensors. *International Journal of Remote Sensing*, *40*(19), 7439 7458.

Bibliography

Permafrost Carbon Network. (n.d.). *Permafrost Carbon Network.* `http://www.permafrostcarbon.org/index.html`. (Accessed: October 28th 2020)

PermaNet Alpine Space. (n.d.). *The PermaNET project.* `http://www.permanet-alpinespace.eu/project.html`. (Accessed: November 16th 2020)

PERMOS. (n.d.). *PERMOS - Swiss Permafrost Monitoring Network.* `http://www.permos.ch/`. (Accessed: November 16th 2020)

Philipp, M., Dietz, A., Buchelt, S., & Kuenzer, C. (2021). Trends in satellite Earth observation for permafrost related analyses A review. *Remote Sensing*, *13*(6), 1217.

Philipp, M., Dietz, A., Ullmann, T., & Kuenzer, C. (2022). Automated Extraction of Annual Erosion Rates for Arctic Permafrost Coasts Using Sentinel-1, Deep Learning, and Change Vector Analysis. *Remote Sensing*, *14*(15), 3656.

Philipp, M., Dietz, A., Ullmann, T., & Kuenzer, C. (2023). A Circum-Arctic Monitoring Framework for Quantifying Annual Erosion Rates of Permafrost Coasts. *Remote Sensing*, *15*(3), 818.

Pierangelo, C., Millet, B., Esteve, F., Alpers, M., Ehret, G., Flamant, P., . . . others (2016). Merlin (methane remote sensing Lidar mission): An overview. In *Epj web of conferences* (Vol. 119, p. 26001).

Piliouras, A., & Rowland, J. C. (2020). Arctic river delta morphologic variability and implications for riverine fluxes to the coast. *Journal of Geophysical Research: Earth Surface*, *125*(1), e2019JF005250.

Ping, C.-L., Michaelson, G. J., Guo, L., Jorgenson, M. T., Kanevskiy, M., Shur, Y., . . . Liang, J. (2011). Soil carbon and material fluxes across the eroding Alaska Beaufort Sea coastline. *Journal of Geophysical Research: Biogeosciences*, *116*(G2).

Plummer, S., Lecomte, P., & Doherty, M. (2017). The ESA climate change initiative (CCI): A European contribution to the generation of the global climate observing system. *Remote Sensing of Environment*, *203*, 2 8.

Poggio, L., De Sousa, L. M., Batjes, N. H., Heuvelink, G., Kempen, B., Ribeiro, E., & Rossiter, D. (2021). SoilGrids 2.0: producing soil information for the globe with quantified spatial uncertainty. *Soil*, *7*(1), 217 240.

Poggio, L., & de Souse, L. (2020). *SoilGrids250m 2.0 - Soil organic carbon stock.* `https://doi.org/10.17027/isric-soilgrids.713396f4-1687-11ea-a7c0-a0481ca9e724`. ISRIC - World Soil Information. (Accessed: November 14th 2022)

Polar Geospatial Center. (2023). *ArcticDEM.* `https://www.pgc.umn.edu/data/arcticdem/`. (Accessed: January 14th 2023)

Porter, C., Morin, P., Howat, I., Noh, M.-J., Bates, B., Peterman, K., . . . Bojesen, M. (2018). *ArcticDEM, Version 3.* `https://doi.org/10.7910/DVN/OHHUKH`. Harvard Dataverse, V1. (Accessed: September 11th 2022)

Pörtner, H.-O., Roberts, D. C., Masson-Delmotte, V., Zhai, P., Tignor, M., Poloczan-ska, E., ... others (2019). IPCC special report on the ocean and cryosphere in a changing climate. *IPCC Intergovernmental Panel on Climate Change (IPCC)*.

Powers, D. M. (2020). Evaluation: from precision, recall and F-measure to ROC, informedness, markedness and correlation. *arXiv preprint arXiv:2010.16061*.

Qingbai, W., Yongzhi, L., Jianming, Z., & Changjiang, T. (2002). A review of recent frozen soil engineering in permafrost regions along Qinghai-Tibet Highway, China. *Permafrost and Periglacial Processes*, *13*(3), 199 205.

Quinton, W., Hayashi, M., & Chasmer, L. (2011). Permafrost-thaw-induced land-cover change in the Canadian subarctic: implications for water resources. *Hydrological Processes*, *25*(1), 152 158.

Quinton, W., Hayashi, M., & Pietroniro, A. (2003). Connectivity and storage functions of channel fens and flat bogs in northern basins. *Hydrological Processes*, *17*(18), 3665 3684.

Rachold, V., Bolshiyanov, D. Y., Grigoriev, M. N., Hubberten, H.-W., Junker, R., Kunitsky, V. V., ... Schneider, W. (2007). Nearshore Arctic subsea permafrost in transition. *Eos, Transactions American Geophysical Union*, *88*(13), 149 150.

Radosavljevic, B., Lantuit, H., Pollard, W., Overduin, P., Couture, N., Sachs, T., ... Fritz, M. (2016). Erosion and flooding threats to coastal infrastructure in the Arctic: a case study from Herschel Island, Yukon Territory, Canada. *Estuaries and Coasts*, *39*(4), 900 915.

Ramage, J. L., Irrgang, A. M., Herzschuh, U., Morgenstern, A., Couture, N., & Lantuit, H. (2017). Terrain controls on the occurrence of coastal retrogressive thaw slumps along the Yukon Coast, Canada. *Journal of Geophysical Research: Earth Surface*, *122*(9), 1619 1634.

Ramage, J. L., Irrgang, A. M., Morgenstern, A., & Lantuit, H. (2018). Increasing coastal slump activity impacts the release of sediment and organic carbon into the Arctic Ocean. *Biogeosciences*, *15*(5), 1483 1495.

Ran, Y., Li, X., & Cheng, G. (2018). Climate warming over the past half century has led to thermal degradation of permafrost on the Qinghai Tibet Plateau. *The Cryosphere*, *12*(2), 595 608.

Raup, B., Racoviteanu, A., Khalsa, S. J. S., Helm, C., Armstrong, R., & Arnaud, Y. (2007). The GLIMS geospatial glacier database: a new tool for studying glacier change. *Global and Planetary Change*, *56*(1-2), 101 110.

Ravanel, L., Magnin, F., & Deline, P. (2017). Impacts of the 2003 and 2015 summer heatwaves on permafrost-affected rock-walls in the Mont Blanc massif. *Science of the Total Environment*, *609*, 132 143.

Rawlins, M. A., Mcguire, A. D., Kimball, J. S., Dass, P., Lawrence, D., Burke, E., ... others (2015). Assessment of model estimates of land-atmosphere CO 2 exchange across Northern Eurasia. *Biogeosciences*, *12*(14), 4385 4405.

Raynolds, M. K., & Walker, D. A. (2016). Increased wetness confounds Landsat-derived NDVI trends in the central Alaska North Slope region, 1985 2011. *Environmental Research Letters*, *11*(8), 085004.

Raynolds, M. K., Walker, D. A., Balser, A., Bay, C., Campbell, M., Cherosov, M. M., . . . others (2019). A raster version of the Circumpolar Arctic Vegetation Map (CAVM). *Remote Sensing of Environment*, *232*, 111297.

Regmi, P., Grosse, G., Jones, M. C., Jones, B. M., & Anthony, K. W. (2012). Characterizing post-drainage succession in thermokarst lake basins on the Seward Peninsula, Alaska with TerraSAR-X backscatter and Landsat-based NDVI data. *Remote Sensing*, *4*(12), 3741 3765.

Reschke, J., Bartsch, A., Schlaffer, S., & Schepaschenko, D. (2012). Capability of C-band SAR for operational wetland monitoring at high latitudes. *Remote Sensing*, *4*(10), 2923 2943.

Rey, D. M., Walvoord, M., Minsley, B., Rover, J., & Singha, K. (2019). Investigating lake-area dynamics across a permafrost-thaw spectrum using airborne electromagnetic surveys and remote sensing time-series data in Yukon Flats, Alaska. *Environmental Research Letters*, *14*(2), 025001.

Richards, J. A., et al. (2009). *Remote sensing with imaging radar* (Vol. 1). Springer.

Riseborough, D., Shiklomanov, N., Etzelmüller, B., Gruber, S., & Marchenko, S. (2008). Recent advances in permafrost modelling. *Permafrost and Periglacial Processes*, *19*(2), 137 156.

Rolph, R., Overduin, P. P., Ravens, T., Lantuit, H., & Langer, M. (2022). ArcticBeach v1. 0: A physics-based parameterization of pan-Arctic coastline erosion. *Frontiers in Earth Science*, *10*, 962208.

Romanovsky, V. E., Smith, S. L., & Christiansen, H. H. (2010). Permafrost thermal state in the polar Northern Hemisphere during the international polar year 2007 2009: a synthesis. *Permafrost and Periglacial processes*, *21*(2), 106 116.

Ronneberger, O., Fischer, P., & Brox, T. (2015). U-net: Convolutional networks for biomedical image segmentation. In *International conference on medical image computing and computer-assisted intervention* (pp. 234 241).

Rouyet, L., Lauknes, T. R., Christiansen, H. H., Strand, S. M., & Larsen, Y. (2019). Seasonal dynamics of a permafrost landscape, Adventdalen, Svalbard, investigated by InSAR. *Remote Sensing of Environment*, *231*, 111236.

Roy, A., Royer, A., Derksen, C., Brucker, L., Langlois, A., Mialon, A., & Kerr, Y. H. (2015). Evaluation of spaceborne L-band radiometer measurements for terrestrial freeze/thaw retrievals in Canada. *IEEE Journal of Selected Topics in Applied Earth Observations and Remote Sensing*, *8*(9), 4442 4459.

Rozhnova, M. (2021). *Impact of dataset errors on model accuracy.* https://medium.com/deelvin-machine-learning/impact-of-dataset-errors -on-model-accuracy-723fef5e0b28. (Accessed on 28 November 2022)

Rudy, A. C., Lamoureux, S. F., Treitz, P., Short, N., & Brisco, B. (2018). Seasonal and multi-year surface displacements measured by DInSAR in a High Arctic permafrost environment. *International journal of applied Earth observation and geoinformation*, *64*, 51 61.

Runge, A., & Grosse, G. (2019). Comparing Spectral Characteristics of Landsat-8 and Sentinel-2 Same-Day Data for Arctic-Boreal Regions. *Remote Sensing*, *11*(14), 1730.

Russakovsky, O., Deng, J., Su, H., Krause, J., Satheesh, S., Ma, S., ... others (2015). Imagenet large scale visual recognition challenge. *International journal of computer vision*, *115*(3), 211 252.

Sakai, T., Matsunaga, T., Maksyutov, S., Gotovtsev, S., Gagarin, L., Hiyama, T., & Yamaguchi, Y. (2016). Climate-Induced Extreme Hydrologic Events in the Arctic. *Remote Sensing*, *8*(11), 971.

Samsonov, S. V., Lantz, T. C., Kokelj, S. V., & Zhang, Y. (2016). Growth of a young pingo in the Canadian Arctic observed by RADARSAT-2 interferometric satellite radar. *The Cryosphere*, *10*(2), 799 810.

Sannel, A., & Kuhry, P. (2011). Warming-induced destabilization of peat plateau/thermokarst lake complexes. *Journal of Geophysical Research: Biogeosciences*, *116*(G3).

Schaefer, K., Lantuit, H., Romanovsky, V. E., Schuur, E. A., & Witt, R. (2014). The impact of the permafrost carbon feedback on global climate. *Environmental Research Letters*, *9*(8), 085003.

Schaefer, K., Liu, L., Parsekian, A., Jafarov, E., Chen, A., Zhang, T., ... Schaefer, T. (2015). Remotely sensed active layer thickness (ReSALT) at Barrow, Alaska using interferometric synthetic aperture radar. *Remote Sensing*, *7*(4), 3735 3759.

Schnabel, W. E., Goering, D. J., & Dotson, A. D. (2020). Permafrost Engineering on Impermanent Frost. *The Bridge*, *50*(1), 16 23.

Schneider, J., Grosse, G., & Wagner, D. (2009). Land cover classification of tundra environments in the Arctic Lena Delta based on Landsat 7 ETM+ data and its application for upscaling of methane emissions. *Remote Sensing of Environment*, *113*(2), 380 391.

Schneising, O., Buchwitz, M., Reuter, M., Bovensmann, H., Burrows, J. P., Borsdorff, T., ... others (2019). A scientific algorithm to simultaneously retrieve carbon monoxide and methane from TROPOMI onboard Sentinel-5 Precursor. *Atmospheric Measurement Techniques*, *12*(12), 6771 6802.

Schubert, A., Miranda, N., Geudtner, D., & Small, D. (2017). Sentinel-1A/B combined product geolocation accuracy. *Remote sensing*, *9*(6), 607.

Schubert, A., Small, D., Miranda, N., Geudtner, D., & Meier, E. (2015). Sentinel-1A product geolocation accuracy: Commissioning phase results. *Remote sensing*, *7*(7), 9431 9449.

Schuur, E. A., McGuire, A. D., Schädel, C., Grosse, G., Harden, J., Hayes, D. J., . . . others (2015). Climate change and the permafrost carbon feedback. *Nature*, *520*(7546), 171 179.

Schwamborn, G., & Wetterich, S. (2015). Russian-German cooperation CARBOPERM: field campaigns to Bol'shoy Lyakhovsky Island in 2014. *Berichte zur Polar-und Meeresforschung= Reports on polar and marine research*, *686*.

SEARCH. (n.d.). *SEARCH - Vision and Mission.* `https://www.searcharcticscience.org/vision`. (Accessed: November 16th 2020)

Segal, R. A., Lantz, T. C., & Kokelj, S. V. (2016). Acceleration of thaw slump activity in glaciated landscapes of the Western Canadian Arctic. *Environmental Research Letters*, *11*(3), 034025.

Séjourné, A., Costard, F., Fedorov, A., Gargani, J., Skorve, J., Massé, M., & Mège, D. (2015). Evolution of the banks of thermokarst lakes in Central Yakutia (Central Siberia) due to retrogressive thaw slump activity controlled by insolation. *Geomorphology*, *241*, 31 40.

Serreze, M. C., & Barry, R. G. (2011). Processes and impacts of Arctic amplification: A research synthesis. *Global and planetary change*, *77*(1-2), 85 96.

Shadrick, J. R., Rood, D. H., Hurst, M. D., Piggott, M. D., Hebditch, B. G., Seal, A. J., & Wilcken, K. M. (2022). Sea-level rise will likely accelerate rock coast cliff retreat rates. *Nature Communications*, *13*(1), 1 12.

Shi, X., Liao, M., Wang, T., Zhang, L., Shan, W., & Wang, C. (2014). Expressway deformation mapping using high-resolution TerraSAR-X images. *Remote Sensing Letters*, *5*(2), 194 203.

Shi, Y., Niu, F., Yang, C., Che, T., Lin, Z., & Luo, J. (2018). Permafrost presence/absence mapping of the Qinghai-Tibet Plateau based on multi-source remote sensing data. *Remote Sensing*, *10*(2), 309.

Shiklomanov, N., Nelson, F., Streletskiy, D., Hinkel, K., & Brown, J. (2008). The circumpolar active layer monitoring (CALM) program: data collection, management, and dissemination strategies. In *Proceedings of the ninth international conference on permafrost* (Vol. 29, pp. 1647 1652).

Short, N., Brisco, B., Couture, N., Pollard, W., Murnaghan, K., & Budkewitsch, P. (2011). A comparison of TerraSAR-X, RADARSAT-2 and ALOS-PALSAR interferometry for monitoring permafrost environments, case study from Herschel Island, Canada. *Remote Sensing of Environment*, *115*(12), 3491 3506.

Short, N., LeBlanc, A.-M., Sladen, W., Oldenborger, G., Mathon-Dufour, V., & Brisco, B. (2014). RADARSAT-2 D-InSAR for ground displacement in permafrost terrain, validation from Iqaluit Airport, Baffin Island, Canada. *Remote Sensing of Environment*, *141*, 40 51.

Siewert, M. B., Hanisch, J., Weiss, N., Kuhry, P., Maximov, T. C., & Hugelius, G. (2015). Comparing carbon storage of Siberian tundra and taiga permafrost ecosys-

tems at very high spatial resolution. *Journal of Geophysical Research: Biogeosciences*, *120*(10), 1973 1994.

Simonyan, K., & Zisserman, A. (2014). Very deep convolutional networks for large-scale image recognition. *arXiv preprint arXiv:1409.1556*.

Siwe, R. N., & Koch, B. (2008). Change vector analysis to categorise land cover change processes using the tasselled cap as biophysical indicator. *Environmental monitoring and assessment*, *145*(1), 227 235.

Sjöberg, Y., Hugelius, G., & Kuhry, P. (2013). Thermokarst lake morphometry and erosion features in two peat plateau areas of northeast European Russia. *Permafrost and Periglacial Processes*, *24*(1), 75 81.

Slater, A. G., & Lawrence, D. M. (2013). Diagnosing present and future permafrost from climate models. *Journal of Climate*, *26*(15), 5608 5623.

Smith, M. W., & Riseborough, D. W. (1996). Permafrost monitoring and detection of climate change. *Permafrost and Periglacial Processes*, *7*(4), 301 309.

Soliman, A., Duguay, C., Saunders, W., & Hachem, S. (2012). Pan-arctic land surface temperature from MODIS and AATSR: Product development and intercomparison. *Remote Sensing*, *4*(12), 3833 3856.

Song, C., Xu, X., Sun, X., Tian, H., Sun, L., Miao, Y., . . . Guo, Y. (2012). Large methane emission upon spring thaw from natural wetlands in the northern permafrost region. *Environmental Research Letters*, *7*(3), 034009.

Song, Y., Jin, L., & Wang, H. (2018). Vegetation changes along the Qinghai-Tibet Plateau engineering corridor since 2000 induced by climate change and human activities. *Remote Sensing*, *10*(1), 95.

Spreen, G., Kaleschke, L., & Heygster, G. (2008). Sea ice remote sensing using AMSR-E 89-GHz channels. *Journal of Geophysical Research: Oceans*, *113*(C2).

Stephan, C., Alpers, M., Millet, B., Ehret, G., Flamant, P., & Deniel, C. (2011). MERLIN: a space-based methane monitor. In *Lidar remote sensing for environmental monitoring xii* (Vol. 8159, p. 815908).

Stephani, E., Drage, J., Miller, D., Jones, B. M., & Kanevskiy, M. (2020). Taliks, cryopegs, and permafrost dynamics related to channel migration, Colville River Delta, Alaska. *Permafrost and Periglacial Processes*, *31*(2), 239 254.

Stettner, S., Beamish, A. L., Bartsch, A., Heim, B., Grosse, G., Roth, A., & Lantuit, H. (2018). Monitoring inter-and intra-seasonal dynamics of rapidly degrading ice-rich permafrost riverbanks in the Lena Delta with TerraSAR-X time series. *Remote Sensing*, *10*(1), 51.

Strozzi, T., Antonova, S., Günther, F., Mätzler, E., Vieira, G., Wegmüller, U., . . . Bartsch, A. (2018). Sentinel-1 SAR interferometry for surface deformation monitoring in low-land permafrost areas. *Remote Sensing*, *10*(9), 1360.

Strozzi, T., Caduff, R., Jones, N., Barboux, C., Delaloye, R., Bodin, X., . . . Schrott, L. (2020). Monitoring Rock Glacier Kinematics with Satellite Synthetic Aperture Radar. *Remote Sensing*, *12*(3), 559.

Strozzi, T., Delaloye, R., Kääb, A., Ambrosi, C., Perruchoud, E., & Wegmüller, U. (2010). Combined observations of rock mass movements using satellite SAR interferometry, differential GPS, airborne digital photogrammetry, and airborne photography interpretation. *Journal of Geophysical Research: Earth Surface*, *115*(F1).

Strozzi, T., Kääb, A., & Frauenfelder, R. (2004). Detecting and quantifying mountain permafrost creep from in situ inventory, space-borne radar interferometry and airborne digital photogrammetry. *International Journal of Remote Sensing*, *25*(15), 2919 2931.

Study of Environmental Change (SEARCH). (2005). *Study of Environmental Arctic Change: Plans for Implementation During the International Polar Year and Beyond.* `https://www.arcus.org/files/publication/23146/siw_report_final .pdf`. Arctic Research Consortium of the United States (ARCUS). (Accessed: October 28th 2020)

Subcommittee, P. (1988). Glossary of permafrost and related ground-ice terms. *Associate Committee on Geotechnical Research, National Research Council of Canada, Ottawa*, *156*.

Sun, Z., Wang, Q., Xiao, Q., Batkhishig, O., & Watanabe, M. (2015). Diverse responses of remotely sensed grassland phenology to interannual climate variability over frozen ground regions in Mongolia. *Remote Sensing*, *7*(1), 360 377.

Surdu, C. M., Duguay, C. R., & Fernández Prieto, D. (2016). Evidence of recent changes in the ice regime of lakes in the Canadian High Arctic from spaceborne satellite observations. *The Cryosphere*, *10*(3), 941 960.

Suzuki, K., Matsuo, K., Yamazaki, D., Ichii, K., Iijima, Y., Papa, F., . . . Hiyama, T. (2018). Hydrological variability and changes in the Arctic circumpolar tundra and the three largest pan-Arctic river basins from 2002 to 2016. *Remote Sensing*, *10*(3), 402.

Swanson, D. K., & Nolan, M. (2018). Growth of retrogressive thaw slumps in the Noatak Valley, Alaska, 2010 2016, measured by airborne photogrammetry. *Remote Sensing*, *10*(7), 983.

Szegedy, C., Ioffe, S., Vanhoucke, V., & Alemi, A. A. (2017). Inception-v4, inception-resnet and the impact of residual connections on learning. In *Thirty-first aaai conference on artificial intelligence*.

Szegedy, C., Vanhoucke, V., Ioffe, S., Shlens, J., & Wojna, Z. (2016). Rethinking the inception architecture for computer vision. In *Proceedings of the ieee conference on computer vision and pattern recognition* (pp. 2818 2826).

Taha, A. A., & Hanbury, A. (2015). Metrics for evaluating 3D medical image segmentation: analysis, selection, and tool. *BMC medical imaging*, *15*(1), 1 28.

Takaku, J., Tadono, T., Tsutsui, K., & Ichikawa, M. (2016). Validation of" AW3D" global DSM generated from Alos Prism. *ISPRS Annals of the Photogrammetry, Remote Sensing and Spatial Information Sciences*, *3*, 25.

Tang, C., Zhu, Q., Wu, W., Huang, W., Hong, C., & Niu, X. (2020). PLANET: improved convolutional neural networks with image enhancement for image classification. *Mathematical Problems in Engineering*, *2020*.

Tang, P., Zhou, W., Tian, B., Chen, F., Li, Z., & Li, G. (2017). Quantification of Temporal Decorrelation in X-, C-, and L-Band Interferometry for the Permafrost Region of the Qinghai Tibet Plateau. *IEEE Geoscience and Remote Sensing Letters*, *14*(12), 2285 2289.

Tanski, G., Wagner, D., Knoblauch, C., Fritz, M., Sachs, T., & Lantuit, H. (2019). Rapid CO2 release from eroding permafrost in seawater. *Geophysical Research Letters*, *46*(20), 11244 11252.

Tape, K. D., Jones, B. M., Arp, C. D., Nitze, I., & Grosse, G. (2018). Tundra be dammed: Beaver colonization of the Arctic. *Global change biology*, *24*(10), 4478 4488.

Tape, K. D., Verbyla, D., & Welker, J. M. (2011). Twentieth century erosion in Arctic Alaska foothills: the influence of shrubs, runoff, and permafrost. *Journal of Geophysical Research: Biogeosciences*, *116*(G4).

Taylor, A. E. (1991). Marine transgression, shoreline emergence: Evidence in seabed and terrestrial ground temperatures of changing relative sea levels, Arctic Canada. *Journal of Geophysical Research: Solid Earth*, *96*(B4), 6893 6909.

Terhaar, J., Lauerwald, R., Regnier, P., Gruber, N., & Bopp, L. (2021). Around one third of current Arctic Ocean primary production sustained by rivers and coastal erosion. *Nature Communications*, *12*(1), 1 10.

Tian, B., Li, Z., Tang, P., Zou, P., Zhang, M., & Niu, F. (2016). Use of intensity and coherence of X-band SAR data to map thermokarst lakes on the Northern Tibetan Plateau. *IEEE Journal of Selected Topics in Applied Earth Observations and Remote Sensing*, *9*(7), 3164 3176.

Tian, B., Li, Z., Zhang, M., Huang, L., Qiu, Y., Li, Z., & Tang, P. (2017). Mapping thermokarst lakes on the Qinghai Tibet Plateau using nonlocal active contours in Chinese GaoFen-2 multispectral imagery. *IEEE Journal of Selected Topics in Applied Earth Observations and Remote Sensing*, *10*(5), 1687 1700.

Torbick, N., Persson, A., Olefeldt, D., Frolking, S., Salas, W., Hagen, S., . . . Li, C. (2012). High resolution mapping of peatland hydroperiod at a high-latitude Swedish mire. *Remote Sensing*, *4*(7), 1974 1994.

Trofaier, A., Bartsch, A., Rees, W., & Leibman, M. (2013). Assessment of spring floods and surface water extent over the Yamalo-Nenets Autonomous District. *Environmental Research Letters*, *8*(4), 045026.

Trofaier, A. M., Westermann, S., & Bartsch, A. (2017). Progress in space-borne studies of permafrost for climate science: Towards a multi-ECV approach. *Remote Sensing of Environment*, *203*, 55 70.

Turner, K. W., Wolfe, B. B., Edwards, T. W., Lantz, T. C., Hall, R. I., & Larocque, G. (2014). Controls on water balance of shallow thermokarst lakes and their relations with catchment characteristics: a multi-year, landscape-scale assessment based on water isotope tracers and remote sensing in Old Crow Flats, Yukon (Canada). *Global change biology*, *20*(5), 1585 1603.

Ulaby, F. T., Moore, R. K., & Fung, A. K. (1982). *Microwave Remote Sensing: Active and Passive, Volume II: Radar Remote Sensing and Surface Scattering and Emission Theory* (Vol. 2). Artech House.

Ulrich, M., Grosse, G., Chabrillat, S., & Schirrmeister, L. (2009). Spectral characterization of periglacial surfaces and geomorphological units in the Arctic Lena Delta using field spectrometry and remote sensing. *Remote Sensing of Environment*, *113*(6), 1220 1235.

Ulrich, M., Grosse, G., Strauss, J., & Schirrmeister, L. (2014). Quantifying wedge-ice volumes in Yedoma and thermokarst basin deposits. *Permafrost and Periglacial Processes*, *25*(3), 151 161.

Ulrich, M., Matthes, H., Schirrmeister, L., Schütze, J., Park, H., Iijima, Y., & Fedorov, A. N. (2017). Differences in behavior and distribution of permafrost-related lakes in Central Yakutia and their response to climatic drivers. *Water Resources Research*, *53*(2), 1167 1188.

University of Maryland Center for Environmental Science. (n.d.). *IAN Symbol Libraries.* `https://ian.umces.edu/symbols/`. (Accessed: September 1st 2020)

University of Oslo - Department of Geosciences. (n.d.). *SatPerm - Satellite-based Permafrost Modeling across a Range of Scales.* `https://www.mn.uio.no/geo/english/research/projects/satperm/`. (Accessed: October 28th 2020)

Van Everdingen, R. O., Association, I. P., et al. (2005). *Multi-Language Glossary of Permafrost and Related Ground-Ice Terms in Chinese, English, French, German, Icelandic, Italian, Norwegian, Polish, Romanian, Russian, Spanish, and Swedish.* Arctic Inst. of North America University of Calgary. (Available at: `https://globalcryospherewatch.org/reference/glossary_docs/Glossary_of_Permafrost_and_Ground-Ice_IPA_2005.pdf`)

Van Vuuren, D. P., Edmonds, J., Kainuma, M., Riahi, K., Thomson, A., Hibbard, K., ... others (2011). The representative concentration pathways: an overview. *Climatic change*, *109*(1), 5 31.

Varon, D., McKeever, J., Jervis, D., Maasakkers, J., Pandey, S., Houweling, S., ... Jacob, D. (2019). Satellite discovery of anomalously large methane point sources from oil/gas production. *Geophysical Research Letters*, *46*(22), 13507 13516.

Veefkind, J., Aben, I., McMullan, K., Förster, H., De Vries, J., Otter, G., ... others (2012). TROPOMI on the ESA Sentinel-5 Precursor: A GMES mission for global

observations of the atmospheric composition for climate, air quality and ozone layer applications. *Remote sensing of environment*, *120*, 70 83.

Veremeeva, A., & Gubin, S. (2009). Modern tundra landscapes of the Kolyma Lowland and their evolution in the Holocene. *Permafrost and periglacial processes*, *20*(4), 399 406.

Vesakoski, J.-M., Nylén, T., Arheimer, B., Gustafsson, D., Isberg, K., Holopainen, M., ... Alho, P. (2017). Arctic Mackenzie Delta channel planform evolution during 1983 2013 utilising Landsat data and hydrological time series. *Hydrological Processes*, *31*(22), 3979 3995.

Vieira, G., Mora, C., Pina, P., & Schaefer, C. E. (2014). A proxy for snow cover and winter ground surface cooling: mapping Usnea sp. communities using high resolution remote sensing imagery (maritime Antarctica). *Geomorphology*, *225*, 69 75.

Villarroel, C. D., Tamburini Beliveau, G., Forte, A. P., Monserrat, O., & Morvillo, M. (2018). DInSAR for a Regional inventory of active rock glaciers in the dry andes mountains of argentina and chile with sentinel-1 data. *Remote Sensing*, *10*(10), 1588.

Voigt, C., Lamprecht, R. E., Marushchak, M. E., Lind, S. E., Novakovskiy, A., Aurela, M., ... Biasi, C. (2017). Warming of subarctic tundra increases emissions of all three important greenhouse gases carbon dioxide, methane, and nitrous oxide. *Global Change Biology*, *23*(8), 3121 3138.

Vonder Mühll, D., Noetzli, J., & Roer, I. (2008). PERMOS - A comprehensive monitoring network of mountain permafrost in the Swiss Alps. In *9th international conference on permafrost, fairbanks, alaska* (pp. 1869 1874). University of Zurich.

Vonk, J. E., Sánchez-García, L., Van Dongen, B., Alling, V., Kosmach, D., Charkin, A., ... others (2012). Activation of old carbon by erosion of coastal and subsea permafrost in Arctic Siberia. *Nature*, *489*(7414), 137 140.

Vorovencii, I. (2014). A change vector analysis technique for monitoring land cover changes in Copsa Mica, Romania, in the period 1985 2011. *Environmental monitoring and assessment*, *186*(9), 5951 5968.

Walker, D., Leibman, M., Epstein, H., Forbes, B., Bhatt, U., Raynolds, M., ... others (2009). Spatial and temporal patterns of greenness on the Yamal Peninsula, Russia: interactions of ecological and social factors affecting the Arctic normalized difference vegetation index. *Environmental Research Letters*, *4*(4), 045004.

Walker, D. A., Raynolds, M. K., Daniëls, F. J., Einarsson, E., Elvebakk, A., Gould, W. A., ... others (2005). The circumpolar Arctic vegetation map. *Journal of Vegetation Science*, *16*(3), 267 282.

Wanchang, Z., Ogawa, K., Besheng, Y., & Yamaguchi, Y. (2000). A monthly stream flow model for estimating the potential changes of river runoff on the projected global warming. *Hydrological Processes*, *14*(10), 1851 1868.

Wang, C., Zhang, Z., Paloscia, S., Zhang, H., Wu, F., & Wu, Q. (2018). Permafrost Soil Moisture Monitoring Using Multi-Temporal TerraSAR-X Data in Beiluhe of Northern Tibet, China. *Remote Sensing*, *10*(10), 1577.

Wang, C., Zhang, Z., Zhang, H., Wu, Q., Zhang, B., & Tang, Y. (2017). Seasonal deformation features on Qinghai-Tibet railway observed using time-series InSAR technique with high-resolution TerraSAR-X images. *Remote sensing letters*, *8*(1), 1 10.

Wang, C., Zhang, Z., Zhang, H., Zhang, B., Tang, Y., & Wu, Q. (2018). Active layer thickness retrieval of Qinghai Tibet permafrost using the TerraSAR-X InSAR technique. *IEEE Journal of Selected Topics in Applied Earth Observations and Remote Sensing*, *11*(11), 4403 4413.

Wang, J., Jiang, L., Cui, H., Wang, G., Yang, J., Liu, X., & Su, X. (2020). Evaluation and analysis of SMAP, AMSR2 and MEaSUREs freeze/thaw products in China. *Remote Sensing of Environment*, *242*, 111734.

Wang, J., Li, D., Cao, W., Lou, X., Shi, A., & Zhang, H. (2022). Remote Sensing Analysis of Erosion in Arctic Coastal Areas of Alaska and Eastern Siberia. *Remote Sensing*, *14*(3), 589.

Wang, L., Jolivel, M., Marzahn, P., Bernier, M., & Ludwig, R. (2018). Thermokarst pond dynamics in subarctic environment monitoring with radar remote sensing. *Permafrost and Periglacial Processes*, *29*(4), 231 245.

Wang, L., Marzahn, P., Bernier, M., Jacome, A., Poulin, J., & Ludwig, R. (2017). Comparison of TerraSAR-X and ALOS PALSAR differential interferometry with multisource DEMs for monitoring ground displacement in a discontinuous permafrost region. *IEEE Journal of Selected Topics in Applied Earth Observations and Remote Sensing*, *10*(9), 4074 4093.

Wang, L., Marzahn, P., Bernier, M., & Ludwig, R. (2018). Mapping permafrost landscape features using object-based image classification of multi-temporal SAR images. *ISPRS Journal of Photogrammetry and Remote Sensing*, *141*, 10 29.

Wang, M., & Overland, J. E. (2009). A sea ice free summer Arctic within 30 years? *Geophysical research letters*, *36*(7).

Wang, M., & Overland, J. E. (2012). A sea ice free summer Arctic within 30 years: An update from CMIP5 models. *Geophysical Research Letters*, *39*(18).

Wang, X., Liu, L., Zhao, L., Wu, T., Li, Z., & Liu, G. (2017). Mapping and inventorying active rock glaciers in the northern Tien Shan of China using satellite SAR interferometry. *The Cryosphere*, *11*(2), 997 1014.

Watanabe, S., Laurion, I., Chokmani, K., Pienitz, R., & Vincent, W. F. (2011). Optical diversity of thaw ponds in discontinuous permafrost: A model system for water color analysis. *Journal of Geophysical Research: Biogeosciences*, *116*(G2).

Watts, J. D., Kimball, J. S., Bartsch, A., & McDonald, K. C. (2014). Surface water inundation in the boreal-Arctic: potential impacts on regional methane emissions. *Environmental Research Letters*, *9*(7), 075001.

Watts, J. D., Kimball, J. S., Jones, L. A., Schroeder, R., & McDonald, K. C. (2012). Satellite Microwave remote sensing of contrasting surface water inundation changes within the Arctic Boreal Region. *Remote Sensing of Environment*, *127*, 223 236.

Wegmann, M., Leutner, B., & Dech, S. (2016). *Remote sensing and GIS for ecologists: using open source software.* Pelagic Publishing Ltd.

Wessel, P., & Smith, W. H. (1996). A global, self-consistent, hierarchical, high-resolution shoreline database. *Journal of Geophysical Research: Solid Earth*, *101*(B4), 8741 8743.

Westergaard-Nielsen, A., Karami, M., Hansen, B. U., Westermann, S., & Elberling, B. (2018). Contrasting temperature trends across the ice-free part of Greenland. *Scientific reports*, *8*(1), 1 6.

Westermann, S., Duguay, C. R., Grosse, G., & Kääb, A. (2014). Remote sensing of permafrost and frozen ground. In *Remote sensing of the cryosphere* (pp. 307 344). John Wiley & Sons, Ltd. doi: 10.1002/9781118368909.ch13

Westermann, S., Elberling, B., Højlund Pedersen, S., Stendel, M., Hansen, B., & Liston, G. (2015). Future permafrost conditions along environmental gradients in Zackenberg, Greenland. *The Cryosphere*, *9*(2), 719 735.

Westermann, S., Langer, M., & Boike, J. (2011). Spatial and temporal variations of summer surface temperatures of high-arctic tundra on Svalbard implications for MODIS LST based permafrost monitoring. *Remote Sensing of Environment*, *115*(3), 908 922.

Westermann, S., Langer, M., & Boike, J. (2012). Systematic bias of average winter-time land surface temperatures inferred from MODIS at a site on Svalbard, Norway. *Remote Sensing of Environment*, *118*, 162 167.

Westermann, S., Østby, T., Gisnås, K., Schuler, T., & Etzelmüller, B. (2015). A ground temperature map of the North Atlantic permafrost region based on remote sensing and reanalysis data. *The Cryosphere*, *9*(3), 1303 1319.

Westermann, S., Peter, M., Langer, M., Schwamborn, G., Schirrmeister, L., Etzelmüller, B., & Boike, J. (2017). Transient modeling of the ground thermal conditions using satellite data in the Lena River delta, Siberia. *The Cryosphere*, *11*(3), 1441 1463.

Westermann, S., Strozzi, T., Wiesmann, A., Aalstad, K., Fiddes, J., Kääb, A., . . . Bartsch, A. (2018, 12). Circumpolar mapping of permafrost temperature and thaw depth in the ESA Permafrost CCI project. In *Agu fall meeting 2018.* Washington, D.C., USA: AGU.

Whiteman, G., Hope, C., & Wadhams, P. (2013). Vast costs of Arctic change. *Nature*, *499*(7459), 401 403.

Whitley, M. A., Frost, G. V., Jorgenson, M. T., Macander, M. J., Maio, C. V., & Winder, S. G. (2018). Assessment of LiDAR and spectral techniques for high-resolution mapping of sporadic permafrost on the Yukon-Kuskokwim Delta, Alaska. *Remote Sensing*, *10*(2), 258.

Widhalm, B., Bartsch, A., Leibman, M., & Khomutov, A. (2017). Active-layer thickness estimation from X-band SAR backscatter intensity. *The Cryosphere*, *11*(1), 483 496.

Woelders, L., Lenaerts, J. T., Hagemans, K., Akkerman, K., van Hoof, T. B., & Hoek, W. Z. (2018). Recent climate warming drives ecological change in a remote high-Arctic lake. *Scientific reports*, *8*(1), 1 8.

Wullschleger, S., Hinzman, L., & Wilson, C. (2011, 04). Planning the Next Generation of Arctic Ecosystem Experiments. *Eos, Transactions American Geophysical Union*, *90*. doi: 10.1029/2011EO170006

Wullschleger, S. D. (2019). *Support for Next-Generation Ecosystem Experiments (NGEE Arctic) Field Campaign Report* (Tech. Rep.). Washington, D.C., USA: DOE Office of Science Atmospheric Radiation Measurement (ARM) Program.

Xia, J., McGuire, A. D., Lawrence, D., Burke, E., Chen, G., Chen, X., . . . others (2017). Terrestrial ecosystem model performance in simulating productivity and its vulnerability to climate change in the northern permafrost region. *Journal of Geophysical Research: Biogeosciences*, *122*(2), 430 446.

Xie, C., Li, Z., Xu, J., & Li, X. (2010). Analysis of deformation over permafrost regions of Qinghai-Tibet plateau based on permanent scatterers. *International Journal of Remote Sensing*, *31*(8), 1995 2008.

Xie, S., Girshick, R., Dollár, P., Tu, Z., & He, K. (2017). Aggregated residual transformations for deep neural networks. In *Proceedings of the ieee conference on computer vision and pattern recognition* (pp. 1492 1500).

Xu, M., Kang, S., Chen, X., Wu, H., Wang, X., & Su, Z. (2018). Detection of hydrological variations and their impacts on vegetation from multiple satellite observations in the Three-River Source Region of the Tibetan Plateau. *Science of the total environment*, *639*, 1220 1232.

Xu, M., Kang, S., Wang, X., Pepin, N., & Wu, H. (2019). Understanding changes in the water budget driven by climate change in cryospheric-dominated watershed of the northeast Tibetan Plateau, China. *Hydrological Processes*, *33*(7), 1040 1058.

Xue, X., Guo, J., Han, B., Sun, Q., & Liu, L. (2009). The effect of climate warming and permafrost thaw on desertification in the Qinghai Tibetan Plateau. *Geomorphology*, *108*(3-4), 182 190.

Yamazaki, T., Ohta, T., Suzuki, R., & Ohata, T. (2007). Flux variation in a Siberian taiga forest near Yakutsk estimated by a one-dimensional model with routine data, 1986 2000. *Hydrological Processes: An International Journal*, *21*(15), 2009 2015.

Yang, M., Nelson, F. E., Shiklomanov, N. I., Guo, D., & Wan, G. (2010). Permafrost degradation and its environmental effects on the Tibetan Plateau: A review of recent research. *Earth-Science Reviews*, *103*(1-2), 31 44.

Yang, W., Wang, Y., Liu, X., Zhao, H., Shao, R., & Wang, G. (2020). Evaluation of the rescaled complementary principle in the estimation of evaporation on the Tibetan Plateau. *Science of the Total Environment*, *699*, 134367.

Yao, F., Wang, J., Yang, K., Wang, C., Walter, B. A., & Crétaux, J.-F. (2018). Lake storage variation on the endorheic Tibetan Plateau and its attribution to climate change since the new millennium. *Environmental Research Letters*, *13*(6), 064011.

Yi, S., Zhou, Z., Ren, S., Xu, M., Qin, Y., Chen, S., & Ye, B. (2011). Effects of permafrost degradation on alpine grassland in a semi-arid basin on the Qinghai Tibetan Plateau. *Environmental Research Letters*, *6*(4), 045403.

Yi, Y., Kimball, J. S., Chen, R. H., Moghaddam, M., & Miller, C. E. (2019). Sensitivity of active-layer freezing process to snow cover in Arctic Alaska. *The Cryosphere*, *13*(1), 197 218.

Yi, Y., Kimball, J. S., Chen, R. H., Moghaddam, M., Reichle, R. H., Mishra, U., . . . Oechel, W. C. (2018). Characterizing permafrost active layer dynamics and sensitivity to landscape spatial heterogeneity in Alaska. *The Cryosphere*, *12*(1), 145 161.

Yi, Y., Kimball, J. S., Rawlins, M. A., Moghaddam, M., & Euskirchen, E. S. (2015). The role of snow cover affecting boreal-arctic soil freeze thaw and carbon dynamics. *Biogeosciences*, *12*(19), 5811 5829.

Yin, G., Niu, F., Lin, Z., Luo, J., & Liu, M. (2017). Effects of local factors and climate on permafrost conditions and distribution in Beiluhe basin, Qinghai-Tibet Plateau, China. *Science of the Total Environment*, *581*, 472 485.

Yin, G., Zheng, H., Niu, F., Luo, J., Lin, Z., & Liu, M. (2018). Numerical mapping and modeling permafrost thermal dynamics across the Qinghai-Tibet engineering corridor, China integrated with remote sensing. *Remote Sensing*, *10*(12), 2069.

Yoshikawa, K., & Hinzman, L. D. (2003). Shrinking thermokarst ponds and groundwater dynamics in discontinuous permafrost near Council, Alaska. *Permafrost and Periglacial Processes*, *14*(2), 151 160.

Yu, L., & Gong, P. (2012). Google Earth as a virtual globe tool for Earth science applications at the global scale: progress and perspectives. *International Journal of Remote Sensing*, *33*(12), 3966 3986.

Yu, Q., Epstein, H. E., Engstrom, R., Shiklomanov, N., & Strelestskiy, D. (2015). Land cover and land use changes in the oil and gas regions of Northwestern Siberia under changing climatic conditions. *Environmental Research Letters*, *10*(12), 124020.

Zakharova, E. A., Kouraev, A. V., Stephane, G., Franck, G., Desyatkin, R. V., & Desyatkin, A. R. (2018). Recent dynamics of hydro-ecosystems in thermokarst depressions in Central Siberia from satellite and in situ observations: Importance for agriculture and human life. *Science of The Total Environment*, *615*, 1290 1304.

Zhang, T., Armstrong, R., & Smith, J. (2003). Investigation of the near-surface soil freeze-thaw cycle in the contiguous United States: Algorithm development and validation. *Journal of Geophysical Research: Atmospheres*, *108*(D22).

Zhang, T., Barry, R. G., & Armstrong, R. L. (2004). Application of satellite remote sensing techniques to frozen ground studies. *Polar Geography*, *28*(3), 163 196.

Zhang, W., Liljedahl, A. K., Kanevskiy, M., Epstein, H. E., Jones, B. M., Jorgenson, M. T., & Kent, K. (2020). Transferability of the Deep Learning Mask R-CNN Model for Automated Mapping of Ice-Wedge Polygons in High-Resolution Satellite and UAV Images. *Remote Sensing*, *12*(7), 1085.

Zhang, W., Witharana, C., Liljedahl, A. K., & Kanevskiy, M. (2018). Deep convolutional neural networks for automated characterization of arctic ice-wedge polygons in very high spatial resolution aerial imagery. *Remote Sensing*, *10*(9), 1487.

Zhang, X., Zhang, H., Wang, C., Tang, Y., Zhang, B., Wu, F., . . . Zhang, Z. (2019). Time-series InSAR monitoring of permafrost freeze-thaw seasonal displacement over Qinghai Tibetan Plateau using Sentinel-1 data. *Remote Sensing*, *11*(9), 1000.

Zhang, Y., Olthof, I., Fraser, R., & Wolfe, S. A. (2014). A new approach to mapping permafrost and change incorporating uncertainties in ground conditions and climate projections. *The Cryosphere*, *8*(6), 2177 2194.

Zhang, Y., Touzi, R., Feng, W., Hong, G., Lantz, T. C., & Kokelj, S. V. (2021). Landscape-scale variations in near-surface soil temperature and active-layer thickness: Implications for high-resolution permafrost mapping. *Permafrost and Periglacial Processes*, *32*(4), 627 640.

Zhang, Z., Wang, C., Zhang, H., Tang, Y., & Liu, X. (2018). Analysis of permafrost region coherence variation in the Qinghai Tibet Plateau with a high-resolution TerraSAR-X image. *Remote Sensing*, *10*(2), 298.

Zhang, Z., Wang, M., Liu, X., Wang, C., Zhang, H., Tang, Y., & Zhang, B. (2019). Deformation Feature Analysis of Qinghai Tibet Railway Using TerraSAR-X and Sentinel-1A Time-Series Interferometry. *IEEE Journal of Selected Topics in Applied Earth Observations and Remote Sensing*, *12*(12), 5199 5212.

Zhao, R., Li, Z.-w., Feng, G.-c., Wang, Q.-j., & Hu, J. (2016). Monitoring surface deformation over permafrost with an improved SBAS-InSAR algorithm: With emphasis on climatic factors modeling. *Remote Sensing of Environment*, *184*, 276 287.

Zhao, S., Zhang, S., Cheng, W., & Zhou, C. (2019). Model simulation and prediction of Decadal Mountain permafrost distribution based on remote sensing data in the Qilian Mountains from the 1990s to the 2040s. *Remote Sensing*, *11*(2), 183.

Zheng, G., Yang, Y., Yang, D., Dafflon, B., Lei, H., & Yang, H. (2019). Satellite-based simulation of soil freezing/thawing processes in the northeast Tibetan Plateau. *Remote Sensing of Environment*, *231*, 111269.

Zhou, Z., Liu, L., Jiang, L., Feng, W., & Samsonov, S. V. (2019). Using long-term SAR backscatter data to monitor post-fire vegetation recovery in tundra environment. *Remote Sensing*, *11*(19), 2230.

Zhou, Z., Siddiquee, M. M. R., Tajbakhsh, N., & Liang, J. (2019). Unet++: Redesigning skip connections to exploit multiscale features in image segmentation. *IEEE transactions on medical imaging*, *39*(6), 1856 1867.

Zhu, X. X., Tuia, D., Mou, L., Xia, G.-S., Zhang, L., Xu, F., & Fraundorfer, F. (2017). Deep learning in remote sensing: A comprehensive review and list of resources. *IEEE Geoscience and Remote Sensing Magazine*, *5*(4), 8 36.

Zou, D., Zhao, L., Wu, T., Wu, X., Pang, Q., & Wang, Z. (2014). Modeling ground surface temperature by means of remote sensing data in high-altitude areas: test in the central Tibetan Plateau with application of moderate-resolution imaging spectroradiometer Terra/Aqua land surface temperature and ground-based infrared radiometer. *Journal of Applied Remote Sensing*, *8*(1), 083516.

Zwieback, S., Kokelj, S. V., Günther, F., Boike, J., Grosse, G., & Hajnsek, I. (2018). Sub-seasonal thaw slump mass wasting is not consistently energy limited at the landscape scale. *The Cryosphere*, *12*(2), 549 564.

Zwieback, S., Liu, X., Antonova, S., Heim, B., Bartsch, A., Boike, J., & Hajnsek, I. (2016). A statistical test of phase closure to detect influences on DInSAR deformation estimates besides displacements and decorrelation noise: Two case studies in high-latitude regions. *IEEE Transactions on Geoscience and Remote Sensing*, *54*(9), 5588 5601.

Zwieback, S., Westermann, S., Langer, M., Boike, J., Marsh, P., & Berg, A. (2019). Improving permafrost modeling by assimilating remotely sensed soil moisture. *Water Resources Research*, *55*(3), 1814 1832.

Eidesstattliche Erklärung

Versicherung an Eides Statt

Ich, Marius Balthasar Philipp, wohnhaft in der Zwergstr. 15, 89407 Dillingen mit der Matrikelnummer 1967700 versichere an Eides Statt durch meine Unterschrift, dass ich die Dissertation „Quantifying the Effects of Permafrost Degradation in Arctic Coastal Environments via Satellite Earth Observation" selbständig und ohne fremde Hilfe angefertigt, alle Stellen, die ich wörtlich oder dem Sinne nach aus Veröffentlichungen entnommen habe, als solche kenntlich gemacht und ich auch keine anderen als die von mir angegebenen Quellen und Hilfsmittel benutzt habe. Ich versichere an Eides Statt durch meine Unterschrift, dass ich die Regeln der Universität Würzburg über gute wissenschaftliche Praxis eingehalten habe, insbesondere, dass ich die Gelegenheit zum Promotionsvorhaben nicht kommerziell vermittelt bekommen und insbesondere nicht eine Person oder Organisation eingeschaltet habe, die gegen Entgelt Betreuer bzw. Betreuerinnen für die Anfertigung von Dissertationen sucht.

Ich versichere an Eides Statt, dass ich die vorgenannten Angaben nach bestem Wissen und Gewissen gemacht habe und dass die Angaben der Wahrheit entsprechen und ich nichts verschwiegen habe. Die Strafbarkeit einer falschen eidesstattlichen Versicherung ist mir bekannt, namentlich die Strafandrohung gemäß § 156 StGB bis zu drei Jahren Freiheitsstrafe oder Geldstrafe bei vorsätzlicher Begehung der Tat bzw. gemäß § 161 Abs.1 StGB bis zu einem Jahr Freiheitsstrafe oder Geldstrafe bei fahrlässiger Begehung.

———————

Dillingen, den 30.03.2023